A search for stable massive particles carrying electric charges in the range of 2e to 6e in proton-proton collisions at $\sqrt{s} = 7$ TeV recorded with the ATLAS detector at the LHC

Dissertation
zur
Erlangung des Doktorgrades (Dr. rer. nat.)
der
Mathematisch-Naturwissenschaftlichen Fakultät
der
Rheinischen Friedrich-Wilhelms-Universität Bonn

von
Simone Zimmermann
aus
Osnabrück

Bonn, 29.04.2013

Dieser Forschungsbericht wurde als Dissertation von der Mathematisch-Naturwissenschaftlichen Fakultät der Universität Bonn angenommen und ist auf dem Hochschulschriftenserver der ULB Bonn `http://hss.ulb.uni-bonn.de/diss_online` elektronisch publiziert.

1. Gutachter: Prof. Dr. Klaus Desch
2. Gutachterin: Prof. Dr. Ian Brock

Tag der Promotion: 11.06.2013
Erscheinungsjahr: 2013

Für Helga

Summary

This dissertation presents a search for long-lived, multi-charged particles using the ATLAS detector at the LHC. Motivation for this search arose from an unexploited search regime at ATLAS of stable massive particles with electric charges of $|q| = 2e$ to $|q| = 5e$. Additional motivation can be found in several beyond the Standard Model physics theories.

Proton-proton collisions recorded during the 2011 LHC running at $\sqrt{s} = 7$ TeV, corresponding to an integrated luminosity of 4.4 fb^{-1}, are examined in a signature-based analysis. The search seeks out charged particle tracks exhibiting anomalously high ionization consistent with stable massive particles with electric charges in the range from $|q| = 2e$ to $|q| = 6e$.

For this search, new variables of specific energy loss per path length ($\mathrm{d}E/\mathrm{d}x$) are used in the candidate selection. One of these variables, the TRT $\mathrm{d}E/\mathrm{d}x$, is developed in the course of this thesis and is described in detail. No excess is observed with respect to the prediction of Standard Model processes. The 95% C.L. upper cross section limits are also interpreted as mass exclusion limits for a simplified Drell-Yan production model.

Contents

5 Development of a TRT dE/dx 41

6 Identification of multi-charged particles 61

CHAPTER 1

Introduction

Particle physics investigates and describes the smallest constituents of matter known to date. In this endeavor one of the most successful theories in the history of science has been established. The Standard Model of Particle Physics (SM) has passed all experimental tests up to now. Nevertheless, there is a consensus among particle physicists, that the SM cannot be the whole truth and many extensions of the model are discussed. To test these theories and the SM, particle collisions at unprecedented energies are studied at the CERN Large Hadron Collider (LHC) [1] near Geneva, Switzerland. In an underground tunnel ring of 27 km circumference, counter-rotating bundles of protons are accelerated in two vacuum beam pipes and brought to collide at four dedicated crossing points. In some of these collisions a large amount of energy and momentum is transferred between two colliding protons. From this, new particles can be produced following Einstein's equation $E = mc^2$. The LHC with its maximal center-of-mass energy of currently $\sqrt{s} = 8$ TeV[1] promises a high discovery potential for particles predicted by physics beyond the Standard Model (BSM).

Around the collision points, particle detectors are located that aim to record the trajectories and the energies of all created particles in the collisions. The ATLAS detector [2] is one of four large experiments at the LHC studying proton-proton collisions. The discovery of a Higgs-like boson at two LHC experiments (ATLAS and CMS [3]) announced in July 2012 [4, 5] likely completes the SM. Despite many dedicated searches, only very few indications for BSM physics have been found at the LHC to date [6, 7].

Most particle physics analyses are done with a particular physics model in mind and designed according to predictions made in this model. A different approach is followed by so-called *blue-sky searches*, which look for what is conceivable independent of particular models. This dissertation presents a blue-sky search for heavy, stable[2] particles carrying multiple charges with the ATLAS detector at the LHC [8]. Any evidence of such particles would be a clear indication for BSM physics. Firstly, the SM does not predict stable particles with masses on the order of $O(100\text{ GeV})$. All known particles in this mass range decay almost immediately into lighter particles unless some conservation law prohibits or suppresses this decay. Furthermore, there are no fundamental particles carrying electric charges $|q| = 2, 3, 4, 5$ and $6e$ predicted in the SM. Any known particle with charge greater than $|q| = 1e$ is a composite particle of quarks and gluons and hence subject to the strong interaction. In this analysis,

---

[1] In particle physics $\sqrt{s} = \sqrt{(p_1 + p_2)^2}$ is commonly used as an abbreviation for center-of-mass energy of the two colliding particles with four momenta $p_{1/2}$.

[2] In this thesis, stable means stable within the dimensions of the detector.

the new particles are assumed to reach the outermost ATLAS subdetector. This automatically excludes strongly interacting particles, such that only lepton-like signatures must be considered.

1.1 Measuring multi-charged particles

The analysis presented in this thesis takes advantage of striking differences between SM particles and hypothetical massive and multi-charged particles in the interaction with the detector material.

A useful variable to describe these interactions can be constructed from the specific energy loss per path length, $\mathrm{d}E/\mathrm{d}x$. It is proportional to the square of the particle charge q. As a consequence, multi-charged particles have a significantly higher energy loss per path length in the detector compared to SM particles. $\mathrm{d}E/\mathrm{d}x$ can thus be used to identify these particles. Moreover, the high mass of the multi-charged particles leads to an additional enhancement of $\mathrm{d}E/\mathrm{d}x$. The high energy losses in the detector slow down the multi-charged particles. As a consequence, their momentum in the outer detector parts can deviate significantly from the momentum measured in the central part of the detector.

Another aspect that needs to be taken into account is the velocity β of the particles. At the center-of-mass energies at the LHC ($\sqrt{s} = 7$ TeV in this analysis), already particles with a mass of 100 GeV have a high probability to be significantly slower than particles that travel at the speed of light, like e.g. muons. Problems arise if the particle becomes too slow to reach the detector subsystems within the time frame of their readout. This time frame is generally chosen to have a high detection efficiency for particles near the speed of light.

Further experimental challenges arise from the momentum reconstruction. The momentum is determined from the curvature of the particle track in a magnetic field assuming charge $|q| = 1e$ of the particle. A track of a particle with electric charge $|q| > 1e$ is bent more strongly in the magnetic field. As a consequence, the momentum is reconstructed a factor of q too low. A particle of charge $|q| = 4e$ and momentum of 200 GeV, for example, appears to carry a momentum of 50 GeV.

1.2 Previous searches for stable massive particles

In the past, there have been numerous searches for stable massive particles, some assuming multiply charged particles, many of which were performed at particle colliders. Even though most searches assume charge $|q| = 1e$, the following review of search results from collider experiments can still give a good idea of previous limits and search techniques. An extensive review of the individual analyses can be found in Appendix A, some important results are summarized in Table 1.1.

The particular charge range chosen in the search presented in this dissertation, $|q| = 2$ - $6e$, bridges a gap between two analyses performed on 2010 ATLAS data: The search for stable massive particles ($|q| = 1e$) [19] and the search for highly ionizing particles ($|q| = 6$ - $17e$) [10]. The latter considers three different particle masses (200, 500 and 1000 GeV) with electric charges $|q| = 6$, 10 and $17e$ each. Highly ionizing tracks are sought out in electron-like signatures. This analysis sets upper cross section limits on the order of 3 - 12 pb at 95% confidence level [10].

The other search, for particles with electric charges $|q| = 1e$, uses three independent measurements of the particle speed β to identify slow stable massive particles in muon-like detector responses. The upper cross section limits derived in this analysis are on the order of 1 pb and are used to exclude several supersymmetric particles[3] with masses below a few hundred GeV at 95% confidence level [19].

Moreover, a search for stable massive particles, assumed to interact hadronically, is performed by ATLAS with data recorded in 2010 [20]. This analysis uses a measurement of $\mathrm{d}E/\mathrm{d}x$ from one ATLAS

---

[3] Particles predicted in Supersymmetry, a BSM theory.

Table 1.1: *Summary of previous searches for stable massive charged particles at colliders. This table only lists one examplary benchmark model in cases were multiple models are considered.*

Collider		Experiment	Charge	cross section 95% CL upper limit	Benchmark Model	Mass exclusion	Ref.
LHC	pp	ATLAS	$\lvert q \rvert = 1e$	$\mathcal{O}(0.001$ pb)	Long-lived $\tilde{\tau}$	<300 GeV	[9]
			$\lvert q \rvert = 1e$	$\mathcal{O}(0.1$ pb)	Long-lived $\tilde{\tau}$	<136 GeV	[9]
			$\lvert q \rvert = 1e$	$\mathcal{O}(1$ pb)	R-hadron	<530 - 544 GeV	[9]
			$\lvert q \rvert = 1e$	$\mathcal{O}(1$ pb)	$\tilde{b}$	<294 GeV	[9]
			$\lvert q \rvert = 1e$	$\mathcal{O}(1$ pb)	$\tilde{t}$	<309 GeV	[9]
			$\lvert q \rvert = 1e$	$\mathcal{O}(1$ pb)	$\tilde{g}$	<562 GeV	[9]
			$\lvert q \rvert = 6e$	$11.5, 7.2, 9.3$ pb	Generic leptons of mass $200, 500, 1000$ GeV	-	[10]
			$\lvert q \rvert = 10e$	$5.9, 4.3, 3.4$ pb	Generic leptons of mass $200, 500, 1000$ GeV	-	[10]
			$\lvert q \rvert = 17e$	$9.1, 5.3, 4.3$ pb	Generic leptons of mass $200, 500, 1000$ GeV	-	[10]
		CMS	$\lvert q \rvert = 1e$	0.0003 - 0.0013 pb	Drell-Yan	<608 GeV	[11]
			$\lvert q \rvert = 2e$	0.0004 - 0.0007 pb	Drell-Yan	<725 GeV	[11]
			$\lvert q \rvert = 3e$	0.0005 - 0.0013 pb	Drell-Yan	<792 GeV	[11]
			$\lvert q \rvert = 4e$	0.0007 - 0.0031 pb	Drell-Yan	<816 GeV	[11]
			$\lvert q \rvert = 5e$	0.001 - 0.010 pb	Drell-Yan	<817 GeV	[11]
Tevatron	$p\bar{p}$	CDF	$\lvert q \rvert = 1e$	0.048 pb	stable $\tilde{t}$	249 GeV	[12]
		D0	$\lvert q \rvert = 1e$	$\mathcal{O}(0.1$ pb)	Gaugino-like chargino	<206 GeV	[13]
				$\mathcal{O}(0.1$ pb)	Higgsino-like chargino	<171 GeV	[13]
				$\mathcal{O}(0.1$ pb)	$\tilde{\tau}$	-	[13]
HERA	ep	H1	$\lvert q \rvert = 1e$	190 pb	-	-	[14]
LEP	e^+e^-	ALEPH	$\lvert q \rvert = 1e$	~ 0.03 pb	$\tilde{\tau}_R$	68 GeV	[15]
					three degenerate co-NLSPs	85 GeV	[15]
		L3	$\lvert q \rvert = 1e$		Generic leptons	102.6 GeV	[16]
		Delphi	$\lvert q \rvert = 1e$	$\mathcal{O}(0.01$ pb)	MSSM stable $\tilde{\mu}$, $\tilde{\tau}$	2 - 88 GeV	[17]
		OPAL	$\lvert q \rvert = 1e$	$\mathcal{O}(0.01$ pb)	CMSSM stable $\tilde{\mu}$, $\tilde{\tau}$	$< \mathcal{O}(98$ GeV)	[18]
			$\lvert q \rvert = 1e$		CMSSM charginos	< 102.0 GeV	[18]
			$\lvert q \rvert = 1e$		heavy charged lepton	< 102.0 GeV	[18]

tracking detector and the particle velocity β determined in the calorimeter. Both variables are utilized to assess the mass of the particle. From these, 95% confidence level upper cross section limits around 1 pb are set, excluding supersymmetric particles below masses of several hundred GeV.

A third search for stable massive particles of charge $|q| = 1e$ was published by ATLAS [9]. This analysis is based on pp collisions recorded in 2011 at a center-of-mass energy of $\sqrt{s} = 7$ TeV. Again the particles velocity β is reconstructed from several measurements of its time of flight, which is complemented by a $\mathrm{d}E/\mathrm{d}x$ measurement. The achieved upper cross section limits are on the order of 0.1 - 0.001 pb and various supersymmetric particles can be excluded below masses in the range of 300 - 1000 GeV.

At the LHC, the CMS collaboration sets further limits on long-lived massive particles with charges $|q| = 1e$ and $|q| = 2$ - $5e$ [11, 21–23]. The limits obtained by CMS for multi-charged particles represent the sole direct comparison for the search performed by ATLAS presented in this thesis. The latest public note released by CMS [23] is based on pp collisions recorded at $\sqrt{s} = 8$ TeV. Production cross sections are constrained to be below 0.01 - 0.001 pb. A simplified Drell-Yan model [24] with pair production of the multi-charged particles via photon or Z-boson exchange [23] yields mass exclusions lower limits between 725 and 817 GeV for particles with charges $|q| = 2,\ 3,\ 4,$ and $5e$.

In addition, limits on the production cross section of stable massive particles carrying $|q| = 1e$ are available from both the D0 [13] and CDF [12, 25] experiment at the $p\bar{p}$ collider Tevatron at Fermilab (Fermi National Accelerator Laboratory). The obtained cross section limits are in the range of $\mathcal{O}(0.05$ - 0.10 pb) excluding several supersymmetric particles below ~200 GeV. The H1 collaboration at HERA, an electron-positron collider at DESY, sets a limit on the production cross section of long-lived charged particles of 0.19 nb [14]. A large variety of searches for long-lived charged particles was performed at LEP, the preceding accelerator in the LHC tunnel. At this e^+e^- collider, all four experiments [15–18] set cross section limits of typically $\mathcal{O}(0.01$ pb), reaching mass exclusions of up to ~100 GeV.

1.3 The 2011 search for multi-charged particles

The analysis in this dissertation follows the approach of a blue-sky search for physics beyond the SM. Additional motivation can be found in models predicting stable massive and sometimes multi-charged particles. A brief overview of possible models is given in Chapter 2 after a review of the Standard Model of Particle Physics. This is followed by an introduction to the Large Hadron Collider and the ATLAS detector (Chapter 3), the experimental setup of this work. A special focus is set on particle identification methods available at ATLAS in Chapter 4. One particular method, the TRT $\mathrm{d}E/\mathrm{d}x$, has been developed in the course of this dissertation and is presented in Chapter 5. The benchmark model and the kinematic features of multi-charged particles are discussed in Chapter 6. The detailed analysis strategy and results of this analysis are subject of Chapter 7 and 8, before the summary in Chapter 9.

CHAPTER 2

From the Standard Model of particle physics to stable multi-charged particles

The motivation to search for multi-charged particles is driven by the possibility to look for their experimental signature, rather than to test a certain theory of BSM physics. Nevertheless, this chapter focuses on the theory side of particle physics. It starts with a review of the Standard Model in Section 2.1, including some of the shortcomings of the model. This is followed by a discussion of models predicting long-lived massive particles in Section 2.2.

2.1 Review of the Standard Model of particle physics

The Standard Model of Particle Physics [26–29] is an extremely successful physics theory. So far it has passed all tests up to the highest precision. Figure 2.1 shows an example of the level of agreement between theoretical predictions and experimental observation. Several production cross sections of different physics processes as measured by the ATLAS collaboration are compared to predictions made in the SM.

The SM unites three of the four fundamental forces, the electro-magnetic, strong and weak force and describes the interactions of all fundamental particles known to date. These particles are introduced in Section 2.1.1, followed by a review of the electroweak theory (Section 2.1.2) and the theory of the strong interactions, quantum chromodynamics, in Section 2.1.3. Motivation for extensions of the SM are listed in Section 2.1.4.

Unless stated otherwise, the following review follows [31] and [32].

2.1.1 The particle content of the Standard Model

The fundamental particles can be grouped according to their spin in fermions (half-integer spin) and bosons (integer spin). All matter consists of fermions, which exist in three *generations* or *families*. Each generation differs from the other in the mass of its particles. Further distinctions can be made into leptons and quarks. Examples for leptons are the electron and its heavier copies called muon (μ^-) and tau (τ^-). In addition to these particles carrying electric charge $-1e$, almost mass-less neutral particles, the neutrinos (ν_e, ν_μ, ν_τ) exist in three generations. Moreover, the SM describes three generations of quarks, with charges 2/3e or -1/3e. No quark q can exist freely, they form baryons made up of three quarks (qqq) or mesons of one quark and one anti-quark ($q\bar{q}$). For each particle, an antiparticle with

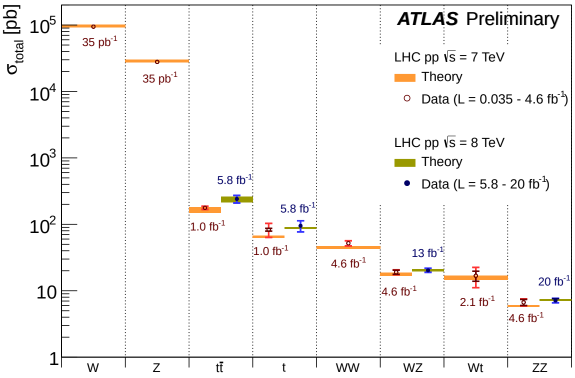

Figure 2.1: *Summary of several Standard Model total production cross section measurements, corrected for leptonic branching fractions, compared to the corresponding theoretical expectations. All theoretical expectations are calculated at NLO or higher [30].*

Table 2.1: *The fermionic particle content of the Standard Model of Particle Physics with the particles' masses, charges and the weak isospin [33].*

			Generation		Charge	Weak Isospin
		First	Second	Third	Q [e]	I_3
Leptons		ν_e	ν_μ	ν_τ	0	$+\frac{1}{2}$
	mass	< 2 eV	< 0.19 MeV	< 18.2 MeV		
		e^-	μ^-	τ^-	-1	$-\frac{1}{2}$
	mass	511 keV	105.66 MeV	1.777 GeV		
Quarks		**u**	**c**	**t**	$+\frac{2}{3}$	$+\frac{1}{2}$
	mass	2.3 MeV	1.275 GeV	173.5 GeV		
		d	**s**	**b**	$-\frac{1}{3}$	$-\frac{1}{2}$
	mass	4.8 MeV	95 MeV	4.18 GeV		

identical properties but opposite charge exists. Matter and antimatter annihilate immediately in the presence of each other and the universe is dominated by matter. Nevertheless, antiparticles can be created in the laboratory. Table 2.1 gives a summary of the fermionic particle content of the Standard Model.

Particles interact with each other via the exchange of bosons, which is why bosons are also referred to as force carriers. The electromagnetic force is mediated by the mass-less photon (γ) and acts upon all particles carrying electric charge. All particles, regardless of their electric charge, are subject to the weak interaction mediated by the massive bosons Z^0, W^+ and W^-. The strong force affects only hadronic particles, that is baryons or mesons. Their constituents, the quarks, carry an additional quantum number called color charge with three allowed states (red, green and blue). Their interaction is mediated via eight mass-less gluons (g). The exchange bosons are summarized in Table 2.2.

2.1.2 Electroweak theory

The electromagnetic interactions are described in a theory called Quantum Electrodynamics (QED), which can be united with the theory of weak interactions in the electroweak theory, based on a $SU(2)_L \times$

Table 2.2: *The exchange bosons of the Standard Model of Particle Physics with their masses and charges.*

	Electroweak			QCD
	γ	$\mathbf{Z}^0$	$\mathbf{W}^\pm$	**g**
charge [e]	0	0	±1	0
mass [GeV]	-	91.19 GeV	80.43 GeV	-

$U(1)_Y$ gauge symmetry. The fundamental vertex of QED is given by the coupling of a photon to a charged lepton or quark (see Figure 2.2a). The weak interaction is mediated either by the Z^0 boson for neutral interactions (Figure 2.2b) or the $W^\pm$ bosons (Figure 2.2c) for interactions with charge exchange. The leptonic weak vertices always connect leptons and neutrinos of the same generation, whereas in the hadronic interactions the quark color is conserved but not it's flavor, that is the type of quark. Therefore, in hadronic weak interactions with charge exchange the weak force couples to pairs of

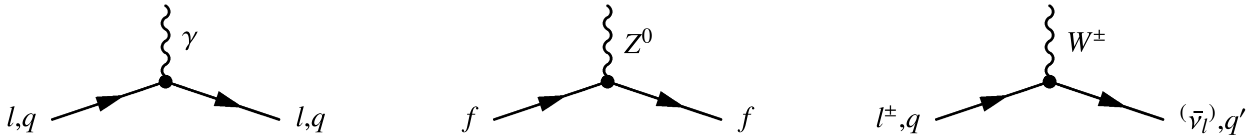

(a) QED (b) Neutral Weak (c) Charged Weak

Figure 2.2: *The fundamental vertices of the electroweak interactions. In QED (a) the photon couples to any charged fermion. The neutral weak interaction (b) is mediated by the Z^0 boson. In this process f stands for any lepton or quark (including neutrinos). (c) shows the charged weak interaction mediated by the $W^\pm$ bosons. Here a (anti-)lepton converts into its corresponding (anti-)neutrino or a (anti-)quark q into its partner (anti-)quark q' of the same generation. The missing charge is carried away by the charged bosons.*

$$\begin{pmatrix} u \\ d' \end{pmatrix}, \begin{pmatrix} c \\ s' \end{pmatrix}, \begin{pmatrix} t \\ b' \end{pmatrix},$$

where d', s' and b' are linear combinations of the quarks d, s and b defined via the CKM matrix

$$\begin{pmatrix} d' \\ s' \\ b' \end{pmatrix} = \begin{pmatrix} V_{ud} & V_{us} & V_{ub} \\ V_{cd} & V_{cs} & V_{cb} \\ V_{td} & V_{ts} & V_{tb} \end{pmatrix} \begin{pmatrix} d \\ s \\ b \end{pmatrix}. \tag{2.1}$$

The combined $SU(2)_L \times U(1)_Y$ gauge transformations are different for left-handed and right-handed fields[1], which are projected out from the usual Dirac field Ψ by

$$\text{left-handed} \qquad \Psi_\mathrm{L} = \frac{1-\gamma_5}{2}\Psi\,, \tag{2.2}$$

$$\text{right-handed} \qquad \Psi_\mathrm{R} = \frac{1+\gamma_5}{2}\Psi\,. \tag{2.3}$$

---

[1] Massless fermions are right-handed if their spin and direction of motion are aligned in the same direction and left-handed if they are aligned in opposite directions.

Here $\gamma^5 := i\gamma^0\gamma^1\gamma^2\gamma^3$ is the product of all four gamma matrices. The *weak isospin group* $SU(2)_L$ has quantum numbers I and I_3. All left-handed fields with $I = 1/2$ occur as doublets of the form

$$\begin{pmatrix}\nu_e\\ e\end{pmatrix}_{\mathrm{L}}, \begin{pmatrix}u\\ d\end{pmatrix}_{\mathrm{L}}, \qquad \begin{pmatrix}\nu_\mu\\ \mu\end{pmatrix}_{\mathrm{L}}, \begin{pmatrix}c\\ s\end{pmatrix}_{\mathrm{L}}, \qquad \begin{pmatrix}\nu_\tau\\ \tau\end{pmatrix}_{\mathrm{L}}, \begin{pmatrix}t\\ b\end{pmatrix}_{\mathrm{L}}$$

and transform under the unitary matrix $U = \exp(i\alpha^a\sigma^a/2)$ with $a = 1, 2, 3$. The right-handed fields have $I = 0$ and are singlets invariant under weak isospin transformation

$$e_{\mathrm{R}}\ u_{\mathrm{R}}\ d_{\mathrm{R}} \qquad \mu_{\mathrm{R}}\ c_{\mathrm{R}}\ s_{\mathrm{R}} \qquad \tau_{\mathrm{R}}\ t_{\mathrm{R}}\ b_{\mathrm{R}}\ .$$

Note that there are no right-handed neutrinos in the SM. This is due to the fact, that they are treated as massless particles[2].

The $U(1)_Y$ gauge symmetry can be represented as a multiplicative phase factor $\exp(i\alpha Y/2)$, with the weak hypercharge Y. It is defined in the *Gell-Mann–Nishijima relation* of the electric charge Q

$$Q = I_3 + \frac{Y}{2}\,. \tag{2.4}$$

Considering the $SU(2)_{\mathrm{L}} \times U(1)_Y$ as the group of gauge transformations under which the Lagrangian is invariant, this gauge symmetry can be incorporated in a gauge invariant field theory which unites the electromagnetic and weak interaction, the electroweak theory. Its full Lagrangian

$$\mathcal{L}_{EW} = \mathcal{L}_{WB} + \mathcal{L}_F + \mathcal{L}_H + \mathcal{L}_Y \tag{2.5}$$

is the sum of the gauge term $\mathcal{L}_{WB}$, the fermion term $\mathcal{L}_F$, the Higgs term $\mathcal{L}_H$ and the Yukawa term $\mathcal{L}_Y$.

In the light of the July 2012 discovery [4, 5] a special emphasis will be put on $\mathcal{L}_H$, the Higgs term. The formalism of the SM assumes zero particle masses, which stands in contradiction to experimental observations. Consequently, an additional field is introduced which leads to particle masses through their interaction with this field. Assuming an isospin doublet of complex-valued scalar fields with hypercharge $Y = 1$

$$\Phi(x) = \begin{pmatrix}\Phi^+(x)\\ \Phi^0(x)\end{pmatrix}, \tag{2.6}$$

in which Φ^+ carries electric charge $Q = 1$ and Φ^0 is neutral, one can construct a Lagrangian

$$\mathcal{L}_H = (D_\mu\Phi)^\dagger(D^\mu\Phi) - V(\Phi) \tag{2.7}$$

with the gauge invariant self interaction

$$\begin{aligned} V(\Phi) &= -\mu^2\Phi^\dagger\Phi + \frac{\lambda}{4}(\Phi^\dagger\Phi)^2 \\ &= \frac{\lambda}{4}(\Phi^\dagger\Phi - \frac{2\mu^2}{\lambda})^2 - \frac{\mu^4}{\lambda}\,. \end{aligned} \tag{2.8}$$

The last term of Equation (2.8) is a constant and can thus be dropped. In the ground state of this potential, the vacuum state, the potential energy must be minimal. For the choice of $\mu^2, \lambda > 0$, the field is of the form of a Mexican hat potential as a function of $|\Phi^+|$ on the z axis and $|\Phi^0|$ on the x and y axes,

---

[2] Recent measurements confirm that neutrinos do have a small mass.

which is minimal for any field configuration of $\Phi^\dagger\Phi = \frac{2\mu^2}{\lambda}$. The resulting vacuum expectation value

$$\langle\Phi\rangle = \frac{1}{\sqrt{2}}\begin{pmatrix}0\\ v\end{pmatrix} \qquad \text{with } v = \frac{2\mu}{\sqrt{\lambda}} \tag{2.9}$$

is not invariant under $SU(2)$ or $U(1)_Y$. Hence the gauge symmetry is broken by the vacuum. Particle excitations arise from deviations of a field from its vacuum expectation value. Rewriting

$$\Phi(x) = \frac{1}{\sqrt{2}}\begin{pmatrix}\Phi_1(x) + i\Phi_2(x)\\ v + H(x) + i\chi(x)\end{pmatrix} \tag{2.10}$$

with real valued Φ_1, Φ_2, $H(x)$ and $\chi(x)$, the Higgs potential can be expressed as

$$V = \mu^2 H^2 + \frac{\mu^2}{v} H(H^2 + \chi^2 + \Phi_1^2 + \Phi_2^2) + \frac{\mu^2}{4v^2}(H^2 + \chi^2 + \Phi_1^2 + \Phi_2^2)^2 \,. \tag{2.11}$$

It can be deduced, that H describes an electrically neutral scalar particle of mass $M_H = \sqrt{2}\mu$, the Higgs boson. Evidence for this particle has presumably been found at the LHC at a mass around 126 GeV [4, 5], completing the particle content of the SM.

2.1.3 Quantum chromodynamics

The strong interactions are described by Quantum Chromodynamics (QCD), a $SU(3)_c$ gauge theory. The index c stands for color and mirrors the fact that the quarks and gluons interact with each other via a color charge associated to this gauge symmetry. Each of the quarks is described by a triplet of color states

$$q = (q_1, q_2, q_3)^T \qquad \text{with } q = u, d, s, c, b, t. \tag{2.12}$$

The gauge fields G^a_μ ($a = 1, \ldots, 8$) represent the 8 possible color states of the gluon. The fundamental vertex of QCD, a gluon coupling to quarks, is shown in Figure 2.3a. Only particles carrying color (quarks and gluons) participate in the strong interactions. Color is conserved in each interaction, taking into account, that no free color is observed. As a consequence, quarks are bound together in colorless singlets, forming color neutral baryons or mesons.

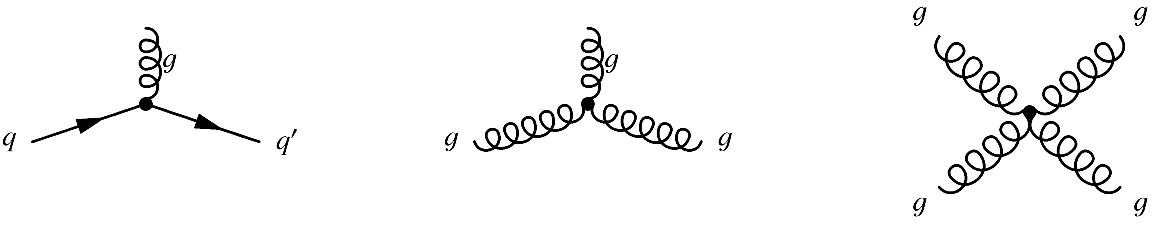

(a) Quark gluon coupling (b) Three gluon self coupling (c) Four gluon self coupling

Figure 2.3: *The fundamental vertices of QCD: $q \to q + g$ (a), three-gluon vertex (b) and four-gluon vertex (c).*

A specialty of QCD in comparison to the electromagnetic theory is the self-interaction of the exchange bosons, the gluons. This is allowed because gluons carry color charge themselves. Furthermore, the coupling constant of QCD α_s is not a real constant as it changes size with the spatial distance between the interacting particles. While it is indeed large for greater distances, it becomes relatively small at very short distances, allowing for the quarks within the proton and neutron to move as quasi free particles. This effect is called *asymptotic freedom*. For small momenta it becomes greater than 1, such that perturbative calculations cannot be applied anymore. The quark mass m_q is a free parameter in QCD.

2.1.4 Open questions in the Standard Model

Even though the SM is an extremely successful theory, it has a few shortcomings [31]. These are discussed in the following.

Gravity

By construction the SM describes only three of the four fundamental forces, making no predictions about gravity at all. Although, gravity governs the dynamics of astrophysical objects like stars and galaxies, it only plays a minor role in the interaction of elementary particles due to its weakness. So far no consistent theory of quantum gravity has been established, but its effect will become important at very high energy scales. Thus, the Standard Model is often regarded as a low energy approximation of some universal theory of all four fundamental forces [31].

Hierarchy problem

A second peculiar problem of the Standard Model is referred to as the hierarchy problem. The mass of the Higgs Boson is measured to be around 126 GeV [4, 5] as was also expected from the scale of the electroweak symmetry breaking $\mathcal{O}(100\ \mathrm{GeV})$. The corrections to this scale, however, are several orders of magnitude higher. To resolve this apparent discrepancy one can resort to *fine-tuning* of tree-level and loop contributions to this Higgs mass or yet undiscovered extensions of the Standard Model [31].

Large number of parameters

Moreover, the SM makes no predictions about the particle masses, coupling strengths or mixing angles, leading to a large number (≈ 19) of free parameters. These have to be set by hand to the experimentally measured values [31].

Matter-antimatter asymmetry

The SM gives no explanation to why the observable universe is dominated by matter particles. A likely explanation is additional CP violation mechanisms. The only observed CP violation is described in the CKM matrix of electroweak theory, which by itself is too small an effect to account for the observed asymmetry. Further CP violation mechanism are thinkable in the lepton sector (*leptogenesis*) or in the strong interactions (*strong CP problem*). None of the two has been observed experimentally to date [32].

Dark matter and dark energy

Finally, the particle content described in the Standard Model makes up only about 5% of the universe. A good quarter of the universe consists of so called dark matter. This matter can, for example, be deduced from astrophysical observations of the rotational velocity of galaxies. They behave as if a vast amount of extra matter is present that interacts only gravitationally with the particles known to date. Obvious candidates for dark matter particles are *Weakly Interacting Massive Particles* (WIMPs) hunted by many dedicated searches at the LHC and in astroparticle physics experiments. Similarly, we have no understanding of 70% of the energy density of the universe that must be present to explain its accelerating expansion [31].

Physics beyond the Standard Model

All these open questions call for extensions or alternative models to the SM. The target particles of the search presented in this thesis are stable massive particles carrying multiple electric charges. Clearly, they are not predicted in the SM. Even though the motivation for this analysis is a so-called *blue sky search*, that is a more experimentally driven approach to look for whatever can be found, a few examples of theories motivating these types of particles are presented in the following.

2.2 Theories predicting stable massive particles

There are numerous theories of physics beyond the Standard Model (SM) predicting long-lived exotic objects with characteristic high ionization. A comprehensive review of stable massive particles at colliders can be found in [34].

The theory of technicolor is based on the idea of replacing the Higgs mechanism by an alternative ansatz for electroweak symmetry breaking inspired by QCD. A new gauge symmetry is introduced alongside a set of massless fermions (techni-fermions), which feel a non-abelian gauge interaction. Problems arise due to Flavor Changing Neutral Currents (FCNC), which are suppressed in the SM and constrained by experimental observations but generally allowed in technicolor models. A possible escape from the problems of classic technicolor is provided in walking technicolor theory [35]. It does not follow QCD-like dynamics and replaces the running coupling constant with a slowly evolving, *walking*, coupling. A model named Minimal Walking Technicolor [35] predicts two techni-quarks U and D, which transform under an adjoint representation of an $SU(2)$ gauge group. The six techni-baryons (UU, UD, DD and their antiparticles) carry a new techni-color but no QCD color charge. Thus, they do not participate in strong interactions and behave as leptons in the detector. They carry electric charges

$$q = \begin{cases} Q+1 \\ Q \\ Q-1 \end{cases} \tag{2.13}$$

for an arbitrary real number Q. In the absence of techni-baryon number violation, the lightest techni-baryon is stable. Furthermore, in this model a fourth family of leptons is postulated. This weakly charged fermionic doublet is a technicolor singlet and carries electric charges

$$q = \begin{cases} (1-3Q)/2 \\ (-1-3Q)/2\,. \end{cases} \tag{2.14}$$

At the LHC, they can be pair-produced and, hence, are an excellent candidate for the multi-charged particles sought for. The production of the techni-baryons, however, is suppressed due to their composite nature. The coupling of the techni-leptons, ζ, to photons and Z bosons can be derived from a generalization of the electron coupling. The resulting cross section is shown for electric charge $-2e$ and weak isospin $I_3 = -\frac{1}{2}$ in Figure 2.4 [36].

In addition, the almost-commutative geometry model [37] describes a new gauge group $U_{AC}(1)$ and charge y. It adds two new massive charged leptons and their antiparticles to the SM. They are $SU(2)$ electroweak singlets with opposite electric charges called A and C and are the only particles carrying the new $U(1)$ gauge charge y. Therefore, they behave as heavy stable leptons. The model makes no

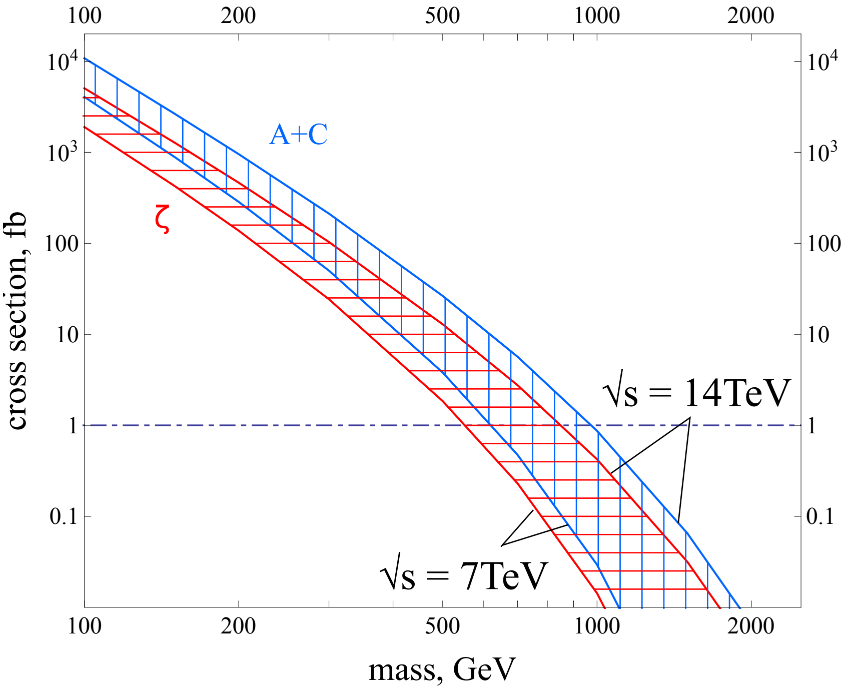

Figure 2.4: Cross section predictions for doubly charged particles in the almost commutative model (A+C) and minimal walking technicolor (ζ) [36]. The shaded area corresponds to cross section predictions at $\sqrt{s}$ = 7-14 TeV.

prediction of the charge of the particles. AC-leptons are sterile to the $SU(2)_L$ gauge group of the SM and hence carry zero weak isospin ($I_3 = 0$). Contrary to SM leptons, their left and right components interact equally leading to an enhancement of the production cross section, shown for $|q| = 2e$ in Figure 2.4 [36].

Due to their electric charges, any of the proposed multi-charged particles introduced above, could be Drell-Yan pair produced at leading order (LO). Additionally, they can be pair produced from radiated photons at next-to-leading order (NLO). The latter leads to an enhancement of the production cross sections. For particles carrying electric charges below $|q| = 6e$, radiative corrections are on the order of $\frac{q^2\alpha}{\pi} < 0.1$. Furthermore, for small velocities β the production cross section is further enhanced [36] (see also [38]). Besides, the additional gauge charge of technicolor or y-charge lead to an enhancement of the production cross section as well. Hence, all NLO corrections to the Drell-Yan production cross section are positive. Therefore, a simplified LO Drell-Yan production cross section can be used as a conservative estimate for the production of multi-charged particles [36]. It is used in the Monte Carlo production for this search described in greater detail in Section 6.1.

Further examples of highly ionizing particles are magnetic monopoles, hypothetical particles consisting of a single magnetic pole, hence carrying a net magnetic charge [33]. Magnetic monopoles have an electromagnetic energy loss in matter three orders of magnitude larger than expected for charge $|q| = 1e$ particles. Similarly, dyons are exotic particles carrying both electric and magnetic charges, predicted in many Grand Unified Theories (GUT) [39]. Moreover, models of low-scale gravity predict long-lived micro black holes [40]. Q-balls are non-topological solitons and exist in minimal supersymmetric models [41]. These could have been produced in the early universe and contribute to dark matter today.

CHAPTER 3

The experimental setup

The search for multi-charged, long-lived particles presented in this dissertation is performed with the full data set recorded by the ATLAS detector in 2011 at the CERN Large Hadron Collider (LHC). This chapter presents the experimental setup for this search. Protons are accelerated and brought to collision by the LHC introduced in Section 3.1. The collisions are recorded with the ATLAS detector. An overview of ATLAS and its individual components is given in Section 3.2. The recorded data is processed and physics objects are reconstructed. A description of the data processing and reconstruction of relevant physics objects (tracks and muons) used in the analysis closes the chapter in Sections 3.3 and 3.4, respectively.

3.1 The Large Hadron Collider

The Large Hadron Collider (LHC) [1] is a proton-proton collider at the Swiss-French border on the outskirts of Geneva, Switzerland. It is 27 km in circumference and hosts four large experiments: ATLAS, CMS [3], ALICE [42] and LHCb [43] (see Figure 3.1). In addition, three smaller experiments, TOTEM [44], LHCf [45] and MoEDAL [46] with very specialized physics programs are installed. The protons accelerated in the LHC originate from a bottle of hydrogen atoms, stripped of their electrons in a strong electric field. These protons undergo a chain of one linear, followed by three ring accelerators at the end of which they are inserted into the two counter-rotating LHC rings at 450 GeV. In the LHC rings, the proton beams are accelerated at a linear stretch with radio frequency (RF) cavities to a design energy of 7 TeV each. This results in a design center-of-mass energy at collision of $\sqrt{s} = 14$ TeV. In 2011, the LHC reached $\sqrt{s} = 7$ TeV (3.5 TeV each beam), which could be upgraded to $\sqrt{s} = 8$ TeV in 2012.

The instantaneous luminosity L is an important variable to judge the performance of a particle accelerator. It gives the number of possible interactions per second and unit area ($\mathrm{cm}^{-2}\,\mathrm{s}^{-1}$) and can be expressed as [33]

$$L = f \frac{n_1 n_2}{4\pi\sigma_x\sigma_y} . \tag{3.1}$$

In this equation f is the collision frequency of two bunches containing n_1 and n_2 particles. σ_x and σ_y describe the Gaussian widths of the transverse beam sizes in the horizontal and vertical direction. Integrated over time $\int L\,\mathrm{d}t$, it is commonly used to express the size of a dataset in inverse picobarn pb^{-1} ($10^{36}\ \mathrm{cm}^{-2}$) or inverse femtobarn fb^{-1} ($10^{39}\ \mathrm{cm}^{-2}$). The cross section σ of a physics process is related

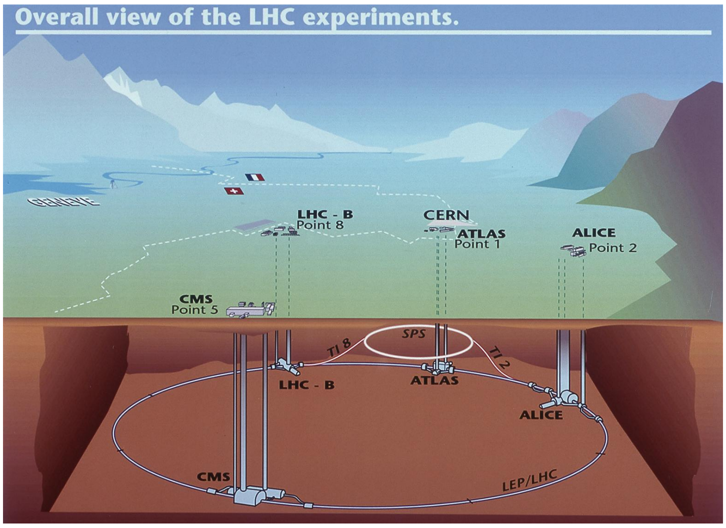

Figure 3.1: *A schematic drawing of the CERN Large Hadron Collider with its four main experiments, ATLAS, CMS, ALICE and LHCb [47].*

to the number of expected occurrences N of this process via

$$N = \sigma \int L \, \mathrm{d}t \, . \tag{3.2}$$

The LHC is designed to reach a luminosity of 10^{34} cm^{-2} s^{-1}. The peak luminosity of $7.73{\times}10^{33}$ cm^{-2} s^{-1} reached in 2012 underlines the excellent performance of the LHC [48] . An overview of the luminosity delivered to ATLAS by the LHC per year can be found in Figure 3.2a. At high instantaneous luminosities multiple interactions take place per bunch crossing. This effect is referred to as *pile-up* in the remainder of this thesis. In 2011, the mean number of interactions $\langle\mu\rangle$ per bunch crossing was 9.1. This number increased significantly in 2012, when on average 20.7 interactions happened within the same recorded event (see Figure 3.2b). In 2011, the time between two bunch crossings was 50 ns, which could again be improved in 2012 to 25 ns design bunch spacing.

Apart from the RF cavities, the rings consist of 1 232 dipole magnets responsible for the initial bending of the protons. About every fourth magnet is a quadrupole magnet, whose task is to focus the beam. Additionally, higher order magnets such as sextupoles, octupoles, decapoles, etc. are used to correct the trajectory and are mostly embedded in the cold mass of the dipole or quadrupole magnets. A total of 9 593 magnets is used to manipulate the protons' trajectories. The maximum energy that can be achieved in a ring accelerator of fixed circumference, is directly proportional to the strength of the dipole fields. In order to reach the $\sqrt{s}$ = 14 TeV design center-of-mass energy, magnetic fields as high as 8.3 T are necessary. These could only be realized with superconducting technology in the magnet system. The niobium-titanium (NbTi) cables used become superconducting below a temperature of 10 K. The LHC operation requires a cooling down to 1.9 K of the whole 27 km ring. This cooling is achieved with super fluid helium in the world's largest cryogenic system.

Both proton beams circulate within the same magnets in two ultrahigh vacuum tubes (10^{-13} atm) side by side. Both of these tubes are surrounded by the high dipole magnet fields in opposite directions. To counteract the strong Lorentz force driving the two beam tubes apart, they are encompassed in 3 mm thick high-strength stainless steel sheets, called collars. At four points in the ring, the two beam lines are crossed, allowing for particle collisions. This is where the four main LHC experiments are located. The

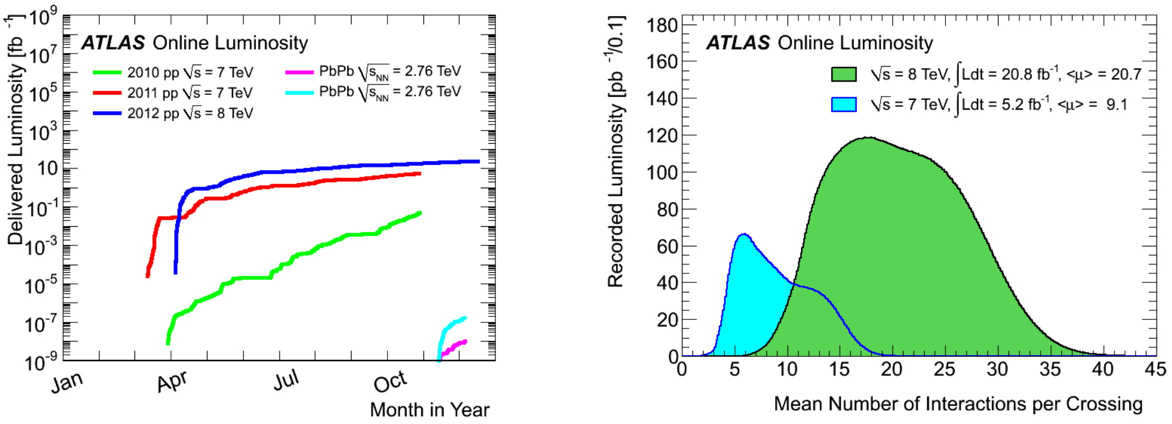

(a) Integrated luminosity as a function of time

(b) Mean number of interactions

Figure 3.2: *Performance of the LHC. (a) The cumulative luminosity delivered by the LHC in 2010, 2011 and 2012. The last months of each running period were devoted to collisions of lead-ions. (b) The luminosity-weighted distribution of the mean number of interactions per bunch crossing for the 2011 (light blue shaded area) and 2012 (dark green shaded area) pp data.*

two multi-purpose experiments CMS and ATLAS are located across from each other (see Figure 3.1). ALICE and LHCb, are both operated with a specialized physics program and are located on both sides of the ATLAS detector close to CERN's main site in Meyrin. In addition to proton-proton collisions, the LHC also provides collisions of lead ions or of lead ions and protons for part of the running periods each. These collisions are investigated in great detail by the ALICE collaboration which is specialized on heavy ion physics. LHCb focuses its physics program on B-mesons and the origin of CP violation.

At the time of this thesis, the LHC had just ended its pp data taking for an approximately 2 year long shut-down for maintenance and upgrade work of the accelerators and experiments. Before this shutdown, in January and February 2013, collisions of lead ions and protons were recorded.

3.2 Overview ATLAS detector

The ATLAS detector [2] is a multi-purpose detector. The complete detector layout is shown in Figure 3.3 alongside its dimensions (22 m in height and 44 m in length) and a labeling of the most important detector components. The layout follows an onion-like structure with the inner tracking detectors, providing space points for the reconstruction of particle trajectories, at the center. They are surrounded by the electro-magnetic calorimeter, which records primarily the energy of electrons and photons. Further out, the hadron calorimeter follows to measure the energies of hadronic particles. The outer part of ATLAS consists of the muon spectrometer, whose main task is to register trajectories of muons, which are not stopped in the calorimeters. Before going into detail of the ATLAS detector components, the ATLAS coordinate system is discussed [2].

3.2.1 The ATLAS coordinate system

The origin of the coordinate system is chosen to be the nominal interaction point. The positive x-direction points towards the center of the LHC ring, while the positive y-direction is defined to point upwards. The z-axis is oriented in the direction of the beam, with positive values in the A-side of the

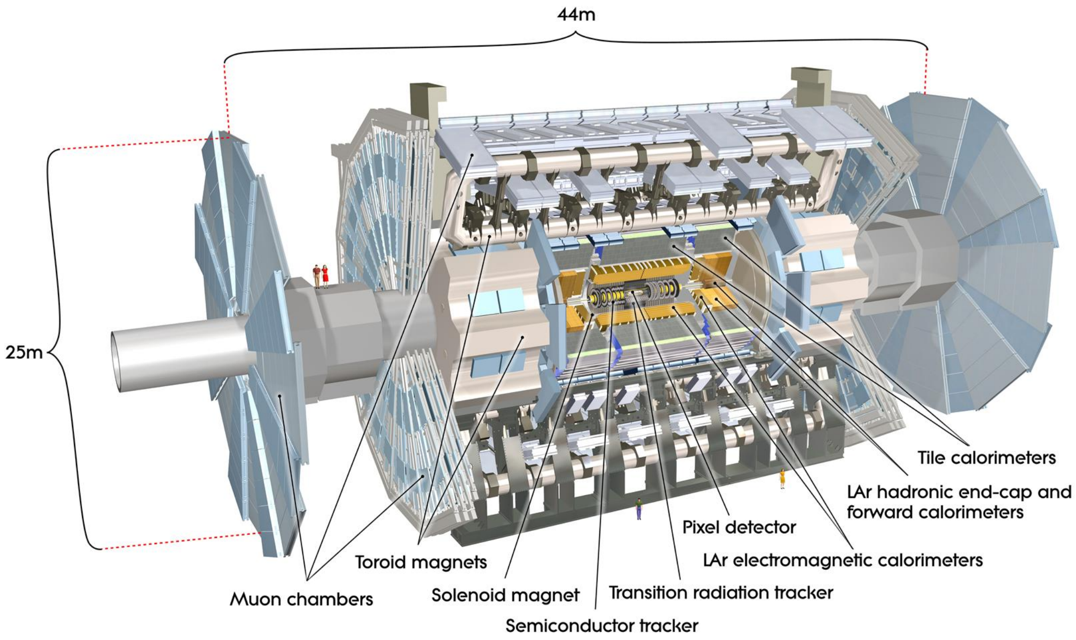

Figure 3.3: *A three-dimensional view of the ATLAS detector. Indicated are the individual subdetectors and the dimensions of the detector [2].*

detector (towards the location of the LHCb experiment) and negative values at the C-side (towards the ALICE experiment). The azimuth ϕ gives the angle in the x-y-plane around the beam axis and the polar angle θ is measured from the z-axis, i.e. the beam axis. All transverse variables like momentum (p_T), energy (E_T) and missing transverse energy (E_T^miss) are measured in the x-y-plane in general. The pseudorapidity is defined as

$$\eta = -\ln\tan\left(\frac{\theta}{2}\right) \tag{3.3}$$

and the distance ΔR is

$$\Delta R = \sqrt{\Delta\eta^2 + \Delta\phi^2}. \tag{3.4}$$

3.2.2 The ATLAS magnet system

The ATLAS magnet system [49] provides a magnetic field that bends the trajectories of charged particles. It is composed of a central solenoid and three toroid components (one barrel and two end-cap), see Figure 3.4 for the structure of the components and Figure 3.3 for the placement of the single components. The 2 T axial magnetic field of the central solenoid magnet [51] enclosing the inner detector is responsible for generating the bending power for the momentum reconstruction of charged particles in the inner tracking detectors. The 5.3 m long and 2.3 m in diameter solenoid uses indirectly cooled aluminum-stabilized superconductors [50] operated at a nominal temperature of 4.5 K to be as transparent to charged particles as possible. For particles arriving at normal incidence ~ 0.66 radiation lengths is achieved [2].

The purpose of the barrel toroid magnet [52] is to generate a tangential magnetic field of 0.5 T to 1 T for the muon spectrometer in and around it. The end-cap toroids [53] are rotated by 22.5° around the

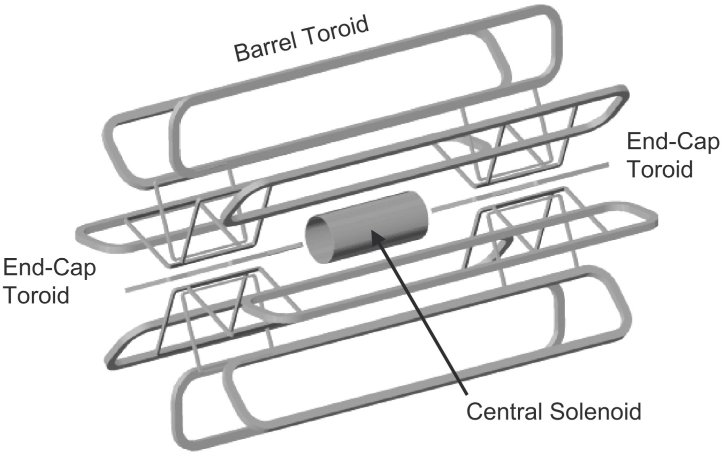

Figure 3.4: *Illustration of the three components of the ATLAS magnet system [50].*

beam axis with respect to the large barrel toroid. They give rise to the magnetic field in the forward region of the muon system and are designed for radial overlap.

3.2.3 The inner detector

The ATLAS Inner Detector [54] shown in Figure 3.5 is housed completely inside the volume of the solenoid magnet. This is shown in the schematic two-dimensional representation of the ATLAS Inner Detector in Figure 3.6 in the z-r-plane, with $r = \sqrt{x^2 + y^2}$. In subsequent order from inside to outside, it is composed of the Pixel detector, the SCT detector and the Transition Radiation Tracker. Table 3.1 gives an overview of the dimensions in r and z of the single subdetectors. They record the space points used to reconstruct trajectories of charged particles created in the collisions. These trajectories are bent by the magnetic field of the solenoid magnet. From the bending radius R (in meter) and the strength of the magnetic field B (in Tesla), the transverse momentum (p_{T}) of the particle can be reconstructed via

$$p_{\mathrm{T}} \sim 0.3 \cdot B \cdot R \left[\frac{\mathrm{GeV}}{\mathrm{Tm}} \right] . \tag{3.5}$$

In general, Equation (3.5) is derived from

$$p_{\mathrm{T}}\,[\mathrm{GeV}] = c\,R\,q\,B \left[10^9 \frac{m}{s}\, m\, e\, T \right] \approx 0.3\, q\, R\, B \left[\frac{GeV}{Tm} \right] . \tag{3.6}$$

Note that this equation is proportional to the charge, q, of the particle, which is assumed to be 1 in the standard ATLAS reconstruction.

The Pixel detector

Directly around the interaction point, the Pixel detector [56] encloses the collisions (see Figure 3.5). It is composed of three layers of silicon pixel chips in the barrel and three layers in the end-cap region, covering $|\eta| < 2.5$, $50.5\ \mathrm{mm} < r < 150\ \mathrm{mm}$ and all ϕ-directions (see Figure 3.6). Overall, there are 1 744 identical pixel sensors which measure $19{\times}63\ \mathrm{mm}^2$, containing 47 232 pixels of size $50{\times}400\ \mu\mathrm{m}^2$ each [2]. In sum, roughly 80.4 million readout channels are operated by the Pixel detector alone [57]. The Pixel detector is the most precise subdetector with a point resolution of 10 μm in r-ϕ and 115 μm

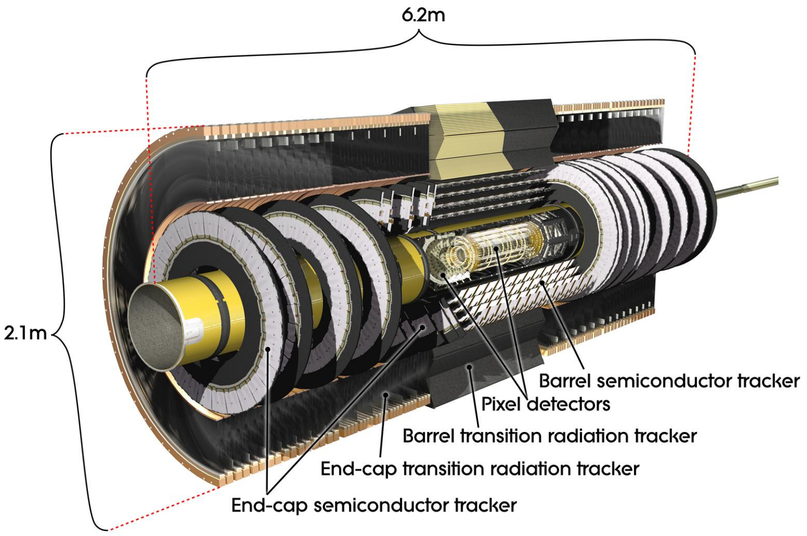

Figure 3.5: *The ATLAS Inner Tracking Detector, indicated are the location of the three subdetectors, the Pixel detector, the SCT and the TRT [2].*

Table 3.1: *Summary of the dimensions and the achieved resolutions of the ATLAS inner tracking detectors [2, 55].*

Inner detector			Pixel	SCT	TRT
Dimensions	r	barrel	50.5 - 122.5 mm	255 - 549 mm	554 - 1082 mm
		end-cap	88.8 - 149.6 mm	251 - 610 mm	617 - 1106 mm
	z	barrel	0 - 400.5 mm	0 - 80.5 mm	0 - 780 mm
		end-cap	495 - 650 mm	810 - 2797 mm	827 - 274 mm
Point resolution	r-ϕ	barrel	10 µm	17 µm	118 µm
		end-cap	10 µm	17 µm	132 µm (z-ϕ)
	z	barrel	115 µm	580 µm	-
	r	end-cap	115 µm	580 µm	-

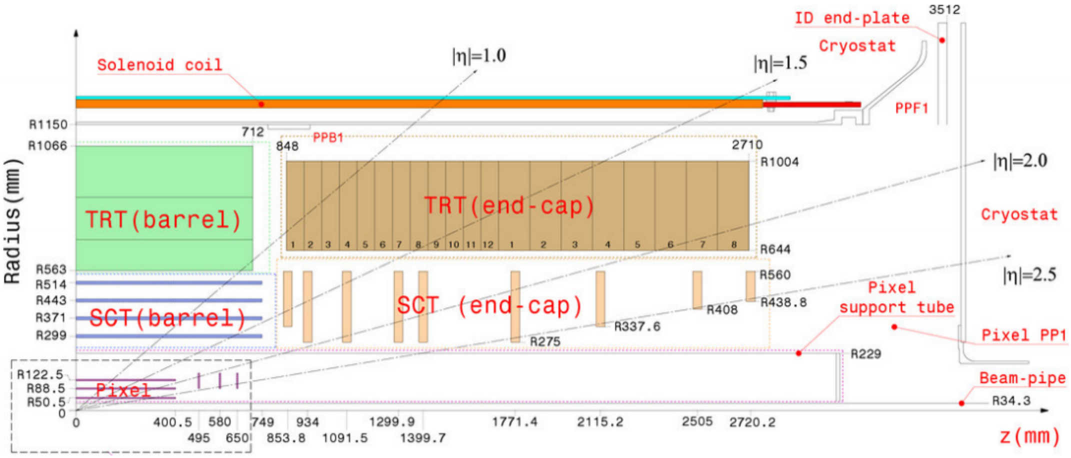

Figure 3.6: *Schematic view of the ATLAS Inner Tracking Detector indicating the active dimensions of each of the three subsystems [2].*

in z in the barrel and r in the end-caps.

The Semiconductor Tracker (SCT)

The Semiconductor Tracker (SCT) [58] complements the three Pixel layers by four concentric barrels of silicon-strip detectors and nine end-cap disks on each side of the detector [57]. The sensitive elements span radial distances from r = 299 mm to r = 560 mm, covering the same η and ϕ-regions as the Pixel detector. Most of the 4 088 modules contain four silicon strip sensors. On each side of the module two sensors are daisy-chained together. On the backside another pair of strip-sensors is glued at a stereo angle of 40 mrad, thus providing space points. The resolution reached with the ~6.3 million readout channels [57] is 17 µm in r-ϕ and 580 µm in z in the barrel and r in the end-caps.

The Transition Radiation Tracker (TRT)

The outermost part of the ATLAS Inner Detector is the Transition Radiation Tracker (TRT) [59]. In contrast to the Pixel and SCT detectors it is not based on semi-conductor technology but consists of 298 304 gas-filled ($Xe/CO_2/O_2$) straw tubes (proportional drift tubes), 4 mm in diameter each. The length of the straw tubes vary from barrel to end-cap, from 144 cm arranged parallel to the beam axis to ~40 cm positioned radially around the beam axis. As the name suggests, the TRT fulfills two purposes. On the one hand, it is a tracking detector that delivers on average 30 space points per charged track originating from the primary vertex. On the other hand, it is equipped with radiator material (foils in the barrel and foam in the end-caps) that causes electrons to emit transition radiation. The emerging low energy photons are absorbed by the gas mixture and induce large signals. The gas mixture is chosen for the good absorption of transition radiation photons in Xe and the high operation stability of mixtures with more then 6% CO_2. The effect of transition radiation gives rise to means of identifying electrons in particular to discriminate them from pions. For this purpose the TRT readout signals are discriminated against two thresholds, one lower threshold intended for tracking and one higher threshold for electron identification. For more details please see Section 4.5. The TRT does not measure the z coordinate in the barrel but has a resolution of 118 µm in r-ϕ in the barrel and of 132 µm in z-ϕ in the end-caps.

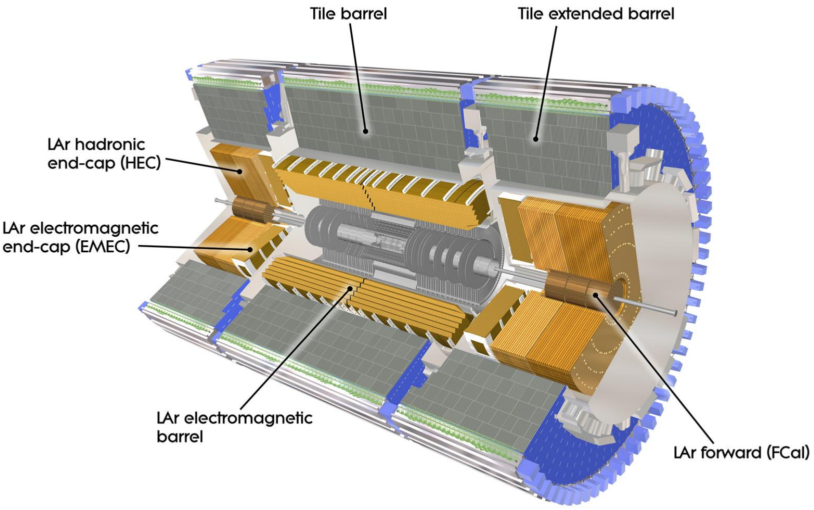

Figure 3.7: *The ATLAS calorimeter subsystems [2].*

3.2.4 The calorimeters

The ATLAS calorimetry is mainly based on two technologies, a liquid argon (LAr) and a tile calorimeter (see Figure 3.7), covering the pseudorapidity region $|\eta| < 4.9$. Within the η-range of the inner detector, the electro-magnetic (EM) calorimeter is finely granulated to be able to perform precision measurements of electrons and photons [2]. For the rest of the calorimeters a larger granularity is sufficient to reconstruct jets and determine E_T^{miss}.

Electromagnetic calorimeter

The liquid argon (LAr) electromagnetic calorimeter [60], a lead-LAr sampling calorimeter with characteristic accordion-shaped lead electrodes is composed of a barrel part stretching out to $|\eta| < 1.475$ and the end-cap components at $1.375 < |\eta| < 3.2$. While the end-caps are each housed in their own cryostat, the barrel shares a vacuum vessel with the solenoid magnet to reduce the material budget. A small gap of 4 mm separates the barrel LAr-calorimeter at $z = 0$. The end-caps are divided into two coaxial wheels from $1.375 < |\eta| < 2.5$ and from $2.5 < |\eta| < 3.2$. Due to the accordion geometry full ϕ coverage can be achieved [2]. The energy resolution in the barrel was determined in testbeams to be [2]

$$\frac{\sigma_E}{E} = \frac{(10.1 \pm 0.4)\%}{\sqrt{E}} \oplus (0.2 \pm 0.1)\% \,.$$

Hadronic calorimeter

The hadronic calorimeter uses two technologies. The barrel and the extended barrel (see Figure 3.7) are covered by the tile calorimeter [61]. It is a sampling calorimeter with steel as absorber material and scintillating tiles as active material [2], covering the η region $|\eta| < 1.0$ in the barrel and $0.8 < |\eta| < 1.7$ in the extended barrel. Signals are read out on two sides of the tiles with wavelength shifting fibers and two separate photomultiplier tubes.

In the forward region, the hadronic calorimeter applies LAr technology as a copper-LAr sampling

Table 3.2: *Fractional energy resolutions σ_E/E of the hadronic calorimeter components as determined from testbeams [2].*

Calorimeter	Tile	LAr hadronic end-cap	LAr forward
Electrons	-	$\frac{(21.4 \pm 0.2)\%}{\sqrt{E}}$	$\frac{(28.5 \pm 1.0)\%}{\sqrt{E}} \oplus (3.5 \pm 0.1)\%$
Pions	$\frac{(56.4 \pm 0.4)\%}{\sqrt{E}} \oplus (5.5 \pm 0.1)\%$	$\frac{(70.6 \pm 1.5)\%}{\sqrt{E}} \oplus (5.8 \pm 0.2)\%$	$\frac{(94.2 \pm 1.6)}{\sqrt{E}} \oplus (7.5 \pm 0.4)\%$

Table 3.3: *Summary of the achieved resolutions of the ATLAS Muon System [2].*

Muon system		MDT	CSC	RPC	TGC
Point resolution	ϕ	-	5 mm	10 mm	3 - 7 mm
	z	35 µm	-	10 mm	-
	r	-	40 µm	-	2 - 6 mm
	time	-	7 ns	1.5 ns	4 ns

calorimeter. The LAr hadronic end-cap calorimeter covers $1.5 < |\eta| < 3.2$ and consequently overlaps with the Tile calorimeter ($|\eta| < 1.7$) and the LAr forward calorimeter ($|\eta| = 3.1$). The LAr forward calorimeter is used as an EM calorimeter in its first module made out of copper. The outer two layers consist of tungsten and are optimized to measure hadronic showers. The fractional energy resolution has been determined from testbeam data separately for each of the components. The results are summarized in Table 3.2.

3.2.5 The muon system

The ATLAS Muon System [62], shown in Figure 3.8 is composed of several subdetectors fulfilling two distinct purposes: the reconstruction of muon tracks and the triggering on events containing muons. The Monitored Drift Tubes (MDT) and the Cathode Strip Chambers (CSC) provide precision space points of muon tracks in the field of the large barrel toroid for $|\eta| < 1.4$ or of the two smaller end-cap toroid magnets at $1.6 < |\eta| < 2.7$. In the transition region $1.4 < |\eta| < 1.6$ a superposition of both magnetic fields deflect the charged particle tracks. In this manner, the magnetic fields are mostly orthogonal to the muon trajectories, thus minimizing the effects of multiple scattering. Moreover, dedicated trigger chambers, the Resistive Plate Chambers (RPC) at $|\eta| < 1.05$ and the Thin Gap Chambers (TGC) at $1.05 < |\eta| < 2.4$ provide bunch-crossing identification, well-defined p_{T} thresholds and measure the muon candidate orthogonal to the tracking chambers [2]. These trigger chambers deliver tracks within $\sim$10 ns after the interaction with the particle, hence allowing for fast muon trigger decisions. Table 3.3 lists an overview of the point and time resolutions in the muon system components.

The Monitored Drift Tubes (MDT)

The MDT chambers consist of three to eight rows of drift tubes with a diameter of 29.970 mm each. The central wire - made of tungsten-rhenium - has a diameter of 50 µm and is kept at high voltage. The tubes are operated with an Ar/CO_2 (93/7) gas mixture at 3 bar selected for its good aging properties. A single tube resolution of 80 µm is reached, whereas the combination of tubes in a given chamber sums up to a resolution of 35 µm. As the maximum drift time from the tube wall to the wire is rather large with

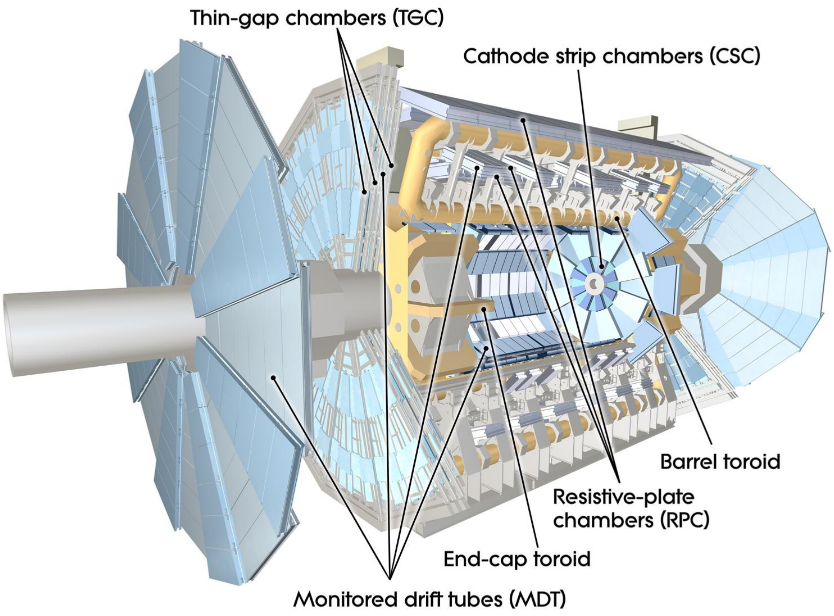

Figure 3.8: *The ATLAS muon detectors in a three-dimensional cutaway view [2].*

700 ns and multiple track hits become more and more likely with changing LHC running conditions, an adjustable dead time has been implemented in the front-end electronics. The chamber shapes vary from barrel to end-cap, from rectangular to trapezoidal, but the direction of the tubes is along ϕ in both cases.

The Cathode Strip Chambers (CSC)

The CSCs are multi-wire proportional chambers, which are read out via cathode planes segmented orthogonally into strips. Via the induced charge distribution both coordinates can be measured with a resolution of 40 µm in the bending plane and $\sim$ 5 mm in the transverse direction. In the chambers (two types called small and large chambers), the wires are oriented parallel to a central wire pointing in the radial direction. The expected particle rate in the forward region is much higher than at low $|\eta|$, exceeding the maximum safe counting rate of the MDT of 150 Hz/cm^2. In this area the detector of choice has to fulfill requirements on a high-rate capability, while maintaining a high spatial, time and double track resolution. All of these requirements are met by the CSC with safe counting rates up to 1000 Hz/cm^2.

The CSC is segmented into two disks of eight chambers. Each chamber consists of four planes, providing four independent η and ϕ measurements along a track. With this setup a resolution of 60 µm can be reached per CSC plane in the bending direction or 5 mm in the transverse direction. This is complemented by a high timing resolution of 7 ns due to the short electron drift times of less than 40 ns.

The Resistive Plate Chambers (RPC)

The Resistive Plate Chambers are gaseous detectors that, instead of a wire, are operated with parallel electrode-plates at a distance of 2 mm. The volume is filled with $C_2H_2F_4$/Iso-C_4H_{10}/SF_6 (94.7/5/0.3) and is permeated by an electric field of 4.9 kV/mm. The RPC forms the barrel muon trigger system with three concentric cylindrical layers (called trigger stations) consisting of two independent detector layers each. The two layers give six η and ϕ measurements for a track passing all three trigger stations. Each

RPC chamber consists of two rectangular detectors, which in turn are made of two independent layers (or gas volumes) read out by two orthogonal pick-up strips. These readout-strip panels are segmented in ϕ direction. A resolution of 10 mm in both ϕ and z direction is achieved. The timing resolution is 1.5 ns.

The Thin-Gap-Chambers (TGC)

The TGCs are multi-wire proportional chambers with a wire-to-cathode distance of 1.8 mm and wire-to-wire distance of 1.4 mm. This special configuration and the high electric fields around the wires ensure a high timing resolution needed for the tagging of the beam-crossing with $\geq$ 99% efficiency. Altogether, the TGC is composed of seven detector layers arranged in two doublets and one triplet unit. The circular disks of detectors are arranged in two concentric rings. The outer (end-cap) ring covers the pseudorapidity range of $1.05 \leq |\eta| \leq 1.92$, while the inner (forward) ring covers $1.92 \leq |\eta| \leq 2.4$. Each of the three TGC planes consists of a wheel divided into eight ϕ-octants, which are in turn divided radially into the forward and end-cap region. Radial information is determined from the anode wires arranged in azimuthal direction, while orthogonal readout strips complement the measurement with ϕ information. A single TGC unit consists of two (double) or three (triplet) chambers, which are gas volumes with a plane of wires in between two cathode planes. The sizes of the single detector components increase with the distance from the interaction point. The achieved resolution in ϕ ranges from 3 - 7 mm and in r from 2 - 6 mm. The timing accuracy is 4 ns.

3.2.6 Forward detectors

In addition to the aforementioned components, ATLAS also operates a dedicated luminosity measurement detector positioned in the end-cap regions at ±17 m from the interaction point. LUCID (LUminosity measurement using Cerenkov Integrating Detector) [63] serves as the main relative luminosity monitor for ATLAS. It is a Cerenkov detector consisting of 20 1.5 m long and 15 mm in diameter polished aluminum tubes. They are arranged at a distance of 10 cm ($|\eta| \approx 5.8$) to the beam pipe pointing towards the interaction point and photomultiplier tubes of the same size [2]. The online luminosity measurement is based on a hit-counting method assuming that the number of interactions per bunch crossing is proportional to the number of particles detected in LUCID and that the probability to measure multiple particles in one tube is rather low.

Additionally, a Zero-Degree Calorimeter (ZDC) [64] located at ±140 m is operated primarily to detect neutrons and photons in heavy-ion collisions as well as pp collisions in one forward direction ($|\eta| > 8.3$) [2]. It can also be used to measure the luminosity. Furthermore, with a time resolution of 100 ps, the interaction point can be determined to a precision of 3 cm in z direction, providing thus a vertex position measure independent of the inner detector.

3.2.7 The trigger

Out of the millions of particle collisions happening within the ATLAS detector per second only very few contain interesting physics. The electronic readout cannot process such a huge data rate. Therefore, to decrease the storage space required by the experiment, it is crucial to have an efficient and reliable filtering of interesting physics events during data taking. This is realized in the three level trigger system operated by ATLAS. At the first stage, the Level-1 (L1) trigger [65] selects events based on custom-made electronics. The Level-2 (L2) trigger and the Event Filter [66] are based on reconstructed physics objects and form together the High-Level Trigger (HLT). As this analysis is based entirely on

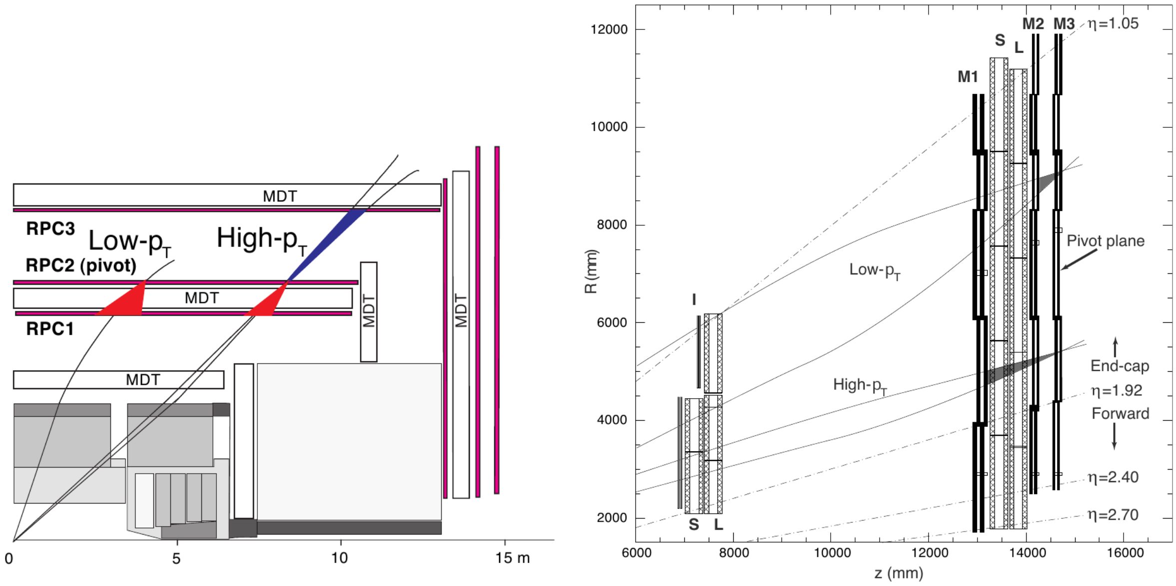

(a) Layout of the RPC system (b) Layout of the TGC system

Figure 3.9: *Sketch of the RPC and TGC detector trigger system. Indicated are the different layers RPC1, RPC2, RPC3 or M1, M2, M3 respectively and the according* pivot planes *[2].*

muon triggers, the following chapter will focus on the description of triggers, which single out events containing one or more muons.

The L1 muon trigger is based on a subset of detectors, namely the Resistive Plate Chambers (RPC) and the Thin-Gap Chambers (TGC) (see Section 3.2.5). A decision to keep or reject the event has to be made available to the front-end electronics within 2.5 µs. Therefore, the main focus in the design of the RPC and TGC lay on a fast detector response and timing accuracy rather than on high measurement precision. The maximum rate of event acceptance in the L1 trigger is 75 kHz [2]. The L1 trigger used in the selection of data for this dissertation (L1_MU11) had an event rate of 8 kHz during 2011 operation [67]. In the events selected by L1, Regions-of-Interest (RoIs), geometrical regions of the detector where potential trigger objects are located, are identified and passed to the L2 trigger. These RoIs are used to decrease the amount of data to be transferred from detector readout. In this manner, the event rate is further reduced to 3.5 kHz, leaving roughly 40 ms on average to process the event [2]. All the events selected by L2 are fully reconstructed and undergo offline analysis for further selection. The events passing this final step are recorded for physics analysis. The processing time per event at this stage is on the order of 4 s at a rate of 400 Hz. The event filter rate for this analysis was about 110 Hz [67].

The muon trigger

The RPC and TGC detectors need to be able to unambiguously identify the bunch crossing where a muon candidate originates from. This puts high requirements on their timing accuracy. To trigger an event a coincidence of hits in different detector layers is required. These layers are illustrated in Figure 3.9a for the barrel detector RPC and in Figure 3.9b for the TGC detector in the end-caps. The algorithm starts with hits on a so-called *pivot plane* (RPC2 or M3, see Figure 3.9) and searches for corresponding hits on the other layers along the connecting line to the primary vertex within a road of variable width depending on the p_{T}-threshold. The lower the p_{T} the wider the search region will be. This coincidence logic allows for six different p_{T}-thresholds at a time, three low p_{T} threshold (≈6-9 GeV) and three high p_{T} thresholds (≈9-35 GeV). The search algorithms vary for low and high p_{T}-thresholds. Each RPC layer consists of a doublet of ϕ and η measurements, where for low p_{T} a three-out-of-four coincidence between the ϕ and η planes in the first two layers (RPC1 and RPC2) are required. For the high-p_{T} algorithms additionally a one-out-of-two coincidence in the third layer (RPC3) is necessary. In the end-caps the pivot plane is the outermost (M3) layer of the TGC detectors. Here the measurements are performed independently in R and ϕ. The search algorithm starts with a line from the hits in M3 to the interaction point and looks for coincidences in roads with variable width corresponding to different p_{T}-thresholds. From the doublet planes M2 and M3 a two-out-of-three coincidence is required for both wires and strips, while the triplet wire planes have to show a two-out-of-three coincidence and the triplet strip planes a one-out-of-two coincidence. The final trigger decision is derived from the combined R and ϕ information.

3.3 Data processing and simulation

The data recorded in events selected by the L1 triggers undergo an online reconstruction optimized for short computation time [66]. These reconstructed objects are input to the L2 triggers and event filters, which classify the events according to their physics content. A schematic representation of this process can be found in the upper right corner of Figure 3.10. For this dissertation, data selected by an event filter requiring at least one muon in the event is analyzed.

In addition, simulated events are needed to develop an analysis strategy. Firstly, the physics processes are calculated with an event generator (MadGraph5 [68] in this case), the output of which determines the final state particles of each event. The propagation of these particles through the detector is simulated taking into account the interactions of the particles with the detector material. To mimic the high luminosity conditions at the LHC, the event is superimposed with multiple low momentum interactions. At this stage, simulated hits are available indicating in which part of the detector an interaction of the particles and the detector material has taken place. In the next step, the digitization, the expected detector response is imitated resulting in equivalent data types as the data recorded by ATLAS (see Figure 3.10).

In the following, recorded and simulated data are treated in the same way. The offline reconstruction processes the space points recorded by the detector to find tracks (trajectories in the detector) in the inner detector and the muon system, determine energy deposits in the calorimeters, etc. This information is stored in a format referred to as Event Summary Data (ESD) with a typical event data size of 500 kB [69]. The hit information stored in ESDs is usually not needed for physics analyses. To reduce the file sizes, the level of detail in the ESD is decreased and the events are stored as Analysis Object Data (AOD) with a target size of 100 kB [69]. For the search for multi-charged stable particles, however, hit information is required for two newly constructed variables that are not part of the standard ATLAS reconstruction yet. Therefore, an alternative path is chosen, instead of removing the hit information, only selected events are stored in Derived ESDs (DESD). These contain the full hit information and are classified again according to their physics content.

In the last step, each analysis chooses information relevant for its needs and stores them in flat n-tuples, the D3PDs (Derived Physics Data). This can be done from AODs or ESD/DESDs alike. The reconstruction of the MDT $\mathrm{d}E/\mathrm{d}x$ and TRT $\mathrm{d}E/\mathrm{d}x$ is included in the creation of Long Lived Particles D3PDs (LLP D3PD). LLP D3PD is the data format of choice for this analysis.

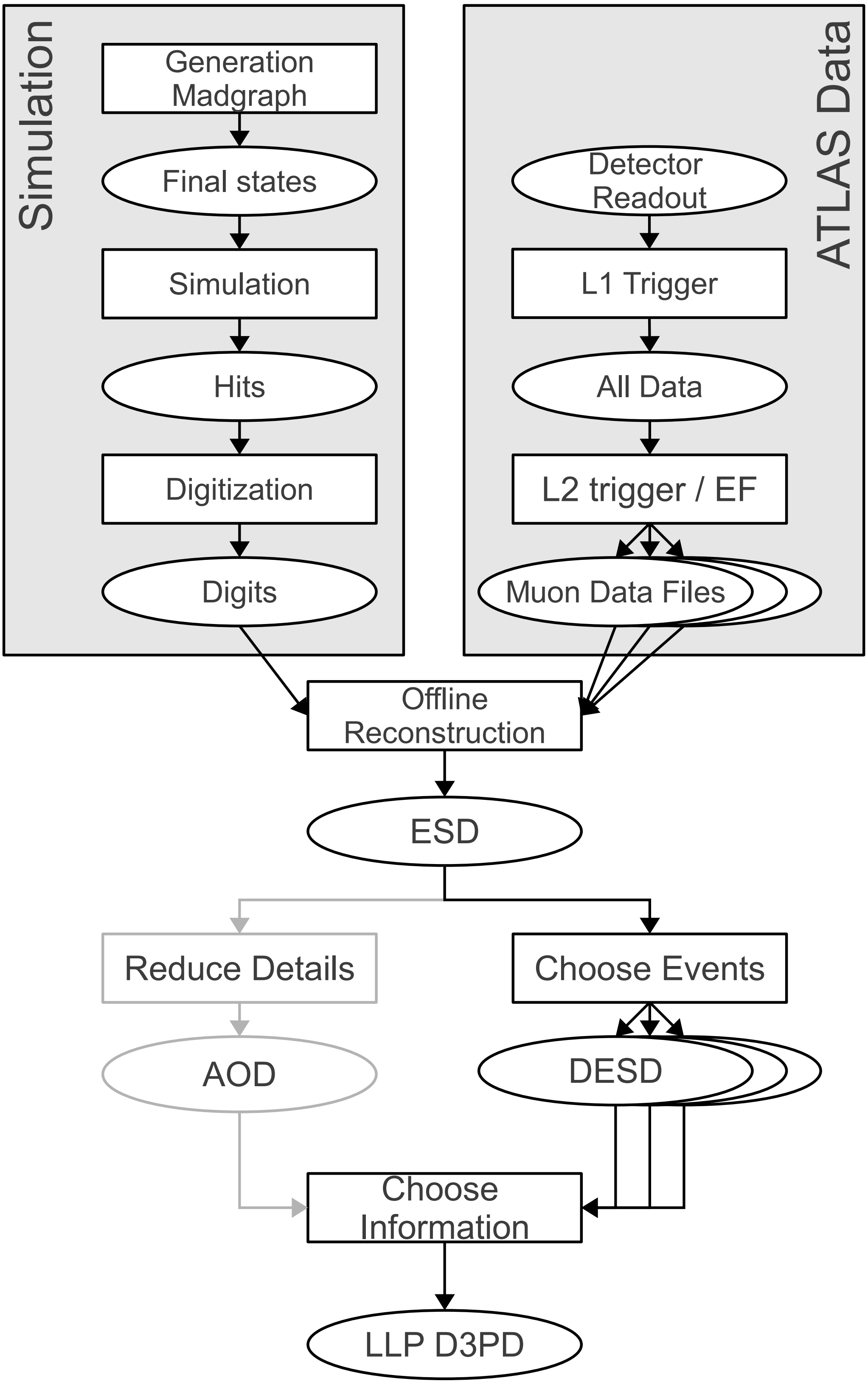

Figure 3.10: *The Monte Carlo generation and data processing chain as used in ATLAS.*

3.4 Reconstruction

The signals recorded in the various ATLAS sub detectors need to be combined and interpreted as tracks to arrive at an understanding of the physics processes which took place in the individual collisions.

3.4.1 Track reconstruction

The track reconstruction combines measurements (hits) from the innermost tracking detectors, the Pixel detector and the SCT, using several track fit algorithms in parallel. The hits are equivalent to three dimensional space points, either from a direct measurement in the Pixel detector or from the combination of two sides of a SCT module taking into account the stereo angle. After the application of quality criteria the tracks are extended into the TRT, where compatible TRT hits are added to the tracks. This inside-out approach is complemented by an outside-in tracking designed to include tracks based on the TRT alone [70]. Further track segments can be reconstructed in the ATLAS Muon System.

3.4.2 Muon reconstruction

Track segments in the muon system play a key role in the reconstruction of muons. Additionally, muons leave a charged track in the inner detector and some energy depositions in the calorimeters. Thus, muons and their transverse momenta can be reconstructed from information gathered in the entire ATLAS detector. Two distinct approaches of muon reconstruction are available at ATLAS, *Staco* and *Muid*, which also divide the muon candidate objects into four inclusive[1] quality levels (tight, medium, loose and very loose). The *Staco* algorithm performs a statistical combination of the track segments in the inner detector and the muon system [71]. *Muid* muons with the quality flag medium [71] are used in the search for multi-charged particles. Three categories of algorithms meet the criteria mentioned above. Starting from a track segment in the muon system, *MuidCombined* associates a track in the Inner Detector and performs a partial refit of the two track segments. Starting from the inner track vector, it adds the hits from the outer track segment. Information from the calorimeters is used to correct the measurement of the transverse momentum. Alternatively, *MuidStandalone* measures the momentum exclusively in the muon system and then extrapolates the track to the inner detector taking energy losses in the calorimeter into account. The third approach, *MuGirl*, performs a fit throughout the entire detector starting with an inner detector track. Any object reconstructed by either of the above mentioned algorithms will be referred to as a *reconstructed muon object* (μ^{reco}) in the remainder of this work. In most cases, a reconstructed muon object is the signal left in the detector by a muon particle (either μ^+ or μ^-), referred to as *muon* (or *true muon*, μ^{true}) in the following.

Independent of the reconstruction algorithm, the muon candidate needs to reach the muon detectors within the 25 ns time frame of their active readout. This imposes a lower threshold on the velocity β a particle has to travel with in order to be reconstructed as a muon object. The muon reconstruction efficiency drops steeply below $\beta \approx 0.7$ [72].

---

[1] A muon classified as tight is also included in the collection of medium, loose and very loose muons, etc.

CHAPTER 4

Particle identification with the ATLAS detector

The reconstructed objects described in the previous chapter allow for a first identification of the particles. A more refined separation of similar detector signatures is made possible by a large variety of particle identification algorithms from numerous subdetectors available at ATLAS. Many are based on the concept of specific energy loss per path length, $\mathrm{d}E/\mathrm{d}x$, introduced in Section 4.1. Others exploit the time of flight of the particles to deduce their velocity β. In addition, these variables can be used to identify unusual signatures of hypothetical BSM particles, like the multi-charged particles of this analysis. A discussion of $\mathrm{d}E/\mathrm{d}x$ in the context of multi-charged particles follows in Section 4.2. Among the existing variables are well established ones such as the Pixel $\mathrm{d}E/\mathrm{d}x$ (Section 4.4), the TRT High Threshold Fraction (Section 4.5), LAr $\mathrm{d}E/\mathrm{d}x$ (Section 4.6) and the Tile β-measurement (Section 4.7). They have recently been complemented by newly developed $\mathrm{d}E/\mathrm{d}x$ measurements from the MDT (see Section 4.8) and the TRT. The development of the latter is part of this thesis and will be described in greater detail in Section 5. The aforementioned variables are reviewed and validated with data / Monte Carlo comparisons of $Z \rightarrow \mu\mu$ samples defined in Section 4.3.

4.1 Bethe-Bloch theory

A charged particle traversing a medium interacts with it via collisions with the electron shells of the material's atoms. In each collision, some amount of energy E is lost by the particle through ionization or excitation of the respective atom. For electrons as incident particles, target and incident particle are equal. The dominant energy loss process at low initial energies of incident electrons or positrons is ionization. Besides, effects from Møller scattering, Bhabha scattering and positron annihilation (see Figure 4.1) contribute to the overall energy loss in this region. At higher energies Bremsstrahlung completely dominates the energy losses.

The scattering of any other particle with charge q from free electrons is described by the classical Rutherford differential cross section [73]

$$\frac{\mathrm{d}\sigma_R(E,\beta)}{\mathrm{d}E} = \frac{2\pi r_e^2 m_e c^2 q^2}{\beta^2} \frac{(1-\beta^2 E/T_{\mathrm{max}})}{E^2} . \tag{4.1}$$

In Equation 4.1, $r_e = \frac{e^2}{4\pi\epsilon_0 m_e c^2} \approx 2.8$ fm is the classical electron radius, m_e the electron mass and the

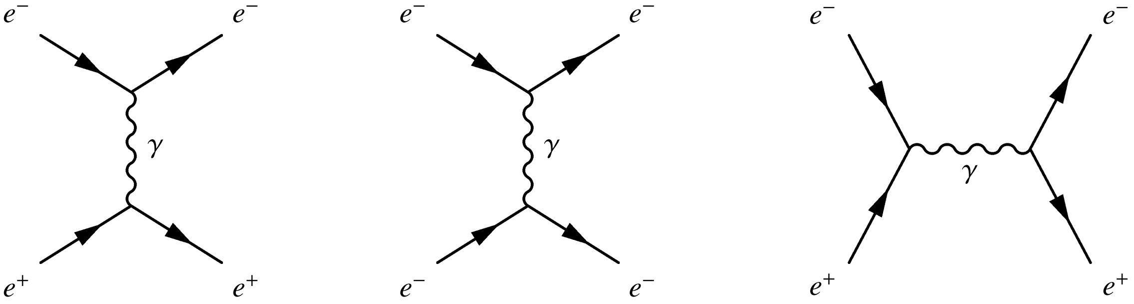

(a) Bhabha scattering (b) Møller scattering (c) Electron-positron annihilation

Figure 4.1: *The processes contributing to the energy loss of electrons and positrons in matter.*

incident particle travels at velocity β.

$$T_{\text{max}} = \frac{2m_e c^2 \beta^2 \gamma^2}{1 + 2\gamma m_e/M + (m_e/M)^2} \tag{4.2}$$

is the maximum energy that can be transferred in one collision of an incident particle with mass M [74]. In matter, however, the electrons are bound in atoms and this cross section must be determined via quantum theoretical calculations first performed by Bethe [75]. The average rate of energy loss in the range $0.1 \lesssim \beta\gamma \lesssim 1000$ is well described by the Bethe-Bloch equation derived from a first-order approximation (adapted from [73])

$$-\langle\frac{\mathrm{d}E}{\mathrm{d}x}\rangle = \frac{4\pi N_e r_e^2 m_e c^2}{\beta^2} q^2 \left[\frac{1}{2}\ln\left(\frac{2m_e c^2 \beta^2 \gamma^2 T_{\text{max}}}{I^2}\right) - \beta^2 - \frac{\delta(\beta\gamma)}{2}\right]. \tag{4.3}$$

Here N_e is the number density of electrons in the medium and I stands for the mean excitation energy of the atom in eV. Below this range in $\beta\gamma$, the velocity of the incident particle approaches values comparable to atomic electrons. Only a phenomenological description of the energy loss rate is available in the range $0.01 < \beta < 0.05$. In Figure 4.2 a representative distribution of $\mathrm{d}E/\mathrm{d}x$ for positively charged muons in copper is shown, indicating this approximation as Anderson-Ziegler after its inventors [76]. For slightly higher energies, multiple corrections to Equation (4.3) need to be included. Examples are higher order corrections to the first order approximation, a shell correction due to the atomic binding of the electrons and a reduction of $\mathrm{d}E/\mathrm{d}x$ for negative particles with respect to positive particles of the same mass and charge (denoted as μ^- in Figure 4.2). For higher energies, the material becomes polarized by the incident particle which limits its energy loss. This density effect is accounted for by the term $\frac{\delta(\beta\gamma)}{2}$ in Equation (4.3). Its effect is illustrated at the lower right part of Figure 4.2, with a lowering of the energy loss through ionization. In this $\beta\gamma$ range, radiative energy losses dominate by orders of magnitude. $E_{\mu c}$ marks the critical energy, for which the energy losses through ionization and excitation of the atoms in the material are of the same magnitude as the energy losses from radiative effects.

For the purpose of this work, solely the region described by Equation (4.3) is of interest. Particles with $\beta\gamma$ values around $\approx 3 - 4$ are in the minimum of the $\mathrm{d}E/\mathrm{d}x$ distribution (see figure 4.2) and are hence called minimum ionizing particles (MIP).

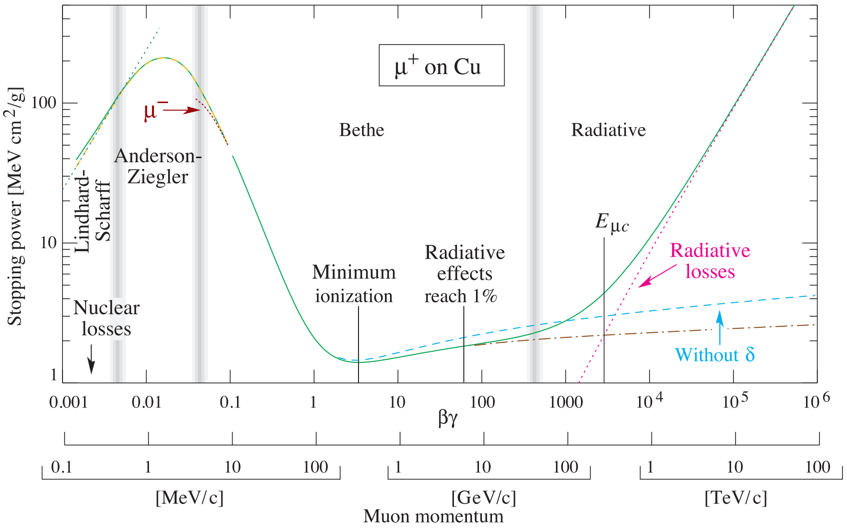

Figure 4.2: *The specific energy loss of particles in matter, shown exemplary for positive muons in copper, as a function of $\beta\gamma$ and the muon momentum [73].*

4.1.1 Most probable energy loss

The energy loss probability of the single collisions can be described by the Landau distribution [77], shown exemplary for pions in silicon in Figure 4.3. The *mean energy loss rate* from Equation (4.3) is significantly higher than the *most probable energy loss* ($\Delta p/x$ in Figure 4.3). This imposes experimental challenges on a measurement of $\mathrm{d}E/\mathrm{d}x$, which is limited in the number of single energy depositions by the size of the detector. A common approach is, therefore, to assess the most probable energy loss by taking the average of typically the 70% lowest energy depositions. This average is often referred to as the *truncated mean*.

4.1.2 Restricted energy loss

Experimentally, the energy loss, $\mathrm{d}E/\mathrm{d}x$, is determined from ionization clusters along a track in a detector. However, from very high energy transfers the ionization electron can become energetic enough to ionize further atoms in the material and thus form a second track [78]. These so-called δ electrons do not contribute to the observed energy loss of the original track if they can be reconstructed separately. This depends on the length of the δ electron track or its bending radius in a magnetic field and likewise the resolution of the detector. Upon introduction of a cut-off energy, E_{max}, this restricted energy loss can be expressed as [78]

$$\left(\frac{\mathrm{d}E}{\mathrm{d}x}\right)_{\mathrm{restricted}} = \frac{4\pi N_e e^4}{m_e c^2}\frac{q^2}{\beta^2}\left[\ln\left(\frac{\sqrt{2m_e c^2 E_{\mathrm{max}}}\beta\gamma}{I}\right) - \frac{\beta^2}{2} - \frac{\delta(\beta)}{2}\right]. \tag{4.4}$$

It is valid for all values of $\beta\gamma$ for which $\gamma^2 \gg E_{\mathrm{max}}/m_e c^2$ as long as E_{max} remains below the kinematic limit. The restricted energy loss is valid for all particles, including electrons, due to the fact that E_{max} replaces the different kinematic limits of electrons and heavier particles. In a given medium, it is a function of the particle velocity, β, alone.

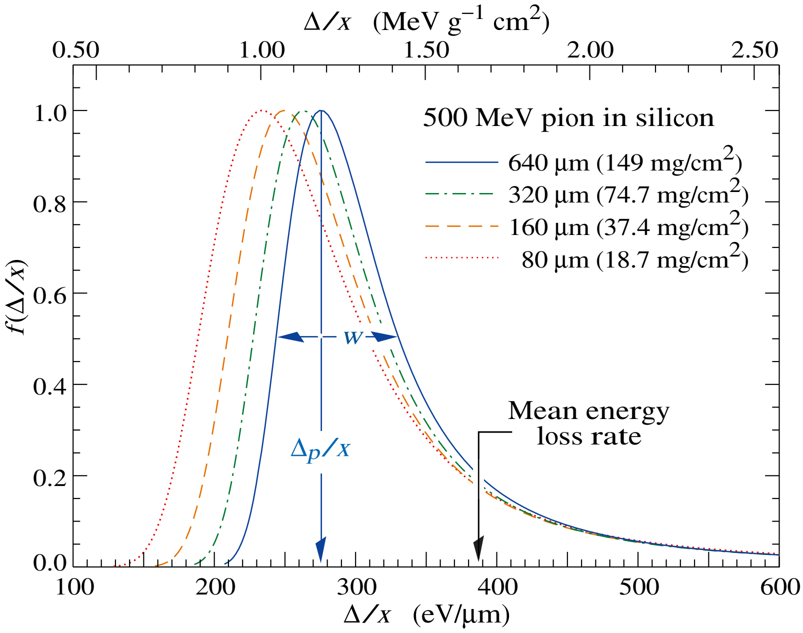

Figure 4.3: *Distribution of the energy losses of 500 MeV pions in silicon of different widths, normalized to unity at the most probable value [73].*

4.1.3 Parametrization

As a result of the universal validity of Equation (4.4), it can be used for particle identification. Often, the curve is determined from a set of particle tracks of the same identity and then applied to make predictions for other particles. For this it is necessary to find a parametrization of (4.4) that can be established from fits to data. One example for charge $|q| = 1e$ particles is the parametrization following Blum-Rolandi [78]

$$\frac{dE}{dx}(\beta\gamma) = \frac{p1}{\beta^{p4}} \cdot \left[p2 - \beta^{p4} - \log\left(p3 + \frac{1}{(\beta\gamma)^{p5}} \right) \right] . \tag{4.5}$$

The five free parameters $p1$ to $p5$ express the material dependence of the estimator and can be extracted from a fit to data. β can additionally be expressed as a function of $\beta\gamma$

$$\beta = \sqrt{\frac{(\beta\gamma)^2}{1 + (\beta\gamma)^2}} , \tag{4.6}$$

which is the ratio of the momentum, p, and the mass, m, of the particle

$$\beta\gamma = \frac{p}{m} . \tag{4.7}$$

Hence, predictions of $\mathrm{d}E/\mathrm{d}x$ can be made for all particles as a function of their momentum. As an example consider Figure 4.4. It shows predictions for several particles extracted from a fit of Equation 4.5 to the TRT $\mathrm{d}E/\mathrm{d}x$ introduced in the next chapter.

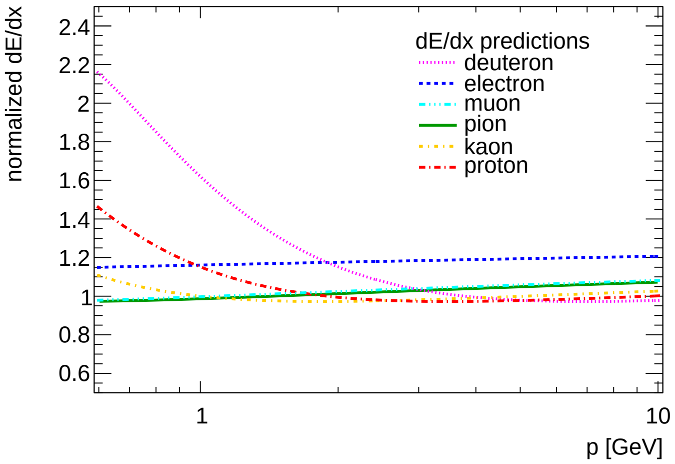

Figure 4.4: *Predictions for dE/dx of different particles.*

4.1.4 Separation Power

The separation power defines a measure of how well one particle species can be distinguished from another by means of the $\mathrm{d}E/\mathrm{d}x$ measurement. Figure 4.4 serves as a good illustration to explain the concept. In regions where the $\mathrm{d}E/\mathrm{d}x$ predictions of two different particles are well separated, $\mathrm{d}E/\mathrm{d}x$ is a good discriminant to distinguish their types. In contrast, at the crossing points of two curves or in regions where the two curves overlap, no statement about the type of the particle can be made.

An additional constraint on the separation power is the resolution of the $\mathrm{d}E/\mathrm{d}x$ measurement. A convenient definition of the separation power $\sigma_{i,j}$ of particles i and j is hence

$$\sigma_{i,j} = \frac{\left|\langle \mathrm{d}E/\mathrm{d}x_i\rangle - \left\langle \mathrm{d}E/\mathrm{d}x_j\right\rangle\right|}{\sqrt{(\sigma(\mathrm{d}E/\mathrm{d}x)_i^2 + \sigma(\mathrm{d}E/\mathrm{d}x)_j^2)/2}}. \tag{4.8}$$

This equation is an adaptation of the separation power D in [79]. In Equation (4.8), $\left\langle \mathrm{d}E/\mathrm{d}x_{i/j}\right\rangle$ is the average $\mathrm{d}E/\mathrm{d}x$ measured at the given momentum p for particles i and j and $\sigma(\mathrm{d}E/\mathrm{d}x)_{i/j}$ are the corresponding resolutions.

4.2 Identifying multi-charged particles

Two factors lead to highly ionizing behavior of massive multi-charged particles. Foremost, the factor of q^2 in Equations (4.3) and (4.4) enhances the energy loss quadratically with the charge of the particle. Furthermore, for a given momentum p a heavy particle has lower values of $\beta\gamma$ resulting in a higher $\mathrm{d}E/\mathrm{d}x$.

The identification is complicated by the momentum reconstruction from the bending radius in the magnetic field, which assumes particles with charges $|q| = 1e$ (see Equation (3.6)). This bending is also proportional to the charge of the particle q, the higher the charge, the more the track bends in the magnetic field. Therefore, the momentum of multi-charged particles is reconstructed a factor of q too low.

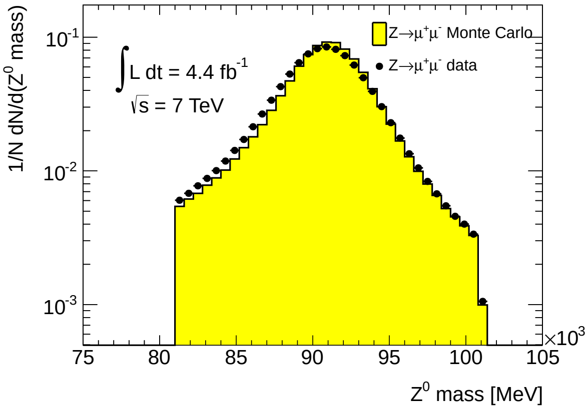

Figure 4.5: *The invariant mass distribution of $Z \rightarrow \mu\mu$ data and Monte Carlo in the window of the Z mass peak (81 to 101 GeV) chosen in the selection of $Z \rightarrow \mu\mu$ events [82].*

4.3 $Z \rightarrow \mu\mu$ control samples

To calibrate and validate the variables considered for the selection of the analysis, $Z \rightarrow \mu\mu$ data and Monte Carlo control samples are used. These samples have a high content of muons. The $Z \rightarrow \mu\mu$ data comes from a distinct readout stream with a high $Z \rightarrow \mu\mu$ event efficiency. The calibration uses the complete 2011 data set, corresponding to an integrated luminosity of 4.4 fb^{-1}. The Monte Carlo samples are simulated in PYTHIA [80] and the response of the ATLAS detector is described in GEANT4 [81].

The same data selection is applied in data and Monte Carlo. The muons are defined by a track reconstructed in the muon system. This muon track needs to be matched to a good quality track in the inner detector with a transverse momentum $p_{\mathrm{T}} > 20$ GeV and pseudorapidity in the range $|\eta| < 2.4$. The two muons in the event are required to belong to a pair of muon objects with opposite charges $|q| = 1e$. The invariant mass of these dimuon systems must be between 81 and 101 GeV. Figure 4.5 shows the invariant mass distribution in the region of the Z boson mass peak in data and Monte Carlo. The distributions are in good agreement. In the following, data or Monte Carlo events selected by these requirements will be referred to as $Z \rightarrow \mu\mu$ data or Monte Carlo.

4.4 The Pixel dE/dx

Unless stated otherwise, the following is based on [83]. The energy deposited in the Pixel detector by a traversing charged particle can be measured directly by a Time over Threshold (ToT) technique. It measures the collected charge in each pixel with a 8-bit dynamic range via the width of the output signal above a threshold (3.5 ke). A minimum ionizing particle (MIP) creates on average approximately 80 electron-hole pairs per micrometer of traversed detector material resulting in a count of ToT of 30 when traversing the 250 µm thick sensors at normal incidence. With a hit efficiency of above 99%, each pixel diode measures charges in the range of 3.5 ke to 170 ke . Apart from dead areas making up roughly 3% of the detector, the charge collection efficiency is uniform over the whole detector. As the charge deposited by a track is rarely confined to one single pixel, neighboring pixels are joint together to form clusters, whose charge Q is used in the dE/dx-measurement. The specific energy loss of a cluster is determined via

$$\frac{dE}{dx} = \frac{QW\cos\alpha}{e\rho d}, \tag{4.9}$$

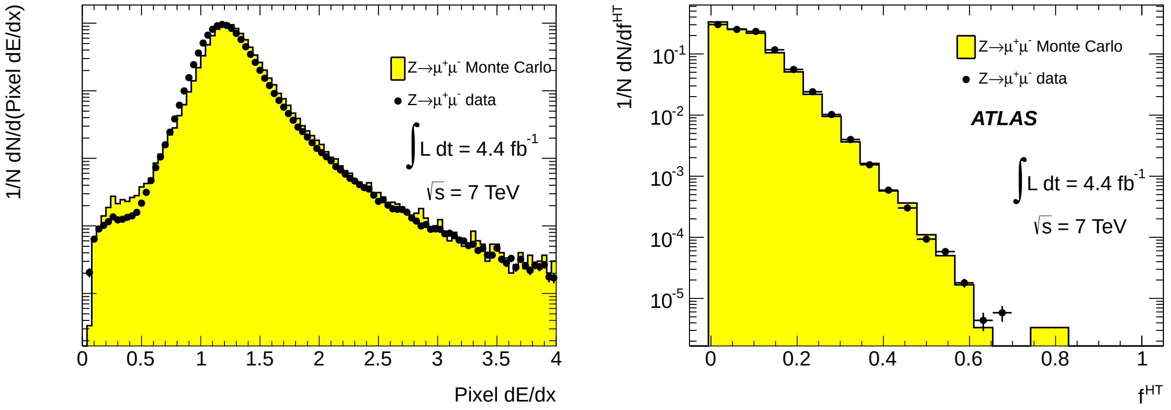

(a) $Z \to \mu\mu$ Pixel dE/dx in MeVg^{-1}cm^2

(b) $Z \to \mu\mu$ f$^{\mathrm{HT}}$

Figure 4.6: *(a) Comparison of data and Monte Carlo distributions of Pixel dE/dx in the $Z \to \mu\mu$ control samples [82] (see also [38]). (b) Comparison of data and Monte Carlo distributions of the TRT High Threshold Fraction f^{HT} in the $Z \to \mu\mu$ control samples [8].*

where $W = 3.68 \pm 0.02$ eV/pair is the average energy needed to create an electron-hole pair and ρ is the density of silicon. α means the spatial incident angle, while d is the thickness of a sensor (= 250 µm), thus the particle's path in silicon, x, becomes $\frac{d}{\cos\alpha}$. This measurement suffers from biases through charge losses which remain below the 3.5 ke threshold, exceed the ToT counter of 255 counts per pixel or are deposited outside of the active detector material. While the latter can easily be avoided via cuts on the fiducial volume applied in the standard selection, the first two biases are unavoidable. Especially the limitation through the maximum size of the ToT counter introduces difficulties in the measurement of multi-charged particles as these particles are expected to deposit significantly more energy in the detector. Another important aspect to be taken into account is the dependence of the cluster charge on the incident angle α. While good agreement between data and Monte Carlo samples is observed above $\cos\alpha = 0.16$, all tracks below this cut-off are excluded. About 91 % of all clusters fulfill these requirements and from these so-called *Good Clusters* the track dE/dx (Pixel dE/dx) is calculated from the truncated mean of the single measurements. In this method the 30% highest charges are discarded. This translates into no truncation for tracks with two or fewer Good Clusters, the truncation of one cluster for tracks with three or four Good Clusters and the highest two cluster charges are rejected on tracks with more than five Good Clusters. Figure 4.6a demonstrates that for the Pixel dE/dx good agreement between the $Z \to \mu\mu$ tuning samples in data and Monte Carlo is observed. The disagreement at lower values could be related to the saturation of the readout at large energy deposits, resulting in the loss of the signal. According to [83] good agreement between data and simulation up to energy deposits of 10 MIPs is achieved. This range is easily exceeded by particles with charges $|q| > 2e$. Additionally, the Pixel detector rejects hits with charge saturation making it a rather unreliable instrument for these particles. Thus, the search cannot rely on information from the Pixel detector for particles $|q| > 2e$ but merely uses it for the $|q| = 2e$ particle search.

4.5 The TRT High Threshold Fraction

The electric signal at the TRT wires is discriminated against two thresholds at 200 eV and 6 keV. During the 75 ns active readout time, the signal of the low threshold (LT) is sampled over 24 bins of 3.12 ns

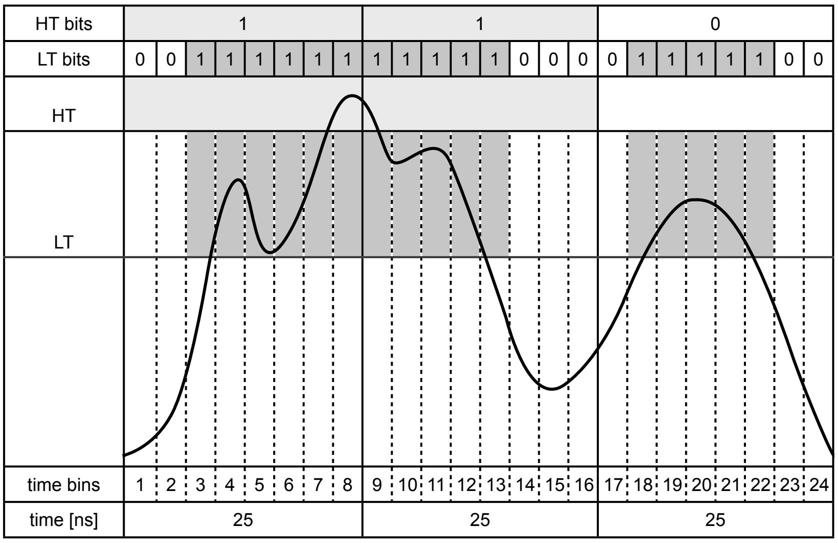

Figure 4.7: *The formation of the TRT bit pattern. The ionization signal is discriminated against two thresholds and readout in 24 time bins over a period of 75 ns. Every time the signal exceeds a threshold during its readout time bin a bit is set to 1 or left at 0 otherwise.*

length each, whereas the high threshold (HT) is read out three times. Each bit is set to one if the electric signal had been above the threshold at least once during the readout time, or to zero otherwise. The formation of the resulting TRT bitpattern is depicted schematically in Figure 4.7. A hit that has at least one of the three high threshold bits set is called a *High Threshold Hit*. The fraction of *High Threshold Hits* on a given track, *High Threshold Fraction* (f^{HT}), is a measure of the amount of ionization deposited on average in the TRT. It is used for particle identification of highly ionizing particles and electrons. By construction, electrons crossing the TRT leave additional energy in the detector due to transition radiation. The radiator material surrounding the TRT straws causes electrons to have a high probability of emitting transition radiation at the boundaries of the radiator material. This leads to additional ionization in the gas in the straw volume and hence a higher f^{HT}. The excellent agreement between data and Monte Carlo in this variable is shown for $Z \to \mu\mu$ in Figure 4.6b. Note, however, that no transition radiation photons are expected in the control samples.

4.6 The LAr dE/dx

The ATLAS calorimeter system is composed of several layers of different materials (see Figure 4.8a for illustration). The Liquid Argon Calorimeter consists of 4 layers: Presampler, EM1, EM2 and EM3 as shown on Figure 4.8a [84] (see also [85]). Most particles are stopped in the calorimeters where they decay into particles with subsequently lower energies. Some, mostly minimum ionizing particles however, traverse the calorimeters without being stopped. Their specific energy loss per path length in these systems is calculated in two steps. Firstly, the energy deposits, $\mathrm{d}E_i$, along the particle's path are summed, leaving out any deposit below the noise threshold in the particular calorimeter cell and any layer with a calorimeter cell marked as bad [84] (see also [85]). In the second step the path length, $\mathrm{d}x_i$, is determined from all calorimeter cells taken into account in the sum of dE as the distance between the entry and exit points in each calorimeter layer. For this step a straight line is assumed, as this variable was developed for an analysis expecting solely straight-line tracks. Finally, the LAr $\mathrm{d}E/\mathrm{d}x$ is taken to be

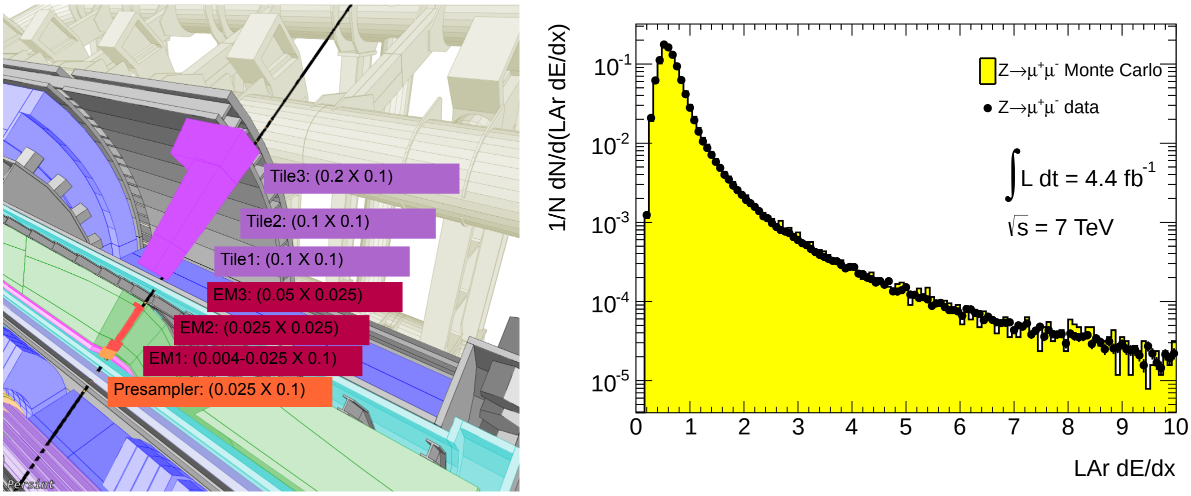

(a) Muon traversing calorimeter

(b) $Z \rightarrow \mu\mu$ LAr dE/dx

Figure 4.8: *(a) Illustration of a muon traversing the calorimeter systems and its energy deposits in the detector [84]. (b) Comparison of data and Monte Carlo distributions of LAr dE/dx in the $Z \rightarrow \mu\mu$ control samples [82] (see also [38]).*

the average of all measured dE/dx values, while truncating the layer with the maximal dE/dx estimate. It is shown in a data Monte Carlo comparison for the $Z \rightarrow \mu\mu$ tuning samples in Figure 4.8b, where an excellent agreement can be observed.

4.7 The Tile beta measurement

The signal pulse for each cell of the Tile Calorimeter can be parametrized as [86] (see also [87])

$$f(t) = A \cdot g(t - t_0) + d, \tag{4.10}$$

with the amplitude, A, $g(t)$ the normalized pulse shape and d the pedestal value. The time, t_0, is defined by the peak of the signal distribution. It is measured relative to a trigger reference time. t_0 is chosen in a way to compensate for the time of flight of a relativistic particle with $\beta = 1$. The time of flight of a given particle can be determined from the Tile Calorimeter via [86] (see also [87])

$$t_{\text{reco}} = t_{\text{true}} - \frac{d_{\text{cell}}}{c}. \tag{4.11}$$

Here c is the speed of light, d_{cell} the distance between the center of the cell and the interaction point and t_{true} denotes the true time of the energy deposit. Due to the definition of t_0 (see Equation (4.10)), t_{reco} of relativistic particles is expected to fluctuate around zero. From Equation (4.11), it is straightforward to calculate the speed β from the cell, by [86] (see also [87])

$$\beta_{\text{cell}} = \frac{d_{\text{cell}}}{t_{\text{true}} \cdot c} = \frac{d_{\text{cell}}}{t_{\text{reco}} \cdot c + d_{\text{cell}}}. \tag{4.12}$$

This variable has already been used in a search for long-lived highly ionizing particles [9]. Together with the information of the track momentum, an estimate of the particle mass, m, can be deduced. In

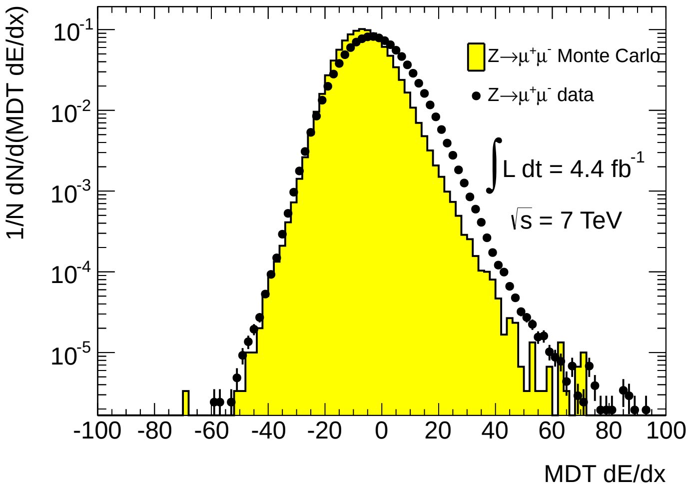

Figure 4.9: *Comparison of data and Monte Carlo distributions of MDT* dE/dx *in the* $Z \to \mu\mu$ *control samples [82] (see also [38]).*

the case of multi-charged particles, this yields the quotient $\frac{m}{q}$, with q the charge of the particle. In the search for multi-charged particles, this variable is intended to determine the mass of the particle in case of a data excess.

4.8 The MDT dE/dx

The MDT readout measures a signal charge within the integration gate of 18.5 ns after the first crossing of the threshold. The working principle of the MDT $\mathrm{d}E/\mathrm{d}x$ is to use the mean number of ADC counts in the MDT as an estimator of the energy lost per path length in the MDT system.

Various corrections have to be made on this first estimate of $\mathrm{d}E/\mathrm{d}x$. Firstly, the mean value of ADC counts fluctuates substantially from tube to tube within a given chamber in data. Thus, a tube calibration is performed on data recorded with the MDT, while the Monte Carlo needs no such correction. Furthermore, it is observed that the mean value of ADC counts is off by a factor of 1.4 in Monte Carlo with respect to data. This difference can be explained by a mismodeling of the gas gain factor in Monte Carlo.

Additionally, the mean of the ADC counts varies by 8% between the different chambers. To remove this effect, the mean number of ADC counts is normalized to 138.1 for each chamber. As a side effect, this correction also normalizes the Monte Carlo to data.

Another correction addresses the dependence of the mean ADC counts to the distance from the track to the readout electronics, which is located at the end of the chambers. This dependence manifests itself as a variation of the ADC value with the azimuth ϕ, reflecting the different distances the signal has to travel to the readout. As this is not modeled in Monte Carlo the correction for this 8% variation has to be applied to data only.

Within the gas tube, the distance from the track to the readout wire (R_{drift}) affects the integrated charge. Therefore, as the final $\mathrm{d}E/\mathrm{d}x$ input the difference between the measured ADC count and its averaged value for the given bin of R_{drift} is used. In applying this correction separately to data and Monte Carlo, the differences in the gas gain factor mentioned above are automatically taken into account.

The final step is the truncation of the hit with the maximal ADC value from the determination of the mean value of ADC counts. This removes differences due to different interpretations of δ-electrons in data and Monte Carlo causing non-matching tails of the distributions. Furthermore, the truncation reduces the RMS of the distribution.

After application of all these corrections, good agreement between data and Monte Carlo is observed. As can be seen in Figure 4.9, the MDT $\mathrm{d}E/\mathrm{d}x$ available for the analysis shows a remaining shift between data and Monte Carlo. This is due to the fact, that at the time of the data processing for the analysis only the correction on R_{drift} and the truncation of the highest ADC count has been implemented in the ATLAS software. Subsequent software releases apply all four corrections and this shift vanishes. For the purpose of the analysis presented here, a systematic uncertainty is assessed from this imperfection of the MDT $\mathrm{d}E/\mathrm{d}x$.

CHAPTER 5

Development of a TRT dE/dx

The development of a dE/dx variable from measurements in the TRT detector and its application in a search for massive particles carrying multiple charges is subject of this thesis. Intensive studies with Minimum Bias data and Monte Carlo defined in Section 5.1 are performed to find a good description of the specific energy loss per path length in the TRT. Previous attempts to define a dE/dx variable form the basis for a more refined description presented in the following. After an introduction to the TRT readout (Section 5.2), different definitions of Time-over-Threshold are discussed in Section 5.3 from which the dE/dx measurement introduced in Section 5.5 is constructed. Note that this chapter reviews only one of two definitions of a TRT dE/dx that have originally been studied. A description of the alternative definition and comparisons of the two versions can be found in Appendix B. The selection of hits and tracks is presented in Section 5.4. Furthermore, the achieved resolution is evaluated (Section 5.6) and the separation power used to assess the quality of the variable in Section 5.7. Finally, theoretical extrapolations of the TRT dE/dx are applied to multi-charged particles and discussed in Section 5.9.

5.1 Data selection

For the development of this variable data and Monte Carlo samples of Minimum Bias events are used. By definition, these events are chosen by a random trigger to minimize potential biases. They contain mostly proton collisions with small energy transfers. The data are recorded in March 2011 (ATLAS run 177986) over the course of 6 hours and 32 minutes with a bunch distance of 75 ns and a mean number of interactions of $\langle\mu\rangle = 5.66$ (see Figure 5.1). A total of 8,784,958 events are recorded. To gain access to low $\beta\gamma$ values and hence the steep rising dE/dx values, the p_T cut in the track selection is fixed to 500 MeV, which is the minimum value in the standard ATLAS track reconstruction. The Monte Carlo events are generated with Pythia [80] are treated in the same way as the data.

5.2 The TRT readout

Within the gas-filled straws of the TRT detector, a charged particle ionizes the gas atoms along its path through the detector. In the electric field applied between the straw walls and the central readout wire, the freed electrons drift towards the center and induce a signal proportional to the path length in the straw and the ionization density at the central readout wire. This process is illustrated in Figure 5.2.

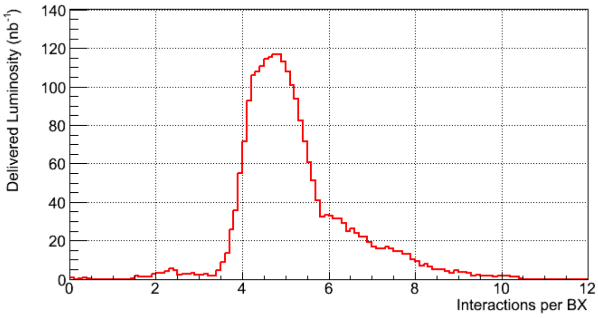

Figure 5.1: *The number of interactions per bunch crossing for ATLAS run 177986 used for the development of the TRT dE/dx [88].*

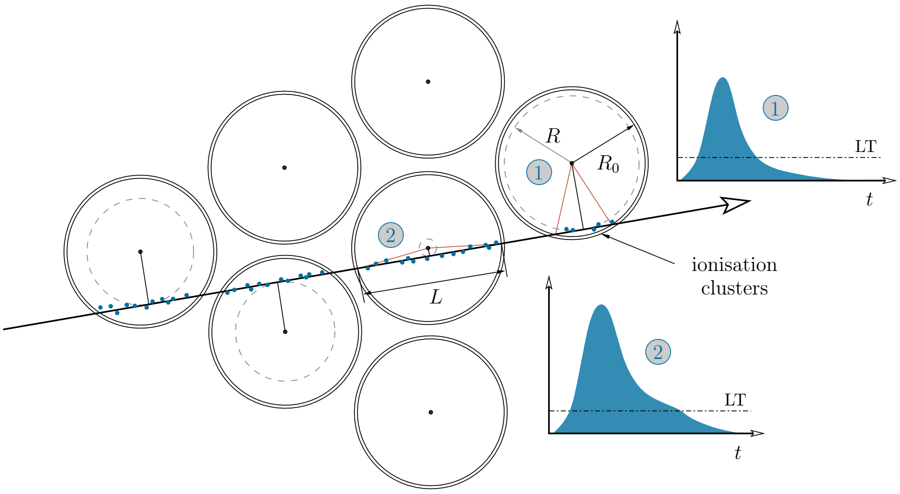

Figure 5.2: *Illustration of a particle traversing the TRT detector. The gas molecules along its way are ionized, the ionization electrons drift towards the anode wire and induce a signal at the wire. In this figure R corresponds to* r_{drift} *in the text and* R_0 *to the straw radius R. Courtesy of [89].*

As previously described in Section 4.5, two thresholds are used to discriminate the signal, the low threshold (LT) at the detection threshold for MIPs (300 eV) insuring precise tracking and determination of the drift time, and the high threshold (HT) at 6 keV chosen for good separation between electron and pion signals. The signal is sampled in 24 time bins over 75 ns. For each time bin in which the signal is higher than LT at least once, a bit is set to 1 and otherwise to 0. The same procedure is applied to the HT in 3 time bins (see also Figure 4.7). The resulting readout, called the TRT bit pattern, can be used to define a Time-over-Threshold (ToT). Each bitpattern different from pure zeros defines a TRT hit and its x-y coordinates are used in the reconstruction of charged particle tracks.

The first ionization electrons to reach the readout wire are those produced closest to it. The position of the ionization of these electrons defines the drift radius r_{drift} (R in Figure 5.2). Therefore, the first bit set to one in the bitpattern, the leading edge (LE), corresponds to the time of arrival of these first electrons at the wire. Accordingly, the last bit set in the bitpattern, the trailing edge (TE), is related to the time of arrival of the ionization electrons produced the furthest away from the wire, that is close to the straw walls.

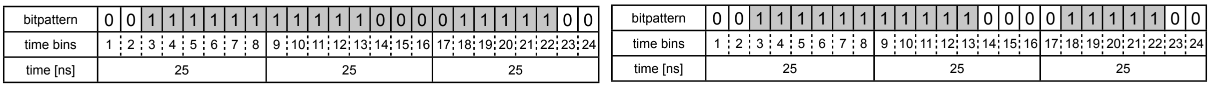

bitpattern	0	0	1	1	1	1	1	1	1	1	1	1	1	1	0	0	0	1	1	1	1	1	0	0
time bins	1	2	3	4	5	6	7	8	9	10	11	12	13	14	15	16	17	18	19	20	21	22	23	24
time [ns]	25								25								25							

(a) ToT^{standard}

bitpattern	0	0	1	1	1	1	1	1	1	1	1	1	1	1	0	0	0	1	1	1	1	1	0	0
time bins	1	2	3	4	5	6	7	8	9	10	11	12	13	14	15	16	17	18	19	20	21	22	23	24
time [ns]	25								25								25							

(b) $ToT^{\text{1-bits}}$

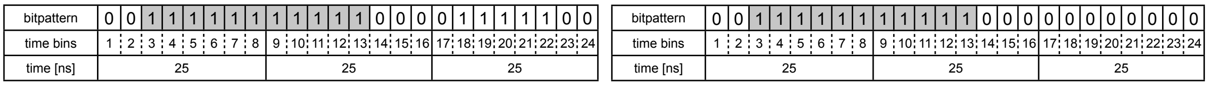

bitpattern	0	0	1	1	1	1	1	1	1	1	1	1	1	1	0	0	0	1	1	1	1	1	0	0
time bins	1	2	3	4	5	6	7	8	9	10	11	12	13	14	15	16	17	18	19	20	21	22	23	24
time [ns]	25								25								25							

(c) ToT^{largest}

bitpattern	0	0	1	1	1	1	1	1	1	1	1	1	1	1	0	0	0	0	0	0	0	0	0	0
time bins	1	2	3	4	5	6	7	8	9	10	11	12	13	14	15	16	17	18	19	20	21	22	23	24
time [ns]	25								25								25							

(d) $ToT^{\text{no hole}}$

Figure 5.3: *The four different definitions of a ToT from the TRT bitpattern considered in this thesis.*

5.3 Time-over-Threshold measurement

Multiple possibilities to extract a Time-over-Threshold from the TRT bitpattern are thinkable. Several definitions are tested with respect to their performance in a TRT $\mathrm{d}E/\mathrm{d}x$.

5.3.1 Definitions of Time-over-Threshold

The first and maybe most obvious definition of a Time-over-Threshold is the number of bins between leading and trailing edge. As this is the standard ToT used in detector operation, it will be referred to as ToT^{standard} in the following. It is illustrated as the colored bits in Figure 5.3a. Alternatively, one could define ToT as the sum of all bits set to one in the bitpattern, here referred to as $ToT^{\text{1-bits}}$(see Figure 5.3b). Often, these two definitions will be identical, if there are no 0-bits in between 1-bits. Another way to treat these 0-bits in the ToT, is selecting the largest cluster of 1-bits and take the length of it as ToT^{largest}. This definition is shown in Figure 5.3c. Furthermore, one could reject all hits with bitpatterns where 0-bits are interleaved with 1-bits. Even though this corresponds to a selection of hits, it is treated as an alternative definition, $ToT^{\text{no hole}}$ (Figure 5.3d), for which all other three definitions become identical.

The best performance is obtained with the ToT^{largest} interpretation, which will be referred to as ToT in the remainder of this chapter. The interested reader is referred to Appendix B for a study of the effects of the alternative ToT definitions on TRT $\mathrm{d}E/\mathrm{d}x$.

Figure 5.4 shows a graphic illustration of the geometry of the TRT straws and some length definitions used in the following. An intuitive construction of $\mathrm{d}E/\mathrm{d}x$ is to divide ToT by the track length L of the charged particle in the straw. L can be derived by simple geometrical reflections, but needs to be treated differently for TRT straws in the barrel and in the end-caps. In the barrel region, the track length within the TRT straw is simply given by

$$L_{\text{barrel}} = \frac{d}{\sin\theta}\,, \tag{5.1}$$

where d is the projection of the track in the x-y-plane. It can be determined from the straw radius $R = 2$ mm and the drift radius r_{drift} via

$$d = 2\sqrt{R^2 - r_{\text{drift}}^2}\,. \tag{5.2}$$

In the end-cap regions, where the straws are oriented radially to z, the track length is derived from

$$L_{\text{end-cap}} = \frac{d}{\sqrt{1 - \sin^2(\theta_{\text{track}})\cos^2(\phi_{\text{track}} - \phi_{\text{straw}})}}\,. \tag{5.3}$$

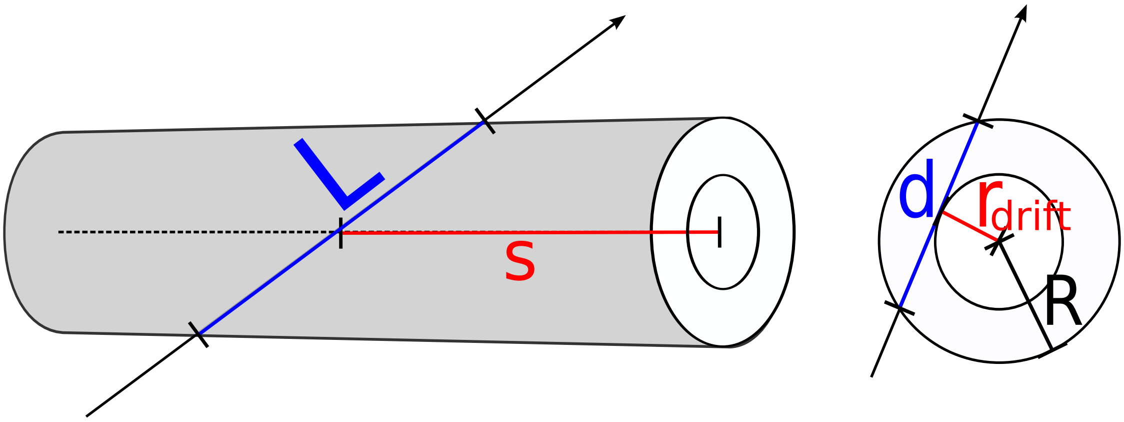

Figure 5.4: *Sketch of a TRT straw with the track length in the straw L, the projection of the track length in the x-y-plane d, the straw radius R (2 mm), the drift radius r_{drift} and the position on the readout wire s.*

5.3.2 Corrections on hit level

The time difference Δt between the first and the last ionization cluster arriving at the readout wire becomes smaller for larger r_{drift}. As a consequence, hits with identical energy deposits can show different ToT depending on the drift radius. Another influence on ToT/L arises from geometric aspects. The straw's length and position in the detector have a large impact on the ToT/L as can be seen in Figure 5.5a. It shows the distribution of ToT/L in the plane of $r = \sqrt{x^2 + y^2}$ and z. Deviations from the average ToT/L ($\overline{ToT/L}$) of up to 20% are observed in certain areas of r and z. Corrections on ToT/L as a function of the drift radius r_{drift} and the position on the wire s (see Figure 5.4 for illustration) are determined individually for all layers and straw layers of the TRT. Note that η can be expressed as a function of s for a given straw, such that η dependencies are corrected for intrinsically. The position on the wire s is equivalent to z in the barrel region and to $r = \sqrt{x^2 + y^2}$ in the end-cap regions. The corrections for each hit stem from the parametrization in Equations (5.4) and (5.5)

$$\text{end-cap} \quad T(r_{\text{drift}}, s) = T_0'(r_{\text{drift}}) + p(r_{\text{drift}}) \cdot s \tag{5.4}$$

$$\text{barrel} \quad T(r_{\text{drift}}, s) = T_0''(r_{\text{drift}}) + q(r_{\text{drift}}) \cdot s^2 \,. \tag{5.5}$$

Equation (5.4) is used in the fits for the end-cap region. $T_0'(r_{\text{drift}})$ and $p(r_{\text{drift}})$ represent third order polynomials. In the barrel region fits $T_0''(r_{\text{drift}})$ and $q(r_{\text{drift}})$ are best described by fifth order polynomials.

Fits to 15 different layers (three barrel layers and 12 end-cap layers) are performed. More precisely, the three barrel layers are split in 19, 24 and 30 straw layers. An iterative fit procedure assures the stability and convergence of the fit. A small remaining offset between barrel and end-cap straws can be observed in the distributions of ToT/L in Figure 5.5b. Overall, the deviations from the mean value remain in the range of ±5%.

5.4 Selection

Not every TRT hit is equally suited for the construction of the specific energy loss per path length. Detector imperfections and geometry influence the ToT. The quality of TRT $\mathrm{d}E/\mathrm{d}x$ can be significantly improved by imposing quality requirements on the hits. In addition, tracks exist for which no meaningful $\mathrm{d}E/\mathrm{d}x$ measurement can be obtained, such that a track selection is introduced as well.

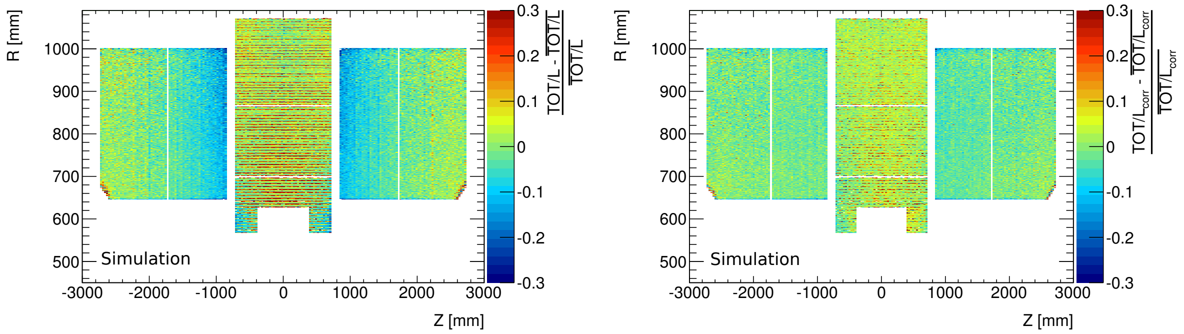

(a) Before Corrections

(b) After Corrections

Figure 5.5: *Relative deviation of* ToT/L *from the mean value shown in the* r-z-*plane before (a) and after (b) the corrections in* r_{drift} *and* s *[90].*

5.4.1 Hit selection

A first improvement arises from the replacement of r_{drift} in Equation (5.2) by a more accurate measure r_{track}. The drift radius, r_{drift}, is constructed from the leading edge of the TRT bitpattern and thus is a binned property. More precise information can be gathered from the fit parameters of the particle track to which the hit belongs to. Taking the shortest distance of the track fit[1] to the wire defines r_{track}.

Tube hits

The TRT straws are operated as drift chambers, in which the limited number of primary ionizations are statistically distributed along the path of the incident charged particle. As a consequence, it is possible, that the closest primary ionization deviates significantly from the distance of closest approach of the track to the wire. Thus, any drift-time measurement from the leading edge of the TRT bitpattern deviating more than 2.5σ from the fitted track-to-wire distance is set to zero with a corresponding error of 4 mm/ $\sqrt{12}$ [91]. These hits are called *tube hits* and are not taken into account for the formation of TRT $\mathrm{d}E/\mathrm{d}x$.

Track radius

The track radius, r_{track}(replacing r_{drift}), is used in the determination of the corrections on ToT/L as well as in the calculation of the track length in the straw, L. Its relation to the measured drift time is shown in Figure 5.6. The fitted r-t-relation is shown as the solid (red) line on the plot. For tracks passing close to the wire, the fit does not describe the mean values of the distribution. To avoid potential biases, hits not well described by the fit are neglected and only hits satisfying

$$0.15 \text{ mm} < r_{\text{track}} < 1.85 \text{ mm} \tag{5.6}$$

are kept. This cut removes less than 10% of all hits. Figure 5.7a shows the normalized distributions of the fraction of tracks as a function of r_{track} before and after the application of this cut.

---

[1] For an unbiased estimation of r_{track} the considered hit is omitted and the track is refit.

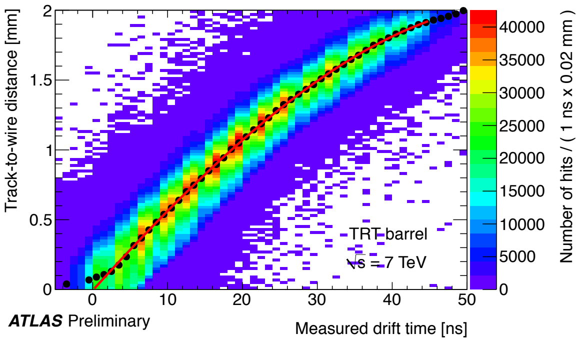

Figure 5.6: *The relation between the drift time and the track radius in the TRT barrel straws. The mean values in each bin of the drift time are given by the black dots. The solid red line describes the fitted r-t-relation used in the calculation of* r_{drift} *[92].*

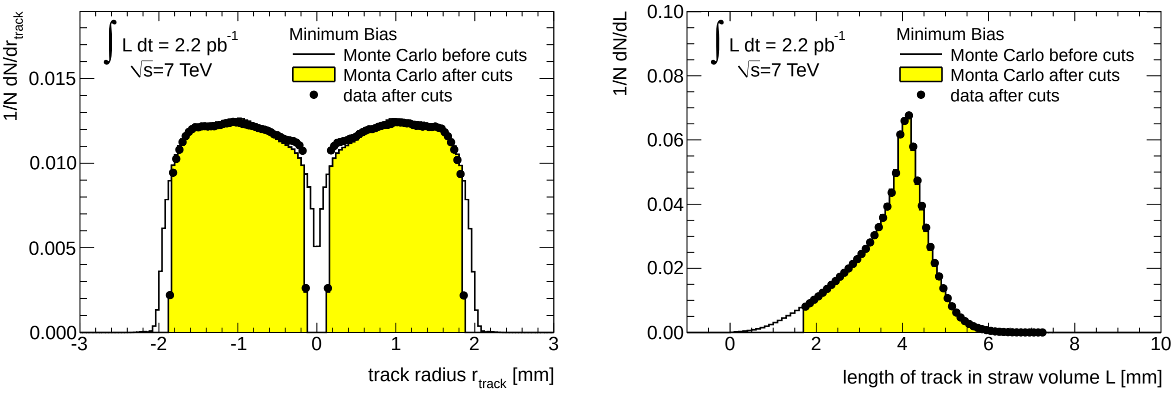

(a) Cut on r_{track}

(b) Cut on L

Figure 5.7: *The distribution of hits as a function of (a)* r_{track} *and (b) L before the cut (solid black line) and after the cut (shaded yellow area) on these variables. The plots show distributions from the Minimum Bias Monte Carlo and data samples [90].*

Track length

Given a specific energy loss $\mathrm{d}E/\mathrm{d}x$ and ionization density, $\rho_{\text{ionization}}$, a minimal number of ionizations is required to get a reliable estimate of the true $\mathrm{d}E/\mathrm{d}x$. In the TRT gas around 40 primary ionizations are expected per mm for a MIP at standard pressure [93]. These are subject to a gas amplification factor of 2.5×10^4. For short track segments $\mathrm{d}x$, the estimate will be biased to higher values of $\mathrm{d}E/\mathrm{d}x$. For this reason, a minimal track length in the straw of 1.7 mm (Equation (5.7), Figure 5.7b) is required

$$L > 1.7\ \text{mm}\,. \tag{5.7}$$

For some choices of the cuts on r_{track}, this cut may be implicitly taken into account. This is not the case in the barrel. However, Equation (5.7) removes less than 1% additional hits.

Summary

A summary of all hit cuts applied in the selection for the construction of a TRT dE/dx is listed in Table 5.1. Any hit passing all three selection criteria is called a *good dE/dx TRT hit*.

Table 5.1: *Summary of the hit cuts applied in the selection of hits for the construction of the TRT dE/dx.*

Property	Cut
Tube hits	Remove
Track radius	0.15 mm $< r_{\text{track}} <$ 1.85 mm
Track length	$L >$ 1.7 mm

5.4.2 Track selection

The track selection in all following studies is defined as an extended version of the standard ATLAS track selection [94]. It requires a minimal transverse momentum p_{T} of 500 MeV which defines the cut-off for track reconstruction in ATLAS. Furthermore, the track should originate from the vecinity of the production vertex within $|d_0| <$ 1.5 mm and $|z_0 \sin\theta| <$ 1.5 mm. The pseudorapidity has to be within $|\eta| < 2.5$. The TRT only reaches out to $|\eta| < 2.0$, which can be considered as an intrinsic cut on η. Additionally, the track is required to be constructed from at least one hit in the Pixel detector and six hits in the SCT detector.

Furthermore, an additional cut of at least 6 good dE/dx TRT hits per track is necessary since dE/dx represents the average of good dE/dx TRT hits. Figure 5.8a demonstrates that only a negligible fraction of tracks does not fulfill this requirement. In addition, Figure 5.8b shows the dE/dx reconstruction efficiency as a function of the cut on the number of good dE/dx TRT hits. The vertical lines indicate the chosen cut of $N_{\text{good d}E/\text{d}x\text{ TRT hit}} > 5$. A reconstruction efficiency above 98% is achieved.

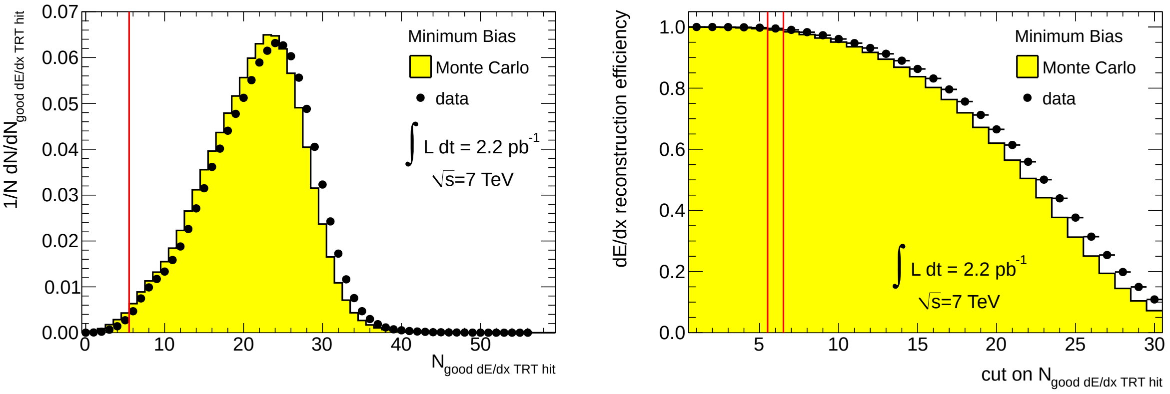

(a) Distribution of good dE/dx TRT hits

(b) dE/dx reconstruction efficiency

Figure 5.8: *The distribution of the number of good dE/dx TRT hits (a) and the dE/dx reconstruction efficiency vs. the cut on* $N_{\text{good d}E/\text{d}x\text{ TRT hit}}$ *(b). The plots show distributions from the Minimum Bias Monte Carlo and data samples [90]. The vertical lines indicate the chosen cut at* $good dE/dx\,TRT hit > 5$.

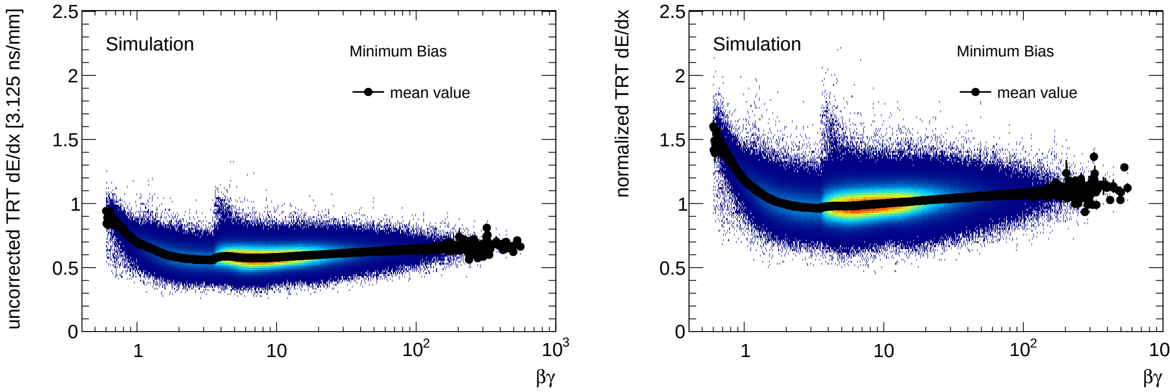

(a) uncorrected TRT $\mathrm{d}E/\mathrm{d}x$

(b) TRT $\mathrm{d}E/\mathrm{d}x$ (corrected)

Figure 5.9: Comparison of TRT $\mathrm{d}E/\mathrm{d}x$ as a function of $\beta\gamma$ before (a) and after (b) the corrections applied to ToT/L on hit level.

5.4.3 Truncated mean

The track $\mathrm{d}E/\mathrm{d}x$ is an average of the selected and corrected ToT/L measurements. As discussed in Section 4.1.1, these single energy deposits follow a Landau-like shape and are randomly distributed. As a consequence, the arithmetic mean of the single energy deposits often is dominated by the highest energy deposits in the tail of the distribution and can deviate significantly from the most probable energy loss. The *truncated mean* aims at an estimation of the most probable value by rejecting a certain number or fraction of the highest (and sometimes also lowest) measured energy deposits.

The arithmetic mean of all but the highest ToT/L on track is chosen as $\mathrm{d}E/\mathrm{d}x$. This definition keeps the loss of information at a minimum, while estimating a value close to the most probable energy loss. Appendix B lists further details on this choice.

5.5 dE/dx measurement

The TRT $\mathrm{d}E/\mathrm{d}x$ is determined via

$$\mathrm{d}E/\mathrm{d}x_{\mathrm{track}} = \frac{\sum\limits_{(ToT/L)_i < (ToT/L)_{\mathrm{highest}}} (ToT/L)_i}{N-1}, \tag{5.8}$$

where $(ToT/L)_i$ denotes the single corrected ToT/L measurements among which $(ToT/L)_{\mathrm{highest}}$ has the highest value on a track with N good $\mathrm{d}E/\mathrm{d}x$ TRT hits. Before all corrections, ToT/L has units of 3.125 ns/mm. Hence, TRT $\mathrm{d}E/\mathrm{d}x$ does not give the actual energy loss per path length. Nevertheless, it is used as an estimator to describe the energy loss behavior. The correction on ToT/L (defined in Section 5.3.2) are chosen in a way to normalize TRT $\mathrm{d}E/\mathrm{d}x$ to one for minimum ionizing particles. Therefore, the final TRT $\mathrm{d}E/\mathrm{d}x$ is a dimensionless property. Figure 5.9 compares the distributions of TRT $\mathrm{d}E/\mathrm{d}x$ as a function of $\beta\gamma$ constructed from uncorrected ToT/L and from corrected ToT/L in the Minimum Bias simulation. It can be deduced, that the corrections on ToT/L result in a shift in TRT $\mathrm{d}E/\mathrm{d}x$ to higher values.

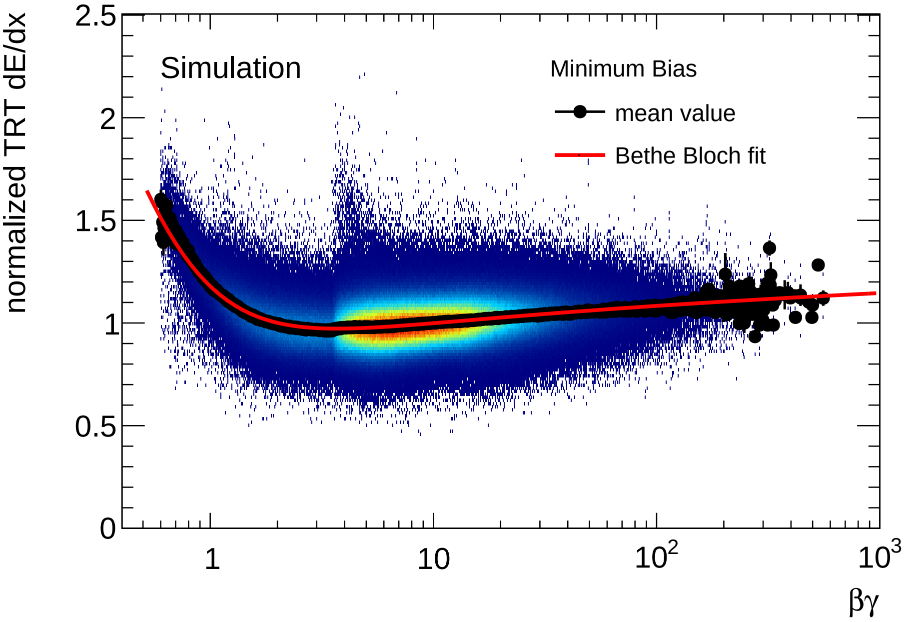

Figure 5.10: *The measured dE/dx as a function of $\beta\gamma$ in the Minimum Bias Monte Carlo sample. Overlaid is the mean value in each bin (black dots) and the result of the fit from Equation* (4.5)*. The structure at $\beta\gamma \approx 3.5$ is an artifact of the particle content of the Minimum Bias Monte Carlo sample (see text) [90].*

5.5.1 Bethe-Bloch fit

If $\mathrm{d}E/\mathrm{d}x_{\mathrm{track}}$ is to be an estimator for the specific energy loss per path length in the TRT detector, it has to follow the restricted energy loss curve defined in Equation (4.4). A fit to $\beta\gamma$ can only be performed in data if a very pure sample of one single particle species is available. Otherwise, the mass m of the particle corresponding to a given track with momentum p is unknown and $\beta\gamma$ can not be determined. In another approach the distribution is taken from Monte Carlo, where the true (simulated) mass of each particle track is known. This can only be done, if sufficient agreement between the distributions in data and Monte Carlo can be expected. In the case of TRT $\mathrm{d}E/\mathrm{d}x$ the corrections are applied independently to data and simulation and are chosen to yield the same scale in both cases. Therefore, the fit can be performed to Monte Carlo and applied to data afterwards.

Figure 5.10 demonstrates an excellent description of the track $\mathrm{d}E/\mathrm{d}x$ by the parametrization described in Equation (4.5). It shows the measured $\mathrm{d}E/\mathrm{d}x_{\mathrm{track}}$ as a function of $\beta\gamma$ in the Minimum Bias Monte Carlo sample, its mean value (black dots) and the fitted function (red line). No simulated data is available below $\beta\gamma \approx 0.5$, such that the fit is only valid in the range above this value. The structure at $\beta\gamma \approx 3.5$ is an artifact of the particle content of the Minimum Bias Monte Carlo sample. It is dominated by pions which populate the $\beta\gamma = p/m$ region above 3.5, because of the cut on $p_{\mathrm{T}} > 500\,\mathrm{MeV}$. Hence, the structure is the *turn-on* of the pion sample.

This fit function can be used to make predictions of $\mathrm{d}E/\mathrm{d}x$ for different particle species in both data and simulation. By substituting $\beta\gamma = p/m$ with the track momentum divided by the particle's mass, one can test the particle content of the data sample under study. The result is shown in Figure 5.11a for Monte Carlo and in Figure 5.11b for data. The particle content of the Minimum Bias samples can be deduced to consist of mainly pions and some kaons, protons and deuterons.

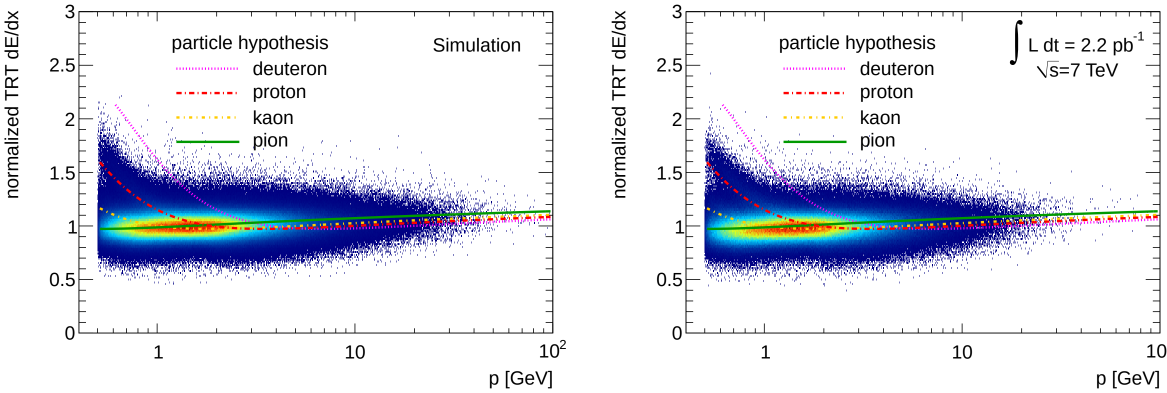

(a) Simulation (b) Data

Figure 5.11: *The measured* dE/dx_{track} *as a function of the track momentum for the Minimum Bias Monte Carlo (a) and data (b) sample. Overlaid are the particle hypothesis for deuterons, protons, kaons and pions [90].*

5.5.2 Track level corrections

Further corrections can be applied at track level, with the advantage that they can be done differently for each analysis using TRT $\mathrm{d}E/\mathrm{d}x$. In the following, some exemplary corrections that are useful for particle identification studies are presented.

Electron parametrization

The TRT has been designed to create extra ionization from transition radiation for electron tracks. As a consequence, the relation between the measured Time-over-Threshold and the true energy lost in the detector is different for electrons than for all other particles. In a dedicated study [90] with electrons from conversions, it is found that correcting the fit function with

$$\mathrm{d}E/\mathrm{d}x^{corr.}_{\text{pred.}} = \frac{\mathrm{d}E/\mathrm{d}x_{\text{pred.}}}{f(p)}\,, \tag{5.9}$$

where

$$f(p) = 0.045 \cdot \log(p) + 0.885 \qquad \text{(p in [MeV])}, \tag{5.10}$$

leads to a good description of the electron behavior. Note that this correction is not applied to the measured $\mathrm{d}E/\mathrm{d}x_{\text{track}}$ but merely to the predictions from the fit function made for electrons.

Pile-up dependence

Due to the high luminosity conditions at the LHC, multiple interactions take place in one bunch crossing. The distribution of the number of interactions in the data sample used for the development of this variable is shown in Figure 5.1. The larger occupancy in the TRT decreases the tracking performance and leads to more tube hits, which are rejected in the TRT $\mathrm{d}E/\mathrm{d}x$ hit selection. This results in a lower reconstructed efficiency of TRT $\mathrm{d}E/\mathrm{d}x$ as fewer tracks have sufficient good $\mathrm{d}E/\mathrm{d}x$ TRT hits to be considered in the construction.

Moreover, the presence of many other particle tracks will influence the behavior of the ToT if more than one track crosses the same TRT straw. As a consequence, the mean value of the $\mathrm{d}E/\mathrm{d}x$ is shifted

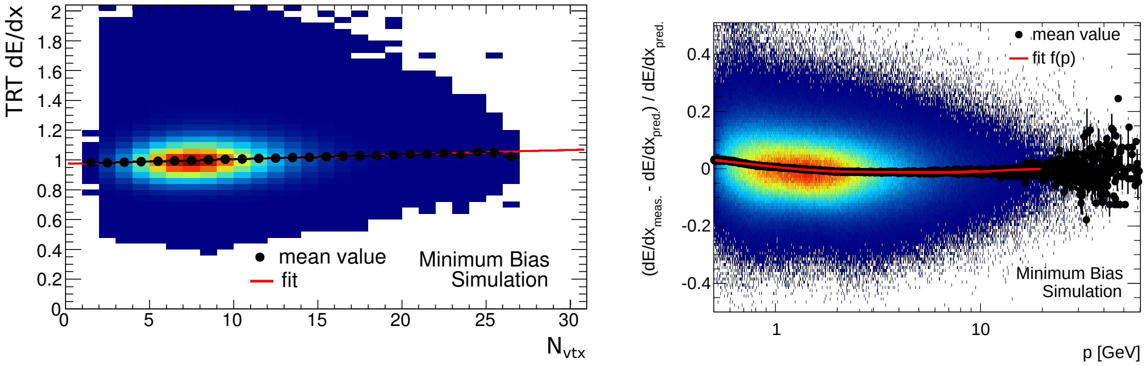

(a) TRT $\mathrm{d}E/\mathrm{d}x$ vs. N_{vtx}

(b) $(\mathrm{d}E/\mathrm{d}x_{\mathrm{meas.}}$-$\mathrm{d}E/\mathrm{d}x_{\mathrm{pred.}})/\mathrm{d}E/\mathrm{d}x_{\mathrm{pred.}}$

Figure 5.12: *(a) TRT dE/dx plotted as a function of the number of primary vertices in the Minimum Bias Monte Carlo sample. Overlaid is the profile distribution (black points) and the linear fit to the profile (red) [90]. (b) The dependence of the relative difference between the predicted* ($dE/dx_{\mathrm{pred.}}$) *and measured dE/dx* ($dE/dx_{\mathrm{meas.}}$) *on track momentum in the Minimum Bias Monte Carlo sample. The black dots represent the mean value in each momentum bin, whereas the red line is the fit on which the momentum correction is based [90].*

as a function of the number of vertices present in a given event shown in Figure 5.12a. The more tracks are present, the higher $\mathrm{d}E/\mathrm{d}x$ becomes.

The profile shows that the effect of pile-up can generally be corrected by a simple linear function with a small slope

$$\mathrm{d}E/\mathrm{d}x_{\mathrm{track}} = (0.975 + 0.003 \cdot N_{\mathrm{vertex}}) \cdot \mathrm{d}E/\mathrm{d}x_{\mathrm{meas.}} \,. \tag{5.11}$$

With the constantly changing pile-up conditions of the LHC, this correction might change over time. It is, however, determined on track level and straightforward to derive in each analysis using the TRT $\mathrm{d}E/\mathrm{d}x$ variable. In the search for multi-charged particles, this correction is included and it is small.

Momentum dependence

After the application of all corrections mentioned above, a remaining small dependence on the track momentum persists for low momentum values. Figure 5.12b shows the relative difference between the predicted ($\mathrm{d}E/\mathrm{d}x_{\mathrm{pred.}}$) and measured $\mathrm{d}E/\mathrm{d}x$ ($\mathrm{d}E/\mathrm{d}x_{\mathrm{meas.}}$) as a function of track momentum. Deviations below 5% can be observed up to a momentum of $\approx$ 2 GeV. The momentum range corresponds to the steep rise of the fit function at low $\beta\gamma$ values. In this regime, the uncertainties of the fit are the largest.

A correction function $f(p)$ chosen to be the product of a decaying exponential function and a third order polynomial (see Equation (5.12)) is derived from this distribution. a_0 to a_4 are parameters determined from the fit of

$$f(p) = \exp(-a_0 p) \cdot (a_1 + a_2 \cdot p + a_3 \cdot p^2 + a_4 \cdot p^3) = \frac{\mathrm{d}E/\mathrm{d}x_{\mathrm{meas.}} - \mathrm{d}E/\mathrm{d}x_{\mathrm{pred.}}}{\mathrm{d}E/\mathrm{d}x_{\mathrm{pred.}}} \,. \tag{5.12}$$

Consequently, a correction factor of

$$\mathrm{d}E/\mathrm{d}x^{\mathrm{corr.}}_{\mathrm{meas.}} = \frac{\mathrm{d}E/\mathrm{d}x_{\mathrm{meas.}}}{1 + f(p)} \tag{5.13}$$

is applied to $\mathrm{d}E/\mathrm{d}x$ on track level for tracks with momenta below 10 GeV. This momentum range is not selected in the search for multi-charged particles, such that this correction is meaningless for the analysis presented in this dissertation.

5.5.3 Summary

TRT $\mathrm{d}E/\mathrm{d}x$ is constructed for selected tracks. On these tracks, single ToT/L values are selected as good $\mathrm{d}E/\mathrm{d}x$ TRT hits and hit-level corrections are applied to them. Next, the track $\mathrm{d}E/\mathrm{d}x$ is constructed and additional corrections for the remaining dependencies on momentum and pile-up are included on track level. The derived TRT $\mathrm{d}E/\mathrm{d}x$ measurements are investigated further hereafter.

5.6 Resolution

The resolution $\sigma(\mathrm{d}E/\mathrm{d}x)$ of the measured $\mathrm{d}E/\mathrm{d}x$ indicates how much it deviates from the prediction made by the Bethe-Bloch fit of Equation 4.5. It is defined as the standard deviation $\sigma(\mathrm{d}E/\mathrm{d}x)$ of the distribution $\delta(\mathrm{d}E/\mathrm{d}x)$ in Equation (5.14)

$$\delta(\mathrm{d}E/\mathrm{d}x) = \frac{\mathrm{d}E/\mathrm{d}x_{\text{meas.}} - \mathrm{d}E/\mathrm{d}x_{\text{pred.}}}{\mathrm{d}E/\mathrm{d}x_{\text{pred.}}}\,, \tag{5.14}$$

where $\mathrm{d}E/\mathrm{d}x_{\text{meas.}}$ is the track's measured $\mathrm{d}E/\mathrm{d}x$ and $\mathrm{d}E/\mathrm{d}x_{\text{pred.}}$ gives the value of the fit of Equation (4.5) to all $\mathrm{d}E/\mathrm{d}x$ for given $\beta\gamma = p/m$.

The resolution allows for important insight on the influences of detector geometry through the pseudorapidity η, the drift radius r_{drift} and track variables such as the momentum. Furthermore, it evaluates the quality of the $\mathrm{d}E/\mathrm{d}x$ variable.

5.6.1 Dependence on the number of good dE/dx TRT hits

The central value $\langle\delta(\mathrm{d}E/\mathrm{d}x)\rangle$ of the distribution of $\delta(\mathrm{d}E/\mathrm{d}x)$ shows a strong dependence on the number of good $\mathrm{d}E/\mathrm{d}x$ TRT hits ($N_{\text{good}\ \mathrm{d}E/\mathrm{d}x\ \text{TRT hit}}$) used in the calculation of $\mathrm{d}E/\mathrm{d}x$. For small values of $N_{\text{good}\ \mathrm{d}E/\mathrm{d}x\ \text{TRT hit}}$ (see Figure 5.13a) $\mathrm{d}E/\mathrm{d}x_{\text{meas.}}$ deviates up to 7% from the prediction of the fit function. This deviation constantly decreases and can be regarded as negligible above $N_{\text{good}\ \mathrm{d}E/\mathrm{d}x\ \text{TRT hit}} = 20$.

The standard deviation of a distribution of mean values decreases with the size of the sample the mean value is determined from. Hence, the resolution of $\mathrm{d}E/\mathrm{d}x$ (an averaged property) depends strongly on the number of good $\mathrm{d}E/\mathrm{d}x$ TRT hits used in its calculation. This dependence is illustrated in Figure 5.13b. The achieved resolution varies from ≈14% at $N_{\text{good}\ \mathrm{d}E/\mathrm{d}x\ \text{TRT hit}} = 6$ to 6% at $N_{\text{good}\ \mathrm{d}E/\mathrm{d}x\ \text{TRT hit}} = 36$.

5.6.2 Dependence on the pseudorapidity

Figure 5.14 shows that the number of hits on track (N_{hit}) has a very strong dependence on η due to the geometry of the ATLAS detector. A study of the impact of η on the resolution of $\mathrm{d}E/\mathrm{d}x$, needs to be performed in a region, where the influence of N_{hit} on the $\mathrm{d}E/\mathrm{d}x$ resolution is small. This remaining dependence on η of $\langle\delta(\mathrm{d}E/\mathrm{d}x)\rangle$ and $\sigma(\mathrm{d}E/\mathrm{d}x)$ is shown for $N_{\text{hit}} > 20$ in Figure 5.15. Deviations from zero of $\langle\delta(\mathrm{d}E/\mathrm{d}x)\rangle$ on the level of ±2% can still be observed, the resolution of $\mathrm{d}E/\mathrm{d}x$ fluctuates around 8%.

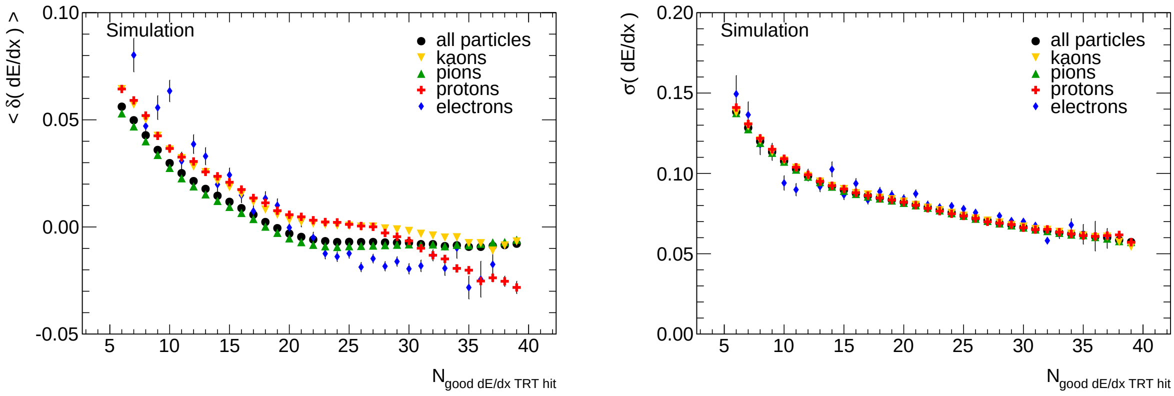

(a) $\langle \delta(\mathrm{d}E/\mathrm{d}x) \rangle$ (b) $\sigma(\mathrm{d}E/\mathrm{d}x)$

Figure 5.13: *The dependence of the central value of the* $\delta(\mathrm{d}E/\mathrm{d}x)$ *distribution (a) and* $\sigma(\mathrm{d}E/\mathrm{d}x)$ *(b) as a function of the number of good* $\mathrm{d}E/\mathrm{d}x$ *TRT hits used in the calculation of* $\mathrm{d}E/\mathrm{d}x$ *[90].*

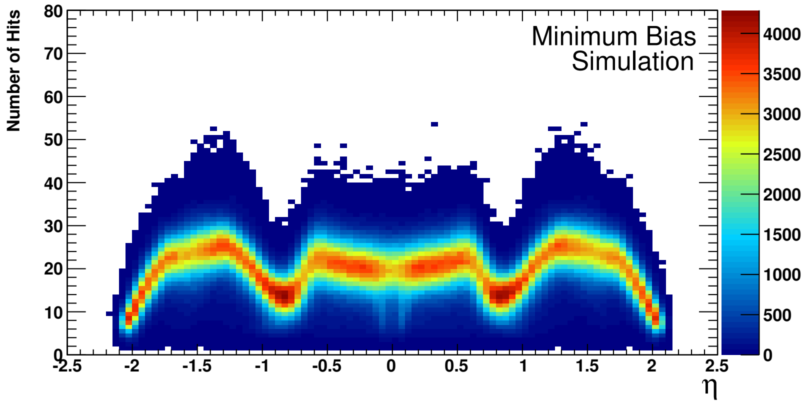

Figure 5.14: *Dependence of the number of hits on track on the pseudorapidity* η *[90].*

5.7 Separation power

Many different definitions of $\mathrm{d}E/\mathrm{d}x$ are tested with the help of the separation power defined in Section 4.1.4. It can be regarded as a tool to decide which definition of $\mathrm{d}E/\mathrm{d}x$ or ToT yields the best $\mathrm{d}E/\mathrm{d}x$ discriminant. The version introduced in this chapter is chosen as the optimal definition based on its separation power. A short summary of the alternative approaches can be found in Appendix B.

5.7.1 Different number of hits

As shown before, the resolution $\sigma(\mathrm{d}E/\mathrm{d}x)$ depends strongly on the number of good $\mathrm{d}E/\mathrm{d}x$ TRT hits available to determine $\mathrm{d}E/\mathrm{d}x$. This results in a strong dependence of the separation power on this number. Figure 5.16 illustrates the predicted $\mathrm{d}E/\mathrm{d}x$ values for electrons, protons, kaons and pions together with their resolutions for a given number of good $\mathrm{d}E/\mathrm{d}x$ TRT hits. A significant improvement of the separation towards large numbers of good $\mathrm{d}E/\mathrm{d}x$ TRT hits can be observed. This fact can also be observed in the separation power shown in Figure 5.17 for 6, 10, 20 and 30 $N_{\text{good d}E/\text{d}x\ \text{TRT hit}}$. Since this dependence is by far the dominating one, all comparisons in Appendix B are made at a fixed number of

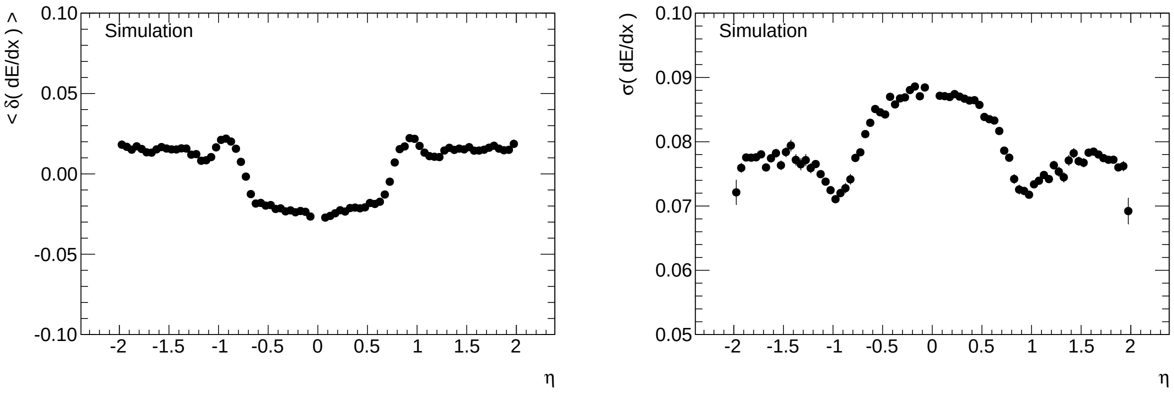

(a) $\langle\delta(\mathrm{d}E/\mathrm{d}x)\rangle$ (b) $\sigma(\mathrm{d}E/\mathrm{d}x)$

Figure 5.15: *The dependence of $\sigma(dE/dx)$ (b) and the central value of the $\delta(dE/dx)$ distribution (a) as a function of η [90].*

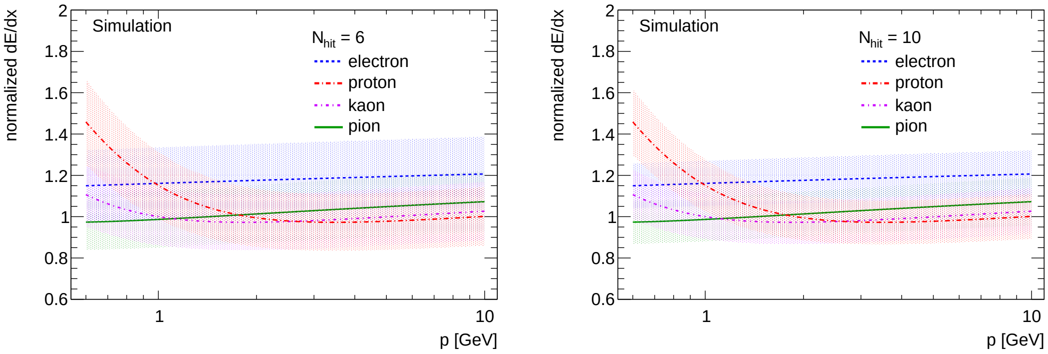

(a) $N_{\text{good d}E/\text{d}x\text{ TRT hit}} = 6$ per track (b) $N_{\text{good d}E/\text{d}x\text{ TRT hit}} = 10$ per track

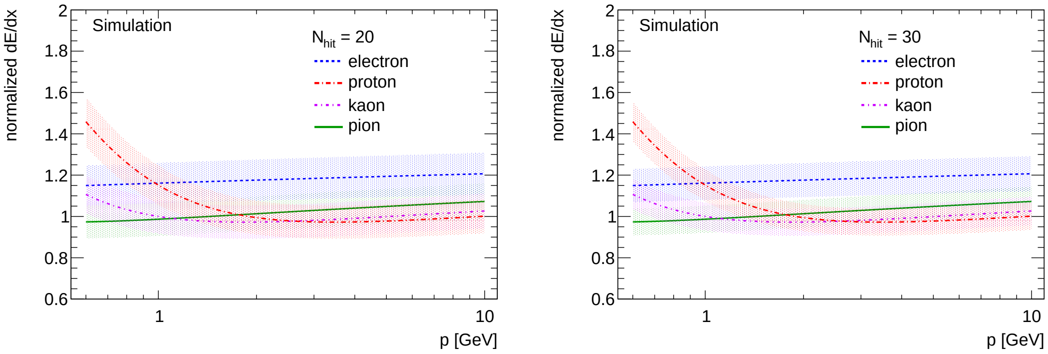

(c) $N_{\text{good d}E/\text{d}x\text{ TRT hit}} = 20$ per track (d) $N_{\text{good d}E/\text{d}x\text{ TRT hit}} = 30$ track

Figure 5.16: *The predicted values of dE/dx for pions, electron, kaons and protons. The bands indicate the resolution for the given value of $N_{\text{good d}E/\text{d}x\text{ TRT hit}}$ of (a) 6, (b) 10, (c) 20 and (d) 30.*

$N_{\text{good d}E/\text{d}x\text{ TRT hit}}$ of 20, which reflects its most probable value (see Figure 5.8a).

5.8 Validation with $\mathbf{Z} \rightarrow \mu\mu$ control samples

The agreement between data and Monte Carlo in the $Z \rightarrow \mu\mu$ control samples defined in Section 4.3 is tested analogous to Sections 4.4 to 4.8. The TRT dE/dx is designed to have the same behavior in data and Monte Carlo. Nevertheless, a small shift of the Monte Carlo distribution of $Z \rightarrow \mu\mu$ events with respect to the data remains. From the $Z \rightarrow \mu\mu$ control samples a scaling $s = 0.9643$ applied to Monte Carlo is extracted. With this a good match of the two distributions is achieved. In the analysis of this thesis, this scaling is applied as an additional track-level correction to all simulated TRT dE/dx. The resulting good agreement between data and Monte Carlo is shown in Figure 5.18.

5.9 Application to multi-charged particles

As shown in Equation (4.4), dE/dx is proportional to the square of the particle charge q. Hence, theoretical predictions of the energy loss of multi-charged particles can be made by introducing this factor q^2 into the fit of Equation (4.5). These extrapolations are discussed in Section 5.9.1. It follows the translation into a prediction for dE/dx as a function of the true particle momentum. The effect of the momentum misinterpretation of the reconstruction is subject of Section 5.9.2.

These extrapolations, however, are purely theoretical. The TRT bitpattern, which serves as input to the construction of the variable has a limited length of 24 bits. This length has been designed and optimized to read out ionization electrons from singly charged particles. Thus, the expected ToT of multi-charged particles exceeds the length of the TRT bitpattern and the dE/dx constructed from it saturates at some point. Furthermore, these hypotheses can not be validated with data, as no stable massive particles carrying multiple electric charges are known to date. Therefore, to make predictions about the highly ionizing behavior of these particles, one relies entirely on predictions made by Monte Carlo simulations (introduced in Chapter 6). The saturation is discussed in more detail with simulated samples in the next Chapter in Section 6.2.3.

5.9.1 Theoretical extrapolation from fit function

The predictions for particles of different charge as a function of $\beta\gamma$ are shown in Figure 5.19 for $|q| = 1e$ - $6e$. The quadratic dependence on charge results in a dramatic shift in the y-axis values of the predicted TRT dE/dx. Using $\beta\gamma = p/m$, this can be translated into comparisons of multi-charged particles of different masses and charges. This is shown for masses 50, 200, 400 and 600 GeV in comparison with the prediction for muons in Figure 5.20. The fit derived in the development of the TRT dE/dx (Section 5.5.1) has a cut-off at $\beta\gamma = 0.5$. Thus the predictions for multi-charged particles are only valid for momenta above $p = 0.5 \cdot m$ to ensure the validity of the fit. For masses 50, 200, 400 and 600 GeV, this implies a momentum cut at 25, 100, 200 and 300 GeV respectively.

5.9.2 Momentum misreconstruction

Moreover, it needs to be considered that the momentum of multi-charged particles is not reconstructed correctly (see Section 1.1 for details). This has implications on the interpretation of their dE/dx information. Figure 5.21 shows the dE/dx as a function of the reconstructed momentum $p_{\text{reco}} = \frac{p_{\text{true}}}{q}$ for multi-charged particles and muons. In this case, the implied momentum cut on the reconstructed momentum due to the validity range of the fit is determined from $p = 0.5 \cdot m \cdot q$. It is thus different for

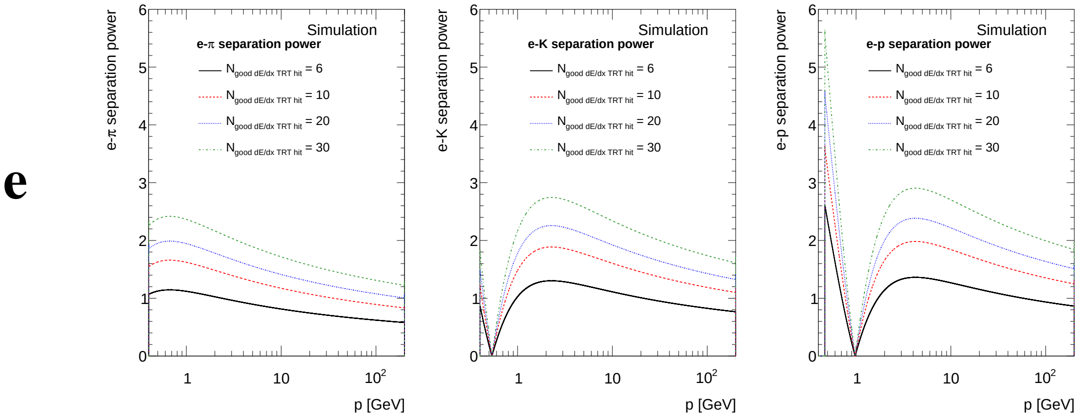

(a) Electrons - Pions (b) Electrons - Kaons (c) Electrons - Protons

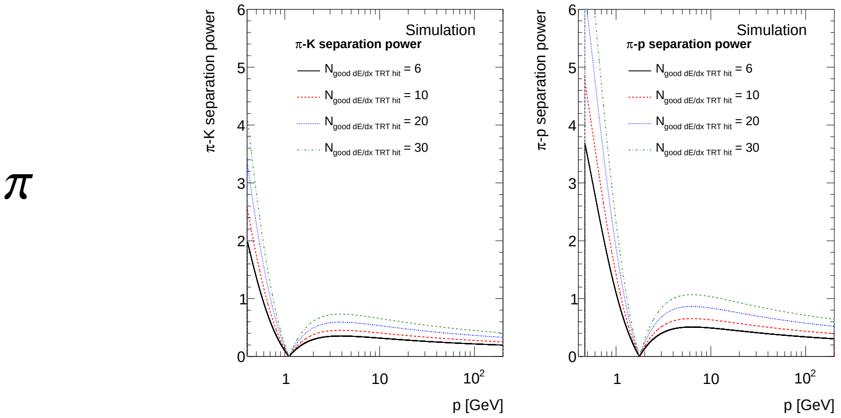

(d) Pions - Kaons (e) Pions - Protons

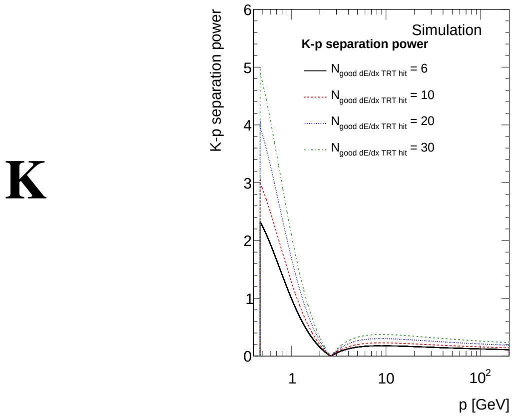

(f) Kaons - Protons

p

Figure 5.17: *The separation power of TRT* dE/dx *for fixed values of* $N_{\text{good}\ dE/dx\ \text{TRT hit}} = 6$*, 10, 20 and 30. A cut on* $\beta\gamma > 0.5$ *is applied to exclude the low* $\beta\gamma$*-region not covered by the fit [90].*

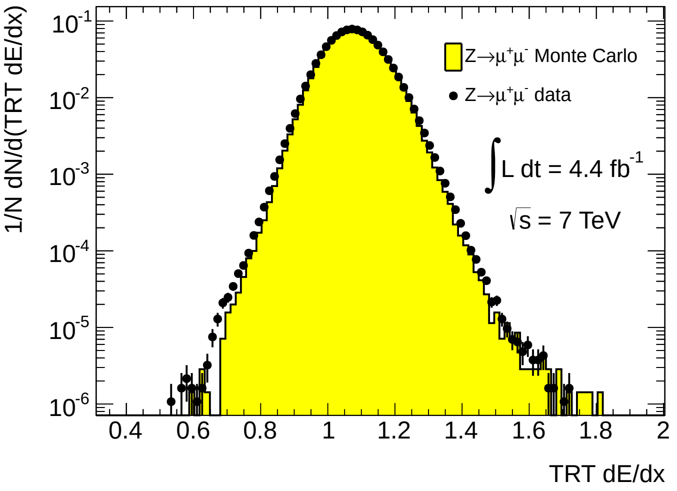

Figure 5.18: *Comparison of data and Monte Carlo distributions of TRT dE/dx in the $Z \rightarrow \mu\mu$ control samples [82] (see also [38]).*

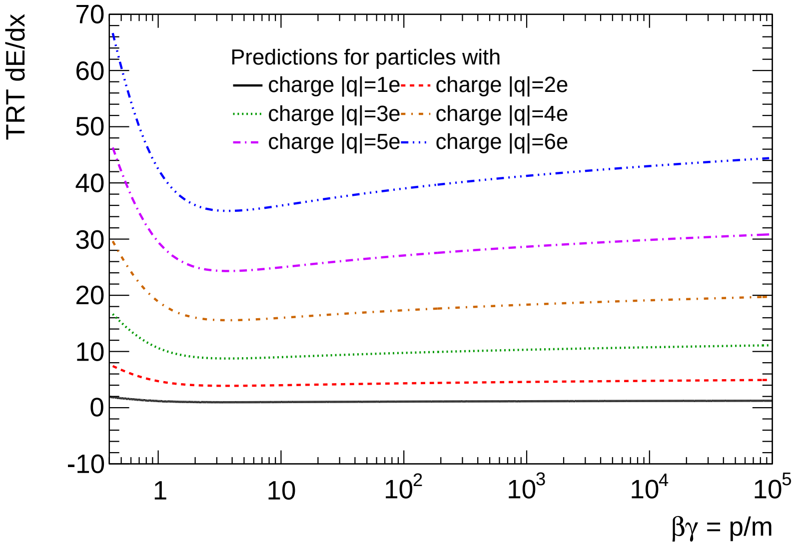

Figure 5.19: *Predictions for the TRT dE/dx for standard model ($|q| = 1e$) and multi-charged particles.*

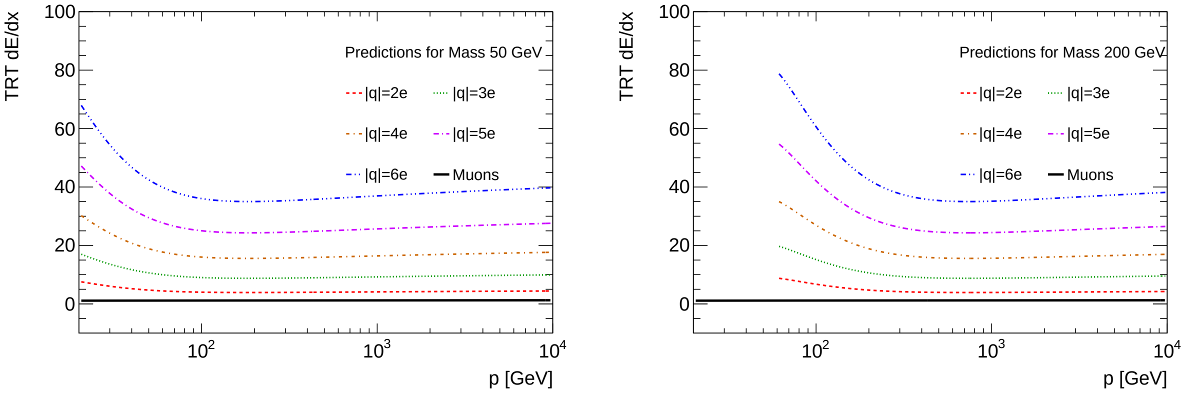

(a) Mass 50 GeV

(b) Mass 200 GeV

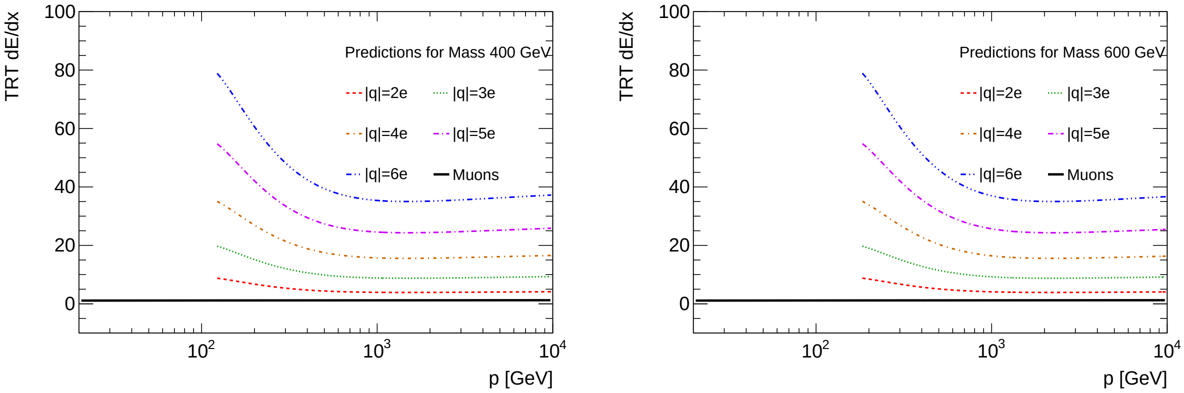

(c) Mass 400 GeV

(d) Mass 600 GeV

Figure 5.20: *The predicted TRT dE/dx for multi-charged particles and muons as extrapolated from the fit to* $|q| = 1e$ *particles versus the true particle momentum* p *for masses 50 GeV (a), 200 GeV (b), 400 GeV (c) and 600 GeV (d). The validity range of the* dE/dx *fit above* $\beta\gamma = 0.5$ *translates into a cut-off at lower momentum values* $p = 0.5m$ *for a given mass* m*.*

each of the signals considered and summarized in Table 5.2. In comparison to Figure 5.20 the $\mathrm{d}E/\mathrm{d}x$ curves appear to be shifted towards higher momentum values as a result of the misinterpretation of the measured momentum.

Table 5.2: *The validity range of the predictions for TRT dE/dx as a function of the reconstructed momentum of multi-charged particles. The table gives the lowest momentum values for which an extrapolation can be done.*

Mass [GeV]	Lower momentum cut [GeV]				
	$\lvert q\rvert = 2e$	$\lvert q\rvert = 3e$	$\lvert q\rvert = 4e$	$\lvert q\rvert = 5e$	$\lvert q\rvert = 6e$
50	50	75	100	125	150
100	100	150	200	250	300
200	200	300	400	500	600
300	300	450	600	750	900
400	400	600	800	1000	1200
500	500	750	1000	1250	1500
600	600	900	1200	1500	1800

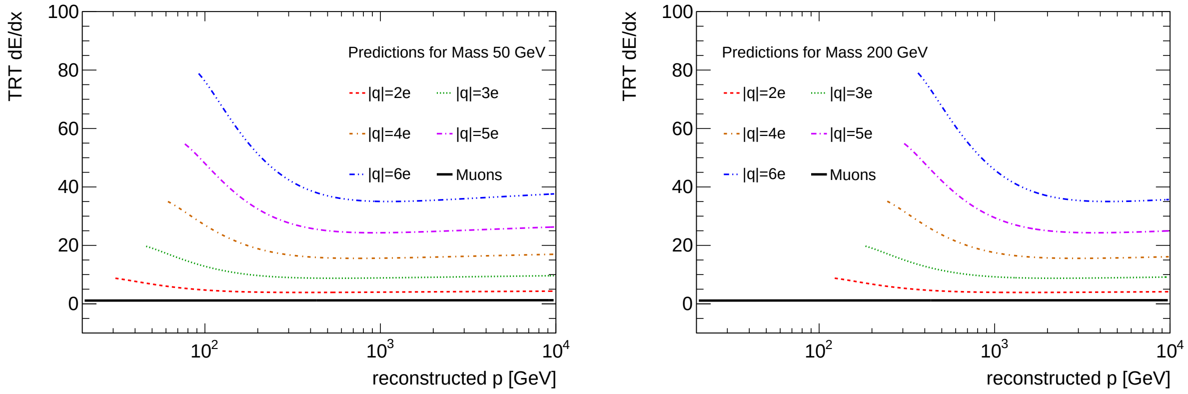

(a) Mass 50 GeV (b) Mass 200 GeV

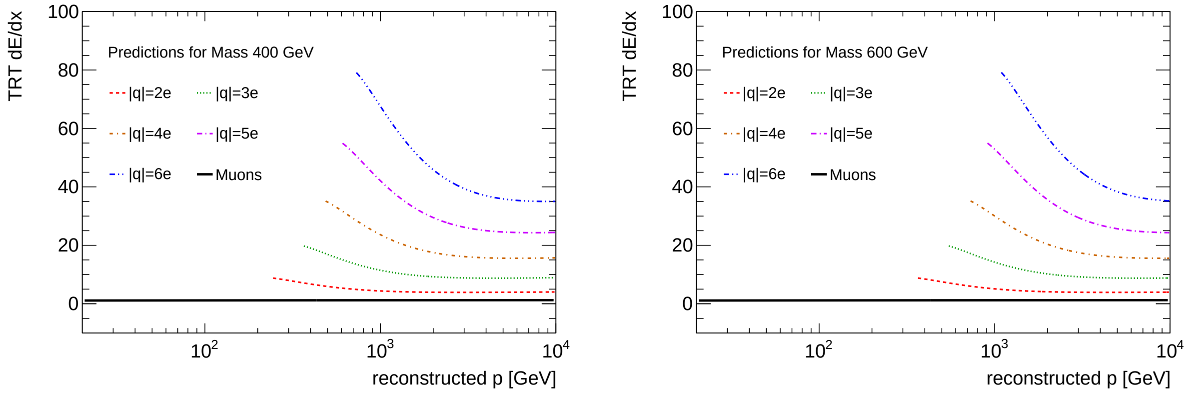

(c) Mass 400 GeV (d) Mass 600 GeV

Figure 5.21: *The predicted TRT dE/dx for multi-charged particles and muons as extrapolated from the fit to* $|q| = 1e$ *particles versus the reconstructed particle momentum* p *and mass 50 GeV (a), 200 GeV (b), 400 GeV (c) and 600 GeV (d). The validity range of the dE/dx fit above* $\beta\gamma = 0.5$ *and the momentum misreconstruction translate into a cut-off at lower momentum values* $p = 0.5mq$ *for a given mass* m *and charge* q*.*

CHAPTER 6

Identification of multi-charged particles

To estimate the discovery potential of multi-charged particles with the ATLAS detector, it is crucial to understand their behavior in the detector in detail. For this purpose, simulated events of multi-charged particles are generated and the detector response is modeled. These datasets (or samples) can be used to design the analysis strategy. Unlike in most analyses, in a signature based search approach, the production process of the hypothetical particles is not defined by a specific physics model. It is, therefore, a choice of the analysis. A very generic and widely applicable model is Drell-Yan pair production [24]. For the search presented in this thesis, generic particle pairs with masses in the range of 50 to 600 GeV and charges ±2, 3, 4, 5, 6 e each are generated in this way. This simulation process is discussed in Section 6.1. A study of the kinematic properties of the resulting signal Monte Carlo samples follows in Section 6.2 and serves as input to the analysis selection. Furthermore, the performance of the particle identification variables introduced in Chapter 4 and 5 is tested with respect to multi-charged particles in Section 6.4.

6.1 Simulation process

The conditions at the LHC are taken into account in the production process, which is modeled in proton-proton collisions at a center-of-mass energy of 7 TeV. The Drell-Yan pair production via photon exchange is implemented in the Monte Carlo generator MadGraph 5 [68]. This simplified Drell-Yan production process is depicted in Figure 6.1. In principle, a production via Z-boson exchange is also thinkable, but is neglected assuming no weak interaction of the particles. As previously discussed in Section 2.2, Drell-Yan production is a conservative estimate for the production cross section of multi-charged particles. Their relative coupling strength to photons and Z bosons depends on the BSM physics model predicting the particles. Thus, neglecting weak interactions of the multi-charged particles avoids assumptions about their coupling strength and adds to the conservative nature of the approximation.

For every benchmark point 10 000 events are simulated. The sole exception are the mass 50 GeV samples, for which 20 000 events with a truth filter of $p_{\mathrm{T}} > 15$ GeV are generated. Due to the very low acceptance of the particles with mass 50 GeV, this step is necessary to ensure sufficient precision in the Monte Carlo predictions. The efficiency of this truth filter is summarized in Table 6.1.

In the following, events are generated with the CTEQ6L1 [95] parton distribution function. The hadronization and underlying event generation is performed by Pythia version 6.425 [80]. The GEANT4 [81] description of the ATLAS detector is used to model the events according to data recorded with the AT-

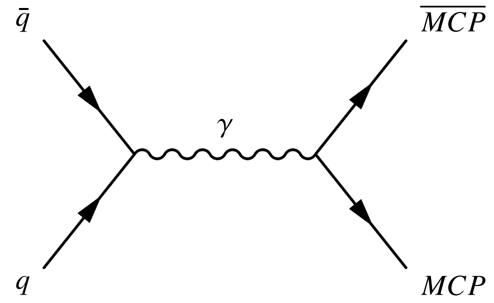

Figure 6.1: *The production process for multi-charged particles (MCP) assumed in the signal Monte Carlo.*

Table 6.1: *The efficiencies of the truth filter applied in the samples produced with mass 50 GeV.*

Mass [GeV]	$\epsilon_{\text{truth filter}}$ [%]				
	$\lvert q\rvert = 2e$	$\lvert q\rvert = 3e$	$\lvert q\rvert = 4e$	$\lvert q\rvert = 5e$	$\lvert q\rvert = 6e$
50	42.47	22.76	12.47	7.44	4.60

LAS detector. These simulated events are treated in the same way as data using identical releases of the standard ATLAS reconstruction and data-handling.

Table 6.2 gives the production cross sections predicted by the simplified Drell-Yan model used in the generation of the signal samples. It is based on the exchange of a photon without any next-to-leading order terms. Figure 6.2 shows the dependency on mass and charge of the signal samples. To facilitate comparisons, the production cross sections of the AC leptons and and the minimal walking technicolor leptons are drawn in the same plots (compare Figure 2.4). Several assumptions are made for the cross sections of the minimal walking technicolor leptons ζ and the A and C leptons of the almost commutative geometry. In principle, techni-leptons can additionally be produced via other techni-particles and W decay to ζ and ν_ζ. However, these processes depend on model parameters not specified in the analysis. Thus, all processes including further new particles are excluded and the sole difference between the two models lies in the weak isospin of the particles. It is $I_3 = -\frac{1}{2}$ in case of techni-leptons and $I_3 = 0$ for AC leptons, resulting in a slightly higher cross section of the latter [36]. The almost commutative geometry model makes no predictions of the masses of A and C, such that they can in general be degenerate and hence indistinguishable. In that case, A and C are treated as one particle with double cross sections [36].

Table 6.2: *Cross sections of simulated Drell-Yan pair production of multi-charged particles in 7 TeV pp collisions.*

Mass [GeV]	Cross section [pb]				
	$\lvert q\rvert = 2e$	$\lvert q\rvert = 3e$	$\lvert q\rvert = 4e$	$\lvert q\rvert = 5e$	$\lvert q\rvert = 6e$
50	15.9074	35.7910	63.6280	99.4189	143.1612
100	1.5435	3.4729	6.1741	9.6469	13.8915
200	0.1136	0.2556	0.4545	0.7101	1.0225
300	0.0199	0.0449	0.0798	0.1246	0.1795
400	0.0050	0.0112	0.0199	0.0311	0.0448
500	0.0015	0.0034	0.0060	0.0094	0.0135
600	0.0005	0.0011	0.0020	0.0032	0.0046

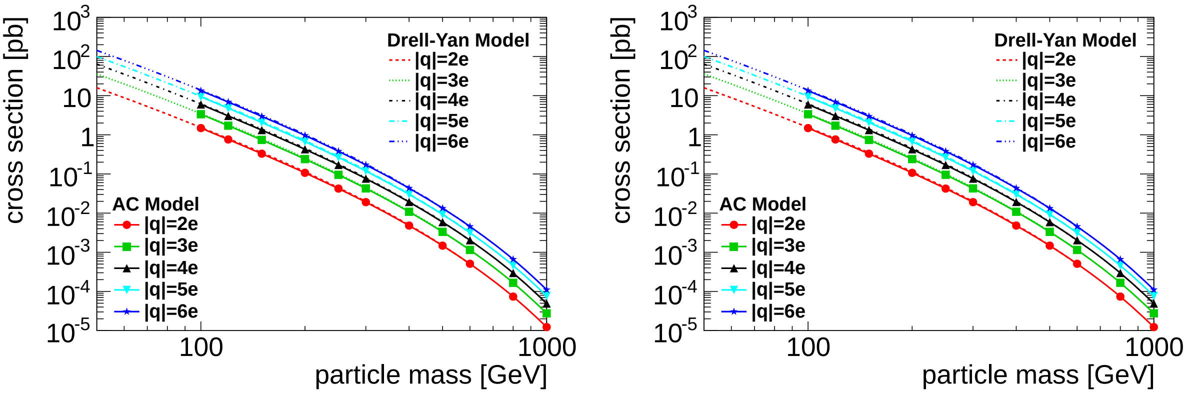

(a) Comparison Drell-Yan / AC model cross sections

(b) Comparison Drell-Yan / MWTC model cross sections

Figure 6.2: *The production cross sections of the Drell-Yan process as a function of the mass of the particle for different charge hypothesis in comparison with the predictions from the almost commutative geometry model (a) and the minimal walking technicolor model (b) [36].*

Therefore, their masses are assumed to be different in the following. As can be seen from Figure 6.2, the cross section predictions of the simplified Drell-Yan model are generally slightly higher than the production cross sections estimated for *AC* leptons and techni-leptons in Section 2.2 but very similar in shape.

6.2 Kinematics of the signal Monte Carlo

As previously mentioned in Section 3.3, the analysis relies on ATLAS data in the format of DESDs. The most efficient DESD stream (DESD_SGLMU) is designed to select events containing at least one reconstructed muon object. The selection criteria for DESD_SGLMU contain cuts on events requiring at least one reconstructed muon object of $p_T > 75$ GeV or at least two reconstructed muon objects of $p_T >$ 15 GeV in the event. These cuts are added to the analysis selection. In treating the simulated events in the same way as the data, this selection is inherent also for simulated events. The kinematic distributions of the multi-charged particles are strongly influenced by this selection. The following discussion of the kinematic properties of the signal Monte Carlo focuses on distributions after the DESD_SGLMU selection, pointing out the effects arising as a consequence and independent of it.

6.2.1 Transverse momentum

One aspect under consideration is the momentum misreconstruction by a factor of $|q|$ for particles carrying multiple charges. The consequence is a decrease in acceptance to higher charges as they are less likely to pass the p_{T} thresholds of the trigger and the analysis selection. This is illustrated in Figure 6.3. The upper two plots correspond to the distributions of $p_{\mathrm{T}}^{\mathrm{reco}} = p_{\mathrm{T}}^{\mathrm{true}}/|q|$ as simulated with charges $|q| = 2e$ on the left and $|q| = 6e$ on the right. The lower four plots are subject to the DESD selection and compare $p_{\mathrm{T}}^{\mathrm{true}}$ on the left hand side with $p_{\mathrm{T}}^{\mathrm{reco}}$ on the right hand side for several mass and charge points. It can be observed, that the distribution of the true transverse momentum does not depend on the charge of the particle but merely on its mass. The spectrum becomes harder with increasing mass. The small differences in the shape in Figures 6.3c and 6.3e are a result of the DESD selection cuts with two different $p_{\mathrm{T}}^{\mathrm{reco}}$ thresholds. Due to the larger bending in the magnetic field of the inner tracking detectors,

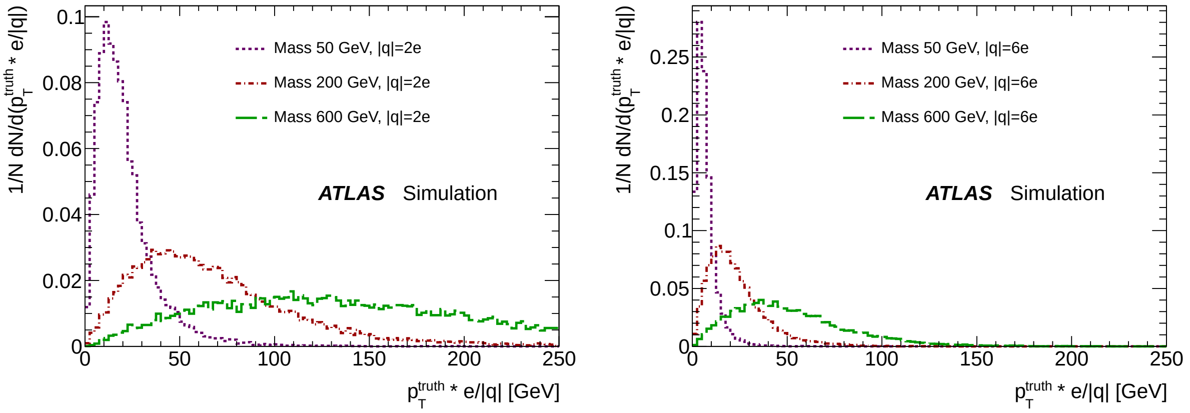

(a) $p_{\mathrm{T}}^{\mathrm{reco}}$, ESD, $|q| = 2e$

(b) $p_{\mathrm{T}}^{\mathrm{reco}}$, ESD, $|q| = 6e$

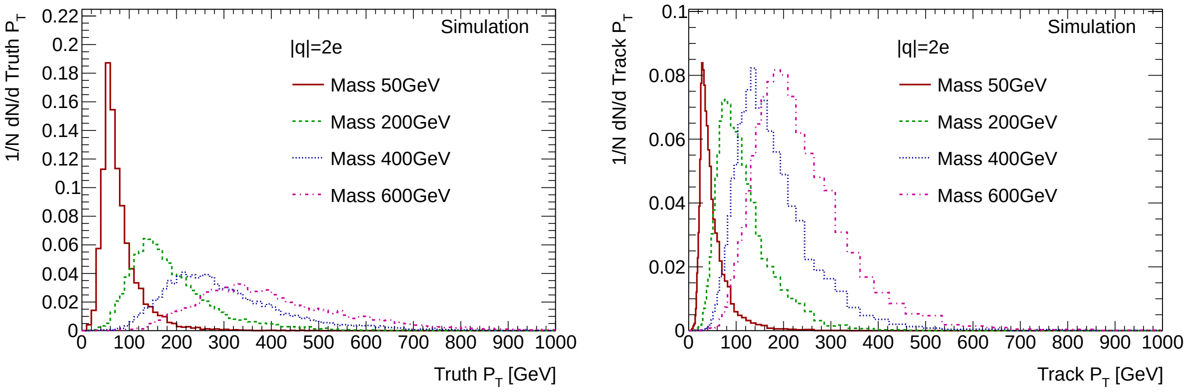

(c) $p_{\mathrm{T}}^{\mathrm{true}}$, DESD, $|q| = 2e$

(d) $p_{\mathrm{T}}^{\mathrm{reco}}$, DESD, $|q| = 2e$

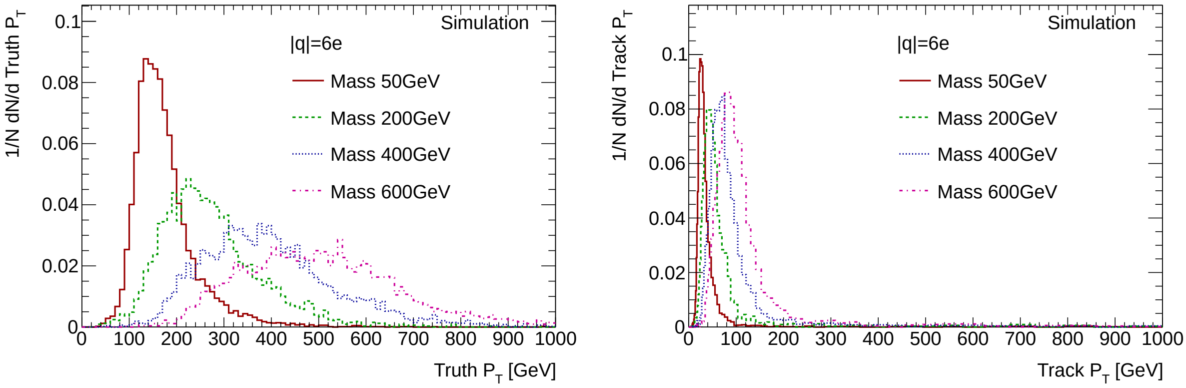

(e) $p_{\mathrm{T}}^{\mathrm{true}}$, DESD, $|q| = 2e$

(f) $p_{\mathrm{T}}^{\mathrm{reco}}$, DESD, $|q| = 2e$

Figure 6.3: *(a), (b) Normalized distributions of the reconstructed transverse momentum of particles with charge* $|q| = 2e$ *(a) and* $|q| = 6e$ *(b) and masses 50, 200 and 600 GeV before the filter cuts of the DESD selection (ESD). (c) - (f) Normalized distributions of the true transverse momentum (left column) vs. the reconstructed transverse momentum (right column) of multi-charged particles with charges 2 and 6e and masses 50, 200, 400 and 600 GeV after the filter cuts of the DESD selection.*

the reconstructed momentum drops by a factor of $|q|$ with respect to the true transverse momentum. Consequently the selection efficiency with respect to any cut on the reconstructed p_{T} will be smallest for low masses and high charges.

6.2.2 Beta and eta

Figure 6.4 illustrates the dependence of the true velocity $\beta = v/c$ of the multi-charged particles on their mass and charge. As expected, the heavier the particle for a given charge, the slower it will be on average. Figures 6.4a and 6.4b demonstrate that without the selection of the DESD stream, the β distributions are identical for the different charges. In the distributions after the DESD selection based on p_{T}, the samples of simulated signal points with higher charges have fewer events and hence higher statistical uncertainties and appear to have more narrow β distributions. Independent of this selection, particles with masses above 200 GeV have a significantly higher probability to be slower than $\beta = 0.7$. The analysis relies on muon objects, which means that the multi-charged particles must reach the ATLAS Muon System within the time window of the muon reconstruction. The muon reconstruction efficiency drops steeply below $\beta = 0.7$ [72] (see also Section 3.4.2). In combination, these two effects lead to a muon reconstruction efficiency which is highest for low masses and high charges, hence compensating partially the effects from the p_{T} distribution. The effects of the β distributions on the reconstruction efficiency will be discussed in more detail in the next Chapter 7.1.2.

Figure 6.5 compares the η distributions of multi-charged particles of charge $|q| = 2e$ and $|q| = 6e$. Within the differences of statistics, these distributions agree with each other.

6.2.3 Saturation of TRT dE/dx

The simulated multi-charged particles are compared to the predictions on the behavior of TRT $\mathrm{d}E/\mathrm{d}x$ derived in Section 5.9.1. First, the distributions of TRT $\mathrm{d}E/\mathrm{d}x$ as a function of $\beta\gamma$ in Figure 6.6 are compared to the predictions shown in Figure 5.19. Note the difference in scale between the y-axis (TRT $\mathrm{d}E/\mathrm{d}x$) between these figures. The readout of the TRT saturates at a ToT of 24×3.125 ns, which manifests itself as a saturation of TRT $\mathrm{d}E/\mathrm{d}x$ at ≈ 2.5. Although the saturation prevents the exploitation of the q^2 dependence, the signals of the multi-charged particles are well separated from the prediction for SM ($|q| = 1e$) particles indicated by the solid red line in the same plots. Overall, the signal for $|q| = 2e$ particles is clustered at lower TRT $\mathrm{d}E/\mathrm{d}x$ values than the higher charges. Besides, the distributions of TRT $\mathrm{d}E/\mathrm{d}x$ of particles with charges $|q| = 3$ to $6e$ do not differ significantly from each other. In summary, the predictions derived in Section 5.9.1 are not applicable to measurements of the TRT $\mathrm{d}E/\mathrm{d}x$.

However, TRT $\mathrm{d}E/\mathrm{d}x$ is still a good variable to discriminate multi-charged particles from SM background. In the momentum range investigated in this analysis ($p_{\mathrm{T}} > 20$ GeV, see Chapter 7) all SM particles' $\mathrm{d}E/\mathrm{d}x$ is expected in the flat plateau of the Bethe-Bloch curve. It is hence sufficient to investigate the separation of multi-charged particles in the one-dimensional distribution of $\mathrm{d}E/\mathrm{d}x$.

6.3 dE/dx significances

To allow for easy comparison of the separation capabilities of the different $\mathrm{d}E/\mathrm{d}x$ estimators in the one-dimensional distributions of SM background and multi-charged particles, the $\mathrm{d}E/\mathrm{d}x$ significance ($S(\mathrm{d}E/\mathrm{d}x)$) is introduced. It is defined as the discriminating power between the measured $\mathrm{d}E/\mathrm{d}x$ and the $\mathrm{d}E/\mathrm{d}x$ expected for muons. The concept is very similar to the separation power defined in Section 4.1.4. $S(\mathrm{d}E/\mathrm{d}x)$ defines the separation of a given measured $\mathrm{d}E/\mathrm{d}x$ from a signal of real muons in units of

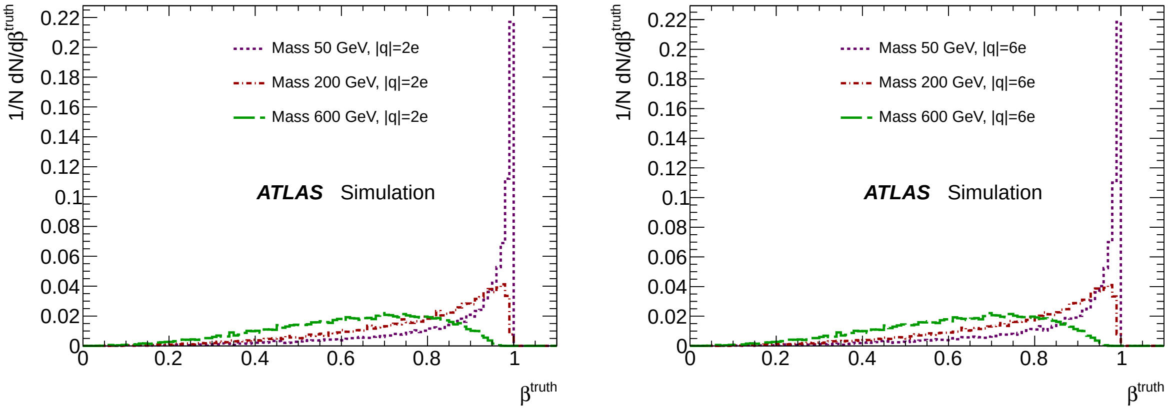

(a) ESD, $|q| = 2e$

(b) ESD, $|q| = 6e$

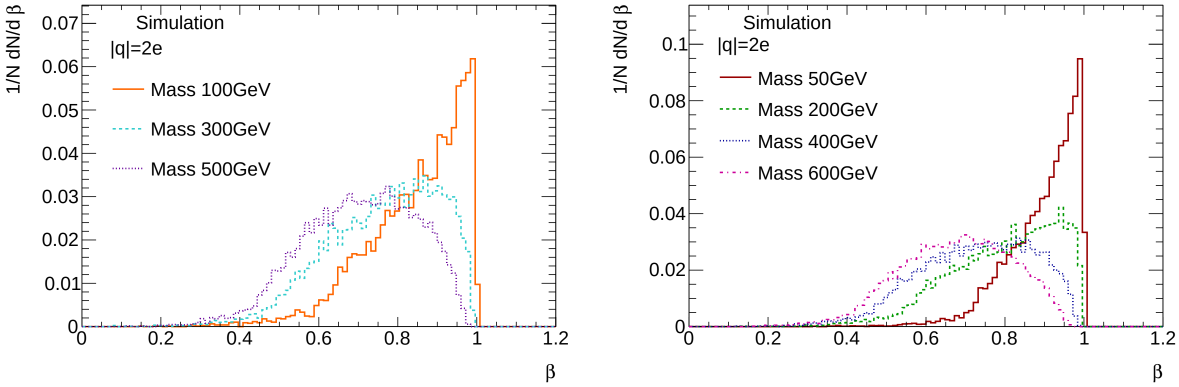

(c) DESD, $|q| = 2e$

(d) DESD, $|q| = 2e$

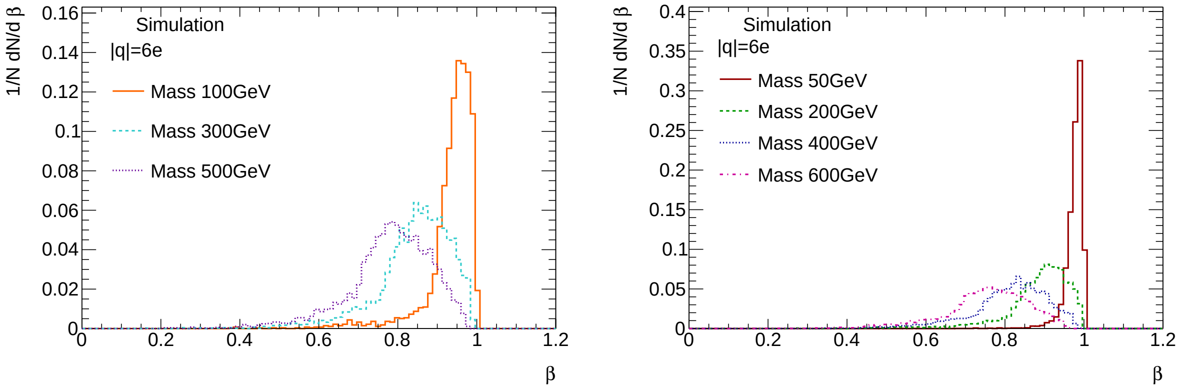

(e) DESD, $|q| = 6e$

(f) DESD, $|q| = 6e$

Figure 6.4: *(a), (b) The distributions of* β *as simulated before the application of the filter cuts for the data stream used in the analysis for charge* $|q| = 2e$ *(a) and* $|q| = 6e$ *(b) [8]. (c) - (f) The normalized distributions of the true* $\beta = v/c$ *after the DESD filter cuts for charges* $|q| = 2e$ *and* $|q| = 6e$ *and masses 100, 300 and 500 GeV (left column) or 50, 200, 400 and 600 GeV (right column).*

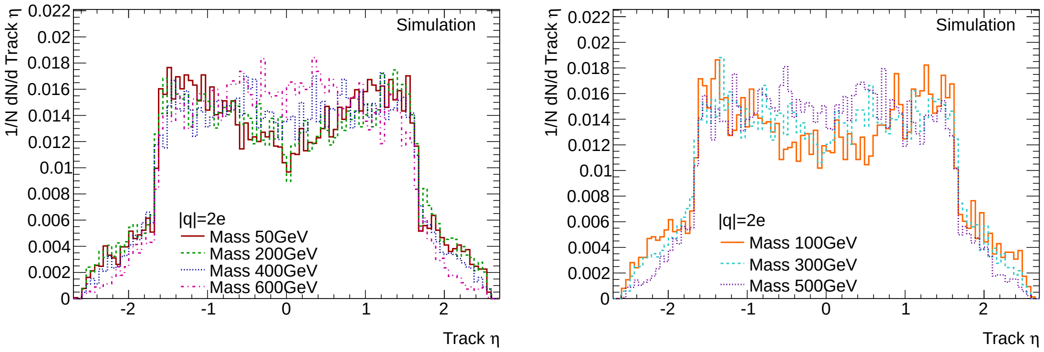

(a) DESD, $|q| = 2e$

(b) DEDS, $|q| = 2e$

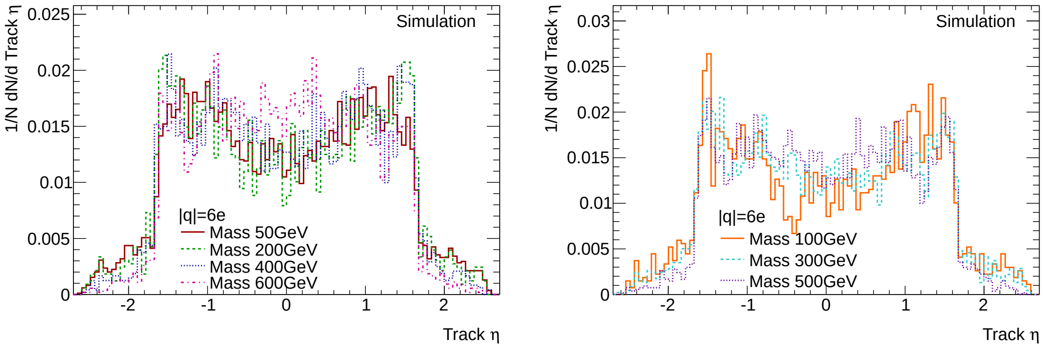

(c) DESD, $|q| = 6e$

(d) DESD, $|q| = 6e$

Figure 6.5: *The normalized distributions of the reconstructed η for charges 2 and 6e and masses 50, 200, 400 and 600 GeV or 100, 300 and 500 GeV after the selection for the DESD.*

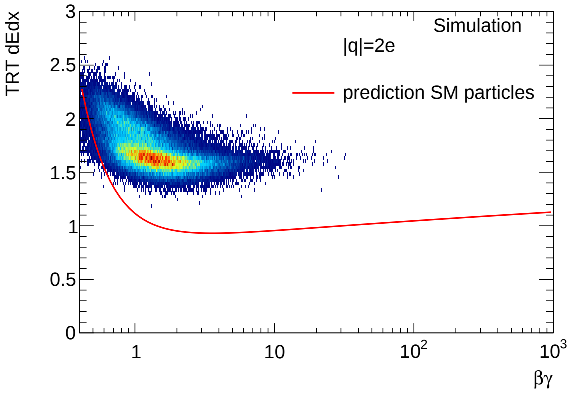

(a) $|q| = 2e$

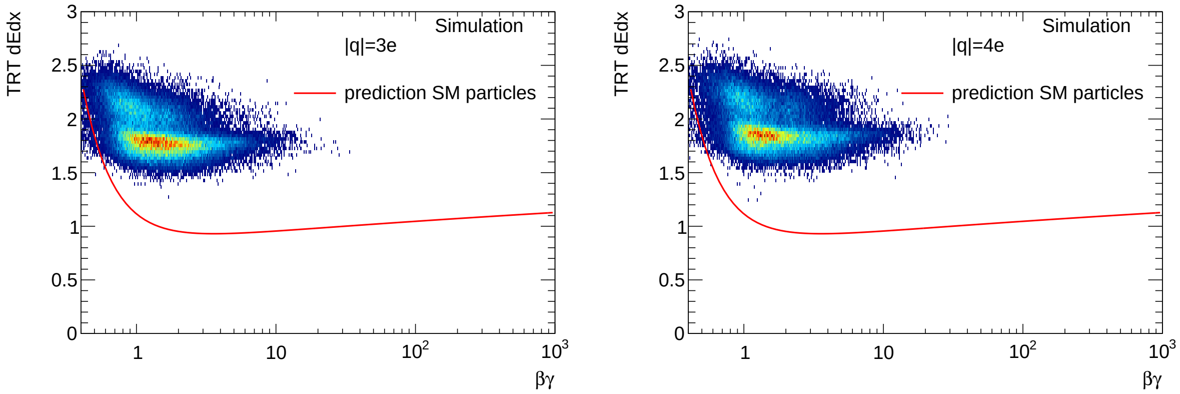

(b) $|q| = 3e$ (c) $|q| = 4e$

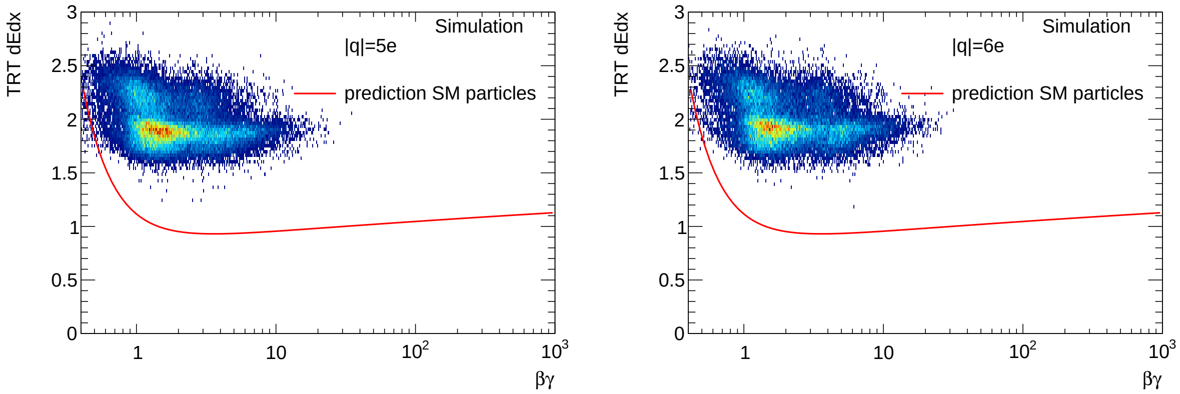

(d) $|q| = 5e$ (e) $|q| = 6e$

Figure 6.6: TRT $\mathrm{d}E/\mathrm{d}x$ as a function of $\beta\gamma$ as predicted from simulation for multi-charged particles of charges (a) $|q| = 2e$, (b) $|q| = 3e$, (c) $|q| = 4e$, (d) $|q| = 5e$ and (e) $|q| = 6e$ in comparison with the prediction of TRT $\mathrm{d}E/\mathrm{d}x$ for SM particles.

Table 6.3: *The extracted* $\langle dE/dx_{muon}\rangle$ *and* $\sigma(dE/dx_{muon})$ *from the distributions of the individual subdetector* dE/dx *in* $Z \rightarrow \mu\mu$ *data and Monte Carlo.*

	Pixel $\mathrm{d}E/\mathrm{d}x$	TRT $\mathrm{d}E/\mathrm{d}x$	LAr $\mathrm{d}E/\mathrm{d}x$	Tile $\mathrm{d}E/\mathrm{d}x$	MDT $\mathrm{d}E/\mathrm{d}x$
			Data		
$\langle \mathrm{d}E/\mathrm{d}x_{\mathrm{muon}}\rangle$	1.19	1.08	0.57	1.12	-3.29
$\sigma(\mathrm{d}E/\mathrm{d}x_{\mathrm{muon}})$	0.15	0.077	0.15	0.26	9.59
			Monte Carlo		
$\langle \mathrm{d}E/\mathrm{d}x_{\mathrm{muon}}\rangle$	1.23	1.08	0.57	1.13	-6.79
$\sigma(\mathrm{d}E/\mathrm{d}x_{\mathrm{muon}})$	0.14	0.074	0.16	0.25	7.72

$\mathrm{d}E/\mathrm{d}x$ resolution, the significance. The exact definition is given in Equation (6.1)

$$S(\mathrm{d}E/\mathrm{d}x) = \frac{\mathrm{d}E/\mathrm{d}x_{\mathrm{track}} - \langle \mathrm{d}E/\mathrm{d}x_{\mathrm{muon}}\rangle}{\sigma(\mathrm{d}E/\mathrm{d}x_{\mathrm{muon}})} . \tag{6.1}$$

Due to the high p_{T} selection (>20 GeV), it is sufficient to consider the one-dimensional distributions of $\mathrm{d}E/\mathrm{d}x_{\mathrm{muon}}$ and determine the mean and the resolution via a simple Gaussian fit. These fits are shown for S(Pixel $\mathrm{d}E/\mathrm{d}x$), S(TRT $\mathrm{d}E/\mathrm{d}x$) and S(MDT $\mathrm{d}E/\mathrm{d}x$) in $Z \rightarrow \mu\mu$ data and Monte Carlo in Figure 6.7. The $\langle \mathrm{d}E/\mathrm{d}x_{\mathrm{muon}}\rangle$ and $\sigma(\mathrm{d}E/\mathrm{d}x_{\mathrm{muon}})$ are shown as μ and σ, respectively, in the legends of the plots. The fit values for the significances of all considered variables are listed in Table 6.3.

6.4 Discriminating variables

The performance of the particle identification variables based on the specific energy loss per path length and the time of flight introduced in Chapter 4 and 5 is investigated. The focus lies on the discrimination of multi-charged particles against real muons. A data / Monte Carlo comparison of the $\mathrm{d}E/\mathrm{d}x$ significances (defined in Equation (6.1)) is performed with the $Z \rightarrow \mu\mu$ data sets defined in Section 4.3.

6.4.1 Pixel dE/dx

The Pixel $\mathrm{d}E/\mathrm{d}x$ variable introduced in Section 4.4, does not yield reliable information for particles with $|q| > 2e$ due to saturation effects. In contrast to the other subdetectors, the Pixel readout does not approach some asymptotic value when saturating, but the measurement itself is lost. Consequently, also the S(Pixel $\mathrm{d}E/\mathrm{d}x$) will only be a good discriminant for particles with charge $|q| = 2e$.

For muons in the $Z \rightarrow \mu\mu$ data sets very good agreement between data and Monte Carlo is observed (see Figure 6.8). As expected, the distributions for muons are centered around zero with Landau-like tails to higher significances. This reflects the Landau distribution of energy deposits in the Pixel detector. The discrepancy between data and Monte Carlo and the small bump in the distributions of the $|q| = 2e$ particles in Figure 6.8b are both around S(Pixel $\mathrm{d}E/\mathrm{d}x$) ≈ -5. The most plausible explanation is that this is the area saturation effects manifest themselves. If the pixel readout is saturated, the information from this pixel hit is lost. Typically a Pixel $\mathrm{d}E/\mathrm{d}x$ measurement is based on charge information from three pixel hits. Hence, the saturation leads to an underestimation of the $\mathrm{d}E/\mathrm{d}x_{\mathrm{track}}$ and thus to negative values of the S(Pixel $\mathrm{d}E/\mathrm{d}x$). The mismatch in data and Monte Carlo in this area indicates that the

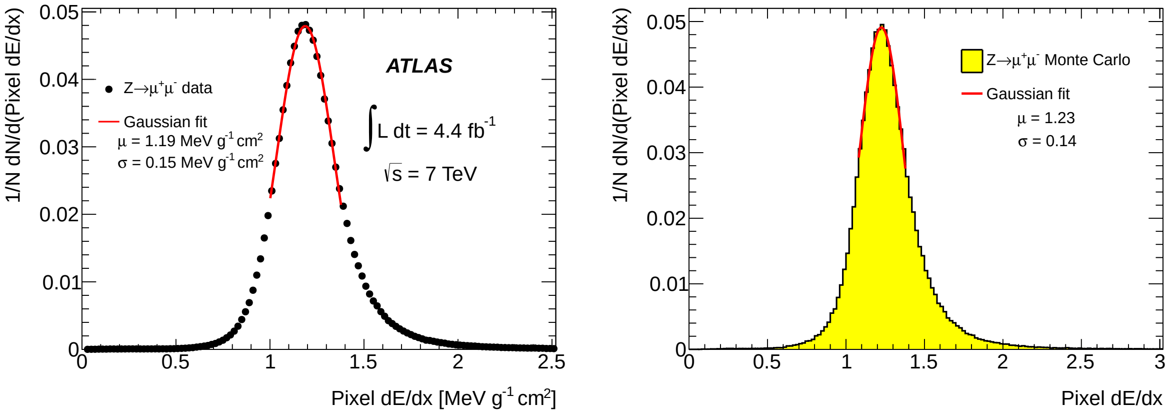

(a) Data Pixel dE/dx

(b) Monte Carlo Pixel dE/dx

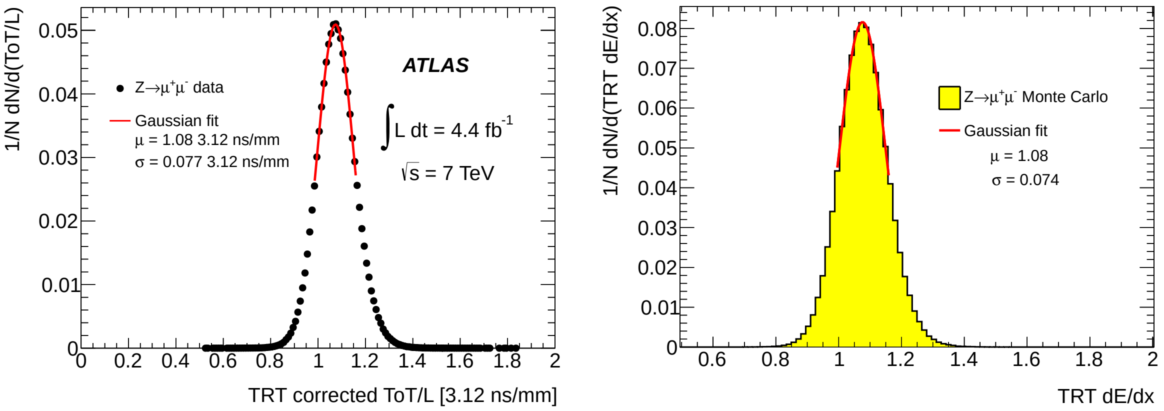

(c) Data TRT dE/dx

(d) Monte Carlo TRT dE/dx

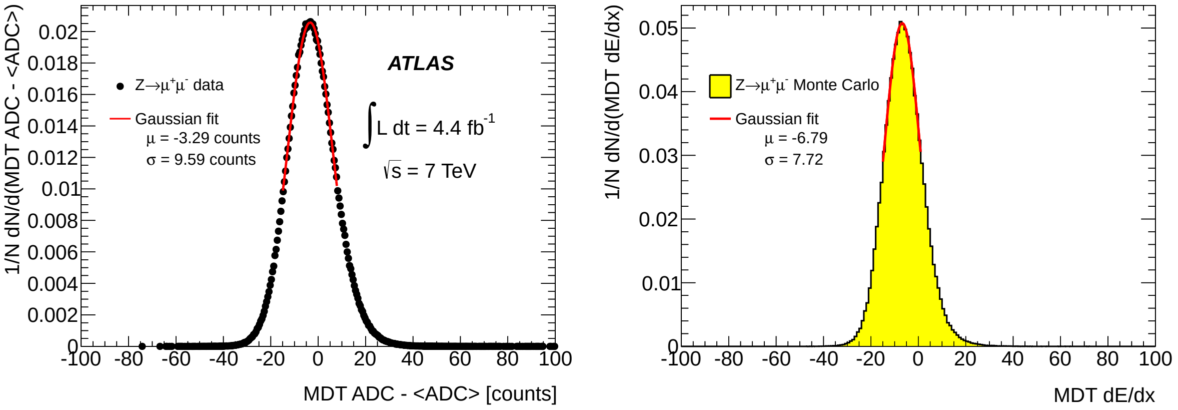

(e) Data MDT dE/dx

(f) Monte Carlo MDT dE/dx

Figure 6.7: *The distributions of Pixel dE/dx (a)/(b), TRT dE/dx (c)/(d) and MDT dE/dx (e)/(f) in data / Monte Carlo. Overlaid is the Gaussian fit to extract $\langle dE/dx_{muon}\rangle$ and $\sigma(dE/dx_{muon})$ for the calculation of the significance [8] / [82] (see also [38]).*

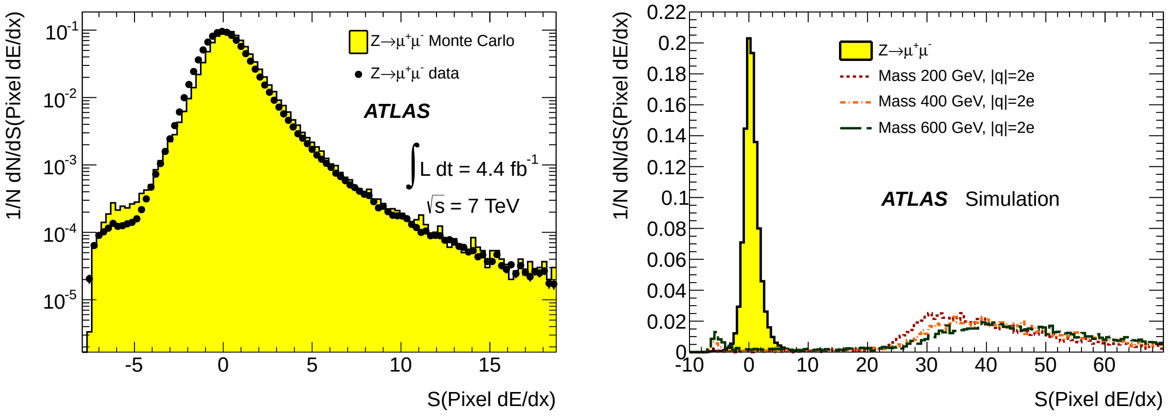

(a) $Z \to \mu\mu$ Data / Monte Carlo comparison (b) $Z \to \mu\mu$-multi-charged particle comparison

Figure 6.8: *The Pixel dE/dx significance S(Pixel dE/dx) in the direct data / Monte Carlo comparison for $Z \to \mu\mu$ [8] (a) and comparing $Z \to \mu\mu$ Monte Carlo to simulated multi-charged particles (b). Both distributions are normalized to one. The artifact at $S(\text{Pixel } dE/dx) \approx -5$ is most likely due to the saturation behavior of the single pixel hits.*

readout saturation is not modeled sufficiently well in Monte Carlo. A similar effect can be observed in the distributions of Pixel dE/dx in Figure 4.6a.

6.4.2 TRT HT fraction

The TRT HT fraction f^{HT} complements $S(\text{Pixel d}E/\text{d}x)$ as it is a very good discriminant for multi-charged particles with charges $|q| > 2e$ but not for $|q| = 2e$. It is a well established variable in ATLAS used mainly for the discrimination of electrons from pions. As shown previously, we observe excellent agreement in data and Monte Carlo for $Z \to \mu\mu$ muons (Figure 4.6b). The comparison of $Z \to \mu\mu$ and multi-charged particle simulation of charges $|q| = 2, 4$ and $6e$ in Figure 6.9 shows a large overlap of $|q| = 2e$ particles with $Z \to \mu\mu$ muons, but excellent separation for all higher charges. This effect is related to the observations drawn from Figure 6.6. Particles of charge $|q| = 2e$ behave highly ionizing in the TRT detector, but their dE/dx values are closest to the predictions for $|q| = 1e$ particles. The dE/dx signals of particles with charges above and including $|q| = 3e$ are very much alike and significantly different from SM $|q| = 1e$ particles.

6.4.3 TRT dE/dx

Due to the very good agreement observed in TRT dE/dx between data and Monte Carlo in $Z \to \mu\mu$ only small discrepancies in the significance variables can be expected as well. This is in fact observed in Figure 6.10a. Furthermore, Figure 6.10b illustrates the clear separation between all signal samples and muons. Additionally, this plot illustrates nicely the saturation effects due to the limited number of bits in the TRT bitpattern discussed previously in Section 6.2.3. This variable gives no discriminating power between particles of charge $|q| > 2e$. Consequently, it serves as a good selection variable for signal tracks, but not to distinguish charge and mass of the signals.

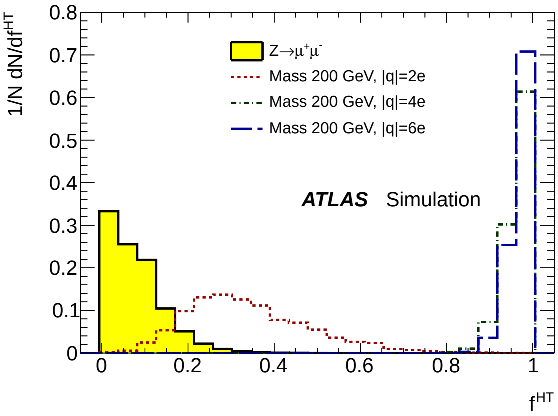

Figure 6.9: *Normalized distribution of f^{HT} for simulated muons and multi-charged particles. The distributions are shown for the signal samples of charge $|q| = 2, 4$ and $6e$ and mass 200 GeV [8].*

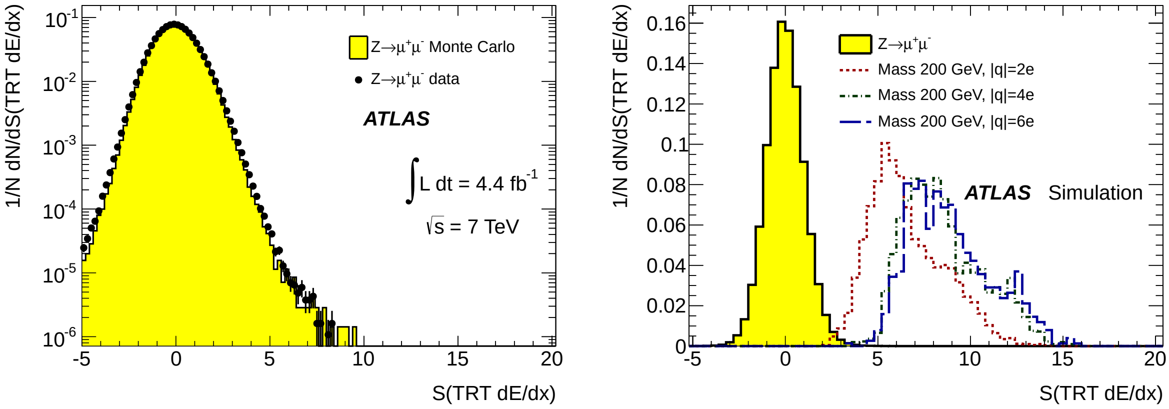

(a) $Z \rightarrow \mu\mu$ Data / Monte Carlo comparison

(b) $Z \rightarrow \mu\mu$, multi-charged particles comparison

Figure 6.10: *Normalized distribution of $S\,(TRT\ dE/dx)$ in the direct data / Monte Carlo comparison of $Z \rightarrow \mu\mu$ events (a) and for simulated muons and multi-charged particles (b). In the latter the distributions are shown for the signal samples of charge $|q| = 2, 4$ and $6e$ and mass 200 GeV [8]*

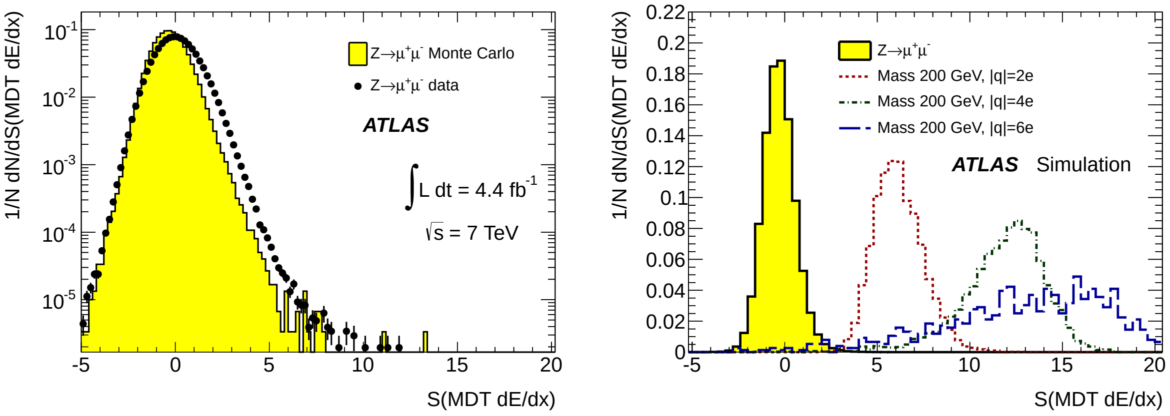

(a) $Z \to \mu\mu$ Data / Monte Carlo comparison

(b) $Z \to \mu\mu$, multi-charged particles comparison

Figure 6.11: *Normalized distribution of $S\,(MDT\ dE/dx)$ in the direct data / Monte Carlo comparison of $Z \to \mu\mu$ events (a) and for simulated muons and multi-charged particles (b). In the latter the distributions are shown for the signal samples of charge $|q| = 2, 4$ and $6e$ and mass 200 GeV [8]*

6.4.4 MDT dE/dx

A somewhat opposite picture can be observed for the MDT $\mathrm{d}E/\mathrm{d}x$ significance. This variable has a remaining shift between data and Monte Carlo distributions, where the data appears shifted to higher values with respect to the simulation. This behavior would have a negative impact on the signal interpretation, but does not influence the limit setting procedure strongly. In later releases of the ATLAS software, this mismatch is eliminated with additional corrections on MDT $\mathrm{d}E/\mathrm{d}x$ (see Section 4.8). At the time the data for this analysis had to be processed, ATLAS reconstruction still used the earlier version with this shift. For all potential future analyses using this variable, good agreement between data and Monte Carlo is to be expected. A look at Figure 6.11b reveals the much better separation power of the different signal samples from each other in addition to the very good separation from muons. The allowed range of ADC counts in the MDT is significantly larger than the maximal ToT range in the TRT.

6.4.5 Calorimeter dE/dx

The calorimeter system is designed to measure energies. Consequently, a $\mathrm{d}E/\mathrm{d}x$ measurement in the LAr calorimeter is a useful variable for the discrimination of multi-charged particles. Figure 6.12b proves the good discrimination power of $S\,(\mathrm{LAr\ d}E/\mathrm{d}x)$ in addition to the excellent data / Monte Carlo agreement shown in Figure 6.12a. In the search for multi-charged particles, a selection based on the four variables mentioned above is sufficient and $S\,(\mathrm{LAr\ d}E/\mathrm{d}x)$ is reserved for a potential signal interpretation with respect to the charge of the signal.

6.4.6 Tile beta

The β_{Tile} is a very useful variable to distinguish between different signal hypothesis, as it can be used to derive a mass measurement via

$$m_{\beta_{\mathrm{Tile}}} = \frac{p}{\beta\gamma} = p_{\mathrm{reco}} \frac{\sqrt{1 - (\beta_{\mathrm{Tile}})^2}}{\beta_{\mathrm{Tile}}}. \qquad (6.2)$$

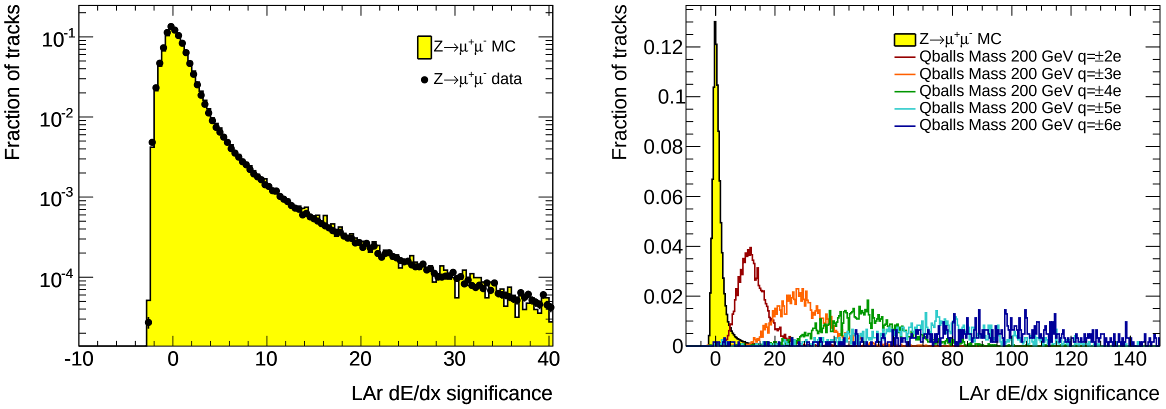

(a) $Z \to \mu\mu$ Data / Monte Carlo comparison

(b) $Z \to \mu\mu$, multi-charged particles comparison

Figure 6.12: *Normalized distribution of* $S\,(LAr\ dE/dx)$ *in the direct data / Monte Carlo comparison of* $Z \to \mu\mu$ *events (a) and for simulated muons and multi-charged particles (b). In the latter the distributions are shown for the signal samples of charge* $|q| = 2$ - $6e$ *and mass 200 GeV [82] (see also [38]).*

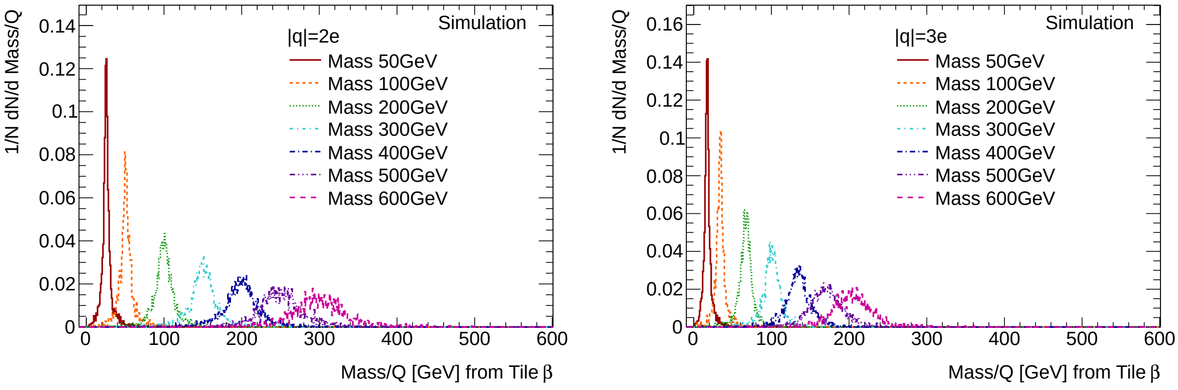

(a) $|q| = 2e$

(b) $|q| = 3e$

Figure 6.13: *The mass/*$|q|$ *measurement extracted from* β_{Tile} *exemplary for signals with charge* $|q| = 2e$ *(a) and* $|q| = 3e$ *(b).*

In the case of multi-charged particles p_{reco} is $|q|$-times lower than the true momentum of the particles. Hence $m_{\beta_{\mathrm{Tile}}}$ is merely a measure for the particle mass divided by its absolute charge.

$$m_{\beta_{\mathrm{Tile}}} \sim \frac{m}{|q|} \tag{6.3}$$

This is nicely illustrated in Figure 6.13 for charge $|q| = 2e$ and $|q| = 3e$. In the first case the $m/|q|$ of the mass 600 GeV signal peaks (the most right one) at 300 GeV and in the second case at 200 GeV. Together with a reconstructed charge from $S(\mathrm{LAr}\ \mathrm{d}E/\mathrm{d}x)$ or $S(\mathrm{MDT}\ \mathrm{d}E/\mathrm{d}x)$, it is possible to distinguish signal from background tracks in the signal region. In this manner, the nature of potential signal candidates can be investigated.

CHAPTER 7

The search for multi-charged particles

The signature based analysis presented in the following is based on the assumption that the multi-charged particles are stable and traverse the entire ATLAS detector, leaving a signal in the muon system. Their highly ionizing behavior is taken into account in the selection on various $\mathrm{d}E/\mathrm{d}x$ estimators of ATLAS subdetectors in the inner detector (Pixel and TRT) and the muon system (MDT). A detailed description of the full analysis selection is given in Section 7.1. The SM background contribution in the signal region is estimated by a purely data-driven method. This method, the ABCD method, is introduced and applied in Section 7.2. To be able to extract a cross-section measurement from this counting experiment, signal efficiencies are studied. Their discussion in Section 7.3 is based purely on the signal Monte Carlo samples introduced in the previous Chapter 6. Another important input to the cross section determination are the systematic uncertainties. They are applicable to the selection efficiencies, the background estimation and the luminosity and addressed separately in Section 7.4. Finally, the search results are summarized in Section 7.5 in preparation for their interpretation in Chapter 8.

7.1 Analysis selection

The analysis selection is optimized to be as efficient as possible for signal tracks, while rejecting a large fraction of the SM background. It exploits the highly ionizing behavior of multi-charged particles, which are assumed to reach the muon system. The muon-like detector signature of the candidate particles is reflected in the data selection presented in detail in Section 7.1.1 and the choice of trigger in Section 7.1.2. The latter includes a discussion of some of the implications of the muon trigger on the detection of multi-charged particles. After a common preselection on tracks and reconstructed muon objects (Section 7.1.3), the analysis is split in a search of particles with charge $|q| = 2e$ and $|q| > 2e$ in the tight selection described in Section 7.1.4. Signal-like tracks are selected as illustrated in Section 7.1.5. The signal region in data is not investigated in data during the design phase of the analysis to avoid biases.

7.1.1 Data selection

A total integrated luminosity of 5.25 fb^{-1} of pp collisions at $\sqrt{s} = 7$ TeV has been recorded by ATLAS in 2011 (see Figure 7.1a). These data events contained on average $\langle\mu\rangle = 6.3$ interactions per bunch

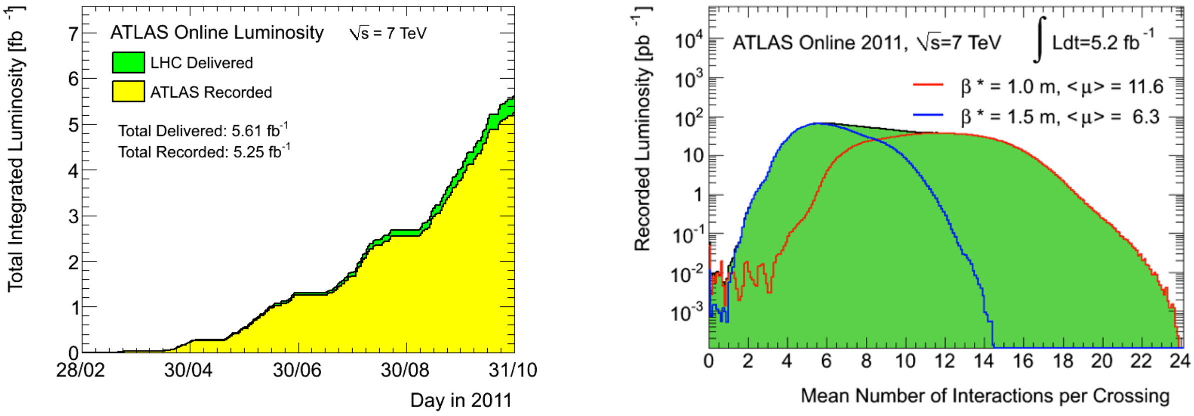

(a) Integrated luminosity by day

(b) Mean number of interactions

Figure 7.1: *(a) The luminosity delivered by LHC in 2011 (green) and recorded by ATLAS (yellow) for pp collisions in stable operation (stable beams). (b) The luminosity-weighted distribution of the mean number of interactions per crossing in 2011. The blue and red lines correspond to data taken before and after the September Technical Stop respectively [48].*

crossing before September and 11.6 after. At this time, the LHC could reduce β^{*1} from 1.5 m to 1.0 m in a technical intervention, which lead to the increase of $\langle\mu\rangle$.

Only events in which the ATLAS detector is fully operational are considered. As discussed in Section 3.3, the usage of the MDT dE/dx and TRT dE/dx relies on the full event information. Therefore, this analysis is based on data in the form of DESDs. The selection with the highest efficiency in the signal samples is retained by a data format designed for single muons (SGLMU_DESD). As a consequence, the most efficient SGLMU_DESD requirements need to be added to the data selection: at least one reconstructed muon object (μ^{reco}) with $p_T > 75$ GeV or two reconstructed muon objects with $p_T > 15$ GeV in the event.

7.1.2 Trigger

To avoid large inefficiencies of multi-charged particles with higher charges, it is desirable to select muon objects with the lowest possible p_{T} threshold. In the 2011 ATLAS data taking, this trigger selects events with muons above 18 GeV transverse momentum. It has not been included for a small portion of data in the beginning of the 2011 data taking. Therefore, the integrated luminosity available in this search is a little lower than the total recorded data at 4.4 fb^{-1}.

RPC scaling

The trigger timing distributions in the RPC, that is the distribution of the arrival times at the trigger chambers, do not agree in data and simulation [72]. Assuming Gaussian timing distributions $f(t)$ (see Equation (7.1)), their mean Δ and width σ are extracted (see Table 7.1 for quantitative statement).

$$f(t) = \frac{1}{\sigma\sqrt{2\pi}} e^{-\frac{(t-\Delta)^2}{2\sigma^2}} \tag{7.1}$$

---

[1] β^* is a property from accelerator physics describing the spread of the beam $\beta(z)$ along the beam axis z around the interaction point, where $\beta(z) = \beta^* + \frac{z^2}{\beta^*}$. The smaller β^* becomes, the denser the particle bunch will be.

Table 7.1: *Parameters of the trigger timing distributions in the RPC in data (ATLAS run 191715 recorded in 2011) and Monte Carlo.* Δ *denotes the position of the mean of the timing distribution relative to the end of the 25 ns readout window.* σ *is the width of the trigger timing distribution [72].*

	data	Monte Carlo
Δ [3.125 ns]	3.45	4.75
σ [3.125 ns]	1.09	0.60

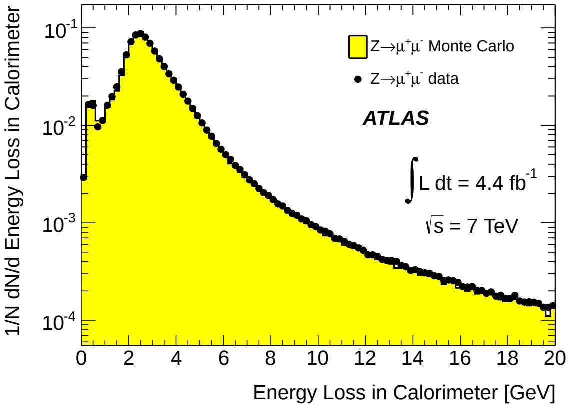

Figure 7.2: *The normalized distributions of the energy lost in the calorimeter of muon objects reaching the ATLAS Muon System in data and Monte Carlo.*

The trigger efficiency ϵ, given by the probability that $f(t)$ exceeds t' can be expressed as the complement of the cumulative distribution function ($\Phi(t)$). This function is sometimes denoted as Q-function. It is given in Equation 7.2.

$$\epsilon(t) = Q(t) = 1 - \Phi(t) \tag{7.2}$$

For Gaussian distributed values $\Phi(t)$ yields

$$\Phi(t) = \frac{1}{\sqrt{2\pi}} \int_{-\infty}^{t} e^{-(t'-\Delta)^2/2\sigma^2}\,\mathrm{d}t' = 0.5\left(1 + \mathrm{erf}\left(\frac{t-\Delta}{\sigma\sqrt{2}}\right)\right), \tag{7.3}$$

with the error function, erf(t). The efficiency of the muon trigger in the RPC can thus be determined to be

$$\epsilon(t) = 0.5\left(1 - \mathrm{erf}\left(\frac{t-\Delta}{\sigma\sqrt{2}}\right)\right) \tag{7.4}$$

as a function of the time delay t at the RPC pivot plane (see Section 3.2.7). This time t can be determined via

$$t = \left(\frac{1}{\beta} - 1\right)\frac{L}{c} \tag{7.5}$$

and

$$L = \frac{d}{\sin\theta}, \tag{7.6}$$

where $d = 10$ m is the distance from the primary vertex to the outermost RPC chamber. As a result of the high energy losses, the velocity β of the particle changes along its way through the detector. To

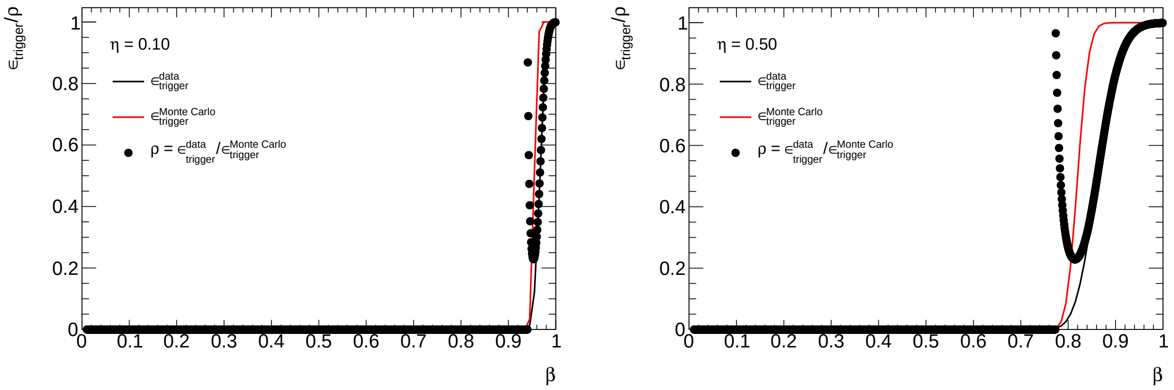

(a) $\eta = 0.10$ (b) $\eta = 0.50$

Figure 7.3: *Examples of the RPC trigger scaling factor for (a)* $|\eta| = 0.10$ *and (b)* $|\eta| = 0.50$ *as a function of the velocity* β*. The red lines represent the expected trigger efficiency in Monte Carlo, the black line in data. The ratio of the efficiencies is shown in the same plot as black dots.*

account for the change in velocity, the time of flight to the muon system is estimated with an effective velocity β^{eff}

$$\beta^{\text{eff}} = \frac{\beta^{\text{ID}} + \beta^{\text{MS}}}{2}, \tag{7.7}$$

determined from the velocity in the inner detector (β^{ID}) and at the muon system (β^{MS}). The latter is derived from the energy lost in the calorimeter. From Figure 7.2 it can be deduced that the energy losses in the calorimeter system agree well in data and Monte Carlo and the change in β can thus be estimated reliably. Note that this effective velocity deviates from the average velocity $\frac{1}{\beta^{\text{mean}}} = \frac{1}{2}\left(\frac{1}{\beta^{\text{ID}}} + \frac{1}{\beta^{\text{MS}}}\right)$ at most 2% in the range of the β acceptance above 0.7.

In order to correct the trigger efficiency determined from Monte Carlo to agree with the trigger efficiency observed in data, it is scaled with the ratio

$$\rho = \frac{\epsilon_{\text{data}}}{\epsilon_{\text{MC}}} = \frac{\left(1 - \text{erf}\left(\frac{t-\Delta_{\text{data}}}{\sqrt{2}\sigma_{\text{data}}}\right)\right)}{\left(1 - \text{erf}\left(\frac{t-\Delta_{\text{MC}}}{\sqrt{2}\sigma_{\text{MC}}}\right)\right)}. \tag{7.8}$$

This scaling has to be applied to each simulated muon object triggered in the RPC chambers. It is strongly dependent on β and η. Examples of this dependence are shown in Figures 7.3. A weight, ρ, is assigned to each reconstructed muon object triggered by the RPC in the calculation of the trigger efficiency.

Beta cut

As discussed previously in Section 3.4.2, the timing window of the muon triggers results in a cut on the particle velocity of $\beta > 0.7$. This imposes an implicit cut on the momentum of the particle track. In order to be fast enough to reach the muon system in time, the multi-charged particles are required to be

Table 7.2: *The implicit cut on the track momentum from the trigger timing acceptance assuming a cut at* $\beta = 0.7$.

	Implicit momentum cut from $\beta > 0.7$ [GeV]						
	mass [GeV]						
$\lvert q\rvert$ [e]	50	100	200	300	400	500	600
2	24.50	49.01	98.02	147.03	196.04	245.05	294.06
3	16.34	32.67	65.35	98.02	130.69	163.37	196.04
4	12.25	24.50	49.01	73.51	98.02	122.52	147.03
5	9.80	19.60	39.21	58.81	78.42	98.02	117.62
6	8.17	16.34	32.67	49.01	65.35	81.68	98.02

faster than $\beta_{\text{min}} = 0.7$ [72]. Translated into a minimal momentum this yields

$$p_{\text{min}} = \frac{\beta_{\text{min}}\, m}{q\sqrt{1-\beta_{\text{min}}^2}}. \tag{7.9}$$

These values range from 8 GeV for mass 50 GeV and charge $|q| = 6e$ to 294 GeV for mass 600 GeV and charge $|q| = 2e$ and are shown in Table 7.2. They can be used to deduce a phase-space of allowed p_{T} values via

$$p_{\text{T}} = p\,\sin\theta\,. \tag{7.10}$$

Figure 7.4 shows the dependence of this implicit p_{T} cut on the polar angle θ for signal samples of mass 50 to 300 GeV. It can be seen that the explicit p_{T} cut applied in the analysis selection of 20 GeV (as will be discussed in Section 7.1.3) has no influence on the efficiency above a mass of 300 GeV, where the implicit cut from the trigger timing is well above the 20 GeV cut. For masses below 300 GeV the explicit cut is above the implicit in certain areas of the $|\eta|$ phase space, indicated by the interior of the two vertical (red) lines in Figure 7.4.

Turn-on curves

The trigger turn-on curves with respect to the particles' β are shown in Figure 7.5. These plots illustrate the timing requirement mentioned in the previous chapter - the trigger efficiency is zero below $\beta \approx 0.7$ for all masses and charges. As can be deduced from Figure 7.5, for some samples especially the ones with high charges, $\beta \approx 0.8$ is the efficiency cut-off. This is the case for low mass signal points, which have an overall small probability to be slow, as was demonstrated in Figures 6.3a and 6.3b. It remains the case in the high mass regime for particles with high charges. These are affected more strongly by the implicit p_{T} cut discussed in the previous Section 7.1.2 and are thus required to have a higher velocity.

The dependence of the trigger efficiency on the true transverse momentum, p_{T}, divided by the charge, q, is shown in Figure 7.6. From these plots it becomes evident that with a p_{T} cut at 20 GeV one remains significantly below the trigger plateau for all signal samples. This is reflected in a large systematic uncertainty to be assigned to the trigger efficiency (see Section 7.4.1). For the larger masses the trigger turn-on curve shows a dip. This can be explained as a geometrical effect from the two different trigger detectors as shown in Figure 7.7 in the distributions of RPC and TGC triggered muons. The transition region matches the position of the dip in Figure 7.6.

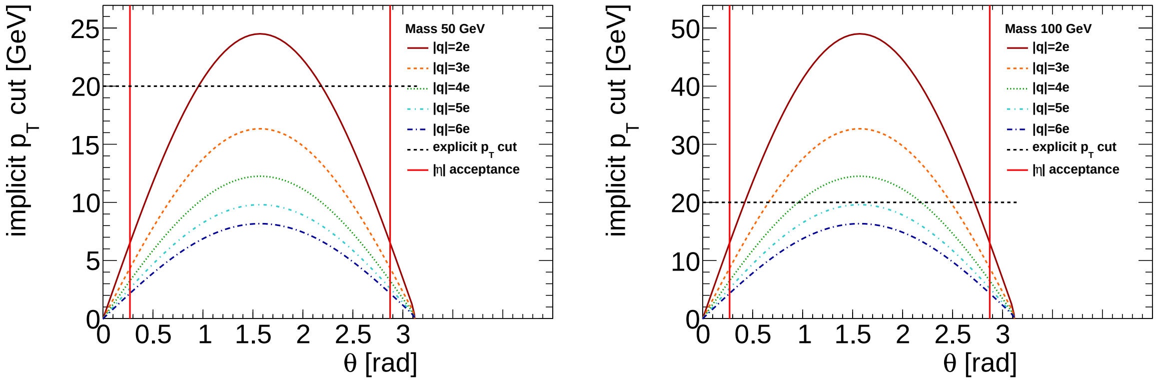

(a) m = 50 GeV (b) m = 100 GeV

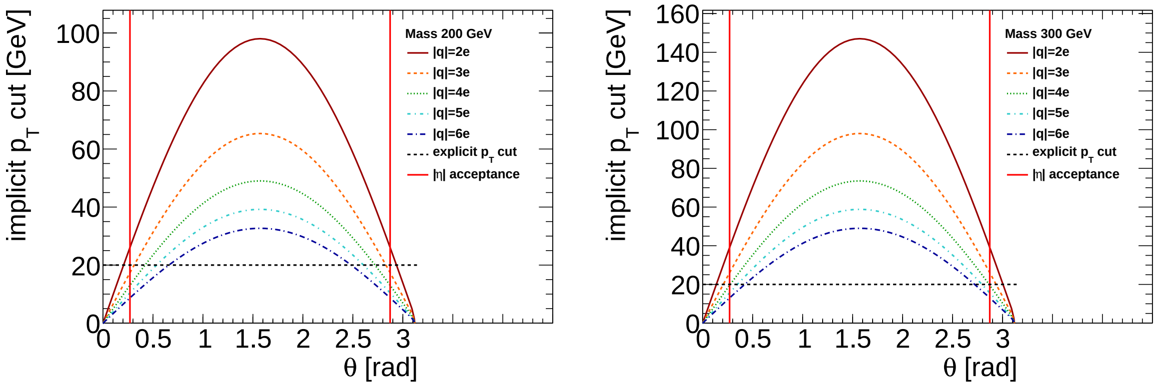

(c) m = 200 GeV (d) m = 300 GeV

Figure 7.4: *The implicit* p_T *cuts from the trigger timing requirement of* $\beta > 0.7$ *for all charges and masses (a) 50 GeV, (b) 100 GeV, (c) 200 GeV, and (d) 300 GeV.*

7.1.3 Preselection

This analysis utilizes $\mathrm{d}E/\mathrm{d}x$ variables from the Pixel, the TRT and the MDT detector, introduced in Chapters 4 and 5, to select signal candidates. The former two are defined on inner detector tracks, whereas the latter is a property of reconstructed muon objects. The necessity to access information from both reconstructed muon objects and associated tracks in the inner detector defines the signal candidates. This search is based on single candidate objects without any requirement on the candidate multiplicity in a given event.

After a selection applied to reconstructed muon objects defined in Section 7.1.3, inner detector tracks are chosen that can be associated to these track segments in the muon system. Their selection is discussed in Section 7.1.3. A summary of the applied cuts can be found in Table 7.3.

Muon selection

In the available events from the single muon DESD data sets (see Section 3.3), muon objects reconstructed by the ATLAS MUID algorithm in the standard ATLAS quality classification medium (see Section 3.4) are selected. This algorithm starts with reconstructed track segments in the muon system

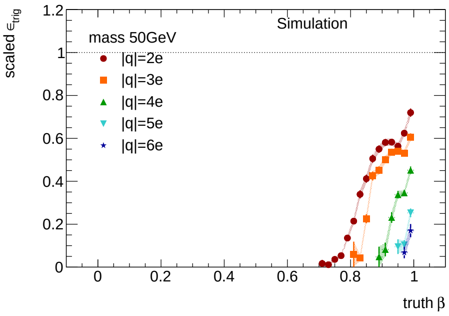

(a) Mass 50 GeV

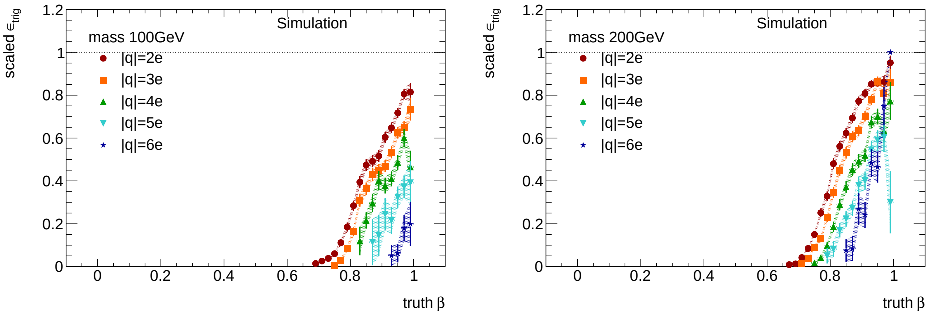

(b) Mass 100 GeV (c) Mass 200 GeV

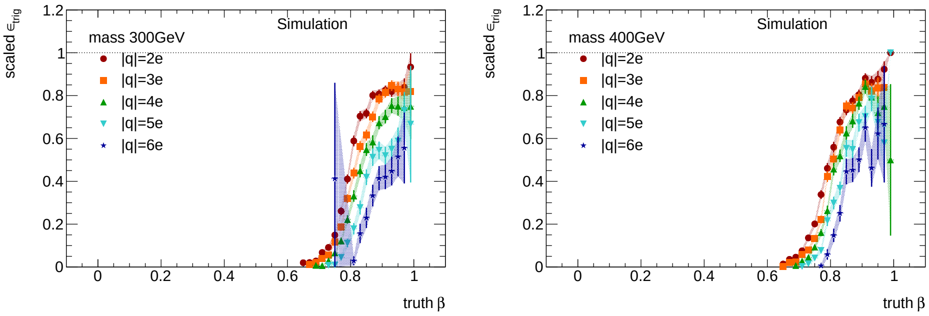

(d) Mass 300 GeV (e) Mass 400 GeV

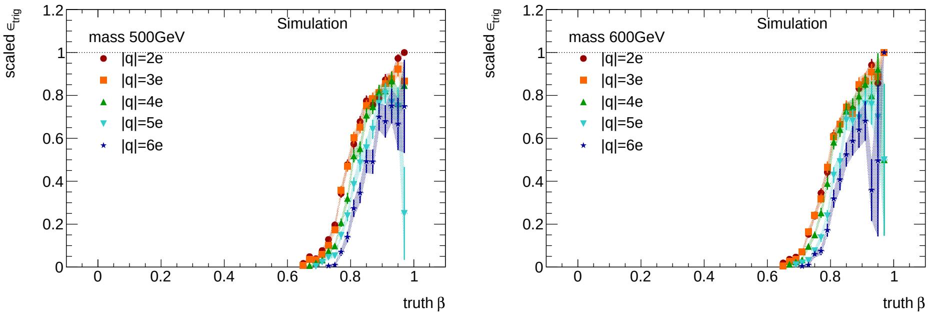

(f) Mass 500 GeV (g) Mass 600 GeV

Figure 7.5: *The trigger turn-on curves as a function of the true* $\beta = v/c$ *for all benchmark points. The shaded areas illustrate the binomial error of the efficiency.*

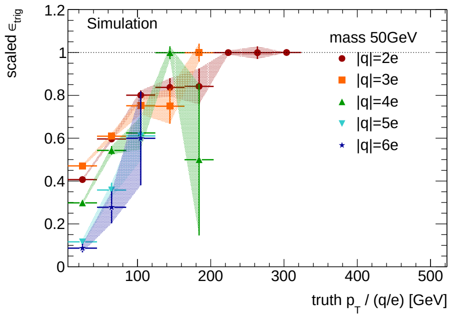

(a) Mass 50 GeV

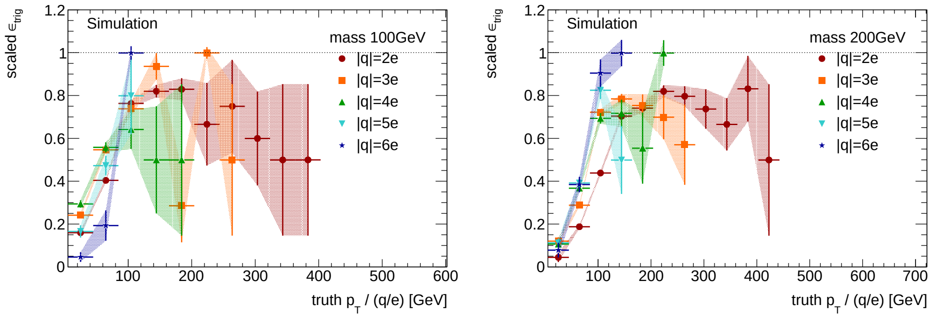

(b) Mass 100 GeV

(c) Mass 200 GeV

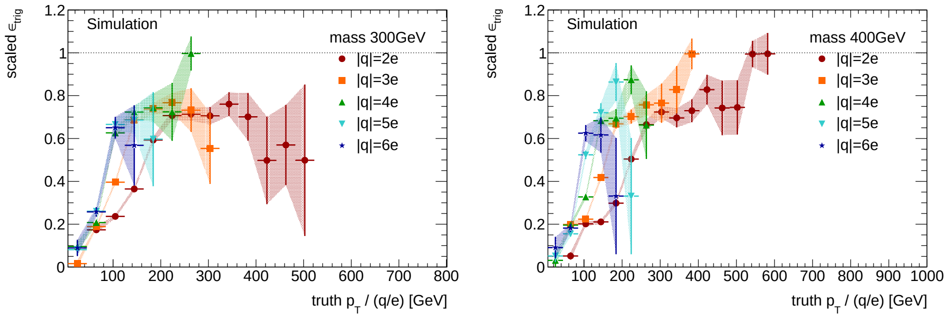

(d) Mass 300 GeV

(e) Mass 400 GeV

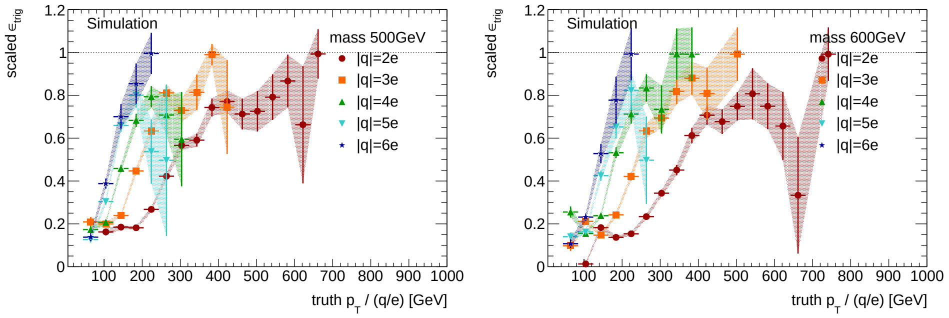

(f) Mass 500 GeV

(g) Mass 600 GeV

Figure 7.6: *The trigger turn-on curves as a function of the true transverse momentum divided by the particles charge for all benchmark points. The shaded areas illustrate the binomial error of the efficiency. Note the varying x-axis ranges.*

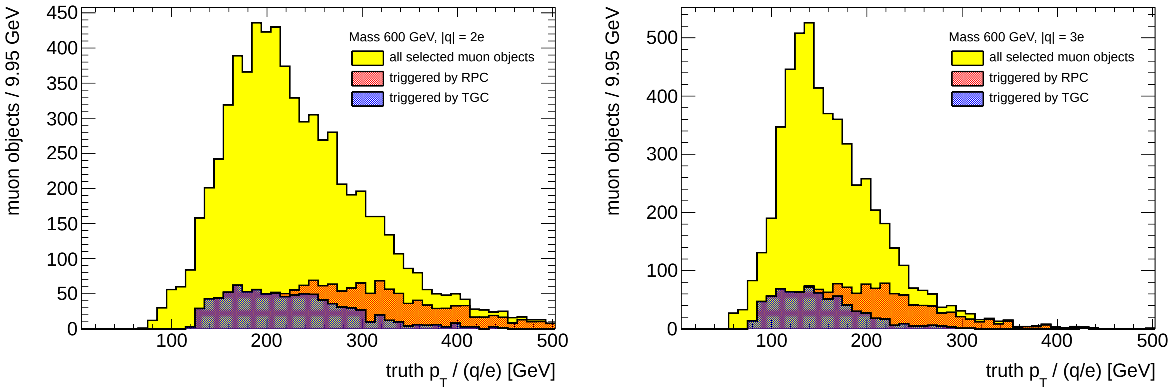

(a) Mass 600 GeV, charge 2e

(b) Mass 600 GeV, charge 3e

Figure 7.7: *The distributions used to determine the trigger efficiency for mass 600 GeV, charge 2e and 3e. The triggered distributions are shown separately for RPC and TGC triggered muons.*

and searches for matching tracks in the inner detector, which are refit together to build a combined muon. Since the signal selection is based on the MDT $\mathrm{d}E/\mathrm{d}x$, this variable needs to be defined for the considered muon objects. All following selection criteria are based on the inner detector track associated to the reconstructed muon object. In the case of multi-charged particles the reconstructed momentum of the muon and track objects do not have to be identical, as the particle loses a significant amount of energy on its way to the muon system.

Track selection

The tracks must lie within the geometrical acceptance of the complete ATLAS Inner Detector, hence the absolute value of the pseudorapidity ($|\eta|$) needs to be less or equal to 2.0 (see Section 3.2.3). Cuts on the impact parameters, $|d_0| < 1.5$ mm and $|z_0 \sin\theta| < 1.5$ mm, assure that the track originates from the primary vertex of the interaction. The transverse momentum of the track should be larger than 20 GeV and the track has to consist of at least 6 hits in the SCT and at least 10 in the TRT. Furthermore, the TRT $\mathrm{d}E/\mathrm{d}x$ has to be defined for this track (a detailed description of these requirements can be found in Chapter 5). Note that no requirement on the number of hits in the Pixel detector is made. This is

Table 7.3: *Summary of preselection cuts.*

Variable	Cut
Algorithm	MUID
Quality	medium
MDT $\mathrm{d}E/\mathrm{d}x$	defined

(a) Muons

Variable	Cut
Pseudorapidity	$\lvert\eta\rvert < 2.0$
Transverse Momentum	$p_{\mathrm{T}} > 20$ GeV
Impact Parameters	$\lvert d_0\rvert < 1.5$ mm $\lvert z_0 \sin\theta\rvert < 1.5$ mm
SCT hits	$N_{\mathrm{SCT}} \geq 6$
TRT hits	$N_{\mathrm{TRT}} \geq 10$
TRT $\mathrm{d}E/\mathrm{d}x$	defined

(b) Tracks

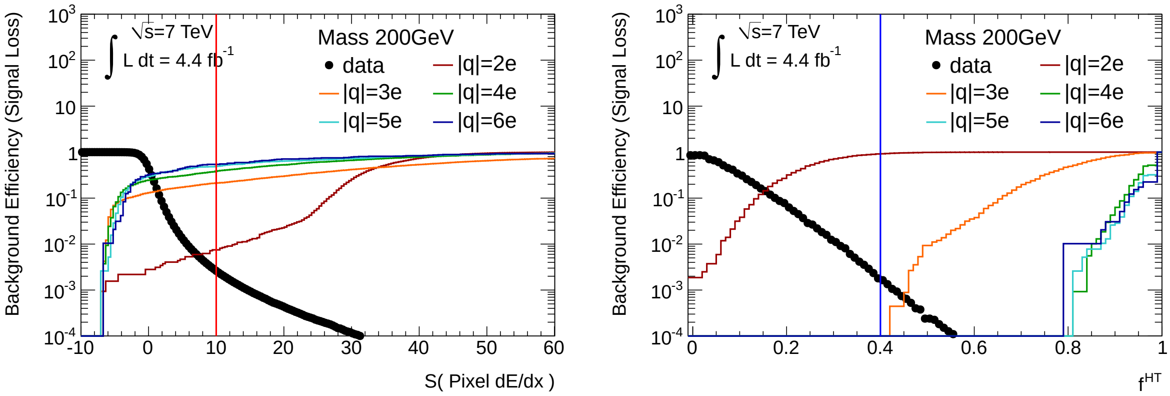

(a) S (Pixel dE/dx) (b) f^{HT}

Figure 7.8: *The background rejection for data in the background regions and the signal efficiency for signal tracks of mass 200 GeV and all possible charges versus the applied cut on the (a)* S *(Pixel d*E/dx*) and (b)* f^{HT}*. The vertical lines illustrate the chosen cut value at (a)* S *(Pixel d*E/dx*)* $= 10$ *and (b)* $\mathrm{f}^{\mathrm{HT}} = 0.4$.

necessary to avoid signal losses from Pixel readout saturation as discussed previously in Section 4.4.

7.1.4 Tight selection

At this stage, it becomes necessary to split the analysis in two branches. One is the search for multi-charged particle tracks with charges $|q| = 2e$ and one for particle tracks with charges $|q| > 2e$.

The Pixel dE/dx significance (S (Pixel dE/dx)) has been shown to be an excellent discriminant from muons for particles with $|q| = 2e$. A cut at S (Pixel dE/dx) > 10 rejects a large portion of the muon background, while ensuring a very high signal efficiency. Figure 7.8a shows the background efficiency vs. signal losses for signal samples of mass 200 GeV and data from the background region (defined in the next Section 7.1.5). The vertical line indicates the chosen cut. It retains almost 100% of the signal, while reducing the background by several orders of magnitude.

Complementary to S (Pixel dE/dx) the TRT HT fraction (f^{HT}, see Section 4.5) is an excellent discriminant for particles of all charges $|q| > 2e$. The background efficiency and signal loss plot shown in Figure 7.8b underlines the good separation of signals with $|q| > 2e$ from data in the background region (defined in the next Section 7.1.5). Shown are all signal samples for mass 200 GeV. The vertical line indicates the position of the chosen cut at $\mathrm{f}^{\mathrm{HT}} = 0.4$, for which the signal loss in samples with $|q| > 2e$ is negligible and the background is strongly suppressed.

The cuts for this *tight selection* are summarized separately for the search for particles with electric charge $|q| = 2e$ and $|q| > 2e$ in Table 7.6.

7.1.5 Signal region

Highly ionizing reconstructed muon objects are sought out in the final signal selection. It relies on the two newly developed dE/dx variables TRT dE/dx and MDT dE/dx. The plane of their significances S (TRT dE/dx) and S (MDT dE/dx) is divided into four regions, called A, B, C and D. Region A is the background region, whereas the signal is located almost entirely in the signal region D. Regions B and C are dominated by background, but can contain a small percentage of signal tracks. Due to the different preselection for charges $|q| = 2e$ and $|q| > 2e$, these regions have to be chosen slightly different in the

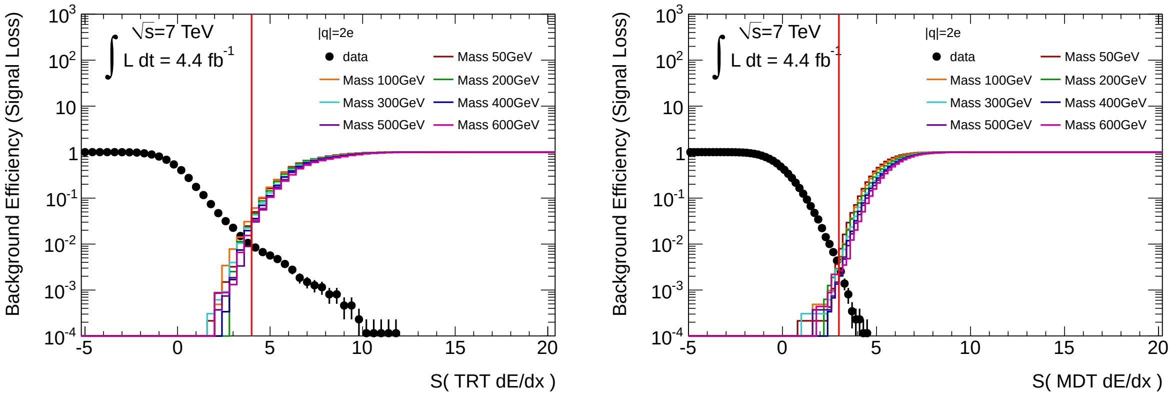

(a) $S\,(\mathrm{TRT}\ \mathrm{d}E/\mathrm{d}x)$ (b) $S\,(\mathrm{MDT}\ \mathrm{d}E/\mathrm{d}x)$

Figure 7.9: *Background efficiency and signal loss versus the cut on (a)* $S\,(\mathrm{TRT}\ \mathrm{d}E/\mathrm{d}x)$ *and (b)* $S\,(\mathrm{MDT}\ \mathrm{d}E/\mathrm{d}x)$ *for data in the background regions (black dots) and all signal samples with* $|q| = 2e$*. The vertical lines show the chosen cut at* $S\,(\mathrm{TRT}\ \mathrm{d}E/\mathrm{d}x) = 4$ *and* $S\,(\mathrm{MDT}\ \mathrm{d}E/\mathrm{d}x) = 3$.

Table 7.4: *Definitions of the regions A, B, C and D in the search for particles with charges* $|q| = 2e$.

	$S\,(\mathrm{TRT}\ \mathrm{d}E/\mathrm{d}x) < 4$	$S\,(\mathrm{TRT}\ \mathrm{d}E/\mathrm{d}x) \geq 4$
$S\,(\mathrm{MDT}\ \mathrm{d}E/\mathrm{d}x) < 3$	A	B
$S\,(\mathrm{MDT}\ \mathrm{d}E/\mathrm{d}x) \geq 3$	C	D

two cases. The signal region is blinded in data until the very last step of the analysis.

In Figure 7.9, the signal loss and background efficiency versus the applied cuts on $S\,(\mathrm{TRT}\ \mathrm{d}E/\mathrm{d}x)$ (Figure 7.9a) and on $S\,(\mathrm{MDT}\ \mathrm{d}E/\mathrm{d}x)$ (Figure 7.9b) for all samples of charge $|q| = 2e$ and data are shown. A good separation between background and signal can be achieved with cuts at $S\,(\mathrm{TRT}\ \mathrm{d}E/\mathrm{d}x) = 4$ and $S\,(\mathrm{MDT}\ \mathrm{d}E/\mathrm{d}x) = 3$, indicated with the vertical lines. These cuts define the four regions A, B, C and D summarized in Table 7.4. One exemplary signal sample (mass 200 GeV, $|q| = 2e$) is shown together with all of the 2011 data passing the selection for regions A, B and C in the plane of $S\,(\mathrm{TRT}\ \mathrm{d}E/\mathrm{d}x)$ and $S\,(\mathrm{MDT}\ \mathrm{d}E/\mathrm{d}x)$ in Figure 7.10a. It illustrates that the data points are almost entirely in region A and the signal in region D. Note that this plot serves only for illustration purposes and the normalization is chosen to give an impression of the maxima and minima within the data / signal distributions, but cannot be compared with each other.

For the selection of particles with $|q| > 2e$ a tighter cut is suggested from the distributions of the signal loss and background efficiency versus applied cut in Figure 7.11. These plots show the distributions for all charges and mass 200 GeV, even though the selection is not applied to particles with charge $|q| = 2e$. It shows that good cut values for $|q| > 2e$ lie at $S\,(\mathrm{TRT}\ \mathrm{d}E/\mathrm{d}x) = 5$ and $S\,(\mathrm{MDT}\ \mathrm{d}E/\mathrm{d}x) = 4$, as indicated by the vertical lines in figures 7.11a and 7.11b. Hence the regions A, B, C and D are defined in the search for particles with charges $|q| > 2e$ as described in Table 7.5. The larger tail in the distribution of $S\,(\mathrm{TRT}\ \mathrm{d}E/\mathrm{d}x)$ observed in Figure 7.10b is an artifact of the correlation of this variable with f^{HT} used in the preselection. This figure again compares the shapes (not the normalization) of an exemplary signal sample (mass 200 GeV, $|q| = 4e$) with all of 2011 data.

Table 7.6 summarizes all cuts applied in both analysis paths ($|q| = 2e$ and $|q| > 2e$).

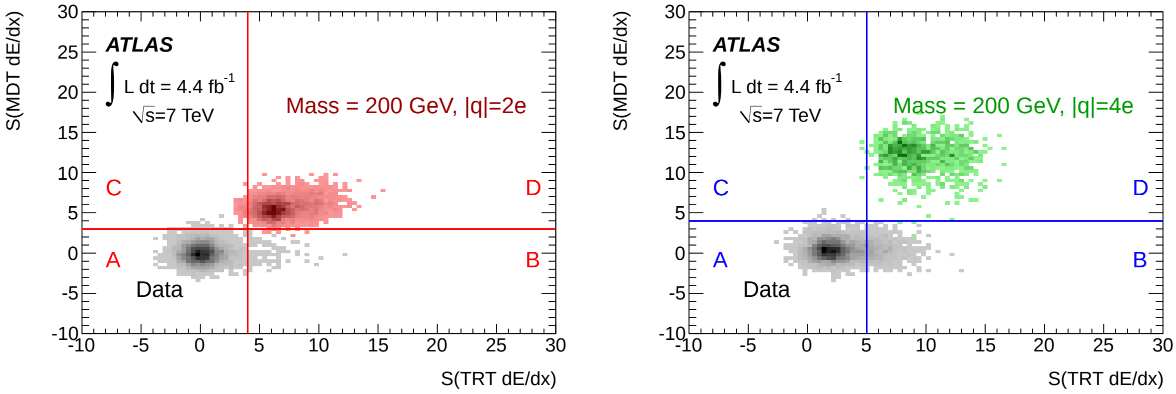

(a) mass 200 GeV $|q| = 2e$

(b) mass 200 GeV $|q| = 4e$

Figure 7.10: *The plane of $S\,(TRT\ dE/dx)$ and $S\,(MDT\ dE/dx)$ for 2011 data and the signal sample with mass 200 GeV and (a) $|q| = 2e$ and (b) $|q| = 4e$. Indicated are the regions A, B, C and D defined by the cuts found from figures (a) 7.9 and (b) 7.11.*

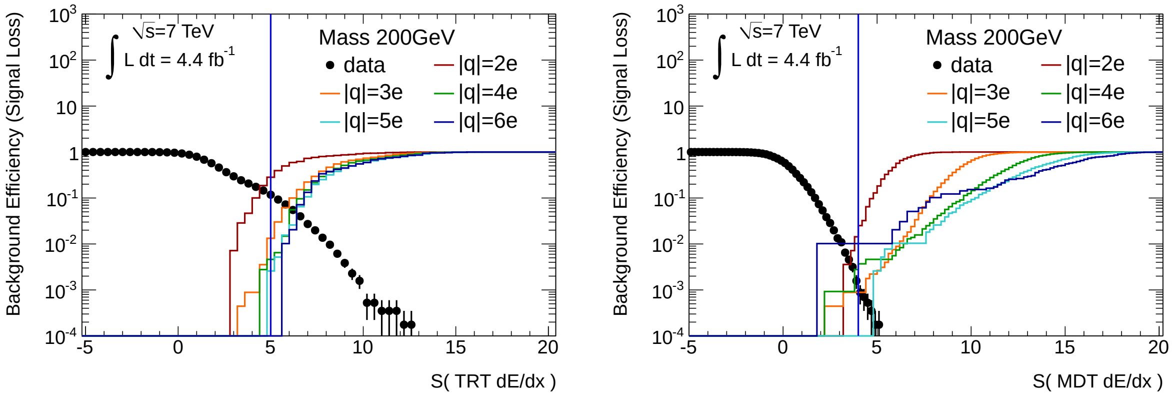

(a) $S\,(\mathrm{TRT\ d}E/\mathrm{d}x)$

(b) $S\,(\mathrm{MDT\ d}E/\mathrm{d}x)$

Figure 7.11: *Background efficiency and signal loss versus the cut on (a) $S\,(TRT\ dE/dx)$ and (b) $S\,(MDT\ dE/dx)$ for data in regions A, B and C (black dots) and all signal samples with mass 200 GeV. The vertical lines show the chosen cut at $S\,(TRT\ dE/dx) = 5$ and $S\,(MDT\ dE/dx) = 4$. Note that the sample with $|q| = 2e$ is only shown for reference and is not affected by this selection.*

Table 7.5: *Definitions of the regions A, B, C and D in the search for particles with charges $|q| > 2e$.*

	$S\,(\mathrm{TRT\ d}E/\mathrm{d}x) < 5$	$S\,(\mathrm{TRT\ d}E/\mathrm{d}x) \geq 5$
$S\,(\mathrm{MDT\ d}E/\mathrm{d}x) < 4$	A	B
$S\,(\mathrm{MDT\ d}E/\mathrm{d}x) \geq 4$	C	D

Table 7.6: *Summary of the selection cuts applied in the searches for multi-charged particles of charge* $|q| = 2e$ *and* $|q| > 2e$.

Data Selection	$N_{\mu^{\mathrm{reco}}} \geq 1$	$p_{\mathrm{T}} > 75~GeV$ OR	
	$N_{\mu^{\mathrm{reco}}} \geq 2$	$p_{\mathrm{T}} > 15~GeV$	
Trigger	$N_{\mu^{\mathrm{reco}}} \geq 1$	$p_{\mathrm{T}} > 18~GeV$	
Preselection	muon objects		
	Inner detector track attached		
	β	> 0.7 (implicit)	
	MDT $\mathrm{d}E/\mathrm{d}x$	defined	
	tracks		
	p_{T}	> 20 GeV	
	$\lvert\eta\rvert$	< 2.0	
	$\lvert d_0\rvert$	< 1.5 mm	
	$\lvert z_0 \sin\theta\rvert$	< 1.5 mm	
	N_{SCT}	≥ 6	
	N_{TRT}	≥ 10	
	TRT $\mathrm{d}E/\mathrm{d}x$	defined	
	Search for particles with	$\lvert q\rvert = 2e$	$\lvert q\rvert > 2e$
Tight selection	S(Pixel $\mathrm{d}E/\mathrm{d}x$)	> 10	-
	f^{HT}	-	> 0.4
Signal selection	S(MDT $\mathrm{d}E/\mathrm{d}x$)	> 3	> 4
	S(TRT $\mathrm{d}E/\mathrm{d}x$)	> 4	> 5

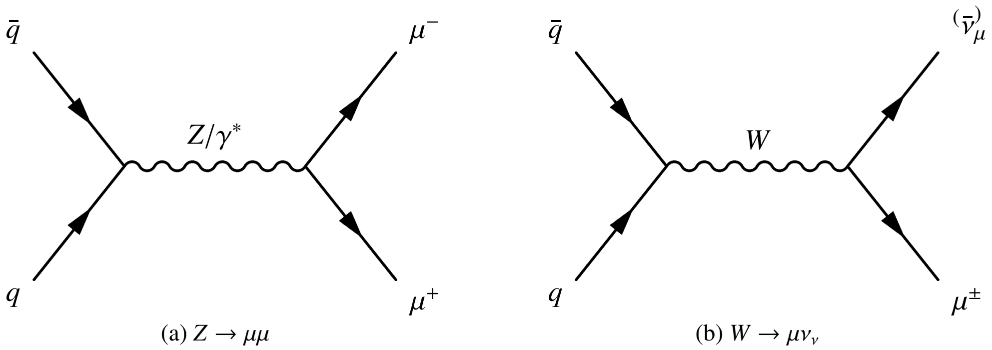

(a) $Z \rightarrow \mu\mu$ (b) $W \rightarrow \mu\nu_\nu$

Figure 7.12: Possible backgrounds of the search for multi-charged particles.

7.1.6 Possible backgrounds

Any physics process including muons in the final state is a possible background for this search. Examples are the processes $Z \rightarrow \mu\mu$, $W \rightarrow \mu\nu$ (see Figure 7.12) and QCD events where a muon is created in the decay of a hadronic particle. The selection does not put any constraints on the full event, but rather selects highly ionizing reconstructed muon objects. $\mathrm{d}E/\mathrm{d}x$ is a statistically distributed variable. Hence, an upward fluctuation in $\mathrm{d}E/\mathrm{d}x$ is generically also possible for SM particles. The coincidence of upward fluctuations over the entire detector, however, makes this extremely unlikely.

Other possible sources of non-signal like tracks in the signal region defined in the previous Section (7.1.5) include malfunctions of the detector or the track and muon reconstruction. However, any known malfunction of the detector is excluded in the event selection and the reconstruction has proven to be very reliable in the past.

The background estimation in this analysis does not rely on Monte Carlo predictions, but uses a purely data-driven approach described in the following Section 7.2.

7.2 Data driven background estimation

Assuming that S(TRT $\mathrm{d}E/\mathrm{d}x$) and S(MDT $\mathrm{d}E/\mathrm{d}x$) are uncorrelated variables, the number of expected candidates in data in region D, N^D_{data}, can be estimated from the number of observed data tracks in regions A, B and C ($N^{A,B,C}_{\text{data}}$). It can safely be assumed that two $\mathrm{d}E/\mathrm{d}x$ estimators from different subdetectors are uncorrelated, such that the number of expected tracks in region D from background is

$$N^D_{\text{data}} = \frac{N^B_{\text{data}} \cdot N^C_{\text{data}}}{N^A_{\text{data}}}. \tag{7.11}$$

The observed number of candidate tracks in region A, B and C and the expected number of candidate tracks in region D for the two cases of $|q| = 2e$ and $|q| > 2e$ are summarized in Table 7.7. It shows that the signal region D is almost background free with an expected number of single background tracks of

$$N^{\text{bkg.}}_{\text{D}}(|q| = 2e) = 0.41 \pm 0.08$$

in the search for particles with charge $|q| = 2e$ and

$$N^{\text{bkg.}}_{\text{D}}(|q| > 2e) = 1.37 \pm 0.46$$

Table 7.7: *Observed track yields in regions A, B and C and expected track yields in region D for an integrated luminosity of 4.4 fb^{-1}.*

Search for	Track yield in region			
particles with	A	B	C	D$^{\text{expected}}$
$\|q\| = 2e$	8543	92	38	0.41±0.08
$\|q\| > 2e$	4940	754	9	1.37±0.46

for particles with charges $|q| > 2e$. In the absence of signal, this translates into a probability to observe zero candidates in the signal region of 66% for $|q| = 2e$ and 28% for $|q| > 2e$ from simple Poissonian calculations.

Three independent cross-checks on this background prediction method are performed, one of which will be described in detail in the context of the estimation of systematic uncertainties (Section 7.4.4).

7.2.1 Cross-check of background prediction by assuming a perfectly uncorrelated state

Even though the variables can be assumed to be uncorrelated, we observe small deviations in the shapes of the distributions of $S(\text{TRT d}E/\text{d}x)$ and $S(\text{MDT d}E/\text{d}x)$ in the background regions A, B and C. For perfectly uncorrelated variables, the shape of one variable is not affected by a cut on the other variable. Hence, from the differences of these shapes and the shape of the overall distribution (the sum of regions A, B and C), scaling factors can be deduced to mimic a perfectly uncorrelated state. Note that for this study no tight selection (cut on $S(\text{Pixel d}E/\text{d}x)$ or f^{HT}) is required to increase the number of tracks and thus the precision of the study.

Table 7.8 lists the unscaled and scaled integrals of the distributions in regions A*, B* and C*, where the * indicates that no tight selection has been required, alongside the expected integral of the distribution in region D*. The relative difference of these background predictions in the signal region is found to be 0.42% or 0.54% in the search for $|q| = 2e$ particles for $S(\text{MDT d}E/\text{d}x)$ and $S(\text{TRT d}E/\text{d}x)$ respectively. Expressed in terms of signal tracks, this corresponds to an uncertainty of 0.002 on the background estimation 0.41±0.08 in both cases. In the search for $|q| > 2e$ particles, the relative differences are 1.95% for $S(\text{MDT d}E/\text{d}x)$ and 2.26% for $S(\text{TRT d}E/\text{d}x)$, translating to 0.027 and 0.031 tracks uncertainty on the background estimate 0.41±0.08. Thus, this cross-check serves as a confirmation that $S(\text{TRT d}E/\text{d}x)$ and $S(\text{MDT d}E/\text{d}x)$ can be assumed to be uncorrelated variables.

7.2.2 Cross-check of variable correlation

In another cross-check the prediction procedure is repeated for different definitions of regions A’, B’, C’ and D’, which lie entirely in the original region A*, where no signal contamination is expected. In this restricted region, see Figure 7.13, the D’ region is varied on both axis. The lower plots, 7.13c and 7.13d, show the relative deviation of the expected number of tracks in region D’

$$N^{D'}_{\text{expected}} = \frac{N^{B'}_{\text{observed}} \cdot N^{C'}_{\text{observed}}}{N^{A'}_{\text{observed}}} \tag{7.12}$$

Table 7.8: *The number of tracks in the three background regions without tight selection (A*, B*, C*) before and after scaling to assume uncorrelated variables for* $S\,(\text{MDT d}E/\text{d}x)$ *and* $S\,(\text{TRT d}E/\text{d}x)$.

Cut positions as in search for particles with $\lvert q\rvert = 2e$ before tight selection				
	$N_{\text{data}}^{\text{A}^*}$	$N_{\text{data}}^{\text{B}^*}$	$N_{\text{data}}^{\text{C}^*}$	$N_{\text{data}}^{\text{expected D}^*}$
$S\,(\text{MDT d}E/\text{d}x)^{\text{unscaled}}$	3 139 529.00	10 169.00	19 248.00	62.34
$S\,(\text{MDT d}E/\text{d}x)^{\text{scaled}}$	3 139 529.14	10 211.25	19 248.00	62.60
			relative error:	0.0042
$S\,(\text{TRT d}E/\text{d}x)^{\text{unscaled}}$	3 139 529.00	10 169.00	19 248.00	62.34
$S\,(\text{TRT d}E/\text{d}x)^{\text{scaled}}$	3 139 529.64	10 169.00	19 352.19	62.68
			relative error:	0.0054

(a) $\lvert q\rvert = 2e$

Cut positions as in search for particles with $\lvert q\rvert > 2e$ before tight selection				
	$N_{\text{data}}^{\text{A}^*}$	$N_{\text{data}}^{\text{B}^*}$	$N_{\text{data}}^{\text{C}^*}$	$N_{\text{data}}^{\text{expected D}^*}$
$S\,(\text{MDT d}E/\text{d}x)^{\text{unscaled}}$	3 162 724.00	3 872.00	2 436.00	2.98
$S\,(\text{MDT d}E/\text{d}x)^{\text{scaled}}$	3 162 724.09	3 947.33	2 436.00	3.04
			relative error:	0.0195
$S\,(\text{TRT d}E/\text{d}x)^{\text{unscaled}}$	3 162 724.00	3 872.00	2 436.00	2.98
$S\,(\text{TRT d}E/\text{d}x)^{\text{scaled}}$	3 162 724.04	3 872.00	2 491.06	3.05
			relative error:	0.0226

(b) $\lvert q\rvert > 2e$

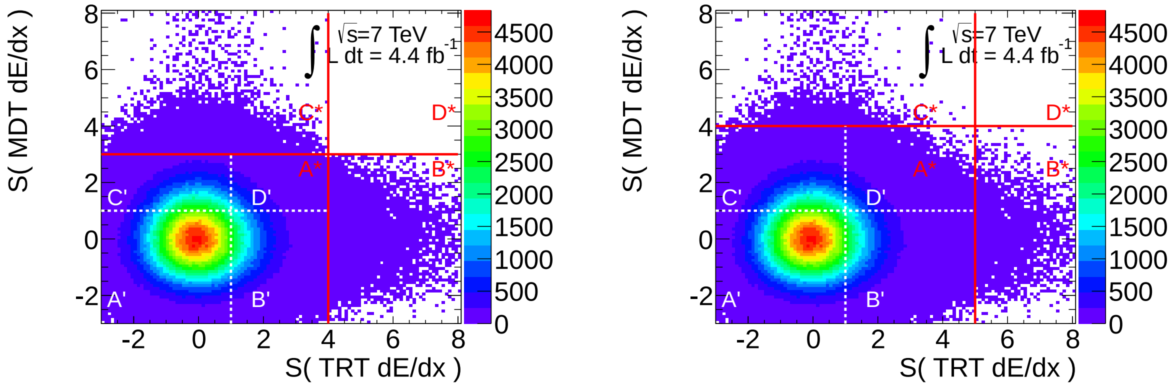

(a) $|q| = 2e$

(b) $|q| > 2e$

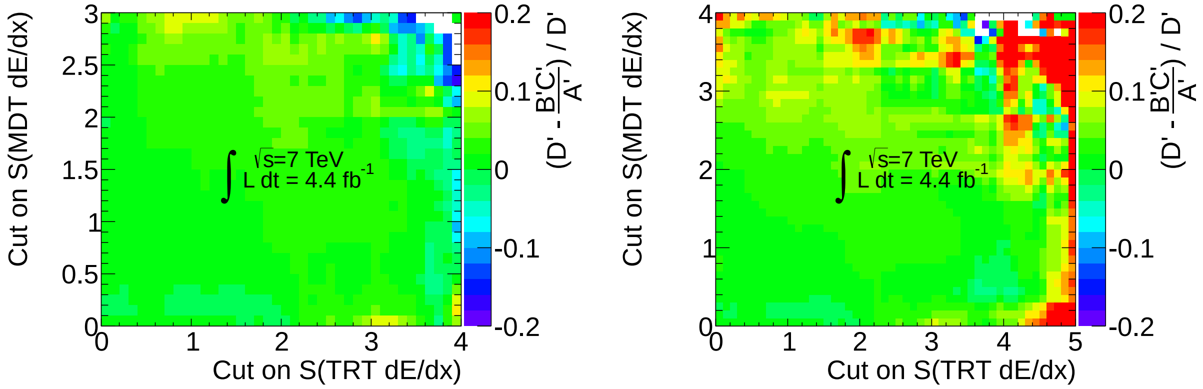

(c) $|q| = 2e$

(d) $|q| > 2e$

Figure 7.13: *Variation of the regions used to extract entries in D. The upper plots show the A, B, C and D regions after the $q = 2$ (a) and $q > 2$ (b) tight selection. The solid lines indicate the region boundaries. The dashed lines in region A mark the regions A', B', C' and D' used to test the correlation of the variables. The lower plots show the relative deviation of the expected number of candidates in regions D' and the observed candidates in D'. In the bins without entries either one of the number of entries in region A', B', C' or D' are zero, making a comparison impossible. The axes in (c) and (d) correspond to cuts defining regions A', B', C' and D' shown as the dashed lines in (a) and (b).*

from the observed tracks in D', $N^{D'}_{\text{observed}}$. This study is performed with the data distribution before the tight selection on f^{HT} or $S(\text{Pixel d}E/\text{d}x)$. Note that D' lies completely in the area not blinded in data. The upper right corners of figures 7.13c and 7.13d correspond to a very small region of D' and are thus dominated by statistical effects due to a limited number of candidates in this area. It can be deduced that within areas containing sufficient data the ABCD methods predicts D' reliably.

7.3 Selection efficiency

In order to extract a cross section measurement / limit from the number of observed candidate tracks in data, the signal efficiency ϵ has to be determined from simulation. It is

$$\epsilon = \frac{N_{\mathrm{MC}}^{\mathrm{rec}}}{N_{\mathrm{MC}}^{\mathrm{gen.\ events}}}, \tag{7.13}$$

the number of reconstructed particles ($N_{\mathrm{MC}}^{\mathrm{rec}}$) over the number of simulated events ($N_{\mathrm{MC}}^{\mathrm{gen.\ events}}$). Defined in this way, ϵ transforms the observed number of tracks in the signal region in a signal efficiency to extract a production cross section of events. This efficiency includes the kinematic acceptance, the trigger efficiency and the selection efficiencies.

The production cross section of multi-charged particle pairs can be determined by inverting Equation (3.2) to be

$$\sigma = \frac{N_{\mathrm{data}}^{\mathrm{rec}}}{\mathcal{L} \cdot \epsilon}, \tag{7.14}$$

where $N_{\mathrm{data}}^{\mathrm{rec}}$ is the number of reconstructed candidate particles above the expected background in data (see Equation (7.15)), $\mathcal{L}$ the integrated luminosity of the analyzed data and ϵ the signal efficiency described above.

$$N_{\mathrm{data}}^{\mathrm{rec}} = N_{\mathrm{data}}^{\mathrm{obs}} - N_{\mathrm{bkg}}^{\mathrm{rec}} \tag{7.15}$$

The cross section obtained in this way can be compared with the predicted cross sections of the simplified Drell-Yan model, used in the production of the signal samples given in Table 6.2. ϵ is the product of the kinematic acceptance, the trigger efficiency and the efficiency of the signal selection. All these values give rise to distinct uncertainties and are hence discussed separately in the following.

7.3.1 Kinematic acceptance

The kinematic acceptance α_{kin} defines how many simulated multi-charged particle candidates passing the preselection are present in the simulated events. It is defined on reconstructed muon objects matched to a true multi-charged particle within the kinematic range ($p_T/q > 20\,\mathrm{GeV}$ and $|\eta| < 2.0$). On these multi-charged particle muon objects, the muon and track cuts described in Section 7.1.3 are applied. The ratio of these candidate muon-track pairs over the number of simulated events defines α_{kin}

$$\alpha_{\mathrm{kin}} = \frac{N_{\text{multi-charged particles}}^{\mathrm{preselected}}}{N_{\mathrm{MC}}^{\mathrm{gen.\ events}}}. \tag{7.16}$$

α_{kin} includes both the reconstruction efficiency and geometrical acceptance. An overview of the kinematic acceptances in the different signal samples can be found in Table 7.9. Note that this acceptance is defined as the ratio of numbers of tracks over numbers of events. Hence, the maximal possible value is 200% in models of pair produced signal particles. α_{kin} is lowest for low mass particles with high charges and highest for high masses and low charges. The decrease in acceptance towards higher charges is a consequence of the momentum mismeasurement. High masses are produced more centrally in the detector and a large fraction of signal tracks with low charges fails the $|\eta|$ cut.

Table 7.9: *Overview over the mass and charge dependence of the kinematic acceptance in % and its binomial error. Note that the numbers for the mass 50 GeV samples have been multiplied with the filter efficiency of the truth filter applied in simulation.*

Mass [GeV]	Kinematic acceptance α_{kin} [%]				
	$\lvert q\rvert = 2e$	$\lvert q\rvert = 3e$	$\lvert q\rvert = 4e$	$\lvert q\rvert = 5e$	$\lvert q\rvert = 6e$
50	18.84 ± 0.15	7.92 ± 0.08	1.87 ± 0.03	0.28 ± 0.01	0.06 ± 0.00
100	43.30 ± 0.50	27.27 ± 0.45	11.20 ± 0.32	2.90 ± 0.17	0.65 ± 0.08
200	62.18 ± 0.48	44.44 ± 0.50	25.07 ± 0.43	9.80 ± 0.30	2.61 ± 0.16
300	68.77 ± 0.46	51.91 ± 0.50	30.67 ± 0.46	14.61 ± 0.35	5.06 ± 0.22
400	68.54 ± 0.46	53.27 ± 0.50	33.10 ± 0.47	17.59 ± 0.38	6.34 ± 0.24
500	70.38 ± 0.46	54.13 ± 0.50	34.47 ± 0.48	18.58 ± 0.39	8.22 ± 0.27
600	68.64 ± 0.46	53.20 ± 0.50	34.64 ± 0.48	18.88 ± 0.39	8.71 ± 0.28

Table 7.10: *The trigger efficiencies in % for all signal samples and their binomial errors.*

Mass [GeV]	Trigger efficiency $\epsilon_{\text{trigger}}$ [%]				
	$\lvert q\rvert = 2e$	$\lvert q\rvert = 3e$	$\lvert q\rvert = 4e$	$\lvert q\rvert = 5e$	$\lvert q\rvert = 6e$
50	47.39 ± 0.53	49.87 ± 0.60	35.21 ± 0.87	19.22 ± 1.44	12.49 ± 2.10
100	41.39 ± 0.75	41.02 ± 0.94	40.54 ± 1.47	30.30 ± 2.70	10.78 ± 2.83
200	41.96 ± 0.63	41.83 ± 0.74	37.30 ± 0.97	36.16 ± 1.53	36.50 ± 2.98
300	38.05 ± 0.59	38.63 ± 0.68	37.61 ± 0.87	34.74 ± 1.25	31.26 ± 2.06
400	32.80 ± 0.57	34.07 ± 0.65	34.16 ± 0.82	32.81 ± 1.12	32.34 ± 1.86
500	28.54 ± 0.54	31.35 ± 0.63	31.05 ± 0.79	31.32 ± 1.08	31.11 ± 1.61
600	23.45 ± 0.51	25.67 ± 0.60	26.45 ± 0.75	24.54 ± 0.99	24.98 ± 1.47

7.3.2 Trigger efficiency

As described in Chapter 7.1.2, the trigger efficiency in the central trigger chambers (RPC, $|\eta| < 1.05$) is mismodeled in the simulation and a corrective scaling has to be applied. This β and η dependent scaling assigns a weight to each simulated muon object triggered by the RPC in the calculation of the trigger efficiency $\epsilon_{\text{trigger}}$. The trigger efficiency of the single muon trigger is calculated as

$$\epsilon_{\text{trigger}} = \frac{N^{\text{trigger matched}}_{\text{scaled multi-charged particles}}}{N^{\text{preselected}}_{\text{multi-charged particles}}}, \tag{7.17}$$

where $N^{\text{preselected}}_{\text{multi-charged particles}}$ is the number of multi-charged particles represented by a pair of reconstructed muon objects and tracks passing the preselection and $N^{\text{trigger matched}}_{\text{scaled multi-charged particles}}$ is the number of those muon-track objects that have fired the trigger. Table 7.10 gives the dependence of $\epsilon_{\text{trigger}}$ on mass and charge of the signal samples. The dependencies of $\epsilon_{\text{trigger}}$ can be understood with the help of Section 7.1.2. A decrease of efficiency towards higher charges originates in the p_{T} threshold at 18 GeV of the trigger and the momentum measurement that is a factor of q below the true momentum of the particle. All particles with masses above 300 GeV are not affected by this explicit cut, because the implicit momentum cut of the timing requirement to reach the muon system within the active readout

Table 7.11: *The signal selection efficiencies in % for all signal samples and their binomial errors. Note that the signal region differs for $|q| = 2e$ multi-charged particles and multi-charged particles with $|q| > 2e$.*

Mass [GeV]	Signal Selection Efficiency $\epsilon_{\text{signal selection}}$ [%]				
	$\lvert q\rvert = 2e$	$\lvert q\rvert = 3e$	$\lvert q\rvert = 4e$	$\lvert q\rvert = 5e$	$\lvert q\rvert = 6e$
50	96.62 ± 0.28	98.87 ± 0.18	99.44 ± 0.23	99.31 ± 0.69	96.78 ± 3.17
100	96.10 ± 0.46	98.80 ± 0.33	99.78 ± 0.22	100.00 ± 0.00	100.00 ± 0.00
200	96.34 ± 0.37	99.38 ± 0.18	99.24 ± 0.28	100.00 ± 0.00	98.99 ± 1.03
300	96.57 ± 0.36	99.06 ± 0.22	99.80 ± 0.13	99.26 ± 0.38	98.48 ± 0.97
400	97.10 ± 0.35	99.01 ± 0.23	99.42 ± 0.23	99.53 ± 0.29	98.73 ± 0.78
500	98.37 ± 0.28	99.66 ± 0.14	99.82 ± 0.13	99.72 ± 0.22	97.94 ± 0.89
600	96.95 ± 0.43	98.99 ± 0.27	99.46 ± 0.24	99.26 ± 0.40	97.70 ± 1.02

exceeds the explicit cut. Consequently, the trigger efficiency for $m > 300$ GeV is roughly stable for a given mass. The softer β spectra of heavier particles explain the drop in efficiency with mass, as these signal particles are less likely to reach the muon system in time to trigger the event.

7.3.3 Signal selection efficiency

The signal selection efficiency (Equation (7.18)) gives the ratio of the number of simulated multi-charged particle candidates in the signal region D over the number of trigger-matched simulated multi-charged particle candidates. Note that for this ratio the muon objects in the numerator and the denominator have the trigger efficiency correction weight assigned (scaled).

$$\epsilon_{\text{signal selection}} = \frac{N^{\text{signal region}}_{\text{scaled multi-charged particles}}}{N^{\text{trigger matched}}_{\text{scaled multi-charged particles}}} \tag{7.18}$$

This number is sensitive to the different tight selections. Its dependence on mass and charge of the signal sample are summarized in Table 7.11. $\epsilon_{\text{signal selection}}$ is nearly 100% efficient for all samples indicating the very low signal contamination in the background regions A, B and C.

7.3.4 Overall efficiencies

The overall selection efficiency needed in the denominator of the cross section limit determination (Equation (7.14)) can be determined via

$$\epsilon = \alpha_{\text{kin}} \cdot \epsilon_{\text{trigger}} \cdot \epsilon_{\text{signal selection}} = \frac{N^{\text{signal region}}_{\text{scaled multi-charged particles}}}{N^{\text{gen. events}}_{\text{MC}}}. \tag{7.19}$$

It transforms the measured number of tracks into an event based signal selection efficiency. Table 7.12 summarizes these efficiencies for all signal samples. It shows the limited sensitivity of the analysis to signal samples of mass 50 GeV, with the lowest ϵ of 0.01% in the case of $|q| = 6e$. The highest signal efficiency around 25% is achieved for $|q| = 2e$ and masses 200 and 300 GeV.

Table 7.12: *The overall selection efficiencies in % and their binomial errors for the visible cross section calculation. ϵ is derived from the product of α_{kin}, $\epsilon_{\text{trigger}}$and $\epsilon_{\text{signal selection}}$, where α_{kin} includes the filter efficiency for the mass 50 GeV.*

Mass [GeV]	Signal Efficiency ϵ [%]				
	$\lvert q\rvert = 2e$	$\lvert q\rvert = 3e$	$\lvert q\rvert = 4e$	$\lvert q\rvert = 5e$	$\lvert q\rvert = 6e$
50	8.63 ± 0.12	3.90 ± 0.06	0.66 ± 0.02	0.05 ± 0.00	0.01 ± 0.00
100	17.22 ± 0.38	11.05 ± 0.31	4.53 ± 0.21	0.88 ± 0.09	0.13 ± 0.04
200	25.13 ± 0.43	18.47 ± 0.39	9.28 ± 0.29	3.54 ± 0.18	0.94 ± 0.10
300	25.27 ± 0.43	19.87 ± 0.40	11.60 ± 0.32	5.04 ± 0.22	1.56 ± 0.12
400	21.83 ± 0.41	17.97 ± 0.38	11.24 ± 0.32	5.74 ± 0.23	2.02 ± 0.14
500	19.76 ± 0.40	16.91 ± 0.37	10.68 ± 0.31	5.80 ± 0.23	2.50 ± 0.16
600	15.61 ± 0.36	13.52 ± 0.34	9.11 ± 0.29	4.60 ± 0.21	2.13 ± 0.14

7.3.5 Signal yields

In analogy to ϵ the signal yields in all four regions of the ABCD method can be determined to

$$\epsilon_{\text{A,B,C,D}} = \frac{N^{\text{region A,B,C,D}}_{\text{scaled multi-charged particles}}}{N^{\text{gen. events}}_{\text{MC}}}. \tag{7.20}$$

These fractions are an important cross-check to verify that the signal is indeed clustered in the signal region D and negligible in regions A, B and C. Table 7.13 gives an overview of the efficiencies of multi-charged particles in all four regions of the ABCD method and all considered masses and charges determined from simulation.

7.4 Systematic Uncertainties

Besides the statistical uncertainties of the background estimation, a range of systematic uncertainties has to be considered. Following Equation (7.14) these can be separated into uncertainties on the signal efficiency, ϵ, defined in Section 7.3, the background estimation (Section 7.2) and the luminosity. The systematic uncertainty on the signal efficiency has several sources, the uncertainty on the trigger efficiency discussed in Section 7.4.1, derived from variation of all cuts in the selection (Section 7.4.2) and due to a limited number of Monte Carlo events presented in Section 7.4.3. The uncertainty on the background estimation is derived from a study of the correlation of $S\,(\text{MDT d}E/\text{d}x)$ and $S\,(\text{TRT d}E/\text{d}x)$ in Section 7.4.4. The uncertainty on the integrated luminosity is the subject of Section 7.4.5, and Section 7.4.6 summarizes all systematic uncertainties.

7.4.1 Trigger efficiency

The uncertainty on the efficiency of muons to be triggered by the single muon trigger used in this analysis has been determined to be 1% [67]. Additionally, the uncertainty on the scaling applied to the trigger efficiency in simulated data sets of pair produced multi-charged particles is taken into account. The scaling procedure is described in detail in Chapter 7.1.2.

The impact of the corrective scaling can be as large as 48% in some samples, as shown in Table C.2 in Appendix C.1. This has to be reflected in the uncertainty on the scaling. Hence, the impact of

Table 7.13: *Contributions of different signal samples to the ABCD quadrants in % in the search for particles with* $|q| = 2e$ *and* $|q| > 2e$*. Note that the numbers for the mass 50 GeV samples have been multiplied with the filter efficiency of the truth filter applied in simulation.*

$\lvert q\rvert = 2e$				
Mass [GeV]	Signal Yield in region [%]			
	A	B	C	D
50	0.00	0.04	0.22	8.63
100	0.00	0.06	0.53	17.22
200	0.00	0.09	0.62	25.13
300	0.00	0.08	0.57	25.27
400	0.00	0.04	0.41	21.83
500	0.00	0.04	0.17	19.76
600	0.00	0.05	0.23	15.61

(a) $|q| = 2e$

$\lvert q\rvert = 3e$				
Mass [GeV]	Signal Yield in region [%]			
	A	B	C	D
50	0.00	0.00	0.05	3.90
100	0.00	0.01	0.13	11.05
200	0.00	0.01	0.10	18.47
300	0.00	0.00	0.19	19.87
400	0.00	0.03	0.14	17.97
500	0.00	0.00	0.05	16.91
600	0.00	0.01	0.13	13.52

(b) $|q| = 3e$

$\lvert q\rvert = 4e$				
Mass [GeV]	Signal Yield in region [%]			
	A	B	C	D
50r	0.00	0.00	0.00	0.66
100	0.00	0.00	0.01	4.53
200	0.00	0.03	0.04	9.28
300	0.00	0.01	0.02	11.60
400	0.00	0.04	0.02	11.24
500	0.00	0.02	0.00	10.68
600	0.00	0.02	0.03	9.11

(c) $|q| = 4e$

$\lvert q\rvert = 5e$				
Mass [GeV]	Signal Yield in region [%]			
	A	B	C	D
50	0.00	0.00	0.00	0.05
100	0.00	0.00	0.00	0.88
200	0.00	0.00	0.00	3.54
300	0.00	0.03	0.01	5.04
400	0.00	0.02	0.01	5.74
500	0.00	0.02	0.00	5.80
600	0.00	0.03	0.00	4.60

(d) $|q| = 5e$

$\lvert q\rvert = 6e$				
Mass [GeV]	Signal Yield in region [%]			
	A	B	C	D
50	0.00	0.00	0.00	0.01
100	0.00	0.00	0.00	0.13
200	0.00	0.01	0.00	0.94
300	0.00	0.02	0.00	1.56
400	0.00	0.03	0.00	2.02
500	0.00	0.05	0.00	2.50
600	0.00	0.05	0.00	2.13

(e) $|q| = 6e$

Table 7.14: *The systematic uncertainty on the trigger efficiency determined from the relative difference between the scaled trigger efficiency and the trigger efficiency from a scaling factor varied by 50%* $\sigma(\epsilon_{\text{trigger}}) = (\epsilon_{\text{trigger}}^{\text{scaled}} - \epsilon_{\text{trigger}}^{\text{scaled with +50\% scaling}})/\epsilon_{\text{trigger}}^{\text{scaled}}$.

Mass [GeV]	Systematic trigger uncertainty $\sigma(\epsilon_{\text{trigger}})$ [%]				
	$\lvert q\rvert = 2e$	$\lvert q\rvert = 3e$	$\lvert q\rvert = 4e$	$\lvert q\rvert = 5e$	$\lvert q\rvert = 6e$
50	5.87	2.24	0.24	0.08	0.06
100	7.55	6.41	2.31	0.65	0.24
200	11.54	10.66	7.80	4.46	1.44
300	12.96	13.53	13.68	9.60	5.63
400	16.28	15.85	16.68	17.06	10.23
500	17.49	17.30	17.93	19.85	15.50
600	21.65	21.47	21.94	24.14	22.39

Table 7.15: *Overview of the varied variables and the amount they were varied by.*

Variable	Varied by [%]
p_{T}	±3
S(Pixel dE/dx)	±5
f^{HT}	±20
S(TRT dE/dx)	±5
S(MDT dE/dx)	−5 +50

varying the scaling by 50% is studied. In particular this means varying ρ by $\rho \pm 0.5(1 - \rho)$, such that the uncertainty on applying no scaling ($\rho = 1$) is zero. The relative difference of the trigger efficiencies with the nominal and the varied scaling is taken as the systematic uncertainty on the trigger efficiency. Table 7.14 summarizes this systematic uncertainty for all signal samples. It varies between less than 1 and 24%.

7.4.2 Cut variations

All the variables the selection (discussed in Section 7.1.1) is based on have intrinsic uncertainties. All these variables are varied within the range of their uncertainties and the influence on the result is assessed as the systematic uncertainty due to this cut. The transverse momentum p_{T} has been varied by ±3%, a value arising from the track resolution [71]. The pile-up dependence of the TRT High Threshold fraction f^{HT} (shown in Figure C.1 in Appendix C.2) motivates a variation of this variable by ±20%. The observed agreement of the mean and width of the distributions between data and simulation in the $Z \to \mu\mu$ control samples motivates a variation of S(Pixel dE/dx) and S(TRT dE/dx) by ±5%. The lower variation of S(MDT dE/dx) follows equivalently. The distribution of S(MDT dE/dx) shows a relative shift of the simulation with respect to the data distribution, which suggests a variation by +50% in the positive direction. While this large discrepancy in the positive direction is potentially problematic for a signal interpretation, it only plays a minor role for the limit setting procedure. Table 7.15 summarizes these variables and their variations. For all other cut variables, variations within their uncertainties have no observable effect on the analysis. The relative uncertainties arising from the cut variations are summarized in Table C.3 in Appendix C.2. From the numbers shown there the quadratic sum for

Table 7.16: *The quadratic sums of the uncertainties from the cut variations in the single signal samples. For these numbers a variation of p_T by ±3%, $S(\textit{Pixel } dE/dx)$ by ±5%, $S(\textit{TRT } dE/dx)$ by ±5% and $S(\textit{MDT } dE/dx)$ by −5% and +50% have been taken into account.*

Mass [GeV]	Uncertainty from upward fluctuation [%]				
	$\lvert q\rvert = 2e$	$\lvert q\rvert = 3e$	$\lvert q\rvert = 4e$	$\lvert q\rvert = 5e$	$\lvert q\rvert = 6e$
50	1.54	2.18	0.51	0.00	0.00
100	1.66	1.44	0.54	0.00	0.00
200	0.91	1.56	0.15	0.53	0.00
300	0.95	0.91	0.19	0.00	0.00
400	0.61	0.84	0.29	0.00	0.49
500	0.98	0.66	0.30	0.15	0.00
600	0.73	0.80	0.13	0.00	0.35

(a) Upward fluctuation

Mass [GeV]	Uncertainty from downward fluctuation [%]				
	$\lvert q\rvert = 2e$	$\lvert q\rvert = 3e$	$\lvert q\rvert = 4e$	$\lvert q\rvert = 5e$	$\lvert q\rvert = 6e$
50	-0.92	-0.64	-0.30	-0.70	-0.00
100	-0.86	-0.63	-0.00	-0.00	-0.00
200	-0.88	-0.23	-0.25	-0.00	-0.00
300	-0.63	-0.48	-0.09	-0.19	-0.00
400	-0.59	-0.28	-0.16	-0.33	-0.49
500	-0.26	-0.17	-0.09	-0.28	-0.49
600	-0.45	-0.44	-0.18	-0.53	-1.19

(b) Downward fluctuation

Table 7.17: *The systematic uncertainty due to limited Monte Carlo statistics as derived from the Poisson error of the efficiency.*

Mass [GeV]	Uncertainty from Monte Carlo statistics [%]				
	$\vert q\vert = 2e$	$\vert q\vert = 3e$	$\vert q\vert = 4e$	$\vert q\vert = 5e$	$\vert q\vert = 6e$
50	1.40	1.55	3.00	8.34	18.25
100	2.19	2.84	4.59	10.62	27.78
200	1.73	2.10	3.13	5.22	10.25
300	1.72	2.01	2.76	4.34	7.95
400	1.89	2.14	2.81	4.05	6.96
500	2.02	2.22	2.89	4.03	6.24
600	2.33	2.53	3.16	4.55	6.79

the upward and downward fluctuations of the result are calculated. These systematic uncertainties are shown in Table 7.16.

7.4.3 Monte Carlo statistics

Only a limited number (usually 10 000) of simulated events is available for each signal point. As a consequence of the small signal efficiencies listed in Table 7.12, only a small fraction of events survives the selection cuts. This leads to a systematic error due to a limited number of Monte Carlo events, deduced from the Poisson error of these efficiencies. This systematic uncertainty, the ratio of uncertainty and value, is summarized in Table 7.17. Note that the datasets for signal particles of mass 50 GeV are produced with an event filter applied. As a result, the overall trend of higher systematic uncertainties towards the lower masses does not apply for these samples. An overall larger uncertainty for samples with higher charges can be observed as well.

7.4.4 Correlation of variables

In order to assess a systematic uncertainty on the data driven background estimate, the prediction procedure is repeated for modified regions A', B' and C'. They are defined as subregions of A*, B* and C*, where bands at the region boundaries are blinded. These bands are shown as the red shaded area in Figures 7.14a and 7.14b. This cross-check is performed on data in the plane of $S(\text{TRT } \mathrm{d}E/\mathrm{d}x)$ and $S(\text{MDT } \mathrm{d}E/\mathrm{d}x)$ before the tight selection (cuts on $S(\text{Pixel } \mathrm{d}E/\mathrm{d}x)$ or f^{HT} for $|q| = 2e$ and $|q| > 2e$, respectively) to ensure sufficient statistics. If $S(\text{TRT } \mathrm{d}E/\mathrm{d}x)$ and $S(\text{MDT } \mathrm{d}E/\mathrm{d}x)$ are indeed uncorrelated variables, the number of estimated candidates in region D* from regions A', B' and C' should not deviate from the estimate made from regions A*, B* and C* (Equation (7.21)).

$$D' = \frac{B'C'}{A'} \approx D^* = \frac{B^*C^*}{A^*} \tag{7.21}$$

The lower two plots of Figure 7.14 show the relative deviation of D* from D'. The axis of Figures 7.14c and 7.14d represent the boundaries of the blinded bands. For areas with sufficient statistics, the deviations remain within ±5% in both cases. Therefore, the assumed systematic uncertainty on the data-driven background estimate is 5%.

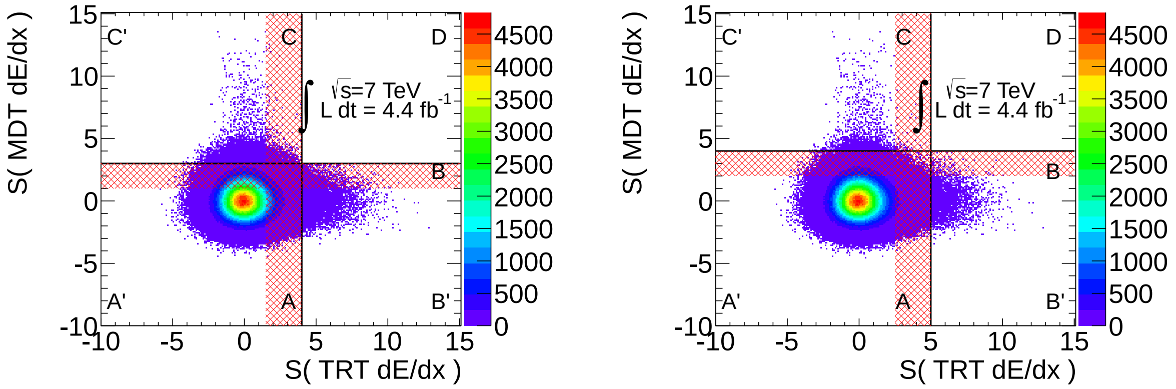

(a) $|q| = 2e$ (b) $|q| = 3e$

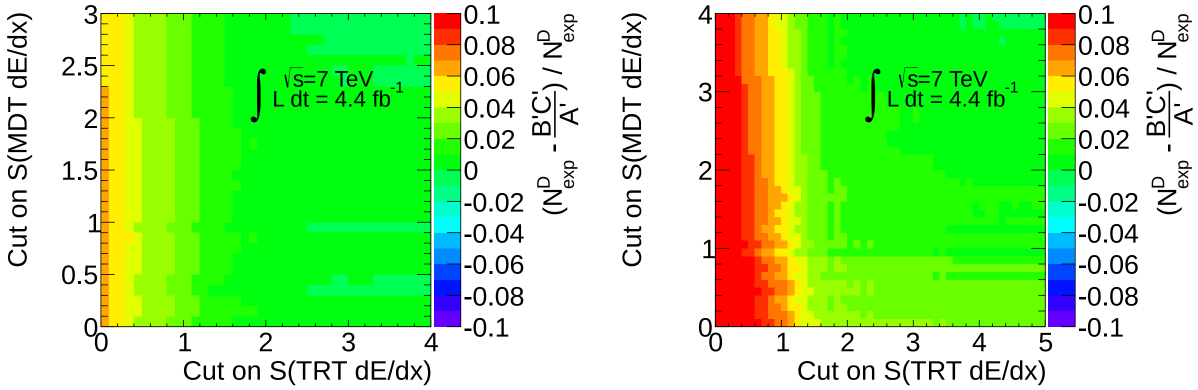

(c) $|q| = 2e$ (d) $|q| = 3e$

Figure 7.14: *Estimation of the uncertainty on the data driven background estimate. The upper plots (a) and (b) show the original A, B, C, D regions together with an exemplary masked band at the region boundaries marking regions A', B', C' and D'. The lower plots (c) and (d) give the relative deviation from the background estimate B'C'/D' to BC/A as a function of the cuts on* $S(TRT\ dE/dx)$*and* $S(MDT\ dE/dx)$*defining A', B', C' and D'.*

Table 7.18: *The quadratic sum of systematic uncertainties on the signal efficiency, i.e. the trigger efficiency, the cut variations, the uncertainties due to the limited Monte Carlo statistics.*

Mass [GeV]	Quadratic sum of systematic uncertainties [%]				
	$\lvert q\rvert = 2e$	$\lvert q\rvert = 3e$	$\lvert q\rvert = 4e$	$\lvert q\rvert = 5e$	$\lvert q\rvert = 6e$
50	±6.31	±3.63	±3.21	±8.40	±18.28
100	±8.10	±7.22	±5.26	±10.69	±27.80
200	±11.75	±11.02	±8.46	±6.95	±10.40
300	±13.15	±13.74	±13.99	±10.58	±9.79
400	±16.44	±16.05	±16.95	±17.56	±12.42
500	±17.66	±17.49	±18.19	±20.28	±16.74
600	±21.81	±21.65	±22.19	±24.59	±23.42

7.4.5 Luminosity

In addition to the systematic uncertainties on the Monte Carlo efficiency, the determination of the underlying luminosity can be determined from Van der Meer scans [96, 97] to be 3.9%. Applied to the integrated luminosity of 4.4 fb^{-1} used in this analysis, this yields an uncertainty of 0.2 fb^{-1}.

7.4.6 Summary

The overall systematic uncertainty on the signal efficiencies is determined from the quadratic sum of the uncertainties on the trigger efficiency, due to the applied cuts and the limited Monte Carlo statistics mentioned above. It ranges from 3.2% up to 27.8% and is documented for each signal point in Table 7.18. The uncertainty of the background prediction is given by the statistical error of the ABCD method and the 5% systematic uncertainty derived above. An uncertainty of 3.9% is applied to the integrated luminosity.

Table 7.19: *The signal efficiencies together with the corresponding systematic uncertainty.*

Mass [GeV]	Signal efficiencies with systematic uncertainties [%]				
	$\lvert q\rvert = 2e$	$\lvert q\rvert = 3e$	$\lvert q\rvert = 4e$	$\lvert q\rvert = 5e$	$\lvert q\rvert = 6e$
50	8.63 ± 0.54	3.90 ± 0.14	0.66 ± 0.02	0.053 ± 0.004	0.007 ± 0.001
100	17.22 ± 1.40	11.05 ± 0.80	4.53 ± 0.24	0.88 ± 0.09	0.13 ± 0.04
200	25.13 ± 2.95	18.47 ± 2.04	9.28 ± 0.79	3.54 ± 0.25	0.94 ± 0.10
300	25.27 ± 3.32	19.87 ± 2.73	11.60 ± 1.62	5.04 ± 0.53	1.56 ± 0.15
400	21.83 ± 3.59	17.97 ± 2.88	11.24 ± 1.91	5.74 ± 1.01	2.02 ± 0.25
500	19.76 ± 3.49	16.91 ± 2.96	10.68 ± 1.94	5.80 ± 1.18	2.50 ± 0.42
600	15.61 ± 3.40	13.52 ± 2.93	9.11 ± 2.02	4.60 ± 1.13	2.13 ± 0.50

7.5 Search results

Altogether, the background prediction in the search for $|q| = 2e$ particles is

$$N_{\mathrm{D}}^{\mathrm{bkg.}} = 0.41 \pm 0.08\,(\mathrm{stat.}) \ \pm 0.02\,(\mathrm{sys.})$$

and in the search for particles with charges above 2e

$$N_{\mathrm{D}}^{\mathrm{bkg.}} = 1.37 \pm 0.46\,(\mathrm{stat.}) \ \pm 0.07\,(\mathrm{sys.})\,.$$

This compares to signal selection efficiencies determined from simulation given for each signal mass and charge together with their corresponding systematic uncertainty in Table 7.19. The integrated luminosity is taken into account as

$$\mathcal{L} = \int L\mathrm{d}t = (4.4 \pm 0.2)\ \mathrm{fb}^{-1}\,.$$

Up to this stage, the signal region D is kept blinded in data. This is a common approach in particle physics searches to avoid biases in the interpretation of results due to cuts optimized to yield the best exclusion limits. After all the analysis parameters are determined, the number of observed candidates in the signal regions is measured in data. In both searches, zero candidate tracks are observed in the signal region D. Therefore, 95% confidence level upper cross section limits can be derived. They are presented in the next Chapter 8.

CHAPTER 8

Interpretation of search results

As discussed in Section 7.5, both signal regions contain zero candidates. Hence, no deviations from Standard Model predictions are observed and 95% confidence level upper cross section limits for the simplified Drell-Yan model are set with the CL_s method. The software package MCLimit, originally developed by Thomas Junk in the CDF collaboration [98] is a convenient tool to set limits and will be described in the following Section 8.1. The 95% confidence level upper cross section limits are derived in Section 8.2 and transformed into mass exclusion ranges of multi-charged particles produced via the Drell-Yan process with photon exchange in Section 8.3. Under certain assumptions summarized in Section 6.1, the cross section limits can also be used to set limits on particles predicted in almost commutative geometry and minimal walking technicolor. These special cases are discussed in Section 8.4 and 8.5, respectively.

8.1 The CL_s method of limit setting

The measured data is compared to predictions of a model including new physics and to a model which does not (Null hypothesis). The result should indicate which of the two can be excluded at which confidence level [99]. Assuming Poissonian statistics, the probability, p, of observing N_{obs} or more candidates while expecting b background candidates is

$$p = \sum_{n=N_{\mathrm{obs}}}^{\infty} = \frac{e^{-b}b^{n}}{n!}\,. \tag{8.1}$$

With this, one can define a test statistics as

$$X(N_{\mathrm{obs}}) = \frac{e^{-(s+b)}(s+b)^{N_{\mathrm{obs}}}}{N_{\mathrm{obs}}!} / \frac{e^{-b}b^{N_{\mathrm{obs}}}}{N_{\mathrm{obs}}!} \tag{8.2}$$

the ratio of the signal and background hypothesis ($s+b$) to the background only hypothesis (b). Here s stands for the number of expected signal candidates and b represents the number of expected background candidates. In this analysis, 0.41 (1.37) background tracks in the $|q| = 2e$ ($|q| > 2e$) search are expected. Together with the observed number of candidates ($N_{\mathrm{obs}} = s + b = 0$ in our case), these are the only numbers known from experiment. In the case of zero candidates, the test statistic reduces to

$$X_{\text{obs}} = X(N_{\text{obs}} = 0) = \frac{e^{-(s+b)}}{e^{-b}}\,. \tag{8.3}$$

The aim is to set a limit on the true number of signal candidates, s_{true}, by inverting Equation (8.1). From this, the number of signal candidates that could have been included in the observed number of candidates N_{obs} under the given expectations for the background b and signal s is determined. This is achieved by finding the maximal s for which the sum of p-values of $N_{\text{obs}}^{\text{test}}$ (where $X_{\text{obs}}(N_{\text{obs}}^{\text{test}}) < X_{\text{obs}}$) fulfills Equation (8.4),

$$\text{CL}_{s+b} = 1 - \alpha = P_{s+b}(X \leq X_{\text{obs}}) = \sum_{X(\{N_{\text{obs}}^{\text{test}}\}) \leq X(\{N_{\text{obs}}\})} \frac{e^{-(s+b)}(s+b)^{N_{\text{obs}}^{\text{test}}}}{N_{\text{obs}}^{\text{test}}!}, \tag{8.4}$$

for a fixed value of α [98]. Usually α is set to 5% and the obtained s_{true} represents the upper 95% confidence level limit on the number of observed signal candidates. A setback of this method arises if downward fluctuations (as is the case in this analysis) are observed. In this case, maximizing s in CL_{s+b} yields limits that are too strong. A solution to this problem is to normalize the confidence level by the confidence level of the background only hypothesis CL_b

$$\text{CL}_b = P_b(X \leq X_{\text{obs}}) = \sum_{X(\{N_{\text{obs}}^{\text{test}}\}) \leq X(\{N_{\text{obs}}\})} \frac{e^{-b} b^{N_{\text{obs}}^{\text{test}}}}{N_{\text{obs}}^{\text{test}}!}\,. \tag{8.5}$$

The resulting CL_s from Equation (8.6) is evaluated for the maximal s to hold the equation for $\alpha = 5\%$. This is realized with the help of toy Monte Carlo, pseudo-experiments, which select a representative outcome of the experiment and compare their test statistics with N_{obs}.

$$\text{CL}_s = \frac{\text{CL}_{s+b}}{\text{CL}_b} = 1 - \alpha \tag{8.6}$$

Systematic uncertainties are incorporated into this limit setting procedure by adding random numbers from Gaussian distributions to s and b. The widths of these distributions are given by the systematic uncertainties of the signal and background expectations.

$$\text{CL}_s \equiv 1 - \alpha = \frac{\text{CL}_{s+b}^{s,b\ \text{smeared}}}{\text{CL}_b^{b\ \text{smeared}}} \tag{8.7}$$

8.2 Cross section exclusion limits

To derive cross section limits 100 000 pseudo-experiments are performed taking into account the number of expected background tracks in the signal region derived in a data-driven method, the selection efficiencies and their uncertainties gained from simulation, the luminosity of the analyzed data and its uncertainty and the zero observed tracks in the signal region. The 95% confidence level upper cross section limits are on the order of 10^{-2} to 10^{-3}pb listed in Table 8.1. A comparison with the simplified Drell-Yan model used in the production of the simulated samples can be found in Figure 8.1. In this figure, the dashed line represents the expected limit, that is the cross section limit found under the assumption that no signal exists. The solid line takes the possibility of a signal into account and the

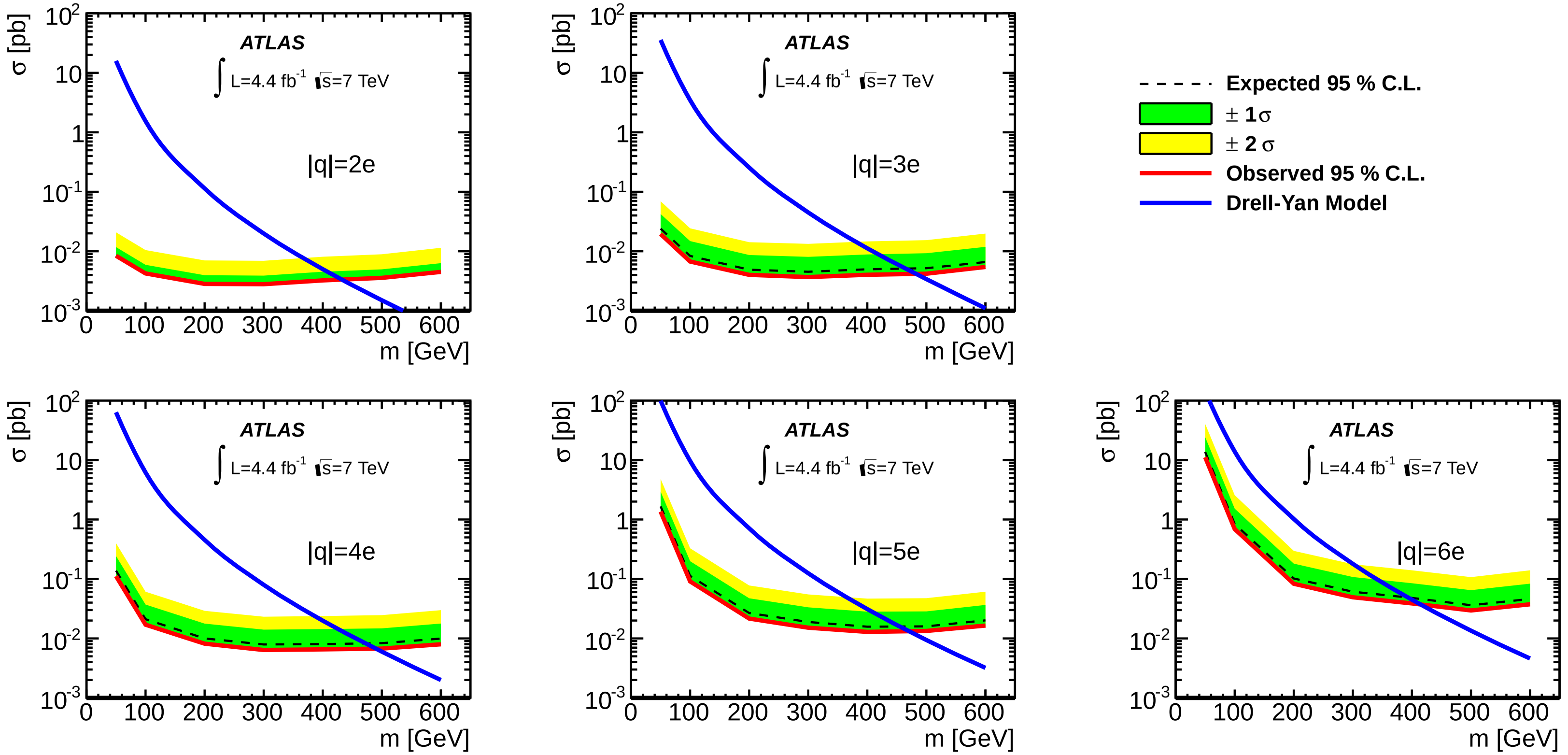

Figure 8.1: *95% CL limits on the production cross section of multi-charged highly-ionizing particles from pair-production. The black dotted line shows the expected limit and the* $\pm 1\sigma$*(green) and* $\pm 2\sigma$*(yellow) uncertainty bands. The observed limit (red) is compared with the predicted cross section from the Drell-Yan model. The plots are shown separately for charges* $|q| = 2e$ *to* $|q| = 6e$ *[8].*

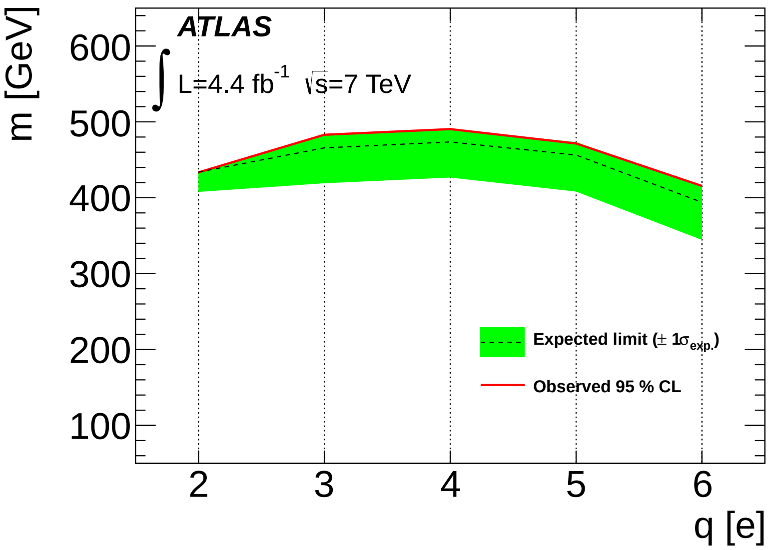

Figure 8.2: *The lower limits on the mass of multi-charged particles in the simplified Drell-Yan model as a function of the absolute charge [8].*

shaded areas indicate the $\pm 2\sigma$ and $\pm 1\sigma$ error bands. This measurement represents the first published LHC result on the production cross sections of stable massive particles carrying electric charges in the range of $|q| = 2 - 5e$ [8]. Moreover, these limits extend the limit on the production cross sections of particles with $|q| = 6e$ set previously by ATLAS [10] by two orders of magnitude.

8.3 Interpretation as mass exclusion limits of Drell-Yan produced particles

From the crossing points of the Drell-Yan prediction and the observed cross section limits in Figure 8.1, mass exclusion limits for the underlying Drell-Yan model can be derived. For each mass point for which the cross section prediction of the Drell-Yan model is higher than the observed cross section limit, the model can be excluded. These lower limits on the mass of multi-charged particles produced in the simplified Drell-Yan pair production without Z-exchange are listed in Table 8.2. Additionally, Figure 8.2 gives a graphic illustration of these derived mass limits for the single charges. Drell-Yan pair production without Z-exchange can be excluded from mass 50 GeV to 433, 483, 490, 471 and 416 GeV for charges $|q| = 2e$, $3e$, $4e$, $5e$ and $6e$, respectively.

8.4 Interpretation in the context of almost commutative geometry

Under the assumptions on the AC model listed in Section 6.1, the obtained cross section limits can be applied to the A and C leptons predicted in the almost commutative geometry model. These assumptions include a mass difference between A and C and no further production process other than Drell-Yan pair production. Further, the limits can only be applied if the kinematic distributions of the AC leptons are similar to the distributions predicted in the simplified Drell-Yan model used in the Monte Carlo production.

Given all these assumptions, Figure 8.3 compares the measured cross section limits derived in the

Table 8.1: *The observed and expected limits on the cross section measurements for all signal points. Shown is also the cross section of the Drell-Yan model, which was used in the Monte Carlo production of the signal samples.*

Mass [GeV]	$\lvert q\rvert = 2e$		
	σ_{obs} [pb]	σ_{exp} [pb]	σ_{DY} [pb]
50	0.0084	$0.0084^{+0.0033}_{-0.0000}$	15.9100
100	0.0042	$0.0043^{+0.0017}_{-0.0000}$	1.5440
200	0.0028	$0.0028^{+0.0011}_{0.0000}$	0.1140
300	0.0028	$0.0028^{+0.0011}_{-0.0000}$	0.0199
400	0.0032	$0.0032^{+0.0013}_{0.0000}$	0.0050
500	0.0036	$0.0035^{+0.0014}_{-0.0000}$	0.0015
600	0.0045	$0.0045^{+0.0018}_{-0.0000}$	0.0005

(a) $|q| = 2e$

Mass [GeV]	$\lvert q\rvert = 3e$		
	σ_{obs} [pb]	σ_{exp} [pb]	σ_{DY} [pb]
50	0.0195	$0.0240^{+0.0183}_{-0.0045}$	35.7900
100	0.0067	$0.0083^{+0.0065}_{-0.0015}$	3.4730
200	0.0040	$0.0049^{+0.0037}_{-0.0009}$	0.2556
300	0.0037	$0.0045^{+0.0035}_{-0.0009}$	0.0449
400	0.0040	$0.0050^{+0.0039}_{-0.0009}$	0.0112
500	0.0042	$0.0052^{+0.0041}_{-0.0010}$	0.0034
600	0.0054	$0.0066^{+0.0053}_{-0.0012}$	0.0011

(b) $|q| = 3e$

Mass [GeV]	$\lvert q\rvert = 4e$		
	σ_{obs} [pb]	σ_{exp} [pb]	σ_{DY} [pb]
50	0.1115	$0.1381^{+0.1051}_{-0.0255}$	63.6300
100	0.0170	$0.0211^{+0.0161}_{-0.0039}$	6.1710
200	0.0082	$0.0100^{+0.0078}_{-0.0018}$	0.4545
300	0.0064	$0.0079^{+0.0061}_{-0.0014}$	0.0798
400	0.0065	$0.0080^{+0.0063}_{-0.0014}$	0.0199
500	0.0067	$0.0083^{+0.0064}_{-0.0016}$	0.0060
600	0.0080	$0.0099^{+0.0079}_{-0.0018}$	0.0020

(c) $|q| = 4e$

Mass [GeV]	$\lvert q\rvert = 5e$		
	σ_{obs} [pb]	σ_{exp} [pb]	σ_{DY} [pb]
50	1.3596	$1.6625^{+1.2847}_{-0.3124}$	99.4200
100	0.0909	$0.1124^{+0.0864}_{-0.0215}$	9.6370
200	0.0216	$0.0267^{+0.0206}_{-0.0052}$	0.7101
300	0.0151	$0.0189^{+0.0144}_{-0.0034}$	0.1246
400	0.0129	$0.0158^{+0.0124}_{-0.0029}$	0.0311
500	0.0134	$0.0159^{+0.0125}_{-0.0030}$	0.0094
600	0.0165	$0.0201^{+0.0164}_{-0.0041}$	0.0032

(d) $|q| = 5e$

Mass [GeV]	$\lvert q\rvert = 6e$		
	σ_{obs} [pb]	σ_{exp} [pb]	σ_{DY} [pb]
50	11.1533	$13.6754^{+10.6493}_{-2.4774}$	143.1610
100	0.6898	$0.8392^{+0.6837}_{-0.1504}$	13.8915
200	0.0831	$0.1019^{+0.0791}_{-0.0189}$	1.0225
300	0.0492	$0.0610^{+0.0469}_{-0.0113}$	0.1795
400	0.0388	$0.0480^{+0.0368}_{-0.0092}$	0.0448
500	0.0295	$0.0362^{+0.0286}_{-0.0064}$	0.0135
600	0.0375	$0.0461^{+0.0373}_{-0.0084}$	0.0046

(e) $|q| = 6e$

Table 8.2: *Expected and observed 95 % CL for the exclusion limit of the mass of multi-charged highly-ionizing particles for charges of* $|q| = 2e$ *to* $|q| = 6e$.

$\lvert q\rvert$ [e]	Expected ($\pm 1\sigma$) mass limit [GeV]	Observed mass limit [GeV]
2	434^{+0}_{-26}	433
3	466^{+17}_{-47}	483
4	474^{+17}_{-47}	490
5	456^{+17}_{-48}	471
6	394^{+21}_{-50}	416

Table 8.3: *Expected and observed 95 % CL for the exclusion limit of the mass of multi-charged highly-ionizing particles in the context of almost commutative geometry for charges of* $|q| = 2e$ *to* $|q| = 6e$.

$\lvert q\rvert$ [e]	Expected ($\pm 1\sigma$) mass limit [GeV]	Observed mass limit [GeV]
2	431^{+0}_{-27}	431
3	463^{+17}_{-47}	481
4	472^{+17}_{-47}	489
5	454^{+17}_{-49}	470
6	391^{+21}_{-50}	412

previous Section 8.2 to the production cross sections of the AC leptons. From the crossing points 95% confidence level lower mass limits for A or C leptons can be derived. Accordingly, AC leptons of charge $|q| = 2e$ need to be heavier than 431 GeV and particles with charge $|q| = 3$, 4, 5 and $6e$ heavier than 481 GeV, 489 GeV, 470 GeV and 412 GeV, respectively, as can be derived from Table 8.3. Within the uncertainties of the measurements, these mass limits are compatible with the limits derived in the Drell-Yan model.

8.5 Interpretation in the context of minimal walking technicolor

Following similar arguments, the cross section limits can also be interpreted in the context of the minimal walking technicolor model as shown in Figure 8.4. In this case the requirements are even more strict as this model predicts additional particles and production processes which are ignored in the cross section predictions because they depend on model parameters. Hence, the mass exclusion limits derived in Table 8.4, 429, 476, 484, 465 and 407 GeV for particles with charge $|q| = 2e$, $3e$, $4e$, $5e$ and $6e$, respectively, are only applicable in very special cases of the minimal walking technicolor model for the techni-leptons ζ. Within the uncertainties, the mass limits derived for particles predicted in the minimal walking technicolor models are compatible with the limits derived in the Drell-Yan model.

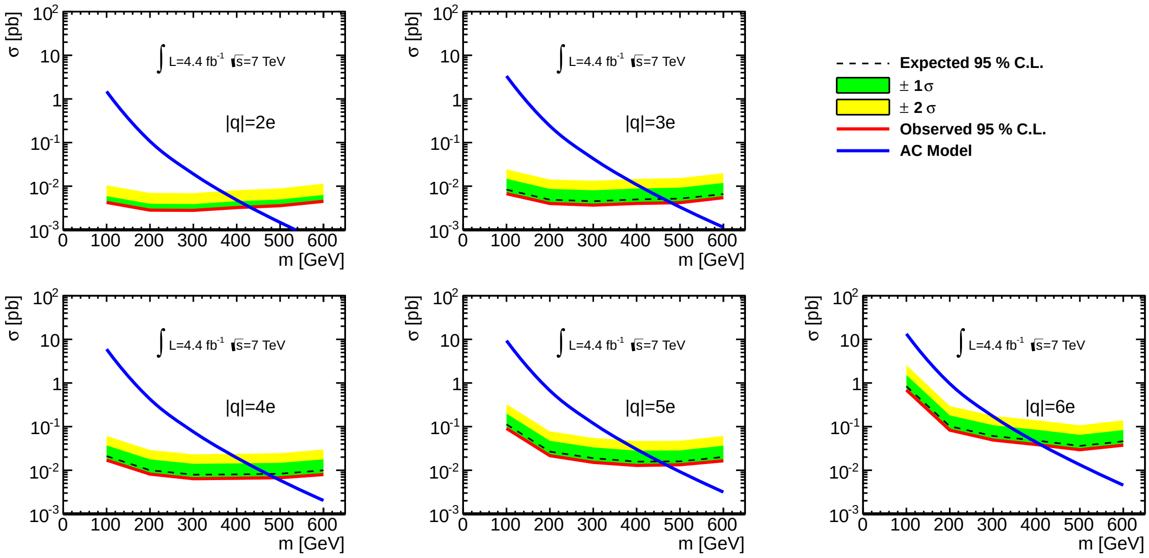

Figure 8.3: *95% CL limits on the production cross section of multi-charged highly-ionizing particles. The black dotted line shows the expected limit and the* $\pm 1\sigma$*(green) and* $\pm 2\sigma$*(yellow) uncertainty bands. The observed limit (red) is compared with the predicted cross section from the almost commutative (AC) model. The plots are shown separately for charges* $|q| = 2e$ *to* $|q| = 6e$.

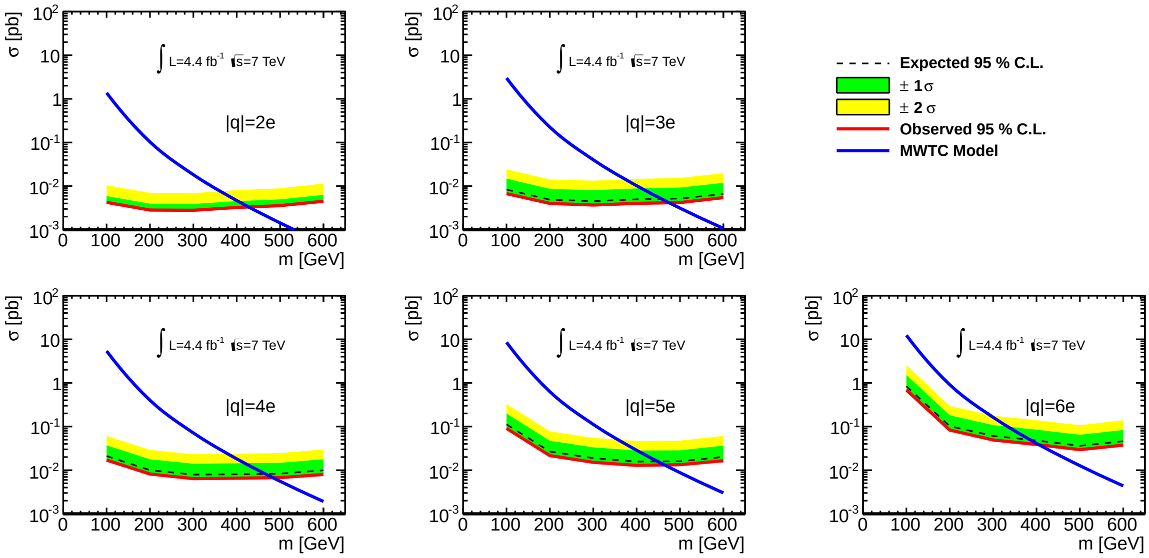

Figure 8.4: *95% CL limits on the production cross section of multi-charged highly-ionizing particles. The black dotted line shows the expected limit and the* $\pm 1\sigma$*(green) and* $\pm 2\sigma$*(yellow) uncertainty bands. The observed limit (red) is compared with the predicted cross section from the minimal walking technicolor (MWTC) model. The plots are shown separately for charges* $|q| = 2e$ *to* $|q| = 6e$.

Table 8.4: *Expected and observed 95 % CL for the exclusion limit of the mass of multi-charged highly-ionizing particles in the context of the minimal walking technicolor model for charges of* $|q| = 2e$ *to* $|q| = 6e$.

$\lvert q\rvert$ [e]	Expected ($\pm 1\sigma$) mass limit [GeV]	Observed mass limit [GeV]
2e	429^{+0}_{-27}	429
3e	459^{+17}_{-47}	476
4e	467^{+17}_{-48}	484
5e	450^{+17}_{-49}	465
6e	386^{+20}_{-50}	407

CHAPTER 9

Summary

A search for stable massive particles carrying electric charges in the range of $|q| = 2e$ to $6e$ has been performed with the ATLAS detector at the LHC. A data set of 4.4 fb^{-1} integrated luminosity of pp collisions recorded in 2011 has been analyzed. Theoretical justification for such particles can be found in minimal walking technicolor and almost commutative geometry models, even though the original motivation of this analysis arose from an unexploited search regime of particles with electric charges of $|q| = 2$ to $5e$.

The search exploits the highly ionizing behavior of such hypothetical particles via estimators for the specific energy loss per path length, $\mathrm{d}E/\mathrm{d}x$, from several ATLAS subdetectors. A factor of q^2 enhances the energy loss significantly. Additionally, following Bethe-Bloch, for a given momentum heavy particles are shifted to lower values of $\beta\gamma = p/m$ locating them in the highly ionizing regime of the Bethe-Bloch curve.

Multiple variables for particle identification available at ATLAS are introduced, including the newly developed TRT $\mathrm{d}E/\mathrm{d}x$. Studies of its separation power between different standard model particles are presented as well as the application of this variable to multi-charged particles. The search is performed by requiring high ionization losses in two to three ATLAS sub detectors including the MDT in the muon system. Based on the assumption of stable particles, where stable means at least within the dimensions of ATLAS, multi-charged particles are expected to reach the muon system and are searched among reconstructed muon objects. No highly ionizing particles are found and cross section exclusion limits on the order of 0.001 - 0.01 pb for $|q| = 2e$ - $5e$ and of 0.01 - 10 pb for $|q| = 6e$, summarized in Figure 9.1, can be set. Predictions of the simplified Drell-Yan model are shown in the same figure. These particles can be excluded in the mass range of 50 GeV to 433, 483, 490, 471 and 416 GeV for charges $|q| = 2, 3, 4, 5$ and $6e$ [8]. Additionally, the cross section limits are compared to predictions of minimal walking technicolor and almost commutative geometry models under certain constraints. The derived mass exclusions for these models are comparable in size to the limits obtained from the simplified Drell-Yan model.

This result presents the first measurement of ATLAS for charges $|q| = 2e$ to $5e$. The upper cross section limit of particles with $|q| = 6e$ is improved by two orders of magnitude compared to a previous ATLAS limit [10]. Recent, yet unpublished, measurements from CMS on the 2012 data set exclude particles with charges $|q| = 2$ to $5e$ below 725, 792, 816 and 817 GeV from a simplified Drell-Yan model including Z-exchange [23]. The deduced cross section limit in this dissertation of particles with $|q| = 6e$ is the most stringent limit to date.

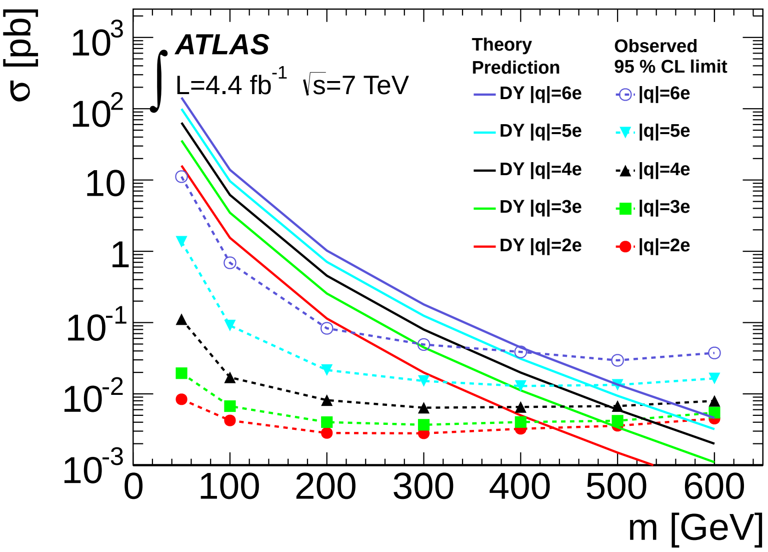

Figure 9.1: *Comparison of the cross sections predicted by the simplified Drell-Yan production of multi-charged particles (solid lines) and the observed 95% confidence level exclusion limit (dashed lines) for all charges as a function of mass [8].*

A repetition of this analysis with ATLAS data recorded in 2012 could significantly improve the obtained limits and is currently investigated. In this analysis, signal samples with higher masses will have to be considered due to the already excluded range of particle masses from this dissertation. Consequently, the muon trigger will be less efficient and a calorimeter trigger could be added to the selection. Furthermore, the selection could be improved using variables of $\mathrm{d}E/\mathrm{d}x$ and time of flight reconstructed from the calorimeters. Another significant improvement is to be expected from the integration of TRT $\mathrm{d}E/\mathrm{d}x$ and MDT $\mathrm{d}E/\mathrm{d}x$ in the standard ATLAS reconstruction. This would allow the use of standard ATLAS data formats without any additional selection cuts on the data.

Appendix

APPENDIX A

Review of previous searches at other experiments

Many searches for long-lived charged and heavy particles have been carried out at previous particle colliders and the LHC. This appendix summarizes the main results from ATLAS (Section A.1.1), another LHC experiment, CMS (Section A.1.2), and from previous colliders namely the Tevatron (Section A.2), HERA (Section A.3) and LEP (Section A.4).

A.1 LHC

Apart from ATLAS and CMS only the MoEDAL [46] collaboration aims to search for long-lived charged particles at the LHC. As the latter has not published any search results to date, the LHC review focuses on the summary of ATLAS (Section A.1.1) and CMS (Section A.1.2) results.

A.1.1 Previous searches at ATLAS

Previous to the analysis presented in this dissertation [8], ATLAS has released four publications on the subject of long-lived massive charged particles to date [9, 10, 19, 20]. The first ATLAS limit on particles with multiple charges was set by the search for highly ionizing particles published on 3.1 pb^{-1} of pp collisions at $\sqrt{s} = 7$ TeV recorded in 2010 [10]. Three mass points at $200, 500$ and 1000 GeV are considered with charges $|q| = 6$, 10 and $17e$ each. Further assumptions require a lifetime longer than 100 ns. Additionally, the considered masses are limited to values below 1000 GeV due to trigger timing constraints. In this mass and charge range couplings to photons are very strong and perturbative calculations are impossible [10]. Any charge above $|q| = 17e$ is not included in the search as the effects of delta electrons and electron recombination in the active detector become overwhelming [10]. The analysis searches for highly ionizing particles in an electron-like signature, that is a track in the inner detector and energy losses in the electromagnetic calorimeter. The search signature includes a track in the outermost inner tracking detector showing highly ionizing behavior and energy fractions in the electromagnetic calorimeter. No signal candidates are observed and cross section limits on the order of 3 - 12 pb are set.

The three additional analyses search for stable massive particles of charge $|q| = 1e$. Two further anal-

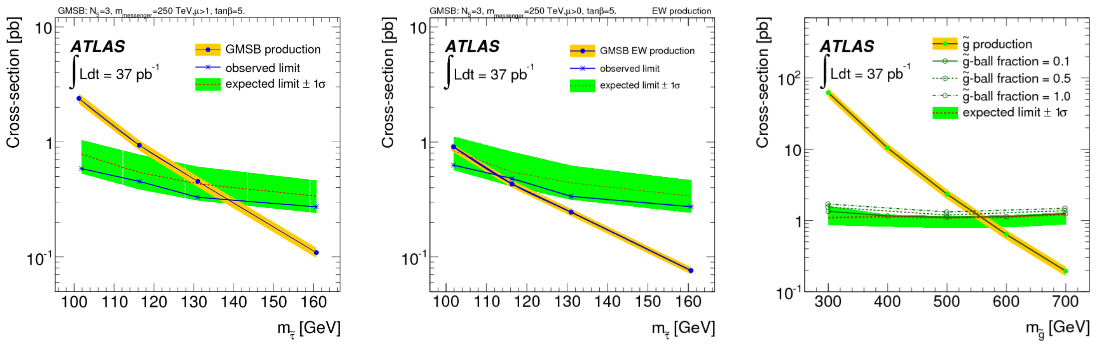

(a) GMSB (b) GMSB EW only (c) R-hadrons

Figure A.1: *The 95% confidence level upper cross section limits for the three scenarios tested by ATLAS in the search for heavy long-lived particles using 37 pb^{-1} of pp collisions recorded at $\sqrt{s} = 7$ TeV [19].*

yses are published on the 2010 dataset: The search for sleptons[1] and R-hadrons[2] based on 37 pb^{-1} [19] and for stable massive particles carrying color charge based on 34 pb^{-1} [20]. In the former analysis [19], the particles are assumed to reach the muon system, where the search for sleptons also requires a track in the inner detector, while R-hadrons are only identified in the muon system. A measure of the particles speed $\beta = v/c$ can be reconstructed from three independent measurements of the time of flight estimated in the muon system. The mass of the particle is determined from β and the momentum cuts are optimized differently for each signal point. Since no significant deviations from the predicted SM background could be found upper limits on the cross sections can be set (see Figure A.1). From this, a stable $\tilde{\tau}$ (electroweakly produced slepton) is excluded below a mass of 136 GeV (110 GeV), while R-hadrons are excluded below a mass of 544, 537, 530 GeV, for $f = 0.1,\ 0.5,\ 1.0$[3], respectively.

The second search from 2010, for hadronically interacting stable massive particles [20], makes no assumption of the particles reaching the muon system but starts from inner detector tracks. These have an extension in the muon system or are consistent with energy depositions in the hadronic calorimeter. The signal selection is mainly based on a dE/dx measurement in the innermost tracking detector and a β measurement from the hadronic calorimeter (derived from the time of flight of the particle). After loose signal selections consistent with slow and highly ionizing particles, the signal region is defined as a mass region derived from β and dE/dx. Again no deviations from SM backgrounds are observed and cross section upper limits together with 95% confidence level mass exclusions for supersymmetric particles such as sbottoms ($\tilde{b}$) at 294 GeV, stops ($\tilde{t}$) at 309 GeV and gluinos ($\tilde{g}$) at 562 GeV can be set (see Figure A.2a). At the time, these limits were the most stringent ones.

The most recent publication, is based on 4.7 fb^{-1} of data taken at the LHC in 2011 at $\sqrt{s} = 7$ TeV [9]. The analysis uses time of flight information from three ATLAS subdetectors in the calorimeter and the muon system to reconstruct a measure for the particle's speed β. Additionally, a dE/dx measurement from the innermost tracking detector is used to reconstruct $\beta\gamma$. After a common preselection, the search is split up and optimized separately for different benchmark models: A search for long-lived sleptons in the context of gauge-mediated supersymmetry breaking models with a light $\tilde{\tau}$ as long-lived particle (LLP), selects events with two muons. A cut on the mass derived from $\beta\gamma$ is required depending on the $\tilde{\tau}$ signal mass point. A second branch of the analysis considers R-hadrons as long-lived massive parti-

---

[1] Supersymmetric partners of leptons (i.e. electrons, muons and taus).

[2] Bound states of hadron-like multi-charged particles with SM quarks or gluons.

[3] f is the $\tilde{g}$-ball fraction, which affects the number of candidates interacting as charged particles in the Inner Detector [19]

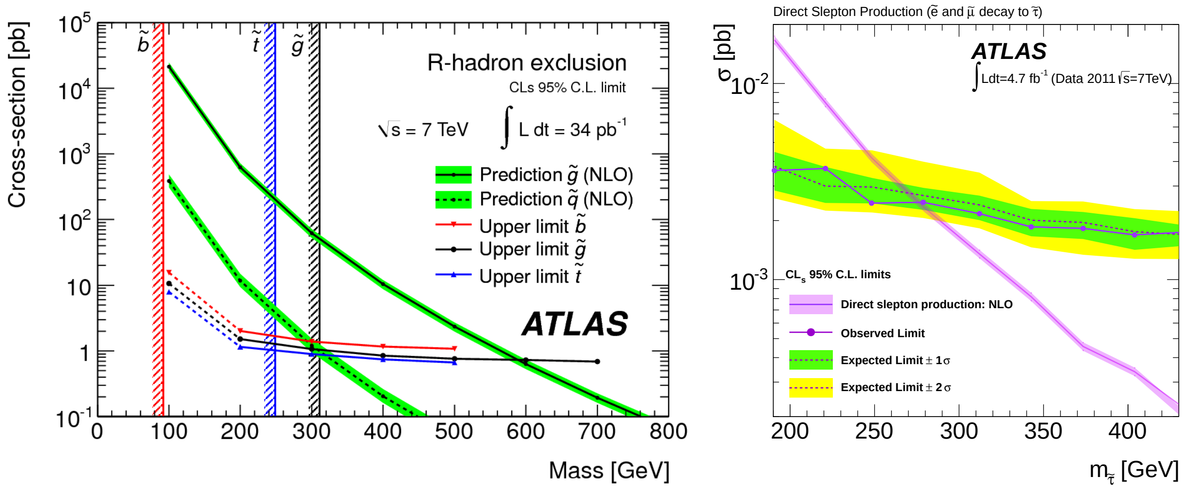

(a) ATLAS 2010 search

(b) ATLAS 2011 search

Figure A.2: *(a) The 95% confidence level upper cross section limits for the production of $\tilde{b}$, $\tilde{t}$ and $\tilde{g}$ as published by ATLAS [20]. The vertical lines indicate the previous limits from ALEPH ($\tilde{b}$), CDF ($\tilde{t}$) and CMS ($\tilde{g}$). (b) The cross section limit as a function of the mass of directly produced sleptons as set by the ATLAS collaboration. This result is based on $\sqrt{s}$ = 7 TeV pp-collisions recorded in 2011 [9].*

cles. Since they can change charge traversing the detector, this search is performed in three approaches assuming a charged particle (a) throughout the whole detector, (b) up to the calorimeter and (c) in the inner detector only. The first two paths called *full-detector* and *MS agnostic* search differ only in the determination of β, where the latter does not utilize measurements from the muon system. The signal region requirement is optimized for each signal point and varies as a function of the masses $m_{\beta\gamma}$ and m_β. In the third approach, the *ID-only* search, harsher cuts are applied to suppress the larger background. The signal selection is defined via a cut on the dE/dx alone. No excess of signal events is observed above the expected background estimated from data, consisting mostly of high p_T muons with mismeasured β. Thus, 95% C.L. upper limits on the production cross sections are set in all four searches, which can be translated into mass exclusion limits of a multitude of model hypotheses. The cross section of long-lived sleptons is limited to below $O(10^{-3}$ pb) imposing a lower limit on the mass of the $\tilde{\tau}$ of around 300 GeV as can be seen in Figure A.2b. For all limits in all search channels, the reader is referred to [9].

A.1.2 CMS

The CMS collaboration has already disseminated a number of searches for long-lived heavy charged particles on 3.1 pb^{-1} at $\sqrt{s}$ = 7 TeV [11] ($|q|$ = 1e), 5.0 fb^{-1} at $\sqrt{s}$ = 7 TeV of $|q|$ = 1e [21] and $2e \leq |q| \leq 5e$ [22]. Recently, results on the full 2011 and 2012 dataset at $\sqrt{s}$ = 7 TeV and $\sqrt{s}$ = 8 TeV of all charges have become available in one public note [23]. This summary will be based on the results presented there.

Various signal benchmark models are considered. In the gauge-mediated supersymmetry breaking (GMSB) model, the next-to-lightest supersymmetric particle (NLSP) can be long-lived, which is considered as a long-lived lepton-like stau ($\tilde{\tau}_1$) both in direct pair production and via decays of heavier supersymmetric particles. Furthermore, the analysis examines R-hadrons from gluinos ($\tilde{g}$) or stop ($\tilde{t}$) pair production. Lepton-like signal samples are generated via a modified Drell-Yan production (only γ or Z^0 exchange). In this case, charges of $|q|$ = 1/3, 2/3, 1, 2, 3, 4, 5e are simulated.

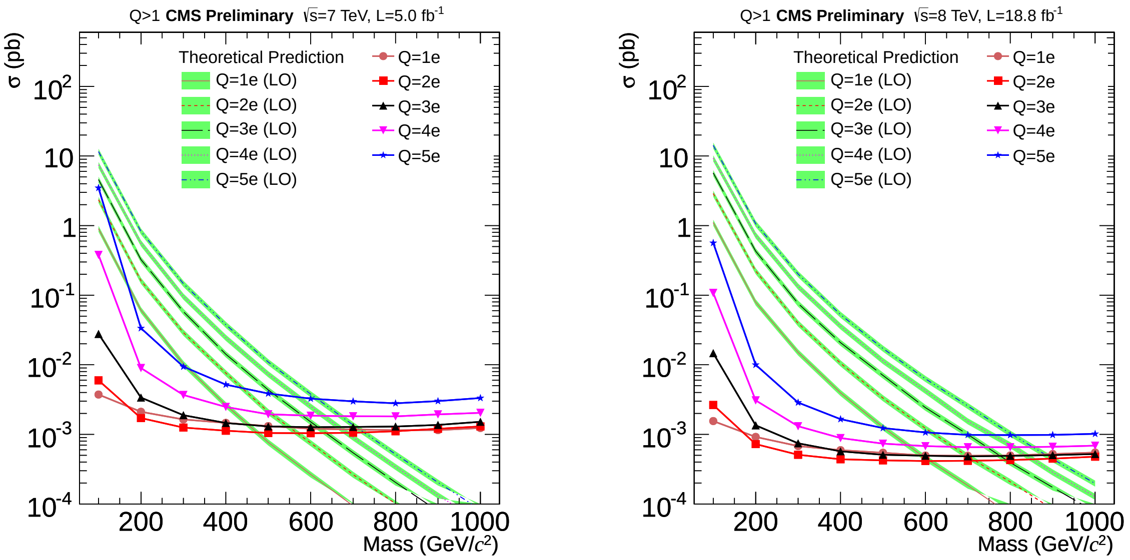

(a) 2011 data

(b) 2012 data

Figure A.3: *The 95% confidence level upper cross section limits derived by CMS in the search for multi-charged particles in data recorded in (a) 2011 and (b) 2012 [23].*

The discriminating variables in all searches are based on dE/dx and time-of-flight (TOF) at the muon system. The track's dE/dx is determined from the N single charge depositions in the silicon detector c_i via the harmonic function I_h

$$I_h = \left(\frac{1}{N}\sum_i c_i^2\right)^{1/2} . \tag{A.1}$$

Furthermore, two discriminators I_{as} and I'_{as} are defined which give the discrimination power of the SM particles from particles with higher or lower dE/dx. The mass of the particle for an assumed charge of $|q| = 1e$ is determined from

$$I_h = K\frac{m^2}{p^2} + C , \tag{A.2}$$

with the empirically determined parameters K and C and the momentum p. The inverse speed of the particles $1/\beta$ is measured via the time-of-flight of the particle to the muon system and is an additional discriminating variable in the searches presented here.

Starting from slightly different preselection, all three searches, singly charged particles, fractional charged particles and particles with multiple charges, use these three variables to discriminate SM background from new physics signals. In all three cases, the background is determined with the data-driven ABCD method. The final signal regions are chosen by selections based on a subset of I_{as}/I'_{as}, p_{T} and $1/\beta$ for all benchmark scenarios, which are optimized to yield the best discovery potential. No significant excesses are observed and upper cross section limits and mass exclusions are set. Figure A.3 shows the most relevant result for this thesis, the search for long-lived massive particles of charges $|q| = 1$ - $5e$. These are excluded in the Drell-Yan production below a mass of 608, 725, 792, 816 and 817 GeV for charges $|q| = 1, 2, 3, 4$ and $5e$ respectively. Further limits exclude gluino $\tilde{g}$ masses below 1322 or 1233 GeV and stop masses below 933 or 818 GeV depending on the chosen interaction model. $\tilde{\tau}_1$ masses are excluded below 435 GeV in the GMSB model and the fractionally charged particles are re-

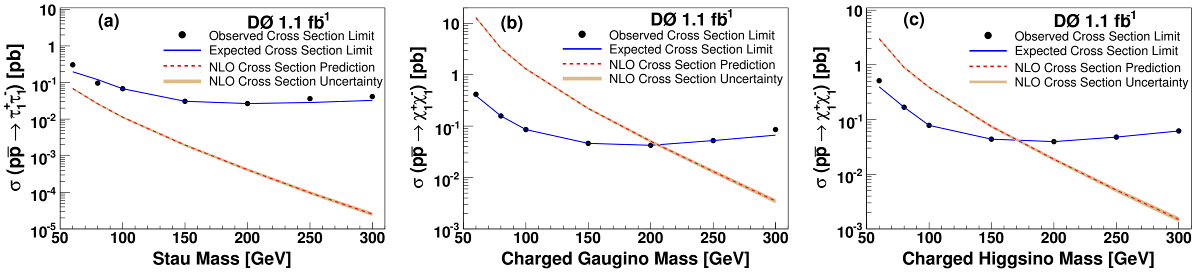

(a) Stau cross section limits (b) Gaugino cross section limits (c) Higgsino cross section limits

Figure A.4: *The expected and observed cross section limits by D0 for stau pair production (a), gaugino-like chargino pair production (b) and higgsino-like charginos (c) as a function of the respective masses [13]. The search was performed at the Tevatron on 1.1 fb^{-1} of $p\bar{p}$ collisions at a center of mass energy of 1.96 TeV.*

quired to have masses above 340 GeV ($|q| = 1/3e$) and 567 GeV ($|q| = 2/3e$) in the Drell-Yan production model. For further details, the reader is referred to the original note [23].

A.2 Tevatron

At the $p\bar{p}$-collider Tevatron at Fermilab, Chicago, USA both experiments CDF and D0 set limits on the production of charged massive stable particles called CHAMPs in CDF terminology or CMSP at D0 respectively.

A.2.1 D0

The D0-collaboration used SUSY[4] benchmark models to set limits on the pair production cross sections of gaugino-like and higgsino-like charginos [13]. In the search for long-lived particles in a dataset of 1.1 fb^{-1}, the collaboration uses time-of-flight (TOF) measurements to determine cross sections for the pair production of stable staus ($\tilde{\tau}$), gaugino-like and higgsino-like charginos. These are interpreted as lower mass limits of 206 (204) GeV in the gaugino-like scenario and 171 (169) GeV in the higgsino-like scenario, using the nominal (nominal - 1σ) values for the NLO cross section prediction. Since the sensitivity is insufficient to set limits on the stau, the cross section limit can be interpreted for any pair produced particle with similar kinematics. The upper cross section limits shown in Figure A.4 are in the range of 0.31 to 0.04 pb.

A.2.2 CDF

In a paper from September 2009 [12], the CDF collaboration sets a model-independent upper limit on the cross section for the production of a single, isolated, weakly interacting charged massive stable particle with mass above 100 GeV. The masses of the particles are determined from the measured time-of-flight (TOF) and the particle's momentum p (see Figure A.5a). The limit is set at a center of mass energy $\sqrt{s} = 1.96\,\text{TeV}$ in 1.0 fb^{-1} of data within the acceptance of $|\eta| < 0.7$, transverse momentum greater than 40 GeV and $\beta = v/c$ between 0.4 and 0.9. The cross section is determined to be smaller than 10 fb at 95% C.L. This result is interpreted in the context of an up-quark-like particle and yields a

---

[4] Supersymmetry

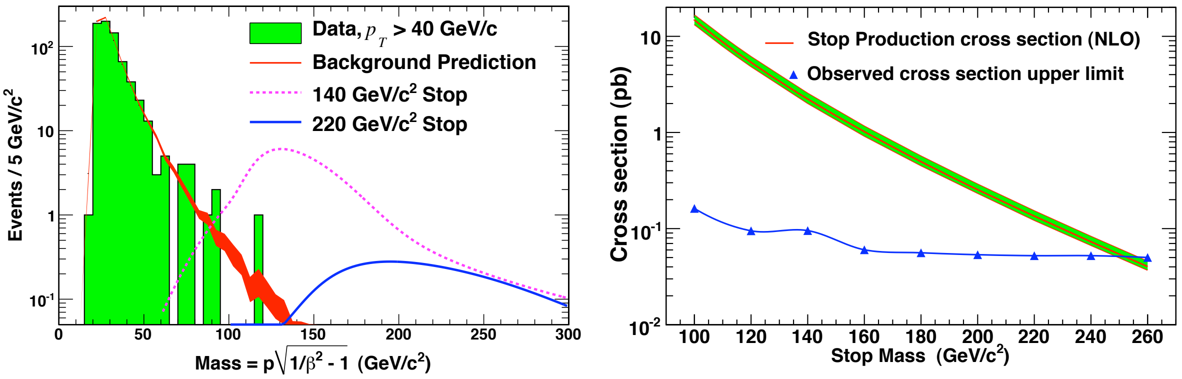

(a) Reconstructed Mass from TOF and momentum

(b) cross section limit

Figure A.5: *The reconstructed mass of candidate particles from the time-of-flight (TOF) and momentum measurements (a) and the cross section limits together with predictions for stop production cross sections (b). The measurements are performed by CDF II on 1.0 fb^{-1} of $p\bar{p}$ collisions at $\sqrt{s}$ = 1.96 TeV [12].*

limit of $\sigma < 48$ fb at 95% C.L. Furthermore, the limit is compared to predictions for stable $\tilde{t}$, the supersymmetric partner of the top quark, in dependence of its mass under consideration of the resolution of the mass measurement. This measurement is determined from the momentum and velocity of the particle (see Figure A.5). A lower limit of 249 GeV on the mass of a stable $\tilde{t}$ is set at 95% C.L., which at the time represented the most stringent limit.

In a previous search published in 2003, the CDF collaboration had already set cross section limits on long-lived particles either from weak or strong production [25]. The results are interpreted with respect to two benchmark models, a long-lived fourth generation quark (strong production) and a Drell-Yan produced supersymmetric lepton from GMSB scenarios (weak production). In samples from three different triggers (muon, electron or missing transverse energy), the analysis selects charged particles tracks with a momentum higher than 35 GeV and $|\eta| = 1$. On these tracks requirements to have a $\mathrm{d}E/\mathrm{d}x$ from two different subdetectors higher than expected for a particle with $\beta\gamma = 0.85$ are put. Furthermore, in the region below $\beta\gamma = 0.85$ the $\mathrm{d}E/\mathrm{d}x$ measurements can be converted into a mass $M_{\mathrm{d}E/\mathrm{d}x}$. This variable is shown for E_T^{miss} and muon data together with the expected background in Figure A.6a. Moreover, isolation cuts are applied to selected tracks for weak production. The derived cross section limits (see Figure A.6b) can be transformed into mass exclusions for quarks of charge $q = -\frac{1}{3}e$ below 190 GeV and of charge $q = \frac{2}{3}e$ below 220 GeV.

A.3 HERA

Also at the electron-proton collider HERA located at DESY, a search for heavy stable and charged particles has been performed with the H1 detector at a mean center-of-mass energy of 200 GeV [14] in photoproduction events. This analysis uses the highly ionizing properties of these yet unknown particles. Via a $\mathrm{d}E/\mathrm{d}x$ measurement and the tracks momentum, a measure of the particle mass M is determined from parametrizations of the energy deposits per path length. The search for new particles is performed in the so found mass spectra. All of the 6 tracks with reconstructed masses above 3 GeV can be lead back to reconstruction software failures, where two overlapping tracks are merged to one seemingly highly ionizing candidate track. As a consequence, a 95% C.L. upper limit on the production cross

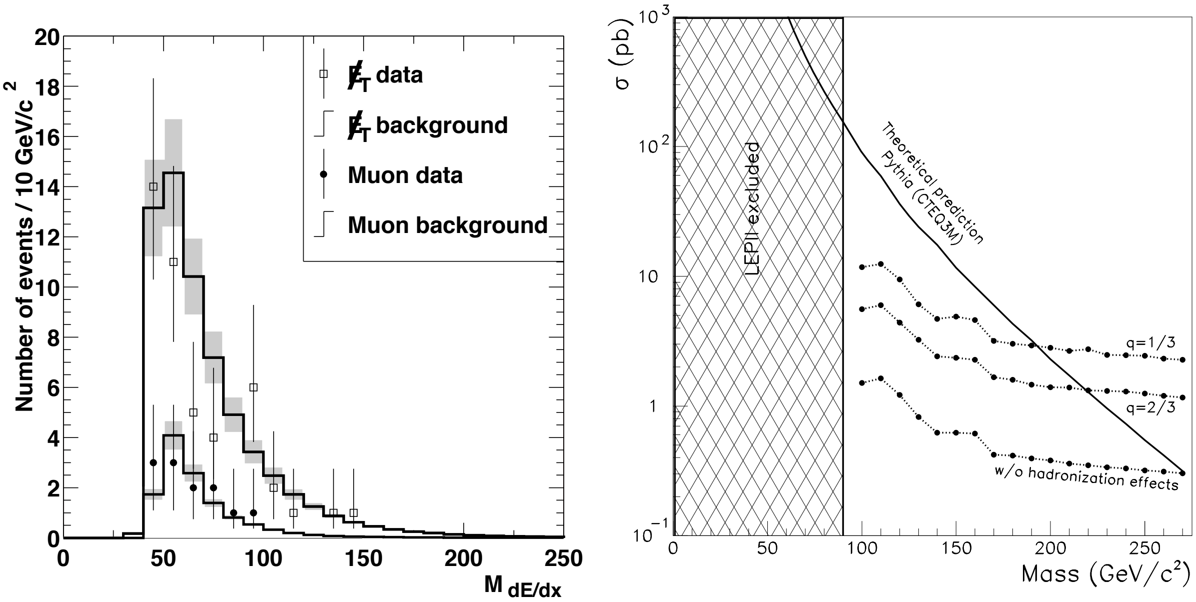

(a) Reconstructed Mass from dE/dx and momentum

(b) cross section limit

Figure A.6: *The reconstructed mass from the dE/dx measurements (a) for data selected by the* $E_T^{\rm miss}$ *and muon trigger recorded by CDF I [25]. (b) shows the cross section limits of long-lived fourth generation quarks.*

section of an arbitrary heavy, stable, charged particle is set at 0.19 nb.

A.4 LEP

The Large Electron Positron Collider (LEP) was operated in the same tunnel as the LHC from 1989 to 2000 and provided collisions of electrons (e^-) with their antiparticle, positrons (e^+). It hosted four large experiments, ALEPH, Delphi, L3 and Opal, each of which set limits on stable massive particles of charge $|q| = 1e$.

A.4.1 ALEPH

The ALEPH collaboration presents search results for gauge mediated supersymmetry breaking (GMSB) topologies in a paper from 2000 using 173.6 pb^{-1} of data recorded at $\sqrt{s}$ = 188.6 GeV [15]. One of the scenarios described there, includes stable supersymmetric leptons as the next-to-lightest supersymmetric particle (NLSP) (sleptons $\tilde{l}$) which can be long-lived in the case of heavy gravitino masses ($\geq \mathcal{O}$(100 GeV)). The analysis distinguishes two scenarios of slepton NLSPs. Either it is represented by three degenerate co-NLSPs ($\tilde{e}$, $\tilde{\mu}$, $\tilde{\tau}$) if the mixing in the stau sector is small, or the NLSP is the stau ($\tilde{\tau}$) for a large mixing in this sector. Events are selected based on the kinematic properties of the expected pair production and high dE/dx in the central tracker, the TPC. From the expected background of 0.9 events and the observed three events in the kinematic search and zero events based on high dE/dx a 95% C.L. upper cross section limit of ~ 30 fb for slepton masses 65-90 GeV can be determined. This transforms into a lower limit on the $\tilde{\tau}_R$ NLSP slepton mass 68 GeV and 85 GeV in the case of degenerate co-NLSPs.

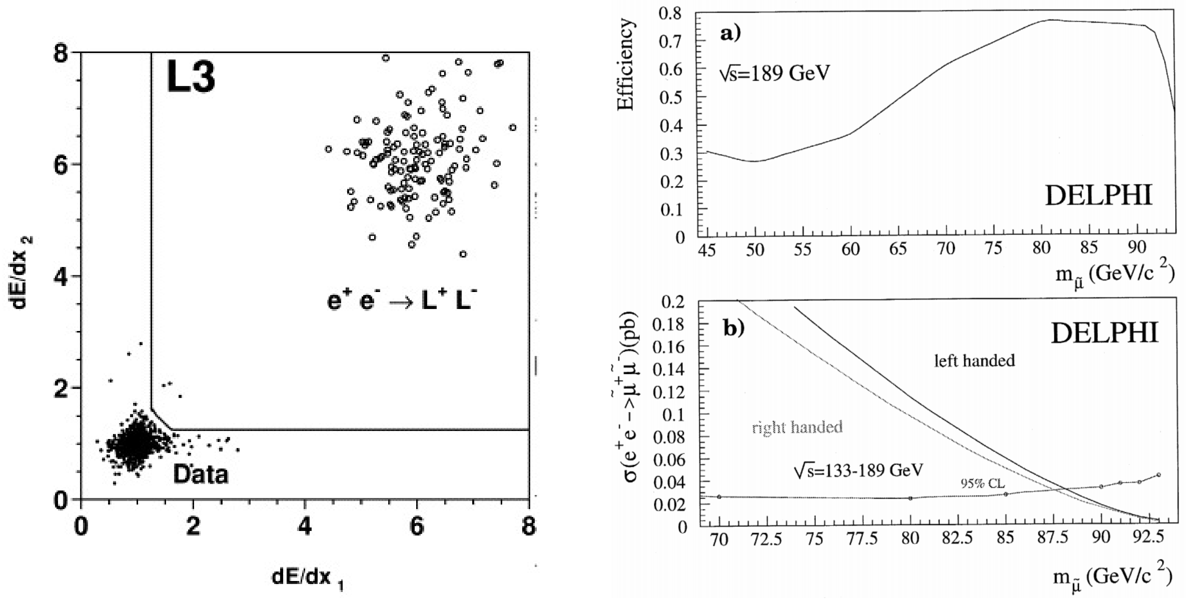

(a) L3

(b) Delphi

Figure A.7: *(a) The plane of the most energetic energy loss dE/dx_1 and the least energetic energy loss dE/dx_2 measured by the L3 collaboration. Data is shown by full circles and concentrates in the lower left corner of the plot. The signal region to the upper right corner is populated with simulated $e^+e^- \to L^+L^-$ events shown by open circles with arbitrary normalization. The lines indicate the cuts applied in the signal selection [16]. (b) The detection efficiency for stable long-lived sparticles (upper plot) and the 95% CL limit on the production cross section together with predictions for right and left handed sparticles (lower plot) as a function of the sparticle mass [17].*

A.4.2 L3

In a search in 450 pb^{-1} of e^+e^- collisions recorded in 1999 at $\sqrt{s}$ = 192 - 202 GeV and 2000 at $\sqrt{s}$ = 200 - 208 GeV, the L3 collaboration sets limits on the pair production of generic exotic charged and heavy leptons L^+ and L^- [16] in combination with earlier results at $\sqrt{s}$ = 133 - 189 GeV. These particles are assumed to couple to all three SM lepton families. In back-to-back topologies of charged tracks with $p_T > 5$ GeV, $|\cos\theta| < 0.82$ and acollinearity angle $< 15°$, the signal region is defined in the plane of the two tracks' $\mathrm{d}E/\mathrm{d}x$ measurements, where $\mathrm{d}E/\mathrm{d}x_1$ denotes the highest energy deposit per path length and $\mathrm{d}E/\mathrm{d}x_2$ the lowest. An upper cut is introduced to evade saturation effects of very high energy depositions. Out of the 16 598 events in data only three lie in the signal region (see Figure A.7a). This is in very good agreement with the expected SM background of 16 715 (mainly $e^+e^- \to e^+e^-$) and 4.1 ± 1.8 events in the signal region. The derived mass limit for L^+ and L^- is 102.6 GeV.

A.4.3 Delphi

In 2000, the Delphi collaboration presented cross section limits on stable sleptons from a dataset of 153.3 pb^{-1} integrated luminosity at a center of mass energy of 189 GeV [17]. The analysis is based on high momentum charged particles with either anomalously high ionization losses in the TPC or the absence of Cerenkov light in the RICH detector indicating the absence of photons. Events are selected if they contained two or three charged tracks originating from the primary vertex of the collision. At least

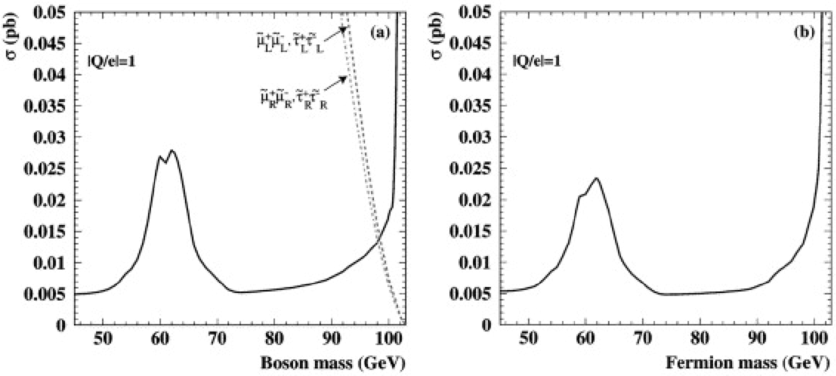

Figure A.8: *The model independent 95% CL cross section upper limits of $|q| = 1e$ particles at a center of mass energy of 206.6 GeV measured by OPAL. The predicted cross sections in the CMSSM model of left- and right-handed $\tilde{\mu}$ and $\tilde{\tau}$ pair production are also shown and are the basis for the derived mass exclusion of these particles [18].*

one of those tracks has $p_T > 5$ GeV and lies inside the RICH acceptance of $|\cos\theta| < 0.68$. Furthermore, a combination of four different selection criteria has to be met: no observed photons in the Gas RICH, less than 5 photons observed in the Liquid RICH, $\mathrm{d}E/\mathrm{d}x$ reconstructed in the TPC twice as high as expected for a minimum ionizing particle or the TPC $\mathrm{d}E/\mathrm{d}x$ below 0.3 of the expectation for protons.

The one observed event in data agrees well with the SM expectation of 1.02 ± 0.13 background events. In combination with previous results left and right handed smuons and staus are excluded in the mass range from 2 GeV to ~88 GeV at 95% confidence level as can be deduced from Figure A.7b.

A.4.4 OPAL

The latest paper from the OPAL collaboration on searches for long-lived stable particles presents limits on the pair production of $|q| = 1e$ and fractionally charged particles of $|q| = 2/3e$, $|q| = 4/3e$ and $|q| = 5/3e$ [18]. The analysis is based on an integrated luminosity of 693.1 pb^{-1} of e^+e^- collisions recorded at $\sqrt{s} = 130$ - 209 GeV between 1995 and 2000. No strong interaction is assumed and the analysis is based purely on the $\mathrm{d}E/\mathrm{d}x$ reconstructed in the jet chamber. In the back-to-back topology of pair produced particles both tracks are required to have a significantly higher or lower $\mathrm{d}E/\mathrm{d}x$ than expected for a minimum ionizing particle. Additionally, it is required that the probability, of the $\mathrm{d}E/\mathrm{d}x$ measurement to be consistent with a SM particle, is less than 30%. The selection for fractionally charged particles and particles with charge $|q| = 1e$ differ slightly to reduce the impact of the unknown interaction within the calorimeters for fractional charges. In the case of $|q| = 1e$ particles, zero candidates are observed for an expected background of 1.1 ± 1.3 events. This yields model independent cross section limits for fermions and bosons between 0.005 to 0.028 pb, shown as a function of their mass in Figure A.8. Similarly, in the search for fractional charges, three candidate events are observed and 3.2 ± 2.4 are expected from SM background. The derived cross section limits on fractional charges lie between 0.005 and 0.020 pb and are shown in Figure A.9 for all three charges. Interpreted in the Constrained Minimal Supersymmetric Model (CMSSM), this yields a lower limit of 98.0 (98.5) GeV on the mass of long-lived right- (left-) handed staus and smuons. Moreover, long-lived heavy leptons and charginos can be excluded below a mass of 102.0 GeV.

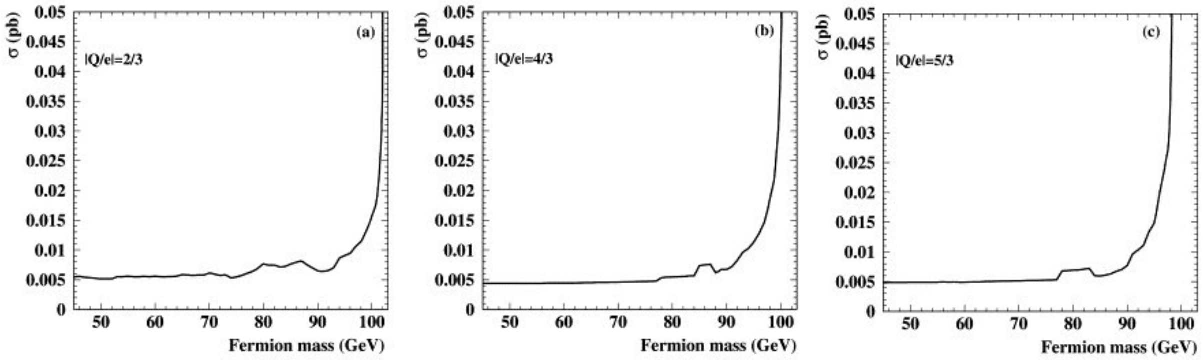

Figure A.9: *The model independent 95% CL cross section upper limits of* $|q| = 2/3e$*,* $|q| = 4/3e$ *and* $|q| = 5/3e$ *particles at a center of mass energy of 206.6 GeV derived from OPAL data [18].*

APPENDIX B

Alternative definitions of a TRT dE/dx

In total, there are two degrees of freedom influencing the definition of the most optimal description of the TRT $\mathrm{d}E/\mathrm{d}x$. The choice of the definition of ToT is discussed in Section 5.3. The second, not mentioned before, whether to divide the single ToT measurements by the track length in the straw before applying the corrections on hit-level is covered in this appendix. In the end, both ansatz yield comparable results, while dividing ToT by the track length in the straw uses less computational power due to simpler corrections. To distinguish between these two ideas, the nomenclature will be $\mathrm{d}E/\mathrm{d}x^{ToT/L}$ for the $\mathrm{d}E/\mathrm{d}x$ described in Section 5 and $\mathrm{d}E/\mathrm{d}x^{ToT}$ for the version constructed from the plain ToT values. The latter is introduced in Section B.1 with a discussion of the definitions of ToT in Section B.2. This is followed by a study of the optimal truncated mean method (Section B.3). The decision which version performs best is based on the separation power comparing $\mathrm{d}E/\mathrm{d}x^{ToT/L}$ and $\mathrm{d}E/\mathrm{d}x^{ToT}$ in Section B.4.

B.1 TRT dE/dx based on ToT ($\mathrm{d}E/\mathrm{d}x^{ToT}$)

In this alternative approach, ToT is not divided by the track length in the straw. Instead, corrections for dependencies on straw types and straw positions in the detector are applied directly to ToT. In this $\mathrm{d}E/\mathrm{d}x^{ToT}$ ansatz, the following functions are used to fit the dependencies in the different straw types and layers:

$$\text{Long barrel straws:} \qquad T(r_{\mathrm{drift}}, s) = T_0(r_{\mathrm{drift}}) + \frac{|s|}{v(r_{\mathrm{drift}})} \cdot e^{\left(\frac{|s|-l}{w(r_{\mathrm{drift}})}\right)}, \tag{B.1}$$

$$\text{Short barrel straws, end-cap straws:} \qquad T(r_{\mathrm{drift}}, s) = T_0(r_{\mathrm{drift}}) + a(r_{\mathrm{drift}}) \cdot s. \tag{B.2}$$

The position on the wire s is equivalent to z in the barrel region and to $r = \sqrt{x^2 + y^2}$ in the end-cap regions and the length of the straw is l. $T_0(r)$, $v(r)$, $w(r)$ and $a(r)$ are parametrized by a fifth order polynomial, with the drift radius r. The fit is performed individually for three layers in the barrel region (which again are split in 19, 24 and 30 straw layers) and 12 layers in the end-cap region. As shown in Equations (B.1) and (B.2), the fit to the long barrel straws requires more parameters due to a stronger dependence on s. After the application of these corrections, $\mathrm{d}E/\mathrm{d}x^{ToT}$ is treated equivalently to $\mathrm{d}E/\mathrm{d}x^{ToT/L}$, except for two exceptions. For one, no cut on the minimal track length in the straw is required. Additionally, the truncated mean is not necessary and $\mathrm{d}E/\mathrm{d}x$ is constructed from all ToT measurements on track.

B.2 Comparisons of different ToT definitions

To determine the best definition of ToT the separation power of $\mathrm{d}E/\mathrm{d}x^{ToT}$ and $\mathrm{d}E/\mathrm{d}x^{ToT/L}$ is compared for all four possible definitions of ToT: ToT^{standard}, $ToT^{\text{1-bits}}$, ToT^{largest} and $ToT^{\text{no hole}}$. In both approaches, ToT^{largest} yields the best separation power (see Figures B.1 and B.2 for $\mathrm{d}E/\mathrm{d}x^{ToT}$ and $\mathrm{d}E/\mathrm{d}x^{ToT/L}$ respectively).

B.3 Comparison of truncated mean methods

Before deciding how to best calculate the truncated mean in the $\mathrm{d}E/\mathrm{d}x^{ToT/L}$ approach, the impact of the truncation method on the separation power is investigated. Two ansatz are studied, truncating a certain percentage of highest (and/or lowest) ToT/L or truncating a fixed number of highest (and/or lowest) ToT/L. Figure B.3 compares the separation powers of a truncation of the highest and lowest 5%, the lowest 5% and highest 10% of hits to no truncation at all. Clearly, the application of a truncated mean method, improves the separation power. In comparison with Figure B.4, which compares different versions of integer truncation, it becomes evident that the best (and certainly easiest) method is to truncate the highest ToT/L from the average ToT/L as TRT $\mathrm{d}E/\mathrm{d}x$.

B.4 Comparing ToT and ToT/l approach

Finally, the two ansatz $\mathrm{d}E/\mathrm{d}x^{ToT}$ and $\mathrm{d}E/\mathrm{d}x^{ToT/L}$ are compared with respect to their separation power in Figure B.5. Overall, the behavior of the two definitions is very similar, with a slight superiority of $\mathrm{d}E/\mathrm{d}x^{ToT}$. Nevertheless, $\mathrm{d}E/\mathrm{d}x^{ToT/L}$ became the standard TRT $\mathrm{d}E/\mathrm{d}x$ as it is less CPU consuming, while yielding very comparable results.

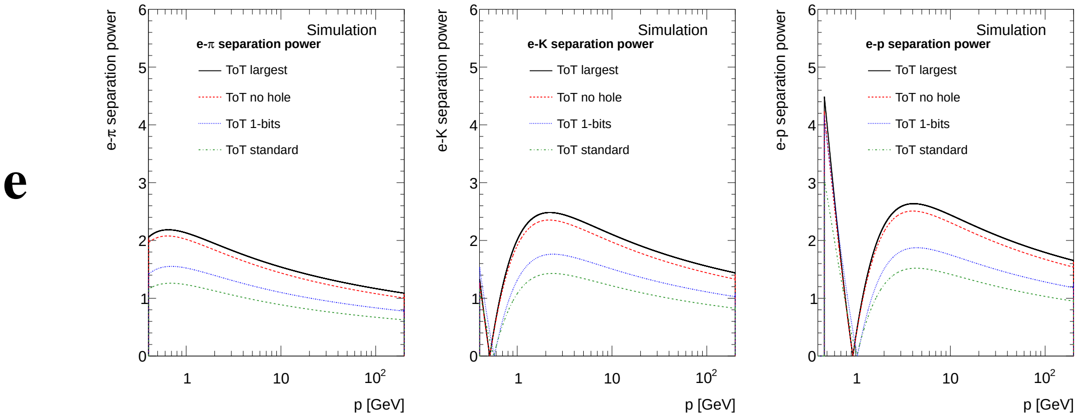

(a) Electrons - Pions (b) Electrons - Kaons (c) Electrons - Protons

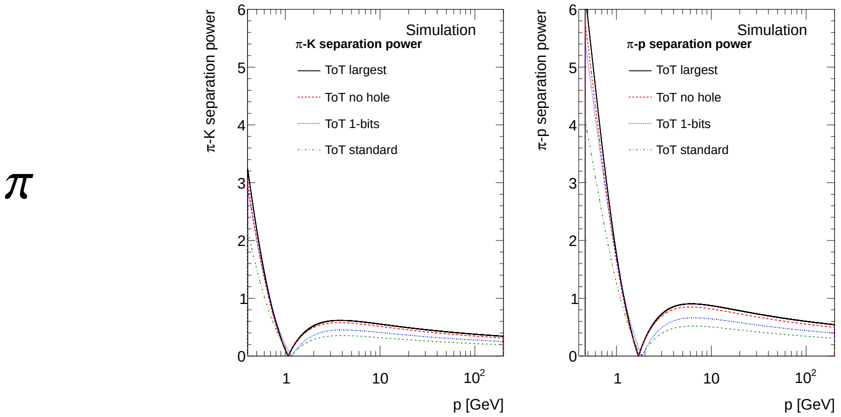

(d) Pions - Kaons (e) Pions - Protons

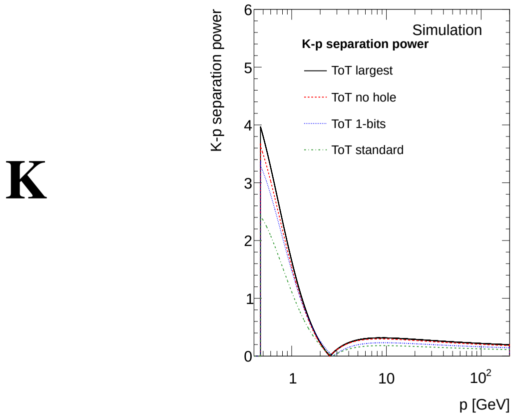

(f) Kaons - Protons

Figure B.1: *The separation power of* dE/dx^{ToT} *for all definitions of* ToT. *A cut on* $\beta\gamma > 0.5$ *has been applied to exclude the low* $\beta\gamma$*-region not covered by the fit.*

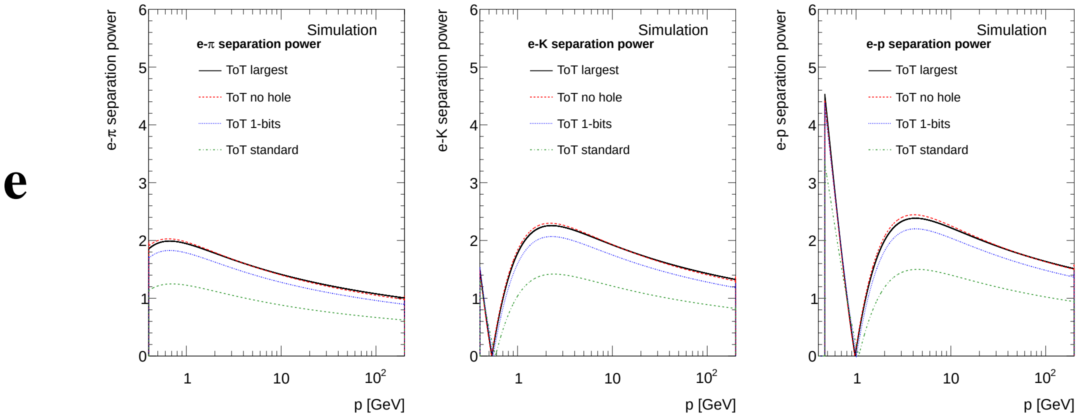

(a) Electrons - Pions (b) Electrons - Kaons (c) Electrons - Protons

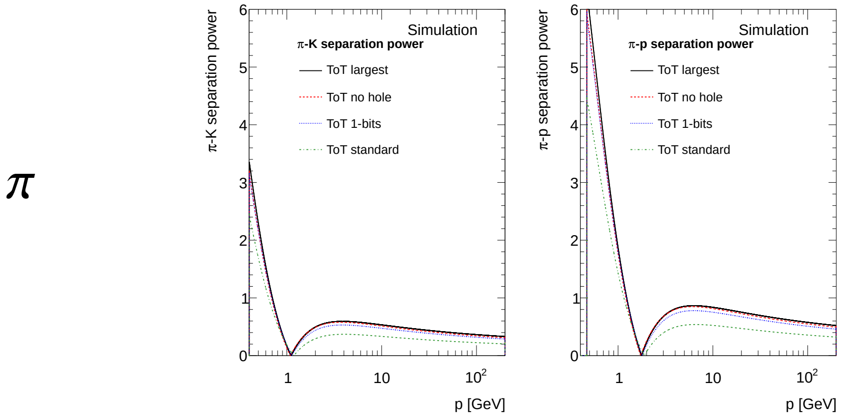

(d) Pions - Kaons (e) Pions - Protons

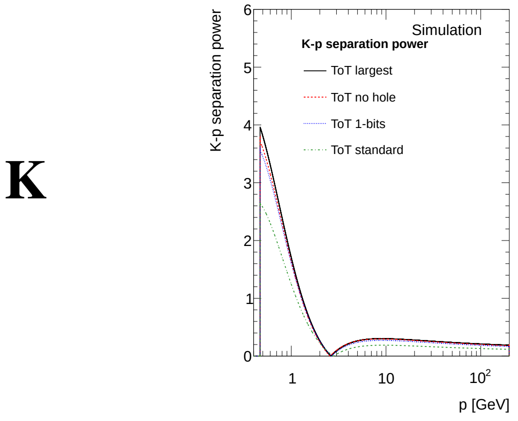

(f) Kaons - Protons

p

Figure B.2: *The separation power of $dE/dx^{ToT/L}$ for all definitions of ToT. A cut on $\beta\gamma > 0.5$ has been applied to exclude the low $\beta\gamma$-region not covered by the fit.*

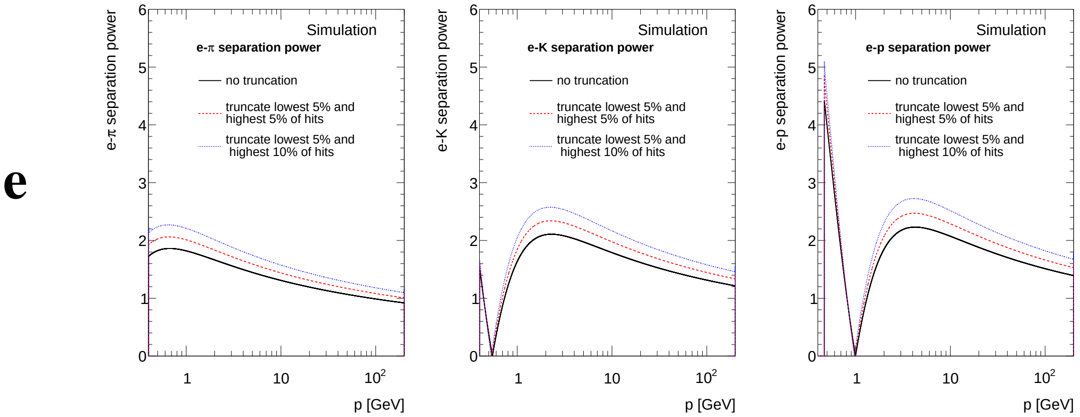

(a) Electrons - Pions (b) Electrons - Kaons (c) Electrons - Protons

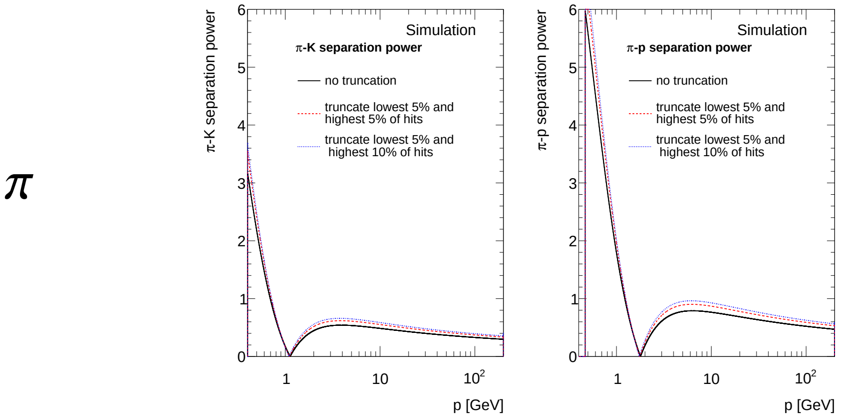

(d) Pions - Kaons (e) Pions - Protons

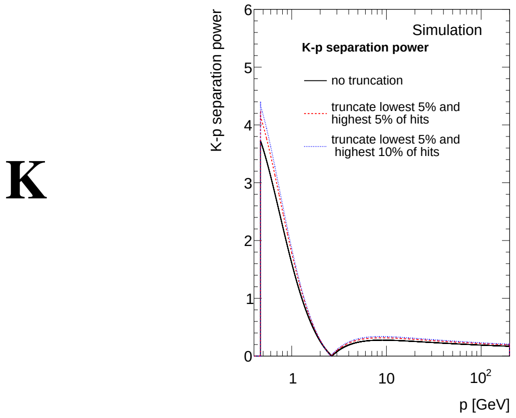

(f) Kaons - Protons

Figure B.3: *The separation powers for the* ToT^{largest} *definition of* $dE/dx^{ToT/L}$*, for different methods of truncating a percentage of hits. A cut on* $\beta\gamma > 0.5$ *has been applied to exclude the low* $\beta\gamma$*-region not covered by the fit.*

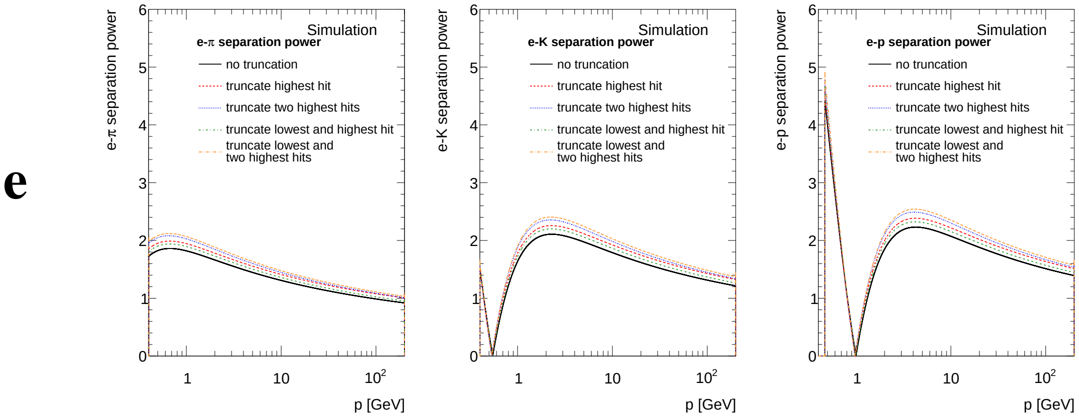

(a) Electrons - Pions (b) Electrons - Kaons (c) Electrons - Protons

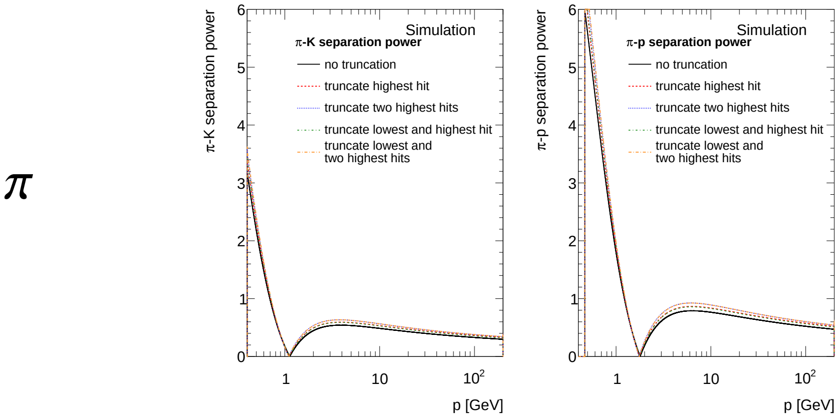

(d) Pions - Kaons (e) Pions - Protons

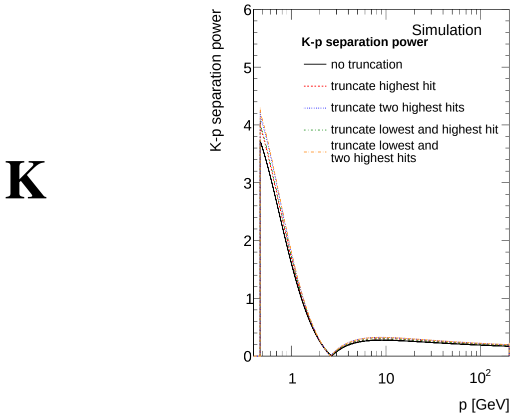

(f) Kaons - Protons

Figure B.4: *The separation powers for the* ToT^{largest} *definition of* $dE/dx^{ToT/L}$*, for different methods of truncating single hits. A cut on* $\beta\gamma > 0.5$ *has been applied to exclude the low* $\beta\gamma$*-region not covered by the fit.*

e

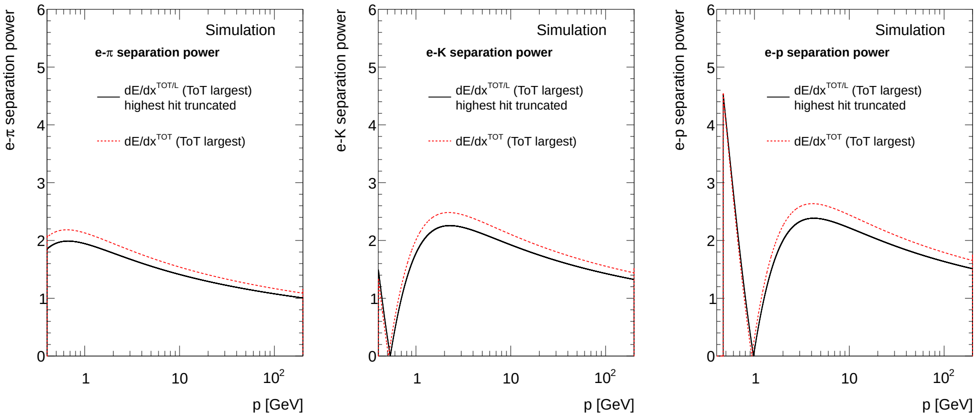

(a) Electrons - Pions (b) Electrons - Kaons (c) Electrons - Protons

π

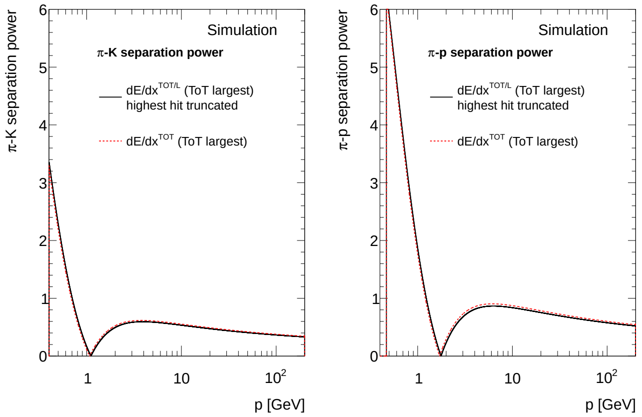

(d) Pions - Kaons (e) Pions - Protons

K

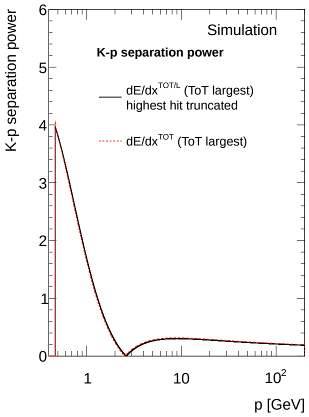

(f) Kaons - Protons

p

Figure B.5: *The separation powers for the* ToT^{largest} *definition of* ToT *comparing a* dE/dx *derived from* ToT *and* ToT/L*. A cut on* $\beta\gamma > 0.5$ *has been applied to exclude the low* $\beta\gamma$*-region not covered by our fit.*

APPENDIX C

Details on systematic uncertainties

This appendix lists details on the systematic uncertainties of the analysis, which were omitted in the main text. In particular, Section C.1 gives further details on the assessment of the systematic uncertainty on the trigger efficiency. Section C.2 provides the detailed results of the cut variations in each variable.

C.1 Trigger efficiency scaling

The main source of systematic uncertainty on the trigger efficiency arises from the scaling applied to the efficiency of simulated muons in the RPC system. Table C.1 compares the trigger efficiency $\epsilon_{\text{trigger}}$ with the scaling applied, to the pure trigger efficiency without any scaling $\epsilon_{\text{trigger}}^{\text{unscaled}}$. The relative difference between these values is shown in Table C.2. As expected, the largest impact of the scaling is observed for high mass signals. These have a larger probability for low velocities β, the region where the corrections to the efficiency are the largest.

C.2 Cut variations

C.2.1 Motivation for variations

The 20% variation of the TRT HT fraction is estimated from the High Threshold occupancy of the TRT in 2011 data shown in Figure C.1. Most of the deviations of Monte Carlo predictions from data observations are well below 20%, which is why a cut variation of this value is believed to yield a conservative estimate of the systematic uncertainty due to a cut on f^{HT}. This method has previously been applied in [100, 101].

Additional systematic uncertainties are determined by the resolution of the cut variables in the analysis selection. Table C.3 lists the relative uncertainty arising from the variation of the cuts on p_{T}, $S\,(\text{Pixel } \mathrm{d}E/\mathrm{d}x)$ or f^{HT} where applicable, $S\,(\text{TRT } \mathrm{d}E/\mathrm{d}x)$ and $S\,(\text{MDT } \mathrm{d}E/\mathrm{d}x)$ separately for each mass and charge point of the simulated signals. The quadratic sum of all these variations is shown in Table 7.16 of Section 7.4.2.

Table C.1: *Comparison of the unscaled trigger efficiency and the scaled trigger efficiency.*

Mass [GeV]	Trigger efficiency without scaling $\epsilon_{\text{trigger}}^{\text{unscaled}}$ [%]				
	$\lvert q\rvert = 2e$	$\lvert q\rvert = 3e$	$\lvert q\rvert = 4e$	$\lvert q\rvert = 5e$	$\lvert q\rvert = 6e$
50	52.96 ± 0.53	52.10 ± 0.60	35.37 ± 0.87	19.25 ± 1.44	12.50 ± 2.10
100	47.64 ± 0.76	46.28 ± 0.95	42.41 ± 1.48	30.69 ± 2.71	10.83 ± 2.84
200	51.64 ± 0.63	50.74 ± 0.75	43.12 ± 0.99	39.39 ± 1.56	37.55 ± 3.00
300	47.91 ± 0.60	49.08 ± 0.69	47.90 ± 0.90	41.41 ± 1.29	34.78 ± 2.12
400	43.48 ± 0.60	44.87 ± 0.68	45.56 ± 0.87	44.00 ± 1.18	38.96 ± 1.94
500	38.52 ± 0.58	42.19 ± 0.67	42.18 ± 0.84	43.76 ± 1.15	40.75 ± 1.71
600	33.61 ± 0.57	36.69 ± 0.66	38.05 ± 0.82	36.39 ± 1.11	36.17 ± 1.63

(a) Unscaled $\epsilon_{\text{trigger}}$

Mass [GeV]	Trigger efficiency with scaling $\epsilon_{\text{trigger}}$ [%]				
	$\lvert q\rvert = 2e$	$\lvert q\rvert = 3e$	$\lvert q\rvert = 4e$	$\lvert q\rvert = 5e$	$\lvert q\rvert = 6e$
50	47.39 ± 0.53	49.87 ± 0.60	35.21 ± 0.87	19.22 ± 1.44	12.49 ± 2.10
100	41.39 ± 0.75	41.02 ± 0.94	40.54 ± 1.47	30.30 ± 2.70	10.78 ± 2.83
200	41.96 ± 0.63	41.83 ± 0.74	37.30 ± 0.97	36.16 ± 1.53	36.50 ± 2.98
300	38.05 ± 0.59	38.63 ± 0.68	37.61 ± 0.87	34.74 ± 1.25	31.26 ± 2.06
400	32.80 ± 0.57	34.07 ± 0.65	34.16 ± 0.82	32.81 ± 1.12	32.34 ± 1.86
500	28.54 ± 0.54	31.35 ± 0.63	31.05 ± 0.79	31.32 ± 1.08	31.11 ± 1.61
600	23.45 ± 0.51	25.67 ± 0.60	26.45 ± 0.75	24.54 ± 0.99	24.98 ± 1.47

(b) Scaled $\epsilon_{\text{trigger}}$

Table C.2: *The relative difference between the unscaled and scaled trigger efficiency,* $(\epsilon_{\text{trigger}}^{\text{unscaled}} - \epsilon_{\text{trigger}}^{\text{scaled}})/\epsilon_{\text{trigger}}^{\text{scaled}}$

Mass [GeV]	$(\epsilon_{\text{trigger}}^{\text{unscaled}} - \epsilon_{\text{trigger}}^{\text{scaled}})/\epsilon_{\text{trigger}}^{\text{scaled}}$ [%]				
	$\lvert q\rvert = 2e$	$\lvert q\rvert = 3e$	$\lvert q\rvert = 4e$	$\lvert q\rvert = 5e$	$\lvert q\rvert = 6e$
50	11.7412	4.4778	0.4770	0.1570	0.1122
100	15.1065	12.8123	4.6249	1.2971	0.4804
200	23.0826	21.3110	15.5957	8.9166	2.8843
300	25.9187	27.0506	27.3530	19.1992	11.2661
400	32.5676	31.6988	33.3569	34.1127	20.4554
500	34.9740	34.6065	35.8597	39.7003	30.9963
600	43.3095	42.9334	43.8769	48.2814	44.7818

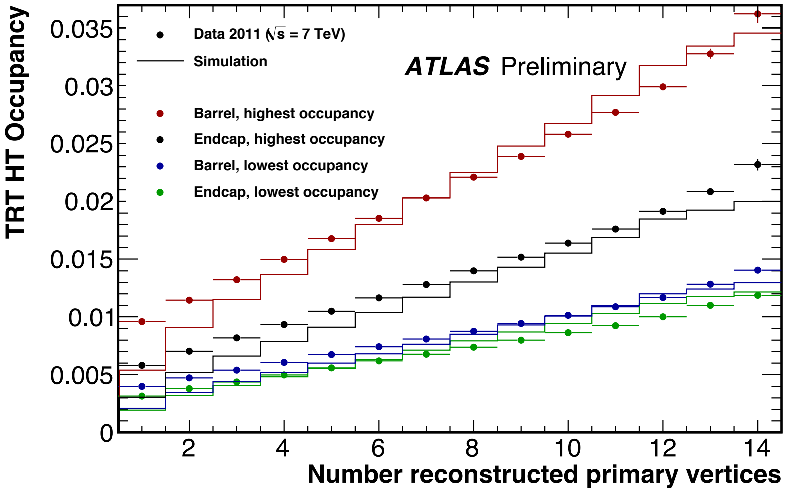

Figure C.1: The TRT HT occupancy as a function of the number of primary vertices per event in data and simulation.

Table C.3: *Relative differences in the signal tracks in the signal region from varying the cuts indicated in the table.*

	p_T		S(Pixel dE/dx)		S(TRT dE/dx)		S(MDT dE/dx)	
	-3%	+3%	-5%	+5%	-5%	+5%	-5%	+50%
Mass [GeV]	charge $\lvert q \rvert = 2e$							
50	0.57%	0.00%	-0.02%	0.07%	-0.83%	1.36%	-0.39%	0.43%
100	0.00%	0.00%	-0.06%	0.00%	-0.80%	1.65%	-0.29%	0.17%
200	0.00%	0.00%	-0.04%	0.00%	-0.81%	0.87%	-0.35%	0.28%
300	0.00%	0.00%	-0.04%	0.04%	-0.56%	0.94%	-0.29%	0.12%
400	0.00%	0.00%	0.00%	0.03%	-0.56%	0.61%	-0.18%	0.01%
500	0.00%	0.00%	-0.05%	0.15%	-0.21%	0.96%	-0.14%	0.10%
600	0.00%	0.00%	0.00%	0.02%	-0.37%	0.73%	-0.24%	0.00%

	p_T		f^{HT}		S(TRT dE/dx)		S(MDT dE/dx)	
	-3%	+3%	-20%	+20%	-5%	+5%	-5%	+50%
Mass [GeV]	charge $\lvert q \rvert = 3e$							
50	0.98%	0.00%	-0.03%	1.71%	-0.64%	0.92%	-0.03%	0.03%
100	0.27%	0.00%	0.00%	1.08%	-0.62%	0.91%	-0.08%	0.09%
200	0.00%	0.00%	0.00%	1.12%	-0.23%	1.10%	-0.05%	0.00%
300	0.00%	0.00%	0.00%	0.40%	-0.48%	0.81%	0.00%	0.00%
400	0.00%	0.00%	-0.05%	0.28%	-0.22%	0.79%	-0.17%	0.00%
500	0.00%	0.00%	0.00%	0.06%	-0.17%	0.66%	0.00%	0.00%
600	0.00%	0.00%	0.00%	0.07%	-0.43%	0.80%	-0.07%	0.02%
Mass [GeV]	charge $\lvert q \rvert = 4e$							
50	0.48%	0.00%	0.00%	0.00%	-0.09%	0.19%	-0.28%	0.00%
100	0.22%	0.00%	0.00%	0.00%	0.00%	0.44%	0.00%	0.22%
200	0.00%	0.00%	0.00%	0.00%	-0.13%	0.11%	-0.22%	0.11%
300	0.00%	0.00%	0.00%	0.00%	-0.03%	0.17%	-0.09%	0.09%
400	0.00%	0.00%	0.00%	0.00%	-0.12%	0.29%	-0.10%	0.00%
500	0.00%	0.00%	0.00%	0.00%	0.00%	0.30%	-0.09%	0.00%
600	0.00%	0.00%	0.00%	0.00%	-0.08%	0.08%	-0.16%	0.11%
Mass [GeV]	charge $\lvert q \rvert = 5e$							
50	0.00%	0.00%	0.00%	0.00%	0.00%	0.00%	-0.70%	0.00%
100	0.00%	0.00%	0.00%	0.00%	0.00%	0.00%	0.00%	0.00%
200	0.00%	0.00%	0.00%	0.00%	0.00%	0.53%	0.00%	0.00%
300	0.00%	0.00%	0.00%	0.00%	0.00%	0.00%	-0.19%	0.00%
400	0.00%	0.00%	0.00%	0.00%	0.00%	0.00%	-0.33%	0.00%
500	0.00%	0.00%	0.00%	0.00%	0.00%	0.15%	-0.28%	0.00%
600	0.00%	0.00%	0.00%	0.00%	0.00%	0.00%	-0.53%	0.00%
Mass [GeV]	charge $\lvert q \rvert = 6e$							
50	0.00%	0.00%	0.00%	0.00%	0.00%	0.00%	0.00%	0.00%
100	0.00%	0.00%	0.00%	0.00%	0.00%	0.00%	0.00%	0.00%
200	0.00%	0.00%	0.00%	0.00%	0.00%	0.00%	0.00%	0.00%
300	0.00%	0.00%	0.00%	0.00%	0.00%	0.00%	0.00%	0.00%
400	0.00%	0.00%	0.00%	0.00%	0.00%	0.00%	-0.49%	0.49%
500	0.00%	0.00%	0.00%	0.00%	0.00%	0.00%	-0.49%	0.00%
600	0.00%	0.00%	0.00%	0.00%	0.00%	0.00%	-1.19%	0.35%

Bibliography

[1] L. Evans and P. Bryant. “LHC Machine”. In: *Journal of Instrumentation* 3.08 (2008), S08001.

[2] ATLAS Collaboration. “The ATLAS Experiment at the CERN Large Hadron Collider”. In: *Journal of Instrumentation* 3 (2008), S08003. 437 p.

[3] CMS Collaboration. “The CMS experiment at the CERN LHC. The Compact Muon Solenoid experiment”. In: *Journal of Instrumentation* 3 (2008), S08004. 361 p.

[4] ATLAS Collaboration. “Observation of a new particle in the search for the Standard Model Higgs boson with the ATLAS detector at the LHC”. In: *Physics Letters B* 716.1 (2012), pp. 1 –29.

[5] CMS Collaboration. “Observation of a new boson at a mass of 125 GeV with the CMS experiment at the LHC”. In: *Physics Letters B* 716.1 (2012), pp. 30 –61.

[6] LHCb Collaboration. “Evidence for CP Violation in Time-Integrated $D^0 \rightarrow h^- h^+$ Decay Rates”. In: *Physical Review Letters* 108 (11 Mar. 2012), p. 111602.

[7] LHCb Collaboration. “Determination of the X(3872) meson quantum numbers”. In: (2013). arXiv:`1302.6269 [hep-ex]`.

[8] ATLAS Collaboration. “Search for long-lived, multi-charged particles in pp collisions at $\sqrt{s}$ = 7 TeV using the ATLAS detector”. In: *Physics Letters B* (2013). arXiv:`1301.5272 [hep-ex]`.

[9] ATLAS Collaboration. “Searches for heavy long-lived sleptons and R-Hadrons with the ATLAS detector in pp collisions at $\sqrt{s}$ = 7 TeV”. In: *Physics Letters B* 720.4 - 5 (2013), pp. 277 –308.

[10] ATLAS Collaboration. “Search for Massive Long-lived Highly Ionising Particles with the ATLAS Detector at the LHC”. In: *Physics Letters* B698 (2011), pp. 353–370.

[11] CMS Collaboration. “Search for heavy stable charged particles in pp collisions at $\sqrt{s}$ = 7 TeV”. In: *Journal of High Energy Physics* 2011 (3 2011), pp. 1–29.

[12] CDF Collaboration. “Search for Long-Lived Massive Charged Particles in 1.96 TeV $p\overline{p}$ Collisions”. In: *Physical Review Letters* 103 (2 July 2009), p. 021802.

[13] D0 Collaboration. “Search for Long-Lived Charged Massive Particles with the D0 Detector”. In: *Physical Review Letters* 102 (2009), p. 161802.

[14] H1 Collaboration. “Measurement of anti-deuteron photoproduction and a search for heavy stable charged particles at HERA”. In: *European Physical Journal C* 36 (2004), pp. 413–423.

[15] ALEPH Collaboration. “Search for gauge mediated SUSY breaking topologies at $\sqrt{s} \sim 189$ GeV”. In: *European Physical Journal C* 16 (2000), pp. 71–85.

[16] L3 Collaboration. “Search for heavy neutral and charged leptons in e^+e^- annihilation at LEP”. In: *Physics Letters B* 517.1-2 (2001), pp. 75 –85.

[17] Delphi Collaboration. “Search for heavy stable and long-lived particles in e^+e^- collisions at $\sqrt{s} = 189$ GeV”. In: *Physics Letters B* 478.1-3 (2000), pp. 65 –72.

[18] OPAL Collaboration. “Search for stable and long-lived massive charged particles in e^+e^- collisions at $\sqrt{s} = 130$ - 209 GeV”. In: *Physics Letters B* 572.1-2 (2003), pp. 8 –20.

[19] ATLAS Collaboration. “Search for Heavy Long-Lived Charged Particles with the ATLAS detector in pp collisions at $\sqrt{s} = 7$ TeV”. In: *Physics Letters* B703 (2011), pp. 428–446.

[20] ATLAS Collaboration. “Search for stable hadronising squarks and gluinos with the ATLAS experiment at the LHC”. In: *Physics Letters B* 701.1 (2011), pp. 1 –19.

[21] CMS Collaboration. “Search for heavy long-lived charged particles in pp collisions at”. In: *Physics Letters B* 713.4 - 5 (2012), pp. 408 –433.

[22] CMS Collaboration. *Search for multi-charged Heavy Stable Charged Particles*. Tech. rep. CMS-PAS-EXO-11-090. Geneva: CERN, 2012.

[23] CMS Collaboration. *Searches for Long-lived Charged Particles*. Tech. rep. CMS-PAS-EXO-12-026. Geneva: CERN, 2013.

[24] J. M. Campbell, J. Huston and W. Stirling. “Hard Interactions of Quarks and Gluons: A Primer for LHC Physics”. In: *Reports on Progress in Physics* 70 (2007), p. 89.

[25] CDF Collaboration. “Search for Long-Lived Charged Massive Particles in $p\overline{p}$ Collisions at $\sqrt{s} = 1.8$ TeV”. In: *Physical Review Letters* 90 (13 Mar. 2003), p. 131801.

[26] S. Weinberg. “A Model of Leptons”. In: *Physical Review Letters* 19 (1967), pp. 1264–1266.

[27] A. Salam. “Weak and Electromagnetic Interactions”. In: *Proc. 8th Nobel Symposium, Ed. N. Svartholm (Almquist and Wiskell, Stockholm)* (1967), pp. 367–377.

[28] S. L. Glashow, J. Iliopoulos and L. Maiani. “Weak Interactions with Lepton-Hadron Symmetry”. In: *Physical Review D* 2 (1970), pp. 1285–1292.

[29] S. Weinberg. “Effects of a Neutral Intermediate Boson in Semileptonic Processes”. In: *Physical Review D* 5 (1972), pp. 1412–1417.

[30] ATLAS Experiment Public Results. `https://twiki.cern.ch/twiki/bin/view/AtlasPublic/CombinedSummaryPlots`.

[31] I. C. Brock and T. Schorner-Sadenius. *Physics at the terascale*. Weinheim: Wiley, 2011.

[32] D. J. Griffiths. *Introduction to elementary particles; 2nd rev. version*. Physics textbook. New York, NY: Wiley, 2008.

[33] J. Beringer et al. (Particle Data Group). “Review of Particle Physics, 2012-2013. Review of Particle Properties”. In: *Physical Review D* 86.1 (2012), p. 010001.

[34] M. Fairbairn et al. “Stable massive particles at colliders”. In: *Physics Reports* 438 (2007), pp. 1–63.

[35] R. Foadi et al. “Minimal walking technicolor: Setup for collider physics”. In: *Physical Review D* 76 (5 Sept. 2007), p. 055005.

[36] M.Yu. Khlopov and K.M. Belotsky. *private communications*.

[37] M. Y. Khlopov, C. A. Stephan and D. Fargion. “Dark matter with invisible light from heavy double charged leptons of almost-commutative geometry?” In: *Classical and Quantum Gravity* 23.24 (2006), p. 7305.

[38] K. M. Belotsky et al. *Search for Multi-charge Objects in pp collisions at sqrt(s)=7 TeV using the ATLAS detector*. Tech. rep. ATL-PHYS-INT-2013-004. Geneva: CERN, Jan. 2013.

[39] J. Schwinger. “Magnetic Charge and Quantum Field Theory”. In: *Physical Review* 144.4 (1966).

[40] S. Dimopoulos and G. Landsberg. “Black Holes at the Large Hadron Collider”. In: *Physical Review Letters* 87 (16 Sept. 2001), p. 161602.

[41] A. Kusenko and M. E. Shaposhnikov. “Supersymmetric Q balls as dark matter”. In: *Physiscs Letters B* 418 (1998), pp. 46–54.

[42] ALICE collaboration. “The ALICE experiment at the CERN LHC. A Large Ion Collider Experiment”. In: *Journal of Instrumentation* 3 (2008), S08002. 259 p.

[43] LHCb Collaboration. “The LHCb Detector at the LHC”. In: *Journal of Instrumentation* 3 (2008), S08005.

[44] TOTEM Collaboration. “The TOTEM Experiment at the CERN Large Hadron Collider”. In: *Journal of Instrumentation* 3 (2008), S08007.

[45] O. Adriani et al. *LHCf experiment: Technical Design Report*. Tech. rep. CERN-LHCC-2006-004. Geneva, 2006.

[46] J. Pinfold et al. *Technical Design Report of the MoEDAL Experiment*. Tech. rep. CERN-LHCC-2009-006. MoEDAL-TDR-001. Geneva: CERN, June 2009.

[47] courtesey of CERN.

[48] ATLAS Luminosity Group. `https://twiki.cern.ch/twiki/bin/view/AtlasPublic/LuminosityPublicResults`.

[49] ATLAS Collaboration. *ATLAS magnet system: Technical Design Report, 1*. Tech. rep. CERN-LHCC-97-18. Geneva, 1997.

[50] A. Yamamoto et al. “The ATLAS central solenoid”. In: *Nuclear Instruments and Methods in Physics Research Section A* 584.1 (2008), pp. 53 –74.

[51] ATLAS Collaboration. *ATLAS central solenoid: Technical design report*. Tech. rep. CERN-LHCC-97-21. 1997.

[52] ATLAS Collaboration. *ATLAS barrel toroid: Technical design report*. Tech. rep. CERN-LHCC-97-19. 1997.

[53] ATLAS Collaboration. *ATLAS endcap toroids: Technical design report*. Tech. rep. CERN-LHCC-97-20. 1997.

[54] ATLAS Collaboration. *ATLAS inner detector: Technical Design Report, 2*. Tech. rep. CERN-LHCC-97-17. Geneva, 1997.

[55] A. Bingül. “The ATLAS TRT and its Performance at LHC”. In: *Journal of Physics: Conference Series* 347.1 (2012), p. 012025.

[56] ATLAS Collaboration. *ATLAS pixel detector: Technical Design Report*. Tech. rep. CERN-LHCC-98-13. Geneva, 1998.

[57] ATLAS Collaboration. “The ATLAS Inner Detector commissioning and calibration”. In: *The European Physical Journal C - Particles and Fields* 70 (3 2010), pp. 787–821.

[58] A. Ahmad et al. “The Silicon microstrip sensors of the ATLAS semiconductor tracker”. In: *Nuclear Instruments and Methods in Physics Research Section A* 578 (2007), pp. 98–118.

[59] The ATLAS TRT collaboration. “The ATLAS Transition Radiation Tracker (TRT) proportional drift tube: design and performance”. In: *Journal of Instrumentation* 3.02 (2008), P02013.

[60] ATLAS Collaboration. *ATLAS liquid-argon calorimeter: Technical Design Report*. Tech. rep. CERN-LHCC-96-41. Geneva, 1996.

[61] ATLAS Collaboration. *ATLAS tile calorimeter: Technical Design Report*. Tech. rep. CERN-LHCC-96-42. Geneva, 1996.

[62] ATLAS Collaboration. *ATLAS muon spectrometer: Technical Design Report*. Tech. rep. CERN-LHCC-97-22, ATLAS-TDR-10. Geneva, 1997.

[63] P. Jenni and M. Nessi. *ATLAS Forward Detectors for Luminosity Measurement and Monitoring*. Tech. rep. CERN-LHCC-2004-010. LHCC-I-014. Geneva: CERN, Mar. 2004.

[64] P. Jenni, M. Nessi and M. Nordberg. *Zero Degree Calorimeters for ATLAS*. Tech. rep. LHCC-I-016. CERN-LHCC-2007-001. Geneva: CERN, Jan. 2007.

[65] ATLAS Collaboration. *ATLAS level-1 trigger: Technical Design Report*. Tech. rep. CERN-LHCC-98-14, ATLAS-TDR-12. Geneva, 1998.

[66] P. Jenni et al. *ATLAS high-level trigger, data-acquisition and controls: Technical Design Report*. Tech. rep. CERN-LHCC-2003-022, ATLAS-TRD-016. Geneva, 2003.

[67] ATLAS Collaboration. *Performance of the ATLAS muon trigger in 2011*. Tech. rep. ATLAS-CONF-2012-099. Geneva: CERN, July 2012.

[68] J. Alwall et al. “MadGraph 5 : Going Beyond”. In: *Journal of High Energy Physics* 1106 (2011), p. 128.

[69] ATLAS Collaboration. *Atlas Computing: technical design report*. Tech. rep. CERN-LHCC-2005-022, ATLAS-TRD-017. Geneva, 2005.

[70] T. Cornelissen et al. *Concepts, Design and Implementation of the ATLAS New Tracking (NEWT)*. Tech. rep. ATL-SOFT-PUB-2007-007. Geneva: CERN, Mar. 2007.

[71] ATLAS Collaboration. *Expected Performance of the ATLAS Experiment - Detector, Trigger and Physics*. Tech. rep. 2009. arXiv:`0901.0512 [hep-ex]`.

[72] Massimo Corradi. *private communications*.

[73] Particle Data Group, K. Nakamura et al. “Review of Particle Physics”. In: *Journal of Physics G* 37 (2010), p. 1.

[74] H. Bhabha. “On the penetrating component of cosmic radiation”. In: *Proceedings of the Royal Society London A* 164 (1938), pp. 257–94.

[75] H. Bethe. “Zur Theorie des Durchgangs schneller Korpuskularstrahlen durch Materie”. In: *Annalen der Physik* 5 (1930), pp. 325–400.

[76] H. Andersen and J. Ziegler. *Hydrogen: Stopping Powers and Ranges in All Elements*. The Stopping and Ranges of Ions in Matter. Pergamon Press, 1977.

[77] L. Landau. “On the Energy Loss of Fast Particles by Ionization”. In: *Journal of Physics-USSR* 8 (1944), p. 201.

[78] W. Blum and L. Rolandi. *Particle Detection with Drift Chambers*. Ed. by F. Bonaudi and C. Fabjan. Springer, 1993.

[79] M. Hauschild et al. “Particle identification with the OPAL jet chamber”. In: *Nuclear Instruments and Methods in Physics Research Section A* 314.1 (1992), pp. 74 –85.

[80] T. Sjostrand, S. Mrenna and P. Skands. “PYTHIA 6.4 Physics and Manual”. In: *Journal of High Energy Physics* 05 (2006), p. 026.

[81] S. Agostinelli et al. “GEANT4: A simulation toolkit”. In: *Nuclear Instruments and Methods in Physics Research Section A* 506 (2003), pp. 250–303.

[82] Yury Smirnov. *private communications*.

[83] ATLAS Collaboration. *dE/dx measurement in the ATLAS Pixel Detector and its use for particle identification*. Tech. rep. ATLAS-CONF-2011-016. Geneva: CERN, Mar. 2011.

[84] M. D. Joergensen and J. B. Hansen. “Search for long lived massive particles with the ATLAS detector at the LHC. oai:cds.cern.ch:1370233”. Presented 06 Feb 2011. PhD thesis. Copenhagen: Bohr Inst., 2011.

[85] P. Mermod et al. *Identifying highly ionizing particles with the ATLAS electromagnetic calorimeter*. Tech. rep. ATL-LARG-INT-2010-002. Geneva: CERN, Apr. 2010.

[86] C. Ohm, D. Milstead and T. Moa. “Searches for exotic stable massive particles with the ATLAS experiment”. Presented 04 Nov 2011. PhD thesis. Stockholm: Stockholm U., 2011.

[87] S. Hellman et al. *Measuring time-of-flight and identifying exotic stable massive particles with the ATLAS Tile calorimeter*. Tech. rep. ATL-TILECAL-INT-2010-006. Geneva: CERN, Sept. 2010.

[88] ATLAS Run Query. `https://atlas.web.cern.ch/Atlas/GROUPS/DATAPREPARATION/DataSummary/2011/run.py?run=177986`.

[89] D. Richter. “Energy Loss Measurements with the ATLAS Transition Radiation Tracker Using Test Beam Data”. Diplom Thesis. Humboldt Universität zu Berlin, 2008.

[90] M. Juengst, M. Schultens and S. Zimmermann. *A time-over-threshold based approach for particle identification with the ATLAS TRT detector*. Tech. rep. ATL-INDET-INT-2012-001. Geneva: CERN, Feb. 2012.

[91] ATLAS Collaboration. *Calibration of the ATLAS Transition Radiation Tracker*. Tech. rep. ATLAS-CONF-2011-006. Geneva: CERN, Feb. 2011.

[92] ATLAS Collaboration. *Calibration of the ATLAS Transition Radiation Tracker*. Tech. rep. ATLAS-CONF-2011-006. Geneva: CERN, Feb. 2011.

[93] C. Grupen, B. Shwartz and H. Spieler. *Particle Detectors*. Cambridge Monographs on Particle Physics, Nuclear Physics and Cosmology. Cambridge University Press, 2008.

[94] ATLAS Collaboration. “Charged-particle multiplicities in pp interactions measured with the ATLAS detector at the LHC”. In: *New Journal of Physics* 13.5 (2011), p. 053033.

[95] J. Pumplin et al. “New generation of parton distributions with uncertainties from global QCD analysis”. In: *Journal of High Energy Physics* 0207 (2002), p. 012.

[96] ATLAS Collaboration. *Luminosity Determination in pp Collisions at $\sqrt{s} = 7$ TeV using the ATLAS Detector in 2011*. Tech. rep. ATLAS-CONF-2011-116. Geneva: CERN, Aug. 2011.

[97] ATLAS Collaboration. “Luminosity Determination in pp Collisions at $\sqrt{s} = 7$ TeV using the ATLAS Detector at the LHC”. In: *European Physics Journal* C71 (2011), p. 1630.

[98] T. Junk. “Confidence level computation for combining searches with small statistics”. In: *Nuclear Instruments and Methods in Physics Research Section A: Accelerators, Spectrometers, Detectors and Associated Equipment* 434.2-3 (1999), pp. 435 –443.

[99] T. Junk. *Sensitivity, Exclusion and Discovery with Small Signals, Large Backgrounds, and Large Systematic Uncertainties*. Tech. rep. CDF 8128. 2007.

[100] ATLAS Collaboration. “Search for Magnetic Monopoles in $\sqrt{s}$=7 TeV pp Collisions with the ATLAS Detector”. In: *Physical Review Letters* 109 (26 Dec. 2012), p. 261803.

[101] S. Burdin, A. Firan and W. Taylor. *A Search for Magnetic Monopoles at ATLAS*. Tech. rep. ATL-PHYS-INT-2013-009. Geneva: CERN, Mar. 2013.

List of Figures

List of Tables

Acknowledgments

Foremost, I would like to thank **Prof. Dr. Klaus Desch** for getting me involved in particle physics early on in Freiburg, talking me into coming to Bonn for my Diploma thesis and keeping me on his team for a PHD. I am especially grateful for the 18 month I was able to spend at CERN. I have moved a lot, but it was all worth it. Thank you for your continuous support, the good working atmosphere and freedom in the choice of my PHD topic.

A special thanks goes to **Philip Bechtle**, who gave excellent feedback about this thesis and regularly dropped by just to see how things were going. I thank **Peter Wagner** for proof-reading this thesis under very tight time constraints.

I would like to thank my colleagues of THE HIGH ENERGY OFFICE: **Thorsten Krautscheid**, **Martin Schultens** and **Michael Lupberger** for making each working day a more agreeable experience than the one before. In addition, **Adrian Vogel**, **Mathias Uhlenbrock**, **Steffen Schaepe**, **Jan Stillings**, **Martin Schultens** and **Till Nattermann** have been part of the CERN experience and I am very happy to have shared it with them. Further thank goes to the Desch group creative department, which constructed my Doktorwagen and Doktorhut (see pictures below), everybody in the groups Desch and Brock for merry times throughout the year and even more so during jamborees and christmas parties. I am grateful to **Prof. Dr. Ian Brock** for being my second referee and for providing the LaTeX template for this thesis.

None of the work that lead to this thesis happened without the participation of **Markus Jüngst**. He was a driving force in both the development of the TRT $\mathrm{d}E/\mathrm{d}x$ and the multi-charged particle analysis. I am very grateful for uncounted hours of lively discussions, in-depth explanations, fantastic team work and all the fun times both during and outside working hours.

Likewise, I would like to thank **Christopher Marino** for all his help and support, the weekly coffee or skype meetings, his leading role in this analysis, proof-reading my thesis and all the little things that made it such a pleasure to work with him.

A big thank goes to the whole analysis team of the multi-charged particle search for an exceptionally good team work: **Christopher Marino**, **Markus Jüngst**, **Yury Smirnov**, **Harold Ogren**, **Daria Zieminska**, **Anatoli Romaniouk**, **Oleg Bulekov**, **Ben Weinert** and **Ari Eisenstadt**. It really was a pleasure working with you. I would like to emphasize the huge help I got from Yury in preparing this thesis by providing custom-made plots in fast turn-around times. Thank you for this good collaboration.

I am grateful to **Maxim Khlopov** and **Konstantin Belotsky** for their support on the theoretical models motivating this search, as well as **Wendy Taylor** and **Philip Mermod** for their support.

Furthermore, I would like to thank **Michael Hauschild** for sharing his deep knowledge on $\mathrm{d}E/\mathrm{d}x$ and **Christoph Rembser** for the important role he played during my time at CERN introducing me to future collaborators and as chair of our Editorial Board.

I thank **Marc Lehmacher** and **Jasmin Vural** for proof-reading parts of this thesis and even more so for enriching my life in Bonn.

Muito obrigada também ãos groupos de capoeira em Bonn e Genebra: Capoeira Equilibrio Bonn, Mestre Indío, e Groupo de Capoeira Angola Africa Bantu, Mestre Braga.

A late thank goes to **Martin Killenberg** and **Jochen Kaminski** for their support during my diploma thesis.

I thank THE GROUP: **Moritz Thomann**, **Florian Posdziech**, **Jochen Barwind**, **Josip Mihaljevic** and **Jannes Harder**, for accompanying me through the semesters in Freiburg.

Ein ganz besonderer Dank gilt meiner Familie, **Brigitte, Bernd und Elmar Zimmermann**.